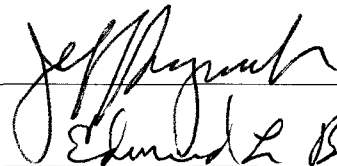


**NUMERICAL STUDIES OF TECTONIC AND LANDSLIDE-GENERATED
TSUNAMIS CAUSED BY THE 1964 GREAT ALASKA EARTHQUAKE**

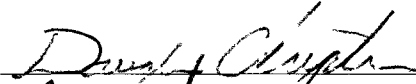
By

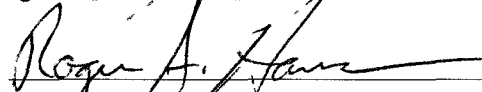
Elena Suleimani

RECOMMENDED:







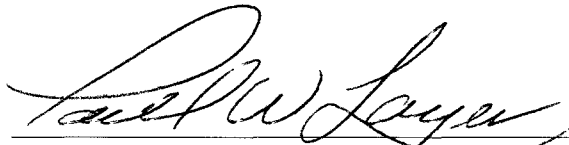


Advisory Committee Chair

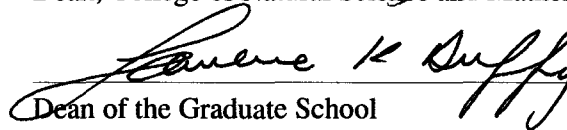


Chair, Department of Geology and Geophysics

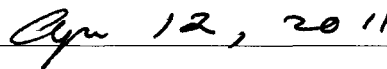
APPROVED:



Dean, College of Natural Science and Mathematics



Dean of the Graduate School



Date

**NUMERICAL STUDIES OF TECTONIC AND LANDSLIDE-GENERATED
TSUNAMIS CAUSED BY THE 1964 GREAT ALASKA EARTHQUAKE**

**A
THESIS**

**Presented to the Faculty
of the University of Alaska Fairbanks
in Partial Fulfillment of the Requirements
for the Degree of**

DOCTOR OF PHILOSOPHY

By

Elena Suleimani, B.S., M.S.

Fairbanks, Alaska

May 2011

©2011 Elena Suleimani

UMI Number: 3463945

All rights reserved

INFORMATION TO ALL USERS

The quality of this reproduction is dependent upon the quality of the copy submitted.

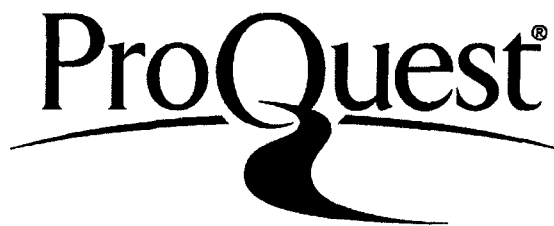
In the unlikely event that the author did not send a complete manuscript and there are missing pages, these will be noted. Also, if material had to be removed, a note will indicate the deletion.



UMI 3463945

Copyright 2011 by ProQuest LLC.

All rights reserved. This edition of the work is protected against unauthorized copying under Title 17, United States Code.



ProQuest LLC
789 East Eisenhower Parkway
P.O. Box 1346
Ann Arbor, MI 48106-1346

Abstract

The focus of my thesis is on the complex source mechanism of tsunami waves generated by the M_w 9.2 1964 Alaska earthquake, the largest instrumentally recorded earthquake in North America. The vertical seafloor displacements produced a trans-Pacific tectonic tsunami that caused loss of life and great damage in Alaska and the west coast of the United States and Canada. In addition to the major tectonic wave, about 20 local tsunamis were generated by submarine mass failures in a number of bays and fjords in south-central Alaska. These locally generated waves caused most of the damage and accounted for 76% of tsunami fatalities.

I use numerical modeling to study tectonic and landslide tsunamis of the 1964 earthquake. The first part of the thesis presents numerical analysis of tsunami inundation at Seward and other locations in Resurrection Bay caused by the combined impact of landslide-generated waves and the tectonic tsunami. This study utilizes the recent geological findings of large-scale submarine slope failures in the bay during the 1964 earthquake and confirms the hypothesis that tsunami waves observed in Seward during and immediately after the earthquake resulted from multiple underwater landslides. The analysis of the simulated composite inundation area caused by the two different tsunami sources explains their relative contributions and demonstrates good agreement with observations.

The second major topic is the source of the 1964 tectonic tsunami. The results of inundation modeling in Kodiak Island show that tsunami runup in the near field strongly depends on coseismic slip in the Kodiak asperity. I test the hypothesis that splay faults played a major role in tsunami generation and evaluate the extent of the Patton Bay fault using near-field tsunami observations. The new source function of the 1964 tsunami is presented, which includes the effects of the splay fault displacements and the component of the vertical deformation of the sea surface due to horizontal displacements on the megathrust.

The results of numerical modeling studies included in this thesis complement the Alaska Tsunami Inundation Mapping Project. This activity provides emergency officials in coastal Alaska with tsunami hazard assessment tools and helps mitigate future tsunami risk.

Table of Contents	Page
Signature Page	i
Title Page	ii
Abstract	iii
Table of Contents	iv
List of Figures	vii
List of Tables	xi
Acknowledgements	xii
Chapter 1 General Introduction	1
1.1 Tsunami hazard in Alaska	3
1.2 Sources of tsunami waves during the M_W 9.2 1964 Alaska earthquake	4
1.3 Numerical modeling of tsunami evolution	6
1.4 Thesis structure	8
Bibliography	10
Figures	14
Chapter 2 Numerical study of tsunami generated by multiple submarine slope failures in Resurrection Bay, Alaska, during the M_W9.2 1964 earth- quake	16
2.1 Abstract	16
2.2 Introduction	16
2.3 Tsunami hazard in Resurrection Bay	18
2.3.1 Study area and tsunami waves of March 27, 1964	19
2.3.2 Justification for the study	20
2.4 Model description	22
2.4.1 Model equations	23
2.4.2 Data	25
2.5 Numerical simulation of the 1964 landslides and tsunami	25
2.5.1 Movement of the sediments and propagation of surface waves	26
2.5.2 Simulated wave records	27
2.6 Discussion and conclusions	29

2.7	Acknowledgments	30
	Bibliography	32
	Tables	36
	Figures	37
Chapter 3	Combined effects of tectonic and landslide-generated tsunami	
	runup at Seward, Alaska during the M_w9.2 1964 earthquake	48
3.1	Abstract	48
3.2	Introduction	49
3.3	Tsunami hazard in south-central Alaska	51
	3.3.1 Tectonic tsunami hazard	52
	3.3.2 Landslide tsunami hazard	53
	3.3.3 1964 tsunami in Resurrection Bay: history and observations	54
	3.3.4 Previous studies	55
3.4	Methodology	58
	3.4.1 Model description	58
	3.4.2 Data and numerical grids	60
3.5	Tsunami sources	62
	3.5.1 Justification of separation of source mechanisms	62
	3.5.2 Landslide tsunami sources	63
	3.5.3 Tectonic tsunami sources	63
3.6	Numerical simulations	65
	3.6.1 Inundation of Resurrection Bay by landslide-generated waves	66
	3.6.2 Inundation of Resurrection Bay by a tectonic tsunami	68
3.7	Conclusions	70
3.8	Acknowledgments	72
	Bibliography	73
	Figures	79
Chapter 4	Inundation Modeling of the 1964 tsunami in Kodiak Island, Alaska	89
4.1	Abstract	89
4.2	Introduction	89
4.3	Numerical Model	90

4.4	The Source Model for the 1964 Tsunami	91
4.5	Modeling of the 1964 Tsunami in Kodiak	93
4.6	Discussion	95
4.7	Acknowledgments	96
	Bibliography	97
	Figures	99
Chapter 5	Near-field modeling of the 1964 Alaska tsunami: a source function study	106
5.1	Abstract	106
5.2	Introduction	107
5.3	Methodology	111
5.3.1	Tsunami data	112
5.3.2	Numerical model and grids	113
5.4	Existing coseismic deformation models of the 1964 earthquake	114
5.4.1	Review of the previous studies	115
5.4.2	Modeling and analysis	117
5.5	The new source function of the 1964 tsunami	119
5.5.1	Discretization of the fault geometry	119
5.5.2	Splay fault contribution to the local tsunami wave field	121
5.5.3	Contribution of horizontal displacements to tsunami generation	126
5.5.4	Coseismic slip in the Kodiak asperity	131
5.6	Discussion and conclusions	136
5.7	Acknowledgments	139
	Bibliography	140
	Tables	146
	Figures	147
Chapter 6	General Conclusions	177

List of Figures		Page
1.1	Locations of aftershock zones of major tsunamigenic earthquakes along the Aleutian Megathrust	14
1.2	The Prince William Sound and Kenai Peninsula areas	15
2.1	Location map of Resurrection Bay and Seward in the Gulf of Alaska	37
2.2	Bathymetric map of the northern end of Resurrection Bay	38
2.3	Oblique bathymetric image, overlain with aerial photograph, of the northwest corner of Resurrection Bay, offshore of the Seward waterfront	39
2.4	Geometry of a submarine landslide	40
2.5	Reconstructed thicknesses and initial extent of slide bodies that were mobilized during the 1964 earthquake	41
2.6	Snapshots from the numerical simulation of slide mass	42
2.7	Snapshots from the first minute of numerical simulation of surface waves in Resurrection Bay generated by the moving slide mass	43
2.8	Snapshots from numerical simulation of surface waves in Resurrection Bay generated by the moving slide mass	44
2.9	Simulated water level at Seward downtown	45
2.10	Simulated water level at Fourth of July Creek	46
2.11	Simulated water level at Lowell Point	47
3.1	Map of south-central Alaska with the rupture zone of the $M_w9.2$ 1964 Great Alaska earthquake	79
3.2	Multibeam bathymetric image of Resurrection Bay	80
3.3	Observed 1964 inundation line at Seward, shown by the dashed yellow contour (from <i>Lemke (1967)</i>), and inundation limits calculated for different tectonic tsunami sources and the landslide source	81
3.4	Observed 1964 inundation line at the head of Resurrection Bay, shown by the dashed yellow contour (from <i>Lemke (1967)</i>), and inundation limits calculated for different tectonic tsunami sources and the landslide source . .	82

3.5	A diagram that shows vertical tectonic land changes during and after the 1964 earthquake	83
3.6	Reconstructed thicknesses and initial extent of the three major slide complexes in the upper Resurrection Bay	84
3.7	Vertical coseismic displacements calculated from each of the three deformation models	85
3.8	Inundation limits calculated for different tectonic tsunami sources and the landslide source at Lowell Point	86
3.9	Inundation limits calculated for different tectonic tsunami sources and the landslide source at Fourth of July Creek	87
3.10	Simulated tectonic tsunami waveforms at Seward waterfront for three different source functions	88
4.1	Area map and slip distribution of the 1964 rupture	99
4.2	Coseismic vertical deformation of the 1964 earthquake	100
4.3	Computed and observed tsunami amplitudes at the tide gauges in Sitka and Yakutat	101
4.4	The Kodiak Island grid of 24 arc-second resolution	102
4.5	Observed and computed inundation lines for the Kodiak downtown area	103
4.6	Observed and computed inundation lines for the US Coast Guard Base	104
4.7	Computed wave history at the Kodiak Naval Station	105
5.1	Map of south-central Alaska	147
5.2	Tsunamigram that shows observed runup heights of the 1964 tsunami along the Kenai Peninsula coast and the Kodiak Island coast	148
5.3	The Kenai Peninsula and Prince William Sound areas	149
5.4	The Kodiak Island area	150
5.5	Kodiak City and Kodiak Naval Station in the St. Paul Harbor	151
5.6	Embedded numerical grids of increasing resolution	152
5.7	Vertical coseismic displacements in the 1964 rupture area	153
5.8	Maximum tsunami amplitudes along the West Coast of the United States and Canada	154

5.9	Maximum tsunami amplitudes in the Kodiak area and in the Prince William Sound area	155
5.10	Time series at points 1-4 on Kenai Peninsula	156
5.11	Time series at points 6-10 on Kodiak Island	157
5.12	Estimated coseismic slip distribution (modified from <i>Suito and Freymueller</i> (2009)	158
5.13	Discretization of finite elements of the slip model by <i>Suito and Freymueller</i> (2009) using the rectangular Okada-type subfault elements	159
5.14	Calculated vertical deformations in the 1964 rupture area corresponding to the coseismic slip model of <i>Suito and Freymueller</i> (2009)	160
5.15	Calculated vertical coseismic deformations due to displacements on the splay fault	161
5.16	Calculated vertical coseismic deformations in the 1964 rupture area corresponding to different extents of the splay fault	162
5.17	Simulated time series of tsunami waves at Rocky Bay and Seward for 4 different source functions of the splay fault	163
5.18	Simulated time series of tsunami waves at Whidbey Bay and Puget Bay for 4 different source functions of the splay fault	164
5.19	The location of the splay fault with respect to the rupture on the megathrust in the coseismic model	165
5.20	Time series points in the far field, along the West Coast of the United States and Canada	166
5.21	Simulated time series of tsunami waves in the far field at Yakutat, Sitka, Tasu Sound and Alert Bay for 3 different source functions	167
5.22	Simulated time series of tsunami waves in the far field at Tofino, Astoria, Presidio and Hilo for 3 different source functions	168
5.23	The diagram illustrating mechanism of tsunami generation by horizontal motion of the ocean bottom	169
5.24	Calculated sea surface displacement due to horizontal motion of the sea floor during the 1964 earthquake	170

5.25 Maximum tsunami amplitudes due to horizontal deformations of the ocean bottom 171

5.26 Simulated time series of tsunami waves generated by vertical motion of the bottom and by the combined vertical and horizontal motion 172

5.27 The resulting vertical coseismic deformations in the 1964 rupture area, derived from the superposition of vertical and horizontal displacements of the megathrust and the vertical displacements on the splay fault of the optimal extent 173

5.28 Simulated maximum tsunami amplitudes in the 8-arcsecond grid of Kodiak Island 174

5.29 Simulated time series of tsunami waves at 4 locations on Kodiak Island . . 175

5.30 Simulated time series of tsunami waves at the Kodiak Naval Station and at the City of Kodiak 176

	List of Tables	Page
2.1	Observations at the Seward waterfront during the earthquake	36
5.1	Compilation of tsunami observations collected after the 1964 earthquake in the Gulf of Alaska	146

Acknowledgements

First and foremost, I am very grateful to my dear parents Eliazveta I. and Nikolai G. Troshin for their endless love, support, encouragement, and readiness to fly to Alaska every time I needed them here. They did everything they could to help me graduate. This work is dedicated to them.

I would like to thank my thesis advisor Roger Hansen for financial support and for his understanding and patience during years of my graduate studies, when I tried to multi-task while being a working mother and a student. I am very grateful for support and advice given to me over the years by the members of the graduate advisory committee: Dr. Jeff Freymueller, Dr. Doug Christensen and Dr. Ed Bueler.

My special thanks go to Dr. Jeff Freymueller who provided valuable guidance on different aspects of my research and practical advice on all issues related to graduate studies, from helping me to define the scope of my thesis to outlining the major problems that I needed to solve in order to present a meaningful piece of work. I am very grateful to Jeff for his willingness to discuss any topics of my research and answer any questions that I had regardless of Jeff's geographical location. His comments on my thesis were extremely helpful. Jeff spent a great deal of time guiding me on the source function study of the 1964 earthquake, and I am grateful for a chance to work with him on such an interesting problem.

I am very grateful to my colleague Dr. Dmitry Nicolsky for developing the Alaska Tsunami Online Mapping web interface, and for providing help in using it. If I have not had this great tool, I would not have been able to perform and analyze as many tsunami model runs. I greatly appreciate his substantial contribution to the tsunami inundation model, and the excellent job he has done on benchmarking and validating the model, and porting the parallelized code on a supercomputer. I am also thankful to him for convincing me to switch from IDL to Matlab, and for answering all my mathematical and numerical questions.

A am particularly thankful to Mitch Robinson, the system administrator of the Seismology Lab, who was always ready to help me with any computer problems, and who is a great person and a co-worker.

I am fortunate to have been working for years with Rod Combellick, from whom I

constantly learn about tectonics and geology of Alaska. I greatly appreciate his excellent knowledge of English grammar and style, and that he is always happy to explain inconsistencies of the English language to me as a non-native speaker. I am grateful for a chance to learn from Rod and to share with him my interest in grammar.

I take particular pleasure in acknowledging Dr. Peter Haeussler, who was my co-author on two out of four papers included in this study. I have learned from him about sedimentation of glacial fjords and different methods used to study this process. He gave me invaluable advice during my research of tsunamis in Resurrection Bay, and helped me greatly in preparation of the manuscripts. I am also thankful to the USGS scientists Holly Ryan and Homa Lee for providing me with data on submarine slides in Seward and for many interesting and productive discussions on the landslide-generated tsunamis in Alaska.

I give many thanks to all members of the Arctic Region Supercomputing Center (ARSC) user support group who were always helpful in answering my questions. I want to express my sincere appreciation to Tom Logan, the HPC specialist at ARSC, who contributed a great amount of his time and effort improving my original tsunami code and optimizing it for the high performance computing. I am thankful to ARSC specialists Dr. Sergei Maurits and Dr. Miho Aoki for their impressive work on visualization of computational results.

Several people deserve special mention here. Prof. Efim N. Pelinovsky, who was the advisor of my first thesis written on tsunami waves, always provided me with help and encouragement. I am glad that finally he can put a check mark next to my name in the list of his graduate students. I greatly enjoyed the Geophysical Fluid Dynamics course taught by Dr. David Newman. I am thankful to him for teaching us the invaluable skill of making effective scientific talks and poster presentations. I am thankful to Dr. John Eickelberger for his advice and support. He is a great teacher and an inspirational and enthusiastic science leader. I owe a debt of gratitude to my dear friends Tatiana and Andrey Proshutinsky for everything they did for me when I first arrived to Alaska to become a graduate student. No words can express how much I appreciate their friendship and love. Just when my life in Fairbanks became relatively stable and comfortable, Tatiana reminded me that my original *raison d'être* in Alaska was to get a Ph.D. degree, and my only choice was to become a student again. My special thanks go to Diana Lingle who supported me during difficult times. It is great to know that this wonderful person is my friend, and that she is a phone

call away. Completing my degree was also possible because of Dr. Craig Lingle, who gave me a precious advice that in order to finish writing a thesis one needs to start writing it. He has taught me useful strategies of putting together a thesis research plan and then turning it into a readable manuscript. I am grateful to my longtime friend Natasha Ruppert for her support, encouragement and believing in my ability to get the work done and to finish the thesis.

I have been fortunate to be a part of the Seismology Lab at the Geophysical Institute. Thanks to all of you who made the Lab and the Alaska Earthquake Information Center a great place to work. It was a pleasure to share the office with Dave West, the ArcGIS Coordinator, who helped me with analyzing spatially distributed data and preparing figures for papers and reports. I also thank Peter Hickman for his help with ArcGIS projects. Deb Coccia suggested for me to learn the Adobe CS and was always ready to answer my never-ending questions. She helped me to put together a number of poster presentations, and I had a chance to appreciate her professionalism and impeccable taste as a graphics designer. I am grateful to all former UAF graduate students who contributed to the LaTeX style file that I used in this thesis.

I have very special feelings of appreciation and love for my family. My husband Sergei and my children Alexander and Catherine were supportive and patient during years of my graduate study. I could always rely on love, support and help from my brother Alexander and his family.

Numerical calculations for this study were supported by a grant of High Performance Computing resources from the Arctic Region Supercomputing Center at the University of Alaska Fairbanks as part of the US Department of Defense HPC Modernization Program. This work was funded by the Geophysical Institute of the University of Alaska Fairbanks, by the National Oceanic and Atmospheric Administration grant NA08AR4320751 through Cooperative Institute for Arctic Research, and by the State of Alaska Reimbursable Service Agreement 0911032.

This work is dedicated to my parents Elizaveta I. and Nikolai G. Troshin. All I have achieved was possible because of their love, encouragement and sacrifices.

Chapter 1

General Introduction

The catastrophic waves that killed more than 230,000 people on December 26, 2004 have forever changed the definition of the word "tsunami". Its meaning was elevated in destructive power from just an infrequent though potentially deadly natural disaster to one capable of inflicting hundreds of thousands of fatalities and reaching every coastline on earth. In the new frame of reference, tsunamis are more threatening in the ever more crowded world. Past tsunamis in Indonesia killed thousands of people: 36,500 perished after the 1883 Krakatoa volcanic tsunami, the 1861 tsunami accounted for 1,700 fatalities, 3,620 people were killed by the tsunami waves of 1899, and 1,500 residents of Flores Island, Indonesia became victims of the 1992 tsunami (*Bernard, 2001*). People tend to forget. The knowledge about the tsunami danger in the region was not passed on to the younger generations. The troubling stories told by survivors about local children running to the shore to gather fish after the initial drawdown of water demonstrated the absence of tsunami preparedness in the Indian Ocean region (*Tyson, 2005*). Even more astonishing was the similar behavior of tourists from developed countries who obviously missed the media coverage of the number of destructive tsunamis at the end of the 20th century, and lacked basic knowledge about tsunami warning signs (*Synolakis, 2006*). However, the shift in paradigm caused by the tragic lessons learned from the Indian Ocean tsunami of 2004 can be used to reduce the potential damage and fatalities from future tsunamis. Ultimately the success of any tsunami mitigation program will be determined by the survival rate of those threatened. If the public recognizes the warning signs and takes the correct steps, many lives will be saved.

Tsunamis are impulsively generated long gravity water waves. They may be caused by earthquakes, submarine and subaerial landslides, volcanic eruptions, nuclear explosions or asteroid impacts. Tsunamis are characterized as shallow water waves with phase speed controlled by the depth as $c = \sqrt{gH}$, where g is gravitational acceleration and H is the water depth. The wavelengths of tsunamis vary from 20 to 1000 *km* and are much greater than the average ocean depth. In the deep ocean they travel with a speed of several hundred kilometers per hour and an amplitude of the order of a meter. Tsunamis are capable of propagating across great distances, retaining their wave energy and destructive force. As

the tsunami wave enters the continental shelf it slows down, and the wavelength shortens in order to maintain its period. Since the total energy is conserved, the energy density increases and the wave amplitude grows. This increase in amplitude due to shoaling, together with refraction and local resonance effects, results in devastating waves.

The scientific understanding of tsunamis has developed substantially over the past two decades, but the largely unexpected disaster of 2004 prompted the global community of tsunami scientists, emergency managers and educators to reevaluate goals and redirect efforts. In his analysis of the current state of tsunami research and its future, *Synolakis* (2006) outlined several critical directions in which developments and breakthroughs are needed: the continuous improvement of tsunami numerical models through testing and validation, understanding the tsunami forces on structures, mapping the continental margins at high resolution for better offshore hazard assessment, and understanding the tsunami source mechanism, or how the initial tsunami wave field is produced by the movements of the seafloor. He pointed out that our current understanding of this important process is marginal, especially for the near-field forecasting of extreme tectonic tsunamis and local landslide-generated waves. The complex source of the 2004 tsunami is considered to be comparable with the two other great subduction zone earthquakes of the recorded history - the M_W 9.5 1960 Chile earthquake and the M_W 9.2 1964 Alaska earthquake. *Plafker et al.* (2006) analyzed data from all 3 events and found that in each case about 75% of the fatalities and most of the damage were caused by local near-field tsunamis. He argues that two factors were responsible for that: slip on relatively steep intraplate splay faults that made the initial tsunami wave higher and closer to the shore, and submarine slides triggered by strong ground shaking in steep-sided fjords. These two factors were combined during the 1964 Alaska tsunami and probably during the 1960 Chile tsunami. The 1964 Alaska tsunami fits into the category of tsunami disasters for which near-field tsunami forecasting is extremely complicated due to proximity of the earthquake rupture zone to the coastal area, and susceptibility of the glacial fjord environment to underwater slope failures. The study of its complex source mechanism therefore provides insights into the tsunami potential of great subduction zone earthquakes.

1.1 Tsunami hazard in Alaska

Alaska has the greatest earthquake and tsunami potential among the U.S. states. Figure 1.1 shows one of the most seismically active regions of the state where the Pacific Plate is subducting under the North American Plate. This subduction zone has a history of producing large and great earthquakes and generating both local and Pacific-wide tsunamis. The most recent sequence of earthquakes began in 1938 and ruptured almost the entire Aleutian arc (*Nishenko and Jacob, 1990*). The Alaska-Aleutian subduction zone makes the adjacent coastal areas especially hazardous with regard to tsunami exposure. The co-seismic crustal movements that characterize this area have a high potential for producing tsunamigenic seafloor displacements. Historic tsunamis that were generated by earthquakes on the Alaska-Aleutian subduction zone have resulted in widespread damage and loss of life along the Alaskan Pacific coast and other exposed locations around the Pacific Ocean (*Lander, 1996*). In each event, the damage caused by the waves considerably exceeded the consequences of the tsunamigenic earthquake itself.

All of the most recent earthquakes of 1938, 1946, 1957, 1964 and 1965 were tsunamigenic. The tsunami generated by the 1946 earthquake killed 5 people in Alaska and 159 in Hawaii, devastating the town of Hilo. As a response to this event, the Pacific Tsunami Warning Center was established in Honolulu, and the official tsunami warning system in the US became operational in 1949. On March 27, 1964, the Prince William Sound area of Alaska was struck by the largest earthquake ever recorded in North America. This magnitude $M_W 9.2$ megathrust earthquake generated the most destructive historic tsunami in Alaska, which impacted the west coast of the United States and Canada. Of the 131 fatalities associated with this earthquake, 122 were caused by tsunami waves (*Lander, 1996*). Although tragic, the number of deaths was fortunately far smaller than in the case of the 2004 Indian Ocean tsunami due to low population density on the Alaska coast. The regional Alaska Tsunami Warning Center was established in 1967 as a direct result of this earthquake in order to provide efficient tsunami warnings to the coastal areas of Alaska.

Tsunamis caused by submarine slope failures are also a serious hazard in glacial fjords of coastal Alaska (*Lee et al., 2002*). In a fjord environment, where the sediment is deposited rapidly, the sediment builds up pore-water pressures and could liquefy under extreme low tide conditions or ground shaking due to low static shear strength (*Hampton et al., 1996*).

The analysis of the tsunami catalog data for the North Pacific coast showed that this region has a long history of tsunami waves generated by submarine and subaerial landslides, avalanches and rockfalls (*Kulikov et al.*, 1998). It was also found that, in the majority of cases, tectonic tsunamis that arrived in bays and fjords from the open ocean were relatively small, but a great number of local landslide-generated tsunamis had much larger wave amplitudes.

Tectonic tsunamis originating in Alaska can travel across the Pacific Ocean and impact coastal areas hours after they are generated. However, these waves are a near-field hazard for Alaska, and can reach Alaskan coastal communities within minutes of the earthquake. Therefore, saving lives and property depends on how well a community is prepared, which makes it essential to estimate the potential flooding of the coastal zone in the case of a local or distant tsunami. The Alaska Earthquake Information Center conducts tsunami inundation mapping for coastal communities in Alaska, providing guidance to local emergency officials in tsunami hazard assessment (*Suleimani et al.*, 2002, 2005, 2010). One of the motivations for the work presented in this thesis is the value of the 1964 tsunami observations and measurements for the Alaska Tsunami Mapping project. For many locations in the Gulf of Alaska, the 1964 tsunami generated by the M_w 9.2 Great Alaska earthquake could be the credible worst-case tsunami scenario, since it was well documented and extensively studied. The numerical modeling studies that are included in this thesis are useful for tsunami inundation mapping of coastal communities located in seismically active regions, where tectonic tsunami hazard is combined with susceptibility of the fjord environment to underwater slope failures and locally generated waves.

1.2 Sources of tsunami waves during the M_w 9.2 1964 Alaska earthquake

The impact of coseismic crustal deformations on the ocean surface and on numerous water bodies in Alaska was very complex. In addition to the major tectonic wave that was generated by the displacement of the ocean floor between the trench and the coastline, about 20 local tsunamis were generated in a number of bays in south-central Alaska (*Lander*, 1996). Local tsunamis caused most of the damage and accounted for 76% of tsunami fatalities. Also, they arrived almost immediately after the shaking was felt, leaving no time for warning or evacuation. Local waves were generated by submarine mass failures from the

steep fjord walls, and also by other mechanisms, such as seiches and subaerial landslides (*Plafker et al.*, 1969). The seiches included free oscillations induced by tilting of water basins as a result of coseismic deformations in the rupture area and those initiated by landslides, and probably forced oscillations caused by passing of seismic waves. Figure 1.2 shows the coast of south-central Alaska that has numerous glacial fjords and is located at the south-eastern end of the 1964 rupture. It presents data compiled by *Plafker et al.* (1969) on the known and inferred subaqueous slides that were triggered by strong ground shaking during the 1964 earthquake. The figure shows that most of the slides occurred along the shores of the bays in northern and western Prince William Sound, and on the south coast of Kenai Peninsula. Based on the analysis of the documented runup data, *Plafker et al.* (1969) noted that the distribution of damage was highly localized and erratic. Figure 1.2 also shows large runup heights observed on the shores of the islands west of Montague Island, which were probably associated with underwater slides, seiches or displacements on local splay faults. *Plafker et al.* (1969) points that an important characteristic of the local waves observed at multiple locations is that single large waves struck during the earthquake or immediately after it. There were many nondestructive sudden water disturbances observed almost everywhere on the coast. This local wave action had largely subsided by the time the initial crest of the tectonic tsunami arrived.

The major tectonic tsunami was generated by vertical coseismic displacements that occurred over an area of about 285,000 km² in south-central Alaska (*Plafker*, 1969). The uplift and subsidence of the sea floor due to the earthquake rupture process caused the displacement of the free water surface, and the long gravity ocean waves propagated away from the earthquake source area. The tectonic tsunami wave train affected the entire south-central coast of Alaska, but it was most damaging along the shores of the Kodiak group of islands and the Kenai Peninsula, the areas that subsided during the earthquake (*Plafker et al.*, 1969). The wave action lasted for about 11 hours after the earthquake, and many communities were inundated by 7 to 10 waves with periods from 30 to 90 minutes. Aside from generating damaging waves, the vertical tectonic movements directly affected all coastal communities. The uplift caused docks and piers to get raised even above the highest tide levels, and harbors and channels had to be dredged to restore the pre-earthquake depths (*Plafker et al.*, 1969). Communities located in the area of coseismic subsidence suffered

from inundation by high tides after the earthquake, and had to relocate homes and infrastructure (Waller, 1966; Lemke, 1967). The greatest damage and casualties however were caused by the local landslide-generated waves. There are two groups of factors that contribute to initiation of submarine slides: those related to geological properties of landslide material (e.g. overpressure due to rapid deposition), and the factors associated with external events (e.g. earthquakes or sea level change) (Masson *et al.*, 2006). In the case of the M_w 9.2 1964 Alaska earthquake, the powerful and prolonged ground shaking was the major trigger for multiple submarine and subaerial slides along the coast of south-central Alaska (Figure 1.2). Other factors that contributed to the large scale of landsliding were the steep underwater slopes of the fjords, and the type of sediment forming these slopes - unconsolidated and fine-grained materials (Lemke, 1967). The towns of Seward and Valdez suffered the greatest damage and loss of life due to landslide-generated waves. The geotechnical investigations conducted in these communities right after the earthquake concluded that the stability of the sediment was also decreased by the low tidal level at the time of the earthquake, and by the rapid drawdown of water due to the initial slope failure (Shannon and Hiltz, 1973).

One of the challenges in the near-field tsunami modeling is to account for coseismic and post-seismic tectonic land changes. When numerical modeling is performed in a geographical domain that located entirely inside the earthquake rupture area and therefore inside the tsunami source zone, the seamless DEMs of combined bathymetry and topography data need to be carefully assessed for pre- and post-earthquake survey dates and the vertical datum. The difference between the tidal datum of the numerical grid and the tide stage at the time of the earthquake is also important, since tidal ranges are large along the south-central Alaska coast. Finally, all observations of amplitudes of approaching waves, and records of wave damage and tsunami runup heights were made relative to the water level at the time of the observation. This needs to be taken into account when analyzing numerical modeling results for tsunami amplitudes and arrival times.

1.3 Numerical modeling of tsunami evolution

Numerical modeling is one of the essential tools in tsunami studies. Numerical simulations help to interpret observations from historical tsunamis and to improve our understanding

of the tsunami source. Accurate numerical models are also important for predicting where future far-field tsunamis will strike. For local tsunami events, when there is almost no time for advance warning, models help to estimate a potential inundation area of a coastal zone in case of a tectonic or landslide-generated tsunami. In tsunami hazard mitigation, numerical modeling is a key component of real-time monitoring of tsunami evolution and operational tsunami forecast (*Titov et al., 2005; Geist et al., 2007*).

Modern numerical codes are now capable of describing all three stages of tsunami evolution, from generation of waves by an underwater earthquake or landslide, to deep-ocean tsunami propagation over realistic bathymetry and flooding coastal areas of complex topography. The initial disturbance of the ocean surface during an earthquake evolves into a long gravity wave that propagates across the ocean. The final and the most destructive phase of tsunami evolution is tsunami runup. The hydrodynamical and mathematical problems associated with the motion of water waves on a sloping solid boundary make simulation of the runup process a challenging task (*Imamura, 1996*). The water motion near the runup front is strongly nonlinear in comparison to the motions away from the front. Waves near the front can break, and the flow can become turbulent. Effects of bottom friction also become significant near the wave front as the water depth decreases to zero at the shoreline. An accurate method for estimating wave behavior for the runup phase is important for the prediction of the destructive effects of tsunamis in a coastal zone.

Over the past twenty years, a number of numerical methods have been developed for simulation of tsunami waves. Many of them use the shallow water approximation to the full set of the 3-D Navier-Stokes equations (*Titov and Synolakis, 1995; Imamura, 1996; Goto et al., 1997; Titov and Synolakis, 1998; Lynett et al., 2002; George and LeVeque, 2006; Liu et al., 2007; Zhang and Baptista, 2008; Nicolsky et al., 2010*). The shallow water approximation assumes that the water depth is small in comparison with the characteristic horizontal length scale of the motion, and that the vertical accelerations of water particles are negligible compared to the gravitational acceleration. This approximation has proven to be robust not only for simulation of tsunami propagation in deep ocean but also for prediction of runup of both non-breaking and mildly breaking waves (*Synolakis, 1986*). This property of the shallow water equations make them applicable for modeling tsunami waves in most geophysical scenarios.

In this study we simulate tsunami propagation and inundation with a nonlinear shallow water model that was developed at the Alaska Earthquake Information Center (*Nicolisky et al.*, 2010). The model is formulated for depth-averaged water fluxes in both spherical and rectangular coordinates. The parallel numerical code solves shallow water equations of motion and continuity using a staggered leapfrog finite-difference scheme. This model was validated through a comprehensive set of analytical benchmarks and tested against laboratory and field data, according to the NOAA's requirements for evaluation of tsunami numerical models (*Synolakis et al.*, 2007, 2008).

1.4 Thesis structure

My thesis is a combination of near-field numerical modeling studies of tectonic and landslide-generated tsunami waves during the M_W 9.2 1964 Alaska earthquake. The four central chapters of the thesis are separate articles, three of which have been published and one is prepared to be submitted for publication. I wrote all of them as first author, and I list my co-authors for each paper in the following paragraphs.

Chapter 2 presents numerical analysis of tsunami waves generated by submarine slides in Resurrection Bay, Alaska. This study utilizes the recent geological findings of the large-scale submarine slope failures in the bay during the 1964 earthquake. We use a viscous slide model coupled with nonlinear shallow water equations to confirm the hypothesis that tsunami waves observed in Seward during and immediately after the earthquake resulted from multiple underwater landslides. We investigate the relative contributions of different submarine slide complexes and demonstrate that three slides in the upper bay were the major contributors of tsunami wave energy during and immediately after the earthquake. My co-authors for this paper are Drs. Roger Hansen and Peter J. Haeussler.

Chapter 3 describes the tsunami inundation of Seward, Alaska, during the M_W 9.2 1964 earthquake. This study extends the previous work by calculating tsunami runup at Seward and other locations in Resurrection Bay caused by the combined impact of landslide-generated waves and the tectonic tsunami, and comparing the composite inundation area with observations. It is demonstrated that the calculated tsunami runup in Seward is in good agreement with observations of the inundation zone. The analysis of inundation caused by two different tsunami sources improves our understanding of their relative contributions,

and supports tsunami risk mitigation in south-central Alaska. This paper is co-authored with Drs. Dmitry J. Nicolsky, Peter J. Haeussler, and Roger Hansen.

Chapter 4 presents numerical modeling results for tsunami impact on the communities of Kodiak City and Kodiak Naval Station, Alaska, and analysis of observed and calculated tsunami time series and inundation zones. In this work two different coseismic deformation models of the 1964 rupture are used to generate the initial ocean surface displacement in the tsunami source region. It is shown that the results of the near-field inundation modeling strongly depend on the slip distribution within the rupture area, because the complexity of the source function is combined with the proximity of the coastal zone. While the simulated runup agrees relatively well with the observed inundation, the calculated and observed arrival times at the Kodiak Naval Station are out of phase. Since the arrival times are more sensitive to the fine structure of the tsunami source than the inundation area, it is concluded that more research on the coseismic slip distribution around Kodiak is required for tsunami modeling studies. My co-authors for this paper are Drs. Zygmunt Kowalik and Roger Hansen.

I finish by describing in Chapter 5 the first near-field numerical modeling study of the 1964 tectonic tsunami source mechanism, outlining the important features of the coseismic slip model and the essential components of the numerical algorithm that affect the near-field inundation modeling of tsunami waves. An improved source function of the 1964 tsunami is presented, which includes the effects of splay fault displacements and the vertical deformation of the sea surface due to horizontal displacements on the megathrust. We propose an approach for discretization of the fault geometry and redistribution of slip that can augment future studies of the 1964 tsunami that use observations and measurements in the near field, where the modeling results are highly susceptible to the complexity of the tsunami source. This paper is co-authored with Dr. Jeffrey T. Freymueller.

Bibliography

- Bernard, E. (2001), Recent developments in tsunami hazard mitigation, in *Tsunami Research at the End of a Critical Decade*, edited by G. T. Hebenstreit, pp. 7–15, Kluwer.
- Geist, E. L., V. V. Titov, D. Arcas, F. F. Pollitz, and S. L. Bilek (2007), Implications of the 26 December 2004 Sumatra-Andaman earthquake on tsunami forecast and assessment models for great subduction-zone earthquakes, *Bull. Seism. Soc. Am.*, 97(1A), S249–270, doi:10.1785/0120050619.
- George, D. L., and R. J. LeVeque (2006), Finite volume methods and adaptive refinement for global tsunami propagation and inundation, *Science of Tsunami Hazards*, 24(5), 319–328.
- Goto, C., Y. Ogawa, N. Shuto, and F. Imamura (1997), Numerical method of tsunami simulation with the leap-frog scheme, *Manuals and guides 35*, Intergovernmental Oceanographic Commission of UNESCO: IUGG/IOC TIME Project.
- Hampton, M., H. Lee, and J. Locat (1996), Submarine landslides., *Rev Geophys*, 34, 33–59.
- Imamura, F. (1996), Review of tsunami simulation with a finite difference method, in *Long-Wave Runup Models*, edited by H. Yeh, P. Liu, and C. Synolakis, pp. 25–42, World Scientific.
- Kulikov, E., A. Rabinovich, I. Fine, B. Bornhold, and R. Thomson (1998), Tsunami generation by landslides at the Pacific coast of North America and the role of tides, *Oceanology*, 38(3), 361–367.
- Lander, J. (1996), *Tsunamis affecting Alaska. 1737–1996*, no. 31 in NGDC Key to Geophysical Research, National Geophysical Data Center, Boulder, Colo.
- Lee, H., W. Schwab, and J. Booth (2002), Submarine landslides: an introduction., in *Submarine Landslides: Selected Studies in the US Exclusive Economic Zone*, *US Geological Survey Bulletin*, edited by W. Schwab, H. Lee, and D. Twichell, pp. 1–13.
- Lemke, R. (1967), Effects of the Earthquake of March 27, 1964, at Seward, Alaska, U.S. Geological Survey Professional Paper 542-E, 48 pp.

- Liu, P. L.-F., H. Yeh, and C. Synolakis (Eds.) (2007), *Advanced Numerical Models for Simulationg Tsunami Waves and Runup*, Advances in Coastal and Ocean Engineering, Vol 10, World Scientific, Proceedings of the Third International Workshop on Long-Wave Runup Models, Catalina, 2004.
- Lynett, P., T.-R. Wu, and P.-F. Liu (2002), Modeling wave runup with depth-integrated equations, *Coastal Engineering*, 46(2), 89–107.
- Masson, D., C. Harbitz, R. Wynn, G. Pedersen, and F. Løvholt (2006), Submarine landslides: processes, triggers and hazard prediction, *Phil. Trans. R. Soc. A*, 364, 2009–2039, doi:10.1098/rsta.2006.1810.
- Nicolisky, D., E. Suleimani, and R. Hansen (2010), Validation and verification of a numerical model for tsunami propagation and runup, *Pure Appl. Geophys.*, doi:10.1007/s00024-010-0231-9.
- Nishenko, S., and K. Jacob (1990), Seismic potential of the Queen Charlotte-Alaska-Aleutian seismic zone, *J. Geophys. Res.*, 95(B3), 2511–2532.
- Plafker, G. (1969), Tectonics of the March 27, 1964 Alaska Earthquake, U.S. Geological Survey Professional Paper 543-I, 74 pp.
- Plafker, G., R. Kachadoorian, E. Eckel, and L. Mayo (1969), Effects of the Earthquake of March 27, 1964 on various communities, U.S. Geological Survey Professional Paper 542-G, 50 pp.
- Plafker, G., S. Nishenko, L. Cluff, and M. Syahril (2006), The cataclysmic 2004 tsunami on NW Sumatra - preliminary evidence for a near-field secondary source along the western Aceh Basin, *Seism. Res. Lett.*, 77, 231.
- Shannon, W., and D. Hilts (1973), Submarine landslide at Seward, in *The Great Alaska Earthquake of 1964. Engineering*, pp. 144–156, National Academy of Sciences, Washington, D.C.

- Suleimani, E., R. Hansen, R. Combellick, G. Carver, R. Kamphaus, J. Newman, and A. Venturato (2002), Tsunami hazard maps of the Kodiak area, Alaska, Report of Investigations 2002-1, State of Alaska Department of Natural Resources, Division of Geological and Geophysical Surveys, 16 p., 4 sheets, scale 1:12,500.
- Suleimani, E., R. Combellick, D. Marriott, R. Hansen, A. Venturato, and J. Newman (2005), Tsunami hazard maps of the Homer and Seldovia areas, Alaska, Report of Investigations 2005-2, State of Alaska Department of Natural Resources, Division of Geological and Geophysical Surveys, 28 p., 2 sheets, scale 1:12,500.
- Suleimani, E., D. Nicolsky, P. Haeussler, and R. Hansen (2010), Combined effects of tectonic and landslide-generated tsunami runup at Seward, Alaska, during the M_W 9.2 1964 earthquake, *Pure Appl. Geophys.*, doi:10.1007/s00024-010-0228-4.
- Synolakis, C. (1986), The Runup of Long Waves, Ph.D. thesis, California Institute of Technology, Pasadena, California, 228 pp.
- Synolakis, C. (2006), Tsunami science before and beyond Boxing Day 2004, *Phil. Trans. R. Soc. A*, 364(1845), 2231–2265, doi:10.1098/rsta.2006.1824.
- Synolakis, C., E. Bernard, V. Titov, U. Kânoğlu, and F. González (2007), Standards, criteria, and procedures for NOAA evaluation of tsunami numerical models, *NOAA Tech. Memo. OAR PMEL-135, NTIS: PB2007-109601*, NOAA/Pacific Marine Environmental Laboratory, Seattle, WA, 55 pp.
- Synolakis, C., E. Bernard, V. Titov, U. Kânoğlu, and F. González (2008), Validation and verification of tsunami numerical models, *Pure Appl. Geophys.*, 165, 2197–2228.
- Titov, V., and C. Synolakis (1995), Modeling of breaking and nonbreaking long-wave evolution and runup using VTCS-2, *Journal of Waterway, Port, Coastal and Ocean Engineering*, 121(6), 308–316.
- Titov, V., and C. Synolakis (1998), Numerical modeling of tidal wave runup, *J. Waterw. Port Coast. Ocean Eng.*, 124, 157–171.

- Titov, V., F. Gonzalez, E. Bernard, M. Eble, H. Mofjeld, J. Newman, and A. Venturato (2005), Real-time tsunami forecasting: challenges and solutions, *Nat. Hazards*, 35(1), 35–41.
- Tyson, P. (2005), Wave of the future, NOVA, "Wave that shook the world", <http://www.pbs.org/wgbh/nova/tsunami/wave.html>.
- Waller, R. (1966), Effects of the Earthquake of March 27, 1964, in the Homer area, Alaska, U.S. Geological Survey Professional Paper 542-D, 28 pp.
- Zhang, Y., and A. Baptista (2008), An efficient and robust tsunami model on unstructured grids. Part I: Inundation benchmarks, *Pure Appl. Geophys.*, 165, 2229–2248.

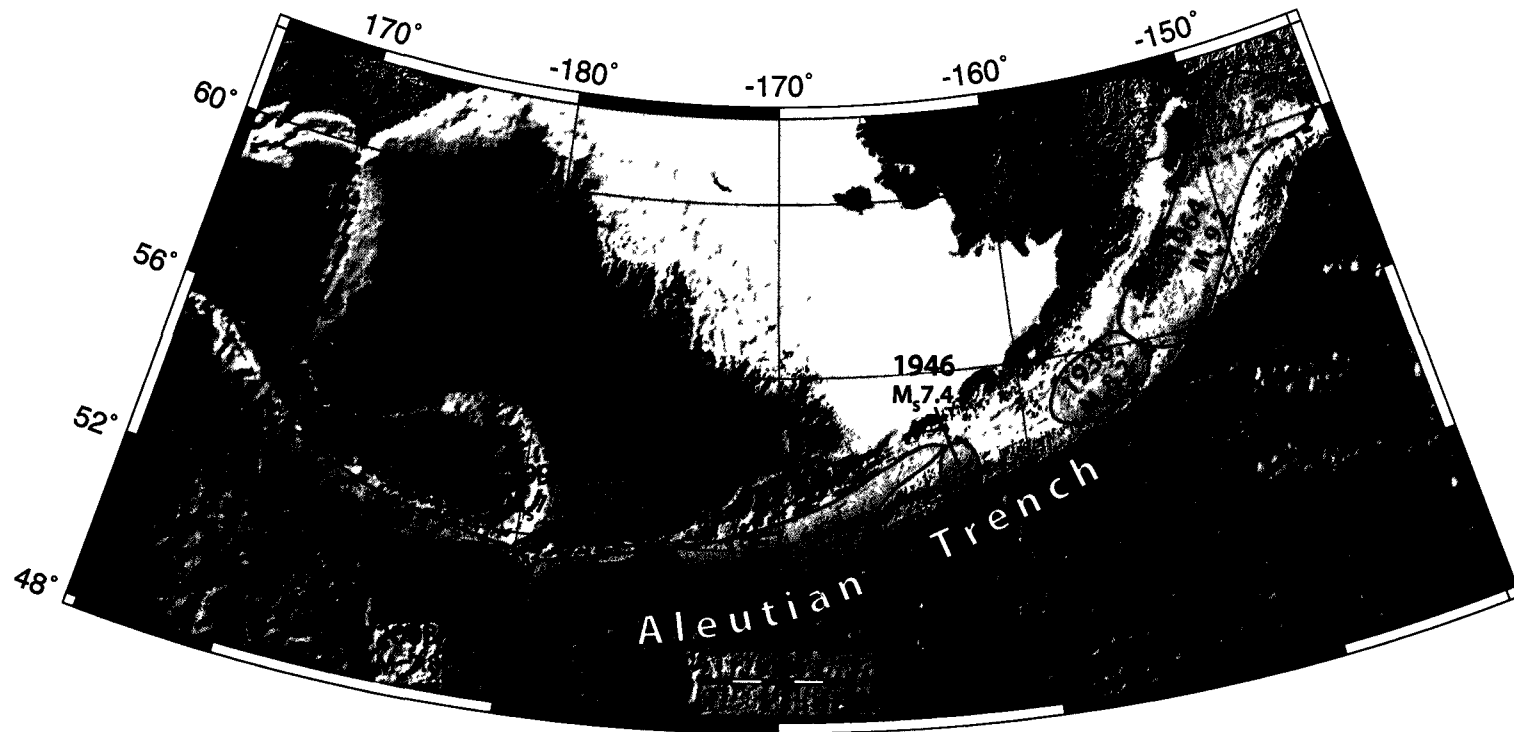


Figure 1.1: Locations of aftershock zones of major tsunamigenic earthquakes along the Aleutian Megathrust. The dashed rectangle outlines the Prince William Sound and Kenai Peninsula areas, shown in detail in Figure 1.2.

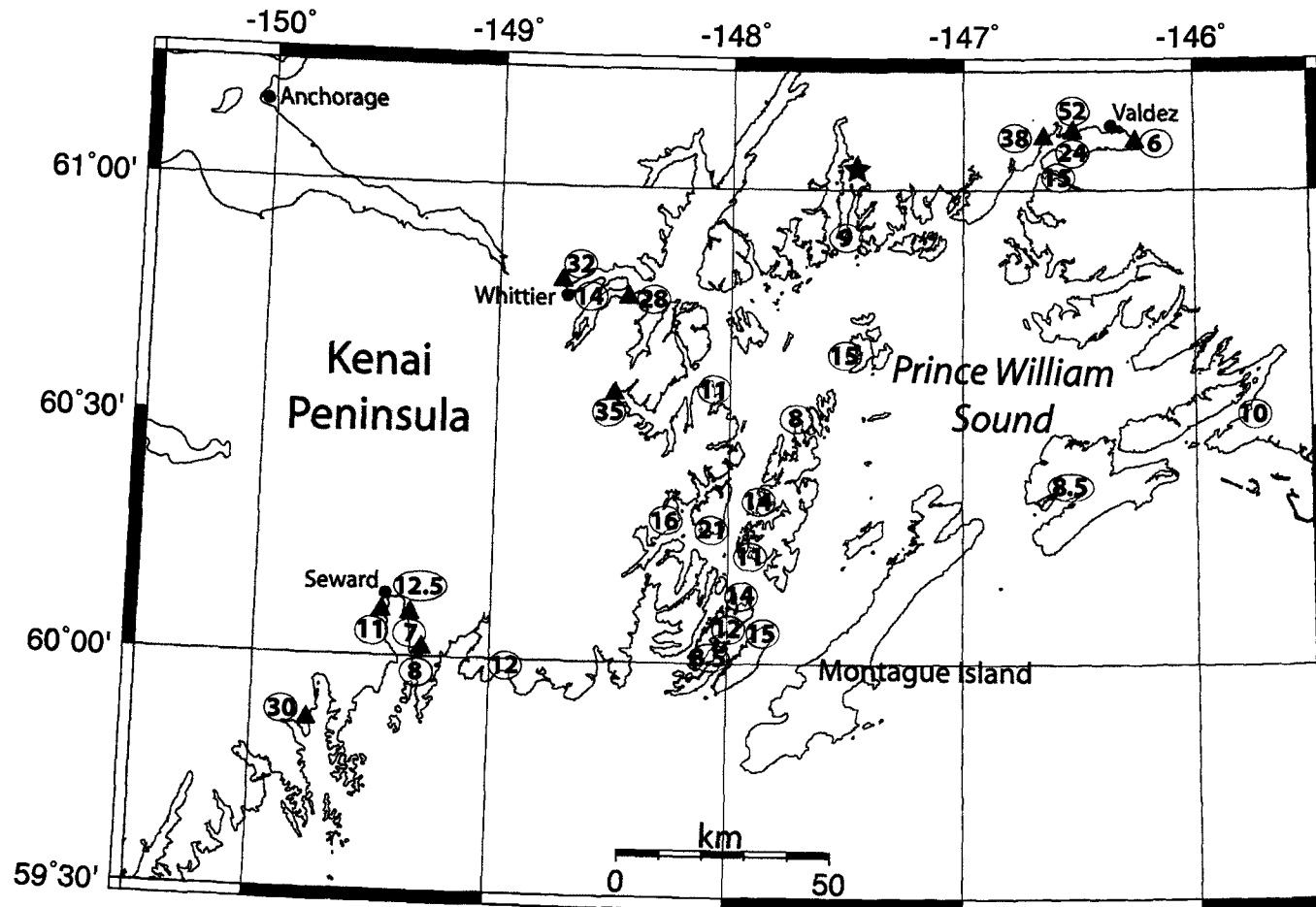


Figure 1.2: The Prince William Sound and Kenai Peninsula areas. The star indicates the epicenter of the $M_w 9.2$ 1964 Alaska earthquake. Red triangles are locations of known and probable large underwater slides triggered by the 1964 earthquake; numbers in circles are maximum observed runup heights in meters (data from *Plafker et al. (1969)*).

Chapter 2

Numerical study of tsunami generated by multiple submarine slope failures in Resurrection Bay, Alaska, during the M_W 9.2 1964 earthquake¹

2.1 Abstract

We use a viscous slide model of *Jiang and LeBlond* (1994) coupled with nonlinear shallow water equations to study tsunami waves in Resurrection Bay, in south-central Alaska. The town of Seward, located at the head of Resurrection Bay, was hit hard by both tectonic and local landslide-generated tsunami waves during the M_W 9.2 1964 earthquake with an epicenter located about 150 km north-east of Seward. Recent studies have estimated the total volume of underwater slide material that moved in Resurrection Bay during the earthquake to be about 211 million m^3 .

Resurrection Bay is a glacial fjord with large tidal ranges and sediments accumulating on steep underwater slopes at a high rate. Also, it is located in a seismically active region above the Aleutian megathrust. All these factors make the town vulnerable to locally generated waves produced by underwater slope failures. Therefore it is crucial to assess the tsunami hazard related to local landslide-generated tsunamis in Resurrection Bay in order to conduct comprehensive tsunami inundation mapping at Seward. We use numerical modeling to recreate the landslides and tsunami waves of the 1964 earthquake to test the hypothesis that the local tsunami in Resurrection Bay has been produced by a number of different slope failures. We find that numerical results are in good agreement with the observational data, and the model could be employed to evaluate landslide tsunami hazard in Alaska fjords for the purposes of tsunami hazard mitigation.

2.2 Introduction

On March 27, 1964, the Prince William Sound area of Alaska was struck by the largest earthquake ever recorded in North America. This magnitude M_W 9.2 megathrust earthquake generated the most destructive tsunami experienced in historical times by Alaskans and, further south, by people on the west coast of the United States and Canada. Of the 131 fatalities associated with this earthquake, 122 were caused by tsunami waves (*Lander,*

¹E. Suleimani, R. Hansen and P. Haeussler, 2009, "Numerical study of tsunami generated by multiple submarine slope failures in Resurrection Bay, Alaska, during the M_W 9.2 1964 earthquake", published in *Pure and Applied Geophysics*, 166, 131–152, DOI 10.1007/s00024-004-0430-3.

1996). Although tragic, the number of deaths was fortunately far smaller than in the case of the 2004 Indian Ocean tsunami due to low population density on the Alaska coast. As a result of the earthquake, more than twenty local tsunamis were generated by submarine and subaerial landslides in coastal Alaska, in addition to the major tectonic tsunami that was generated by displacement of the ocean bottom between the trench and the coastline. Local tsunamis caused most of the damage and accounted for 76% of the tsunami fatalities. Also, they arrived almost immediately after the shaking began, leaving no time for warning or evacuation. The community of Seward in Resurrection Bay (Figure 2.1) suffered from the combined effects of local landslide-generated waves and the major tectonic tsunami that propagated from the main earthquake rupture zone in the Gulf of Alaska. The earthquake triggered a series of slope failures offshore of Seward, which resulted in landsliding of part of the coastline into the water, along with the loss of the port facilities. The town sustained great damage, and 12 people perished due to the tsunamis. Seward has grown considerably since the 1964 earthquake. As an ice-free harbor, it is an important supply center for Interior Alaska. The town is one of the major tourist destinations in Alaska. Seward hosts more than 90 cruise ship dockings per year, and it is also a port for the state ferry system. Because local tsunamis were responsible for most of the damage and deaths in Seward during the 1964 earthquake, the future potential of similar events needs to be evaluated for comprehensive inundation mapping. Underwater slides could be triggered almost instantaneously during a future large earthquake, with tsunami waves arriving without warning, as they did in 1964. For tsunami hazard mitigation it is important to estimate the inundation areas, depths of inundation and velocity currents in Resurrection Bay.

Tsunamis caused by submarine slope failures are a serious hazard in glacial fjords of coastal Alaska and other high-latitude fjord coastlines. *Lee et al.* (2002) studied different environments of the US Exclusive Economic Zone and found that Alaskan fjords is likely the most susceptible environment to slope failures. In a fjord setting, rivers and streams drain the glacier that initially eroded the valley, forming a fjord-head delta and depositing sediment that easily loses strength during an earthquake. *Hampton et al.* (1996) note that in a fjord environment, where the deltaic sediment is deposited rapidly, the sediment builds up pore-water pressures and could liquefy under extreme low tide conditions or ground shaking due to low static shear strength. *Bornhold et al.* (2001) identify the most common

triggering mechanisms that can cause underwater slope failures as earthquakes, extreme low tides, and construction activities in ports and harbors. Because of these diverse mechanisms, prediction of landslide-generated tsunamis is a challenging task. Estimation of landslide tsunami risk for a coastal community requires assessment of locations of potential underwater failures using high-resolution bathymetry, known or reasonably estimated physical parameters of the underwater materials, and an adequate numerical model. The most probable locations of unstable sediment bodies in Resurrection Bay will be at the head of the bay where the Resurrection River had constructed a delta, and steep submarine slopes located elsewhere in the bay (*Haeussler et al., 2007*).

This paper is the first numerical modeling study of tsunami waves in Resurrection Bay that utilizes the recent findings of the large-scale submarine slope failures in the bay during the 1964 earthquake (*Haeussler et al., 2007*). It was shown that submarine failures initiated along the fjord walls at shallow depths and sediment was transported 6 to 13 km into the deepest part of the basin. The total volume of slide material that moved in Resurrection Bay during the earthquake was estimated to be about 211 million m³ (*Haeussler et al., 2007*). The purpose of this study is to recreate the sequence of tsunami waves observed in Resurrection Bay during the 1964 earthquake, and to test the hypothesis that the local tsunami was produced by a number of different slope failures. We perform numerical modeling of submarine slides and associated water waves and compare numerical results with the observations. In this preliminary analysis, our goal is not to model the inundation of dry land, but to create a foundation for future studies that will address runup of landslide-generated waves in Resurrection Bay. We will show that our modeling approach is a useful tool for estimating the landslide tsunami hazard at Seward and other tsunami-prone communities in southern Alaska.

2.3 Tsunami hazard in Resurrection Bay

Resurrection Bay is a deep glacial fjord, typical of many in south-central and south-eastern Alaska. *Kulikov et al. (1998)* analyzed tsunami catalog data for the North Pacific coast and showed that this region has a long history of tsunami waves generated by submarine and subaerial landslides, avalanches and rockfalls. The authors also found that, in the majority of cases, tectonic tsunamis that arrive in bays and fjords from the open ocean have relatively

small amplitudes, but a great number of local landslide-generated tsunamis have much larger wave amplitudes. For example, as a result of the 1964 earthquake, about 20 local submarine and subaerial landslide tsunamis were generated in Alaska (*Lander, 1996*). Following the earthquake, Seward was the only place hit by both landslide-generated tsunamis and a major tectonic tsunami (*Haeussler et al., 2007*), while several other communities experienced only locally generated waves (*Plafker et al., 1969*). *Kulikov et al. (1998)* also noted that, due to the sparse population of the area, the actual number of historical landslide tsunami events is unknown, and probably much greater than the number of events observed or recorded. *Bornhold et al. (2001)* addressed the problem of estimation of risk from landslide-generated tsunami waves for the coast of Alaska and British Columbia. They outlined the specific features of the long-term prediction of landslide-generated tsunamis at selected sites, and developed an approach for estimating tsunami risk. The long-term approach consists of two steps: analysis of historical events and verification of model results with runup observations at the site; and numerical simulation of hypothetical tsunami scenarios. Although for many communities historical observations do not exist, Seward is an exception. The effects of the 1964 earthquake and tsunami waves in Resurrection Bay, including wave amplitudes and extent of inundation, are well documented (*Wilson and Tørum, 1968; Lemke, 1967*) and are ideal for numerical modeling studies.

2.3.1 Study area and tsunami waves of March 27, 1964

The town of Seward is located at the northwest corner of Resurrection Bay, and is built mostly on the alluvial fan of Lowell Creek. Lowell Point, Tonsina Point, and the Fourth of July Creek (Figure 2.2) are locations of other alluvial fans that extend into the bay as fan deltas (*Lemke, 1967*). The entire head of Resurrection Bay is a fjord-head delta that was built by the Resurrection River. *Haeussler et al. (2007)* used the word "bathtub" to describe a flat depression in the middle of the bay extending north to south (Figure 2.2). The deepest part of the bathtub is about 300 meters. The average pre-earthquake offshore slopes in the vicinity of Seward ranged from 10° to 20°, decreasing to 5° at the depth of about 200 m (*Lemke, 1967*). Today, the same area has an average slope of about 25° (*Lee et al., 2006*). A natural barrier formed by Caines Head and a glacial sill divide the bay into two deep basins, separated by a narrow "neck" with maximum depth above the sill of 195 m. This

sill inhibits sediment transport by tidal currents to the southern part of the bay (*Haeussler et al.*, 2007). Our study focuses on the northern basin of Resurrection Bay, north of the sill area (Figure 2.2).

There were several types of waves observed in Resurrection Bay on March 27, 1964: landslide-generated waves, a tectonic tsunami wave train, and probably seiches (*Wilson and Tørum*, 1968), all resulting in a complicated wave pattern. The Seward tide gauge was located on a dock that collapsed into the bay as a result of massive submarine slope failures. The instrument was heavily damaged, and the record was lost. Although the sequence of waves was reconstructed from observations provided by eyewitnesses, there are uncertainties in the time estimates of wave arrivals (*Wilson and Tørum*, 1968). Table 2.1 is a portion of the eyewitness report compiled by *Wilson and Tørum* (1968) that covers the period when the ground was shaking. An initial drawdown of water was observed at the Seward waterfront about 30 seconds after the ground started to shake. At the same time, fuel tanks ruptured, leaked, and subsequently exploded; the tanks slid into the bay, and the receding water was covered with burning oil. The highest wave at Seward was about 6-8 m high observed about 1.5-2 minutes after the shaking began (Table 2.1). The tectonic tsunami wave, covered with burning oil, came into the bay about 25 minutes after the earthquake, spanning the entire width of the bay (*Wilson and Tørum*, 1968). This wave was as high as the initial landslide-generated waves. Because the source of local waves in the bay ceased at the end of ground shaking (*Wilson and Tørum*, 1968), about 20 minutes before the arrival of the tectonic tsunami, we can assume that these events are independent, and model them separately. In this paper we focus only on waves generated by local submarine slope failures in Resurrection Bay.

2.3.2 Justification for the study

Geologic investigations were conducted in the Resurrection Bay area right after the earthquake by several researchers (*Lemke*, 1967; *Wilson and Tørum*, 1968; *Plafker et al.*, 1969; *Shannon and Hiltz*, 1973). From these studies, it was concluded that strong ground motion during the earthquake caused several submarine slope failures along the Seward waterfront and other areas within upper Resurrection Bay. *Hampton et al.* (1996) described the triggering mechanism as dynamic forces imposed by large seismic accelerations that added

to the downslope component of the gravitational force on the steep slopes of the Lowell Creek and Resurrection River deltas. *Hampton et al.* (2002) notes that the stability of the sediment was also decreased by the low tidal level at the time of the earthquake, and by the rapid drawdown of water due to the initial slope failure, which prevented the pore water from draining from the sediment quickly enough to maintain hydrostatic conditions. The underwater slope failures generated large waves that were observed during ground shaking (*Wilson and Tørum, 1968*). The major factors that contributed to the total volume and aerial extent of the slide material were the long duration of ground motion (3 to 4 min), the configuration of underwater slopes, and the type of sediment forming these slopes - unconsolidated and fine-grained materials (*Lemke, 1967*). *Hampton et al.* (1996) added that high artesian pressure within aquifers of the delta combined with the extra load caused by waterfront artificial fill and the shoreline development also contributed to the slope failures. The authors summarized all the environmental loads in Resurrection Bay and concluded that although it was a unique combination of conditions, most of them had been documented separately during slope failures in other fjords.

Studies by *Lee et al.* (2006) and *Haeussler et al.* (2007) provided analysis of pre- and post-earthquake bathymetric data and high resolution subbottom profiles of Resurrection Bay and showed convincing evidence of massive submarine landsliding. They utilized a 2001 NOAA high-resolution multibeam bathymetry survey of Resurrection Bay to study the morphology and depth changes of the fjord bottom. A shaded relief map derived from this bathymetric data shows a variety of seafloor features related to submarine slides. *Lee et al.* (2006) identified remains of the Seward waterfront that failed in 1964 as a result of strong ground shaking. These remains are visible as blocky debris extending offshore Seward for about 750 m (Figure 2.3). The authors also identified dispersed debris flows that correspond to failures of the Resurrection River delta, and they concluded that the 1964 earthquake could potentially have triggered different failure types simultaneously. *Haeussler et al.* (2007) concluded that several failures initiated along the fjord walls at relatively shallow depths, and the mass flows produced by these failures transported most of the material as far as 6 to 13 km into the bathtub, covering the entire basin with a flow deposit.

Engineering studies conducted after the 1964 earthquake (*Lemke, 1967*) showed that

additional onshore and submarine landslides can be expected along the Seward waterfront in the event of another large earthquake, and that sediment from the Resurrection River and smaller creeks will continue to accumulate on underwater slopes of Resurrection Bay. The recent results of sediment chemistry monitoring in Port Valdez, located in a glacial fjord setting similar to that of Resurrection Bay (Figure 5.1), demonstrated high sediment accumulation rates of about 1.5 cm/year at the head of the fjord (*Savoie et al.*, 2006). Sediment could be released not only by the ground shaking due to an earthquake, but also by other triggering events, such as extreme low tide conditions and construction activities. Because short-term prediction of landslide tsunamis is not applicable for tsunami risk assessment (*Bornhold et al.*, 2001), we will need to use the long-term approach described at the beginning of section 2.3 for estimating the local tsunami hazard at Seward. The essential part of this approach is numerical modeling of historical landslide tsunami events, as well as simulating future hypothetical underwater slope failures.

2.4 Model description

A number of studies of tsunami waves generated by landslides employed depth-integrated numerical models. *Harbitz* (1992) simulated tsunamis generated by Storegga slides using linear shallow water equations. *Jiang and LeBlond* (1992, 1994), *Fine et al.* (1998), *Thomson et al.* (2001), *Imamura et al.* (2001), *Titov and Gonzalez* (2001) used non-linear shallow water approximation to model the slide-water system as a two-layer flow. *Lynett and Liu* (2002) discussed the limitations of the depth-integrated models with regards to landslide-generated waves, and developed fully nonlinear weakly dispersive model for submarine slides that is capable of simulating waves from relatively deep water to shallow water. The model was later extended to employ the multilayer approach (*Lynett and Liu*, 2004a,b) that allowed for accurate simulation of landslides in shallow and intermediate water (*Lynett and Liu*, 2005). *Grilli and Watts* (2005) derived and validated a two-dimensional fully nonlinear dispersive model that does not have any restrictions on tsunami amplitude, wavelength, or landslide depth, and describes the motion of the landslide by that of its center of mass.

To simulate tsunami waves produced by multiple underwater slope failures in Resurrection Bay on March 27, 1964, we use a three-dimensional numerical model of a viscous underwater slide with full interactions between the deforming slide and the water waves

that it generates. This model was initially proposed by *Jiang and LeBlond* (1994). *Fine et al.* (1998) improved the model by including realistic bathymetry, and also by correcting errors in the governing equations. The model assumptions as well as its applicability to simulate underwater mudflows are discussed by Jiang and LeBlond in their formulation of the viscous slide model (*Jiang and LeBlond*, 1992, 1994). The model uses long-wave approximation for water waves and the deforming slide, which means that the wavelength is much greater than the local water depth, and the slide thickness is much smaller than the characteristic length of the slide along the slope (*Jiang and LeBlond*, 1994). *Assier-Rzadkiewicz et al.* (1997) argued that the long-wave approximation could be inaccurate for steep slopes, that is for slopes greater than 10° . *Rabinovich et al.* (2003) studied the validity of the long-wave approximation for slopes greater than 10° and found that for the slope of 16° the possible error was 8%, and for the maximum slope in their study of 23° the possible error was 15%. Based on this analysis, for the average pre-earthquake offshore slopes that ranged from 10° to 20° in the vicinity of Seward, the possible error introduced by a slide moving down these higher gradient slopes could be around 10%.

The advantage of the vertically integrated model that includes two horizontal dimension effects is its ability to simulate real landslide tsunami events using high-resolution numerical grids based on multibeam bathymetry data. Although model runs require use of high-performance computing, the computational times are still reasonable. This model was successfully applied to simulate tsunami waves in Skagway Harbor, Alaska, generated by collapse of the PARN dock on November 3, 1994 (*Fine et al.*, 1998; *Thomson et al.*, 2001). The results of numerical simulations were in good agreement with the tide gauge record in Skagway Harbor, one of the numerous fjords in south-eastern Alaska. *Rabinovich et al.* (2003) simulated potential underwater landslides in British Columbia fjords, settings that are similar to Resurrection Bay, and demonstrated that this model can be used for tsunami hazard assessment.

2.4.1 Model equations

The geometry of the slide is shown in Figure 2.4. The physical system consists of two layers - the upper one is water with density ρ_1 , and the lower layer is slide material with density ρ_2 and dynamic viscosity μ . The slide is assumed to be an incompressible viscous

fluid. We assume a sharp interface between the layers, with no mixing allowed between water and sediments. The disturbance of the water surface produced by slide motion is described by free surface elevation $\xi(x, y, t)$ and horizontal components of water velocity $u(x, y, t)$ and $v(x, y, t)$. The horizontal velocity of the slide \mathbf{U} has components $U(x, y, t)$ and $V(x, y, t)$. The thickness of the slide is $D(x, y, t)$, the undisturbed water depth is $H(x, y)$, and $H_t(x, y, t) = H + \xi - D$ is the total water depth above the slide. The equations for the slide were initially derived under the assumption that the underwater slide rapidly reaches its equilibrium velocity (*Jiang and LeBlond, 1994*), which means that changes of horizontal components of the slide velocity in the vertical direction can be approximated by a parabolic function. It is also assumed that the slide mass does not cross the boundary of the computational domain.

The slide equations that we use in this study are the equations from *Jiang and LeBlond (1994)* that were corrected by *Fine et al. (1998)*:

$$\frac{\partial U}{\partial t} - \frac{1}{5D} \frac{\partial D}{\partial t} + \frac{4}{5} \left(U \frac{\partial U}{\partial x} + V \frac{\partial U}{\partial y} \right) = -\frac{3}{2} g \left(\frac{\partial D}{\partial x} - \frac{\partial H}{\partial x} \right) - \frac{3}{2} g \frac{\rho_1}{\rho_2} \frac{\partial H_t}{\partial x} - \frac{3\mu}{\rho_2} \frac{U}{D^2}, \quad (2.1)$$

$$\frac{\partial V}{\partial t} - \frac{1}{5D} \frac{\partial D}{\partial t} + \frac{4}{5} \left(U \frac{\partial V}{\partial x} + V \frac{\partial V}{\partial y} \right) = -\frac{3}{2} g \left(\frac{\partial D}{\partial y} - \frac{\partial H}{\partial y} \right) - \frac{3}{2} g \frac{\rho_1}{\rho_2} \frac{\partial H_t}{\partial y} - \frac{3\mu}{\rho_2} \frac{V}{D^2}, \quad (2.2)$$

$$\frac{\partial D}{\partial t} = -\frac{2}{3} \left(\frac{\partial(DU)}{\partial x} + \frac{\partial(DV)}{\partial y} \right). \quad (2.3)$$

The equations that describe the upper layer are the nonlinear shallow water equations:

$$\frac{\partial u}{\partial t} + u \frac{\partial u}{\partial x} + v \frac{\partial u}{\partial y} = -g \frac{\partial \xi}{\partial x}, \quad (2.4)$$

$$\frac{\partial v}{\partial t} + u \frac{\partial v}{\partial x} + v \frac{\partial v}{\partial y} = -g \frac{\partial \xi}{\partial y}, \quad (2.5)$$

$$\frac{\partial H_t}{\partial t} = -\frac{\partial(H_t u)}{\partial x} - \frac{\partial(H_t v)}{\partial y}. \quad (2.6)$$

The variable that couples the two systems of equations is the total water depth above the slide, $H_t(x, y, t)$. In this study we do not calculate the inundation of dry land due to

landslide-generated waves, which implies that the normal velocity component is set to zero at the shoreline. At the open boundary, we apply the radiation boundary condition for surface waves.

2.4.2 Data

The two data sets used in this study are the bathymetry of Resurrection Bay, and the initial distribution and thickness of the slide material. In order to simulate underwater slope failures of 1964 in Resurrection Bay, we use a bathymetry grid of 15-m resolution that covers the northern part of the bay (Figure 2.2). The source of the data is the 2001 NOAA high-resolution multibeam survey of Resurrection Bay, and the 2006 survey of the Seward harbor and surrounding areas (*Labay and Haeussler, 2008*).

Haeussler et al. (2007) have conducted a comprehensive study of submarine slope failures in Resurrection Bay during the 1964 earthquake. The location and extent of submarine mass failures were estimated based on analysis of pre- and post-earthquake bathymetry. The authors created a bathymetric difference grid that shows depth changes in the bay resulting from the 1964 slope failures. The estimated total volume of slide material is 211 million m^3 (*Haeussler et al., 2007*). A map of the slide thickness, derived from the bathymetric difference grid, is shown in Figure 2.5. This distribution of the slide material serves as an initial condition for the slide surface in system of equations (2.1)-(2.3). *Haeussler et al. (2007)* identified 10 different landslide areas and calculated their volumes (Figure 2.5). We use their results shown in Figure 2.5 to better understand the contribution of different slide complexes to the observed tsunami amplitudes in Resurrection Bay.

2.5 Numerical simulation of the 1964 landslides and tsunami

We use an explicit in time finite-difference method to numerically solve equations (2.1)-(2.6) on a staggered leap-frog grid. *Thomson et al. (2001)* describe the construction of the numerical scheme and provide the final discretized equations. The computational domain is shown in Figure 2.2. This area is covered by a grid of 711×1310 grid points with horizontal space steps $\Delta x = 13.75$ m and $\Delta y = 15$ m, and time step $\Delta t = 0.01$ sec. *Shannon and Hiltz (1973)* conducted a subsurface geotechnical investigation of materials that failed in Resurrection Bay during the 1964 earthquake. They found that the density of the slide

material ranged from $2.0 \text{ g} \cdot \text{cm}^{-3}$ to $2.11 \text{ g} \cdot \text{cm}^{-3}$. We do not have any measurements of the slide viscosity, but sensitivity studies by *Rabinovich et al.* (2003) demonstrated that the influence of kinematic viscosity on tsunami wave heights is small. We assume slide density of $\rho = 2.0 \text{ g} \cdot \text{cm}^{-3}$ and slide viscosity of $\mu = 0.05 \text{ m}^2 \cdot \text{s}^{-1}$. The upper and lower surfaces of the slide mass are defined by the initial slide thickness distribution (Figure 2.5), and they are given on the same 711×1310 grid used for bathymetric data. The slide thicknesses are added to the bathymetry values in order to define the pre-earthquake depths in Resurrection Bay. It is assumed that the slide mass is initially at rest, and gravity is the only driving force. Although it is possible that individual slides were triggered at different times after the initial ground shaking, there is no independent evidence to support this hypothesis. Therefore we assume in the model that all slides start moving at the same time.

2.5.1 Movement of the sediments and propagation of surface waves

The initial thickness and extent of the slide mass is shown in Figure 2.5. The strong ground shaking associated with the earthquake acted as a trigger that released unstable sediments in the bay. The slide masses moved downslope, spreading out and filling the bathtub from all directions (Figure 2.6). Because the bottom of the bathtub is nearly flat, slide speed decreased dramatically when the sediments reached the deepest part of the fjord (Figure 2.6, C, D). Only a relatively small amount of sediments from the South End slide complex (Figure 2.5) moved out of the basin to the southern slope of the glacial sill that extends across the bay and keeps sediment in the basin (Figure 2.6, D). Results of numerical simulations show that it took about 30 minutes for the sediment flow to completely cover the bathtub.

The wave modeling results show that each slope failure produced a cylindrical wave with a crest propagating toward the opposite shore, and the trough moving toward the generation area (frames A–F in Figures 2.7 and 2.8). This wave pattern is in agreement with previous numerical studies of waves generated by viscous underwater slides (*Thomson et al.*, 2001; *Rabinovich et al.*, 2003). In frame B ($t = 40 \text{ sec}$), the wave crests from the Lowell Point (LP), Seward downtown (SDT), and Fourth of July Creek (FJC) slides are clearly visible (white dashed lines). At $t = 1 \text{ min}$ the crests pass the middle of the bay and continue moving toward the opposite shores, while the wave from the LP slide is approaching the southern end of Seward (Frame C). At $t = 1 \text{ min } 40 \text{ sec}$ the wave from the FJC

slide hits Seward at the south-eastern point of the fan delta (Frame D, white dashed lines). Frames D and E show complicated patterns of multiple reflections and wave interactions in the bay. About 5 minutes after the beginning of ground shaking the wave action subsides (Frame F). Our modeling results agree with the observation that sliding appeared to terminate at the end of the shaking (that lasted about 4.5 minutes), and therefore the source of the waves ceased as well. This is consistent with the assumption that most of sediment was released during the period of ground shaking.

The waves generated in the southern part of the bay by the South End and Thumb Cove slide complexes (Figure 2.5) propagated mostly to the west, in the direction of Caines Head, and to the south, toward the open boundary (Figure 2.7, B, C). Two waves, produced by the eastern and western slides of the South End slide complex, are visible on frames C and D (yellow arrows), diffracting around Caines Head.

2.5.2 Simulated wave records

We conducted a numerical experiment to investigate how individual slide failures contributed to the observed tsunami amplitudes. The equations that describe water waves in this problem are nonlinear shallow water equations. The time series of water waves generated by multiple slope failures can not generally be represented as a linear superposition of a time series of waves generated by individual slides. This is especially true if interacting waves propagate at a small angle with respect to each other and for a long enough time for nonlinear effects to grow. But in cases where the relative angles are not small, and especially when waves propagate in the opposite directions (crossing waves) with very small interaction time, the nonlinear effects can be neglected. For example, in the scope of shallow water equations, the mathematical problem of two crossing waves is equivalent to a problem of a wave reflecting from a vertical wall (*Pelinovsky, 1996*), in which case the nonlinear effects have been shown to be minimal. In our analysis we superpose the waves that propagate either in the opposite directions or at angles greater than 45° with short interaction time, and therefore the linear approximation is valid.

The numerical experiment consisted of three steps. First, we selected the slides that are the closest to Seward, and also have substantial volumes and relatively shallow initiation depth. In Figure 2.5 these slide complexes are: SDT (Seward downtown, 27.5 million m^3),

LP (Lowell Point, 18.1 million m³) and FJC (Fourth of July Creek, 35 million m³). We modeled each of these slides separately, and calculated time histories for generated waves at all three locations shown in Figure 2.2. Then, we modeled the three slides together, and calculated the time histories at the same locations. Finally, we calculated time histories for waves resulting from all 10 slides.

The results of the water level simulation at Seward are shown in Figure 2.9. The Seward slide first generated a trough, which was observed as a massive drawdown of water about 30 seconds after the initial ground shaking in the waterfront area, followed by the wave crest (Figure 2.9a). The highest simulated wave at Seward was the one generated by the FJC slide that arrived in 1 min 40 seconds after the earthquake. It was the superposition of this wave and two smaller crests from the Seward slide and the Lowell Point slide that resulted in the maximum observed wave height at Seward (Table 2.1). Figure 2.9b shows the time series of waves resulted from the slides SDT, LP, and FJC combined, compared to the time series of waves generated by all slides. It is evident that the waves generated by slides in the lower part of the bay had relatively little impact on the wave amplitudes in the upper bay during ground shaking (first 250 seconds).

As was the case in Seward, the initial trough at Fourth of July Creek (Figure 2.10a) was generated by the local slide, but the following crest was not as high as the crest generated by the Seward slope failure. The waves from the opposite shore, induced by the SDT slide and the LP slide, arrived at Fourth of July Creek almost at the same time, in about 105 sec, and their superposition generated the highest crest at this location. This was probably the wave that, according to observations, ran inland 400 meters (*Wilson and Tørum, 1968*). Figure 2.10b shows that the amplitude of the second trough is much smaller if the wave field is calculated from all 10 slides, compared to its amplitude produced by the slides in the upper bay only. This trough was diminished by the superimposed wave crest produced by the Bathtub East failure (Figure 2.5), which arrived to Fourth of July Creek in about 140 sec. This crest is indicated by the white arrow on frames B–E of Figures 2.7 and 2.8.

The Lowell Point time series are shown in Figure 2.11. There is a short first positive wave at this location, due to a combination of the slide geometry and the location of the time series point (Figures 2.2 and 2.5). The slide complex consists of two major areas, and the crest from the northern part of the slide that propagates toward the opposite shore

reaches the time series point faster than the trough from the southern section of the slide complex does. The wave from Fourth of July Creek arrives at Lowell Point in 1 min 40 sec, and the wave from Seward arrives 20 sec later (Figure 2.11a). Superposition of these waves (Figure 2.11b) generates a 6.5 m high crest at Lowell Point.

2.6 Discussion and conclusions

We performed numerical simulations of tsunami waves generated by submarine slides in Resurrection Bay, Alaska, during the M_W 9.2 1964 earthquake. Our numerical results confirm the hypothesis that tsunami waves observed in Seward during and immediately after the earthquake resulted from multiple submarine slope failures (*Lee et al., 2006; Haessler et al., 2007*). Results of numerical simulation of water waves at Seward for the first 5 minutes after the initial ground shaking are in good agreement with the eyewitness observations (Figure 2.9b, Table 2.1). Our numerical experiments were designed to investigate the relative contributions of different submarine slide complexes. The results show that the Seward downtown (SDT) slide, the Lowell Point (LP) slide, and Fourth of July Creek (FJC) slide were the major contributors of tsunami wave energy in the upper bay during the first 3 minutes after slide initiation.

Eyewitness descriptions of events at Seward on March 27, 1964, (*Wilson and Tørum, 1968*) report that a 6-8 m high, north-moving wave arrived at the Seward waterfront 1.5-2 minutes after the earthquake. The simulated time history at downtown Seward (Figure 2.9b) agrees very well with observation of this wave (Table 2.1). Also, several observers noted the north-moving wave crossing the wave coming from the east. We interpret these observations as the interaction of the waves generated by LP and FJC slides (Figure 2.7, frame C, red arrow). The numerical results show that the highest waves at Seward were the result of positive interference of the three major waves in the upper part of Resurrection Bay, generated by the SDT, LP and FJC slides (Figure 2.9b).

Wilson and Tørum (1968) describe "boils" of water observed about 1.5 km west of the Fourth of July Creek and speculate they could be the result of an underwater slide. Numerical experiments conducted by *Fine et al. (2003)* show that the total wave energy generated by a slide strongly depends on the initial position of the slide. For submarine slides, wave amplitude quickly decreases when initial depth of the slide increases. It is

unlikely that the sliding mass could have generated a big wave in the middle of the bay, at a depth of about 200 m. It is possible, though, that the Mid-bay Channel slide experienced a delayed trigger, caused by the motion of the FJC slide when the latter reached the middle of the bay and scoured the bottom (*Haeussler et al., 2007*). This would have caused a significant increase in the total volume of the moving mass. This hypothesis could be verified by additional numerical experiments.

Observers at Lowell Point reported a wave coming from Seward, and at the same time, a wave radiating toward Fourth of July Creek (*Wilson and Tørum, 1968*). We interpret these observations as waves generated by SDT and LP slides. The highest reported wave at Lowell Point was about 6 m high (*Wilson and Tørum, 1968*), which agrees with the modeling results (Figure 2.11b).

Future work will include simulation of runup of tsunami waves generated by slope failures in Resurrection Bay and comparison of results with inundation patterns observed in 1964. For the purposes of tsunami hazard mitigation, we plan to study tsunami waves generated by hypothetical underwater slides and estimate the landslide tsunami hazard. Engineering studies conducted after the 1964 earthquake in Seward and Valdez (*Lemke, 1967; Coulter and Migliaccio, 1966; Shannon and Hiltz, 1973*) concluded that underwater slope failures have not improved slope stability, meaning that the same slopes could fail again during the next large earthquake. Moreover, some of the streams draining into Resurrection Bay, such as Lowell Creek and Fourth of July Creek, have been rerouted by humans. These creeks are now depositing sediments in new locations, which may lead to new unstable sediment accumulations and future submarine slides.

2.7 Acknowledgments

This study was supported by NOAA grants 27-014d and 06-028a through Cooperative Institute for Arctic Research, and by the USGS. We thank Michelle Coombs, Chris Waythomas and anonymous reviewers for helpful suggestions that improved this manuscript. The authors also thank Keith Labay for the construction of the high-resolution DEM of Resurrection Bay, and Dave West for data processing in ArcGIS and his help in preparing the figures. Numerical calculations for this work are supported by a grant of High Performance Computing (HPC) resources from the Arctic Region Supercomputing Center (ARSC) at the

University of Alaska Fairbanks as part of the US Department of Defense HPC Modernization Program. We thank ARSC specialists Miho Aoki and Sergei Maurits for visualizations of computational results.

Bibliography

- Assier-Rzadkiewicz, S., C. Mariotti, and P. Heinrich (1997), Numerical simulation of submarine landslides and their hydraulic effects, *J. Waterw. Port Coast. Ocean Eng.*, 123(4), 149–157.
- Berg, E., D. Cox, A. Furumoto, K. Kajiura, H. Kawasumi, and E. Shima (1964), Field survey of the Tsunami of 28 March 1964 in Alaska, Report, Hawaii Institute of Geophysics (unpublished).
- Bornhold, B., R. Thomson, A. Rabinovich, E. Kulikov, and I. Fine (2001), Risk of landslide-generated tsunamis for the coast of British Columbia and Alaska, in *2001 An Earth Odyssey. Proceedings of the Canadian Geotechnical Conference*, pp. 1450–1454.
- Coulter, H., and R. Migliaccio (1966), Effects of the Earthquake of March 27, 1964, at Valdez, Alaska, U.S. Geological Survey Professional Paper 542-C, 36 pp.
- Fine, I., A. Rabinovich, E. Kulikov, R. Thomson, and B. Bornhold (1998), Numerical modelling of landslide-generated tsunamis with application to the Skagway Harbor tsunami of November 3, 1994, in *Proc. Int. Conf. on Tsunamis*, pp. 211–223, Paris.
- Fine, I., A. Rabinovich, R. Thomson, and E. Kulikov (2003), Numerical modeling of tsunami generation by submarine and subaerial landslides, in *Submarine Landslides and Tsunamis, NATO Science Series, Series IV: Earth and Environmental Sciences, vol. 21*, edited by A. Yalciner, E. Pelinovsky, E. Okal, and C. Synolakis, pp. 69–88, Kluwer Academic Publishers.
- Grilli, S., and P. Watts (2005), Tsunami generation by submarine mass failure. I: Modeling, experimental validation, and sensitivity analysis., *J. Waterw. Port Coast. Ocean Eng.*, 131(6), 283–297, doi:10.1061/(ASCE)0733-950X(2005)131:6(283).
- Haeussler, P., H. Lee, H. Ryan, K. Labay, R. Kayen, M. Hampton, and E. Suleimani (2007), Submarine slope failures near Seward, Alaska, during the M9.2 1964 earthquake, in *Submarine Mass Movements and their consequences*, edited by V. Lykousis, D. Sakellariou, and J. Locat, pp. 269–278.

- Hampton, M., H. Lee, and J. Locat (1996), Submarine landslides., *Rev Geophys*, 34, 33–59.
- Hampton, M., R. Lemke, and H. Coulter (2002), Submarine landslides that had a significant impact on man and his activities: Seward and Valdez, Alaska., in *Submarine Landslides: Selected Studies in the US Exclusive Economic Zone*, *US Geological Survey Bulletin*, edited by W. Schwab, H. Lee, and D. Twichell, pp. 123–134.
- Harbitz, C. (1992), Model simulations of tsunamis generated by the Storegga Slides, *Marine Geol.*, 105, 1–21.
- Imamura, F., K. Hashi, and M. Imteaz (2001), Modeling for tsunamis generated by landsliding and debris flow, in *Tsunami Research at the End of a Critical Decade*, edited by G. T. Hebenstreit, pp. 209–228, Kluwer.
- Jiang, L., and P. LeBlond (1992), The coupling of a submarine slide and the surface waves which it generates, *J. Geophys. Res.*, 97(C8), 12,731–12,744.
- Jiang, L., and P. LeBlond (1994), Three-dimensional modeling of tsunami generation due to a submarine mudslide, *J. Phys. Oceanogr.*, 24(3), 559–572.
- Kulikov, E., A. Rabinovich, I. Fine, B. Bornhold, and R. Thomson (1998), Tsunami generation by landslides at the Pacific coast of North America and the role of tides, *Oceanology*, 38(3), 361–367.
- Labay, K., and P. Haeussler (2008), Combined high-resolution LIDAR topography and multibeam bathymetry for upper Resurrection Bay, Seward, Alaska, U.S. Geological Survey Digital Data Series 374, <http://pubs/usgs.gov/ds/374/>.
- Lander, J. (1996), *Tsunamis affecting Alaska. 1737–1996*, no. 31 in NGDC Key to Geophysical Research, National Geophysical Data Center, Boulder, Colo.
- Lantz, B., and M. Kirkpatrick (1964), *Seward Quake, Good Friday, 1964*, Kirkpatrick Printing Co., Seward, Alaska.

- Lee, H., W. Schwab, and J. Booth (2002), Submarine landslides: an introduction., in *Submarine Landslides: Selected Studies in the US Exclusive Economic Zone*, US Geological Survey Bulletin, edited by W. Schwab, H. Lee, and D. Twichell, pp. 1–13.
- Lee, H., H. Ryan, R. Kayen, P. Haeussler, P. Dartnell, and M. Hampton (2006), Varieties of submarine failure morphologies of seismically-induced landslides in Alaska fjords, *Norwegian Journal of Geology*, 86, 221–230.
- Lemke, R. (1967), Effects of the Earthquake of March 27, 1964, at Seward, Alaska, U.S. Geological Survey Professional Paper 542-E, 48 pp.
- Lynett, P., and P.-F. Liu (2002), A numerical study of submarine landslide generated waves and runup., *Proc. Royal Society of London A*, 458, 2885–2910.
- Lynett, P., and P.-F. Liu (2004a), A two-layer approach to water wave modeling, *Proc. Royal Society of London A*, 460, 2637–2669.
- Lynett, P., and P.-F. Liu (2004b), Linear analysis of the multi-layer model, *Coastal Eng.*, 51, 439–454.
- Lynett, P., and P.-F. Liu (2005), A numerical study of the runup generated by three-dimensional landslides, *J. Geophys. Res.*, 110(C03006), 1–16, doi: 10.1029/2004JC002443.
- Pelinovsky, E. (1996), *Tsunami Waves Hydrodynamics*, Institute of Applied Physics, RAS, Nizhny Novgorod, Russia.
- Plafker, G., R. Kachadoorian, E. Eckel, and L. Mayo (1969), Effects of the Earthquake of March 27, 1964 on various communities, U.S. Geological Survey Professional Paper 542-G, 50 pp.
- Rabinovich, A. B., R. E. Thomson, B. D. Bornhold, I. V. Fine, and E. A. Kulikov (2003), Numerical modelling of tsunamis generated by hypothetical landslides in the Strait of Georgia, British Columbia, *Pure Appl. Geophys.*, 160(7), 1273–1313.

- Savoie, M., J. Savoie, J. Trefry, C. Semmler, D. Woodall, R. Trocine, J. Brooks, and T. McDonald (2006), Port Valdez sediment coring program: Final 2004 monitoring report, Kinnetic Laboratories, Inc., Contract No. 961.04.1 for Prince William Sound Regional Citizens' Advisory Council.
- Shannon, W., and D. Hilts (1973), Submarine landslide at Seward, in *The Great Alaska Earthquake of 1964. Engineering*, pp. 144–156, National Academy of Sciences, Washington, D.C.
- Thomson, R. E., A. B. Rabinovich, E. A. Kulikov, I. V. Fine, and B. D. Bornhold (2001), On numerical simulation of the landslide-generated tsunami of November 3, 1994 in Skagway Harbor, Alaska, in *Tsunami Research at the End of a Critical Decade*, edited by G. T. Hebenstreit, pp. 243–282, Kluwer.
- Titov, V., and F. Gonzalez (2001), Numerical study of the source of the July 17, 1998 PNG tsunami, in *Tsunami Research at the End of a Critical Decade*, edited by G. T. Hebenstreit, pp. 197–207, Kluwer.
- Wilson, B., and A. Tørum (1968), The tsunami of the Alaskan Earthquake, 1964: Engineering evaluation, U.S. Army Corps of Engineers, Technical memorandum No. 25, 401 p.

Table 2.1: Observations at the Seward waterfront during the earthquake (from *Wilson and Tørum* (1968)).

Estimated time points and heights (zero time is at the start of the quake)

Whiteness	Source	Time	Event
Ted Pedersen	Genie Chance	30 seconds	Drawdown at Standard Oil Dock
Hal Gilfillen		45 "	
Robert Clark		45 "	
Many Eyewitnesses	Genie Chance <i>Berg et al.</i> (1964) <i>Lantz and Kirkpatrick</i> (1964)	1.5 - 2 minutes	+20-25 feet at ARR docks Rose over box cars on railroad tracks Reached corner of Third Ave. and Washington

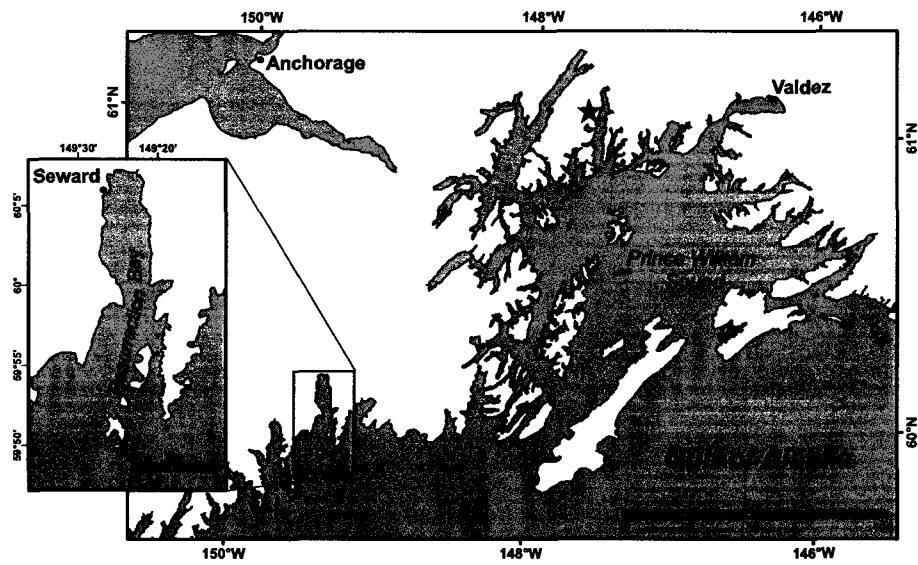


Figure 2.1: Location map of Resurrection Bay and Seward in the Gulf of Alaska. The star indicates the epicenter of the $M_W 9.2$ 1964 earthquake.

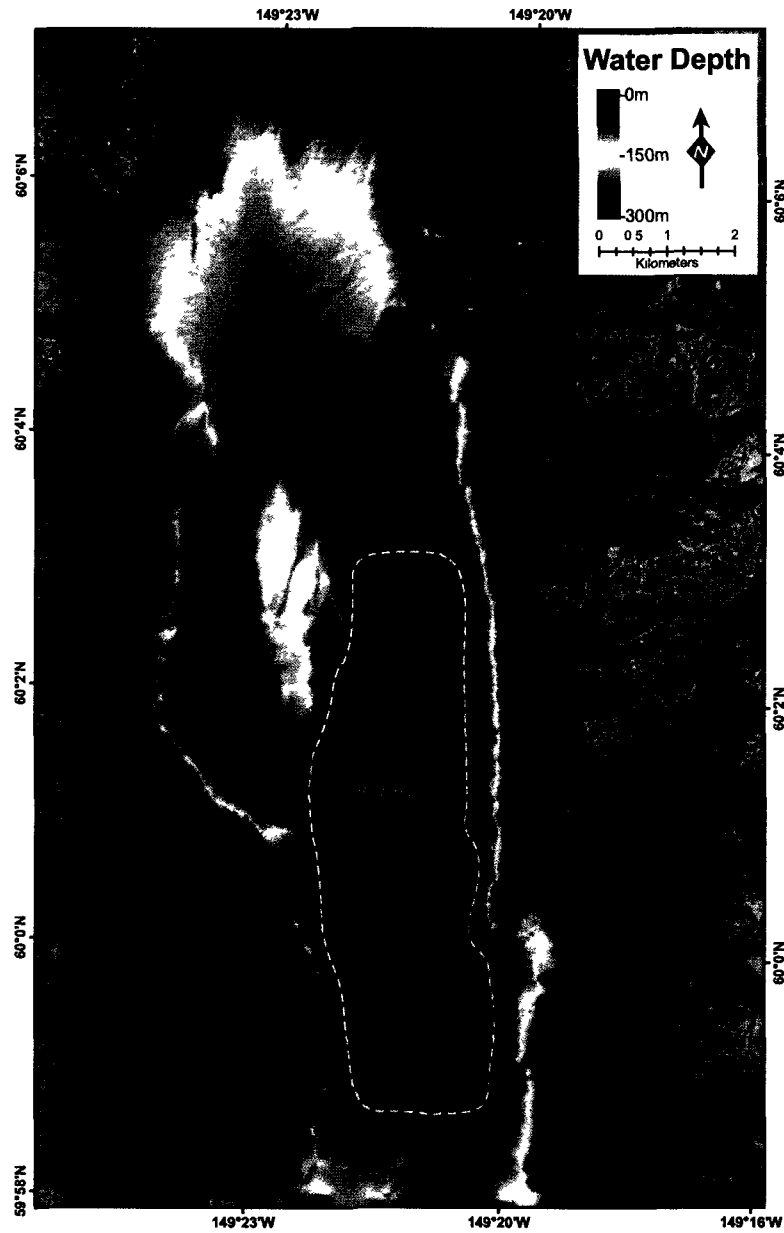


Figure 2.2: Bathymetric map of the northern end of Resurrection Bay (Data source: NOAA hydrographic surveys H-11072, H-11073, H-11074, H-11075, from National Geophysical Data Center, Boulder, Colorado). Dashed line shows the "bathtub" basin where sediments accumulated in 1964 (*Haeussler et al.*, 2007). Black triangles indicate the sites of calculated time series.

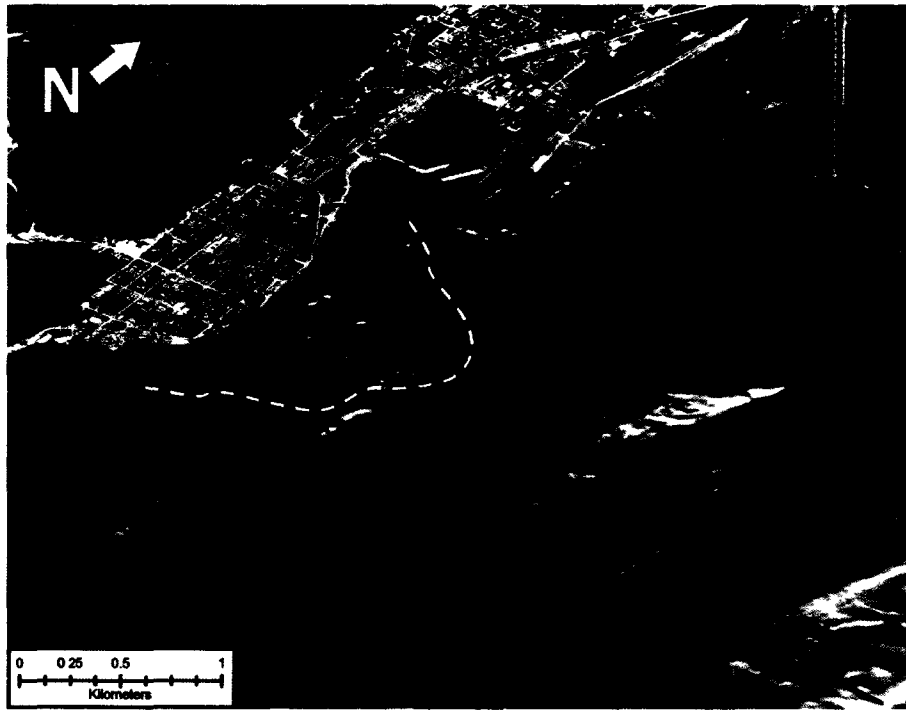


Figure 2.3: Oblique bathymetric image, overlain with aerial photograph, of the northwest corner of Resurrection Bay, offshore of the Seward waterfront. Dashed line delineates the blocky debris that are remains of the 1964 waterfront failure. The scale was made for downtown Seward.

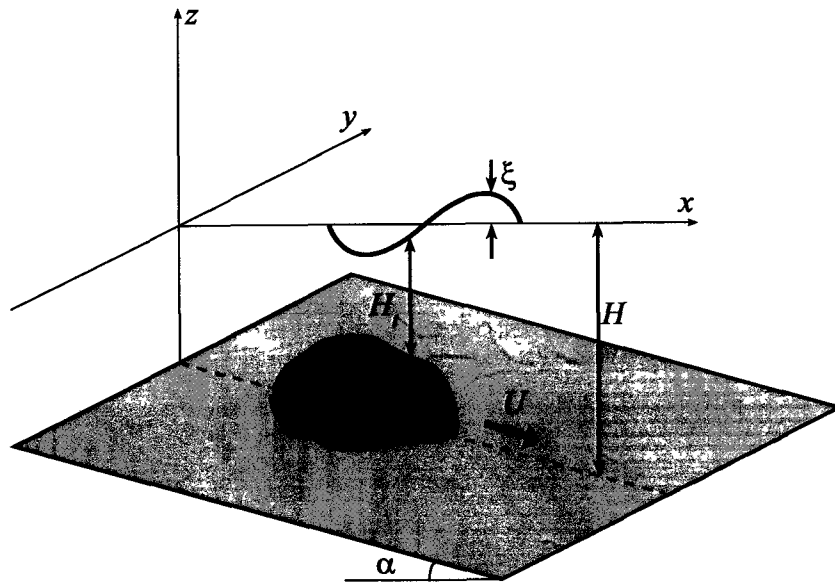


Figure 2.4: Geometry of a submarine landslide.

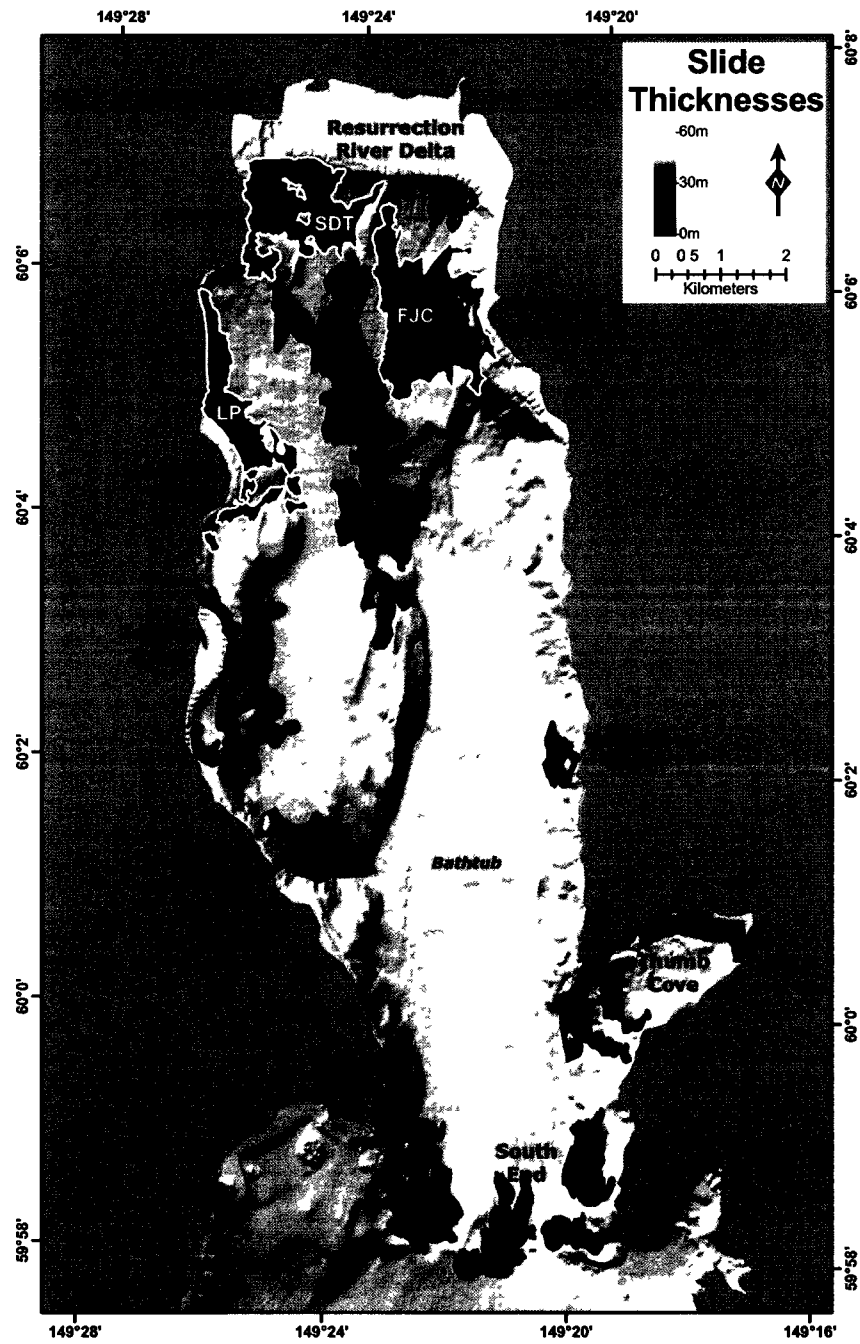


Figure 2.5: Reconstructed thicknesses and initial extent of slide bodies that were mobilized during the 1964 earthquake (modified from *Haeussler et al. (2007)*).

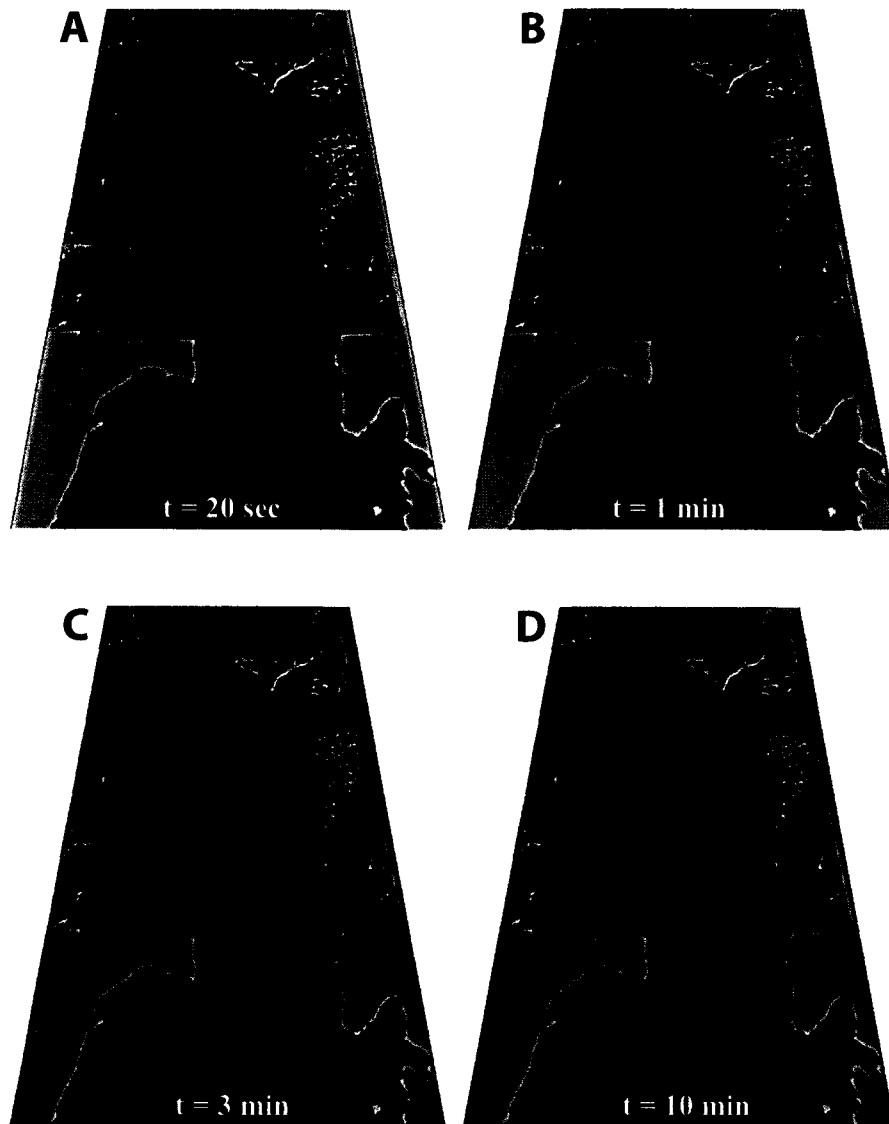


Figure 2.6: Snapshots from the numerical simulation of slide mass.

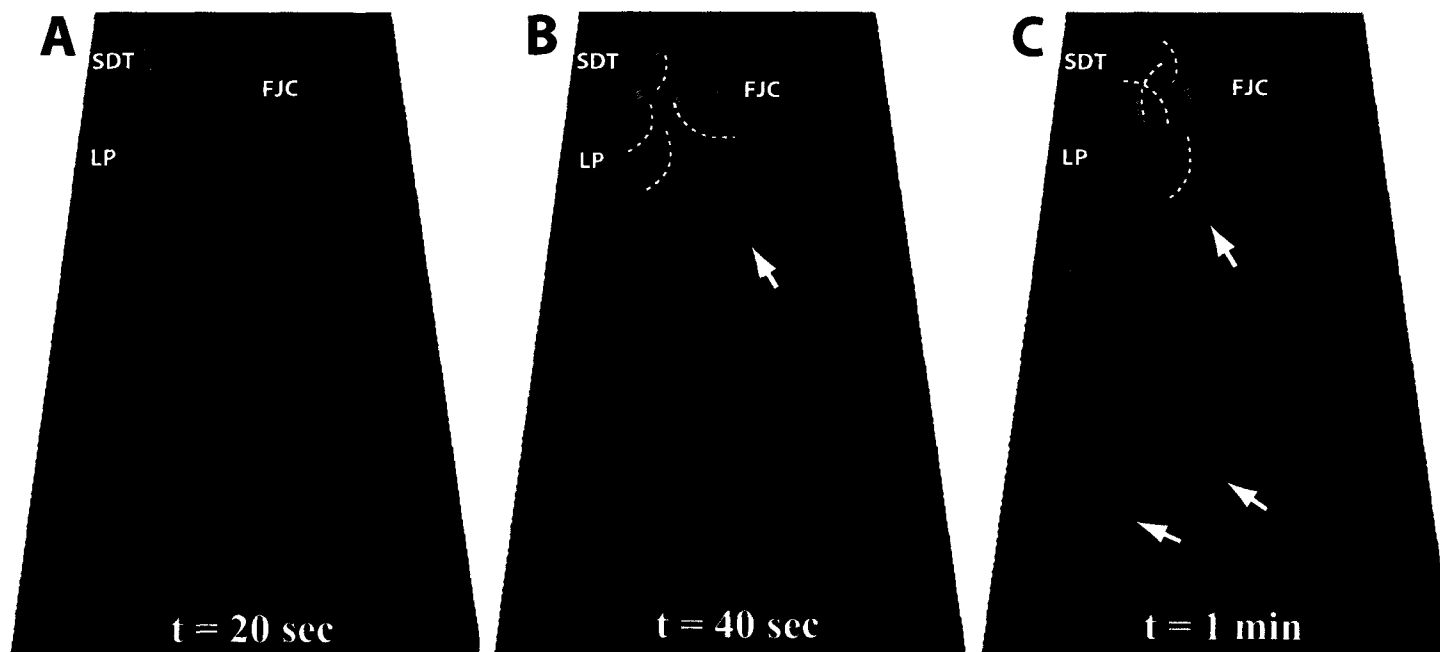


Figure 2.7: Snapshots from the first minute of numerical simulation of surface waves in Resurrection Bay generated by the moving slide mass. Slide locations: SDT - Seward downtown, LP - Lowell Point, FJC - Fourth of July Creek. Dashed lines and arrows indicate positions of different wave fronts (see text for reference).

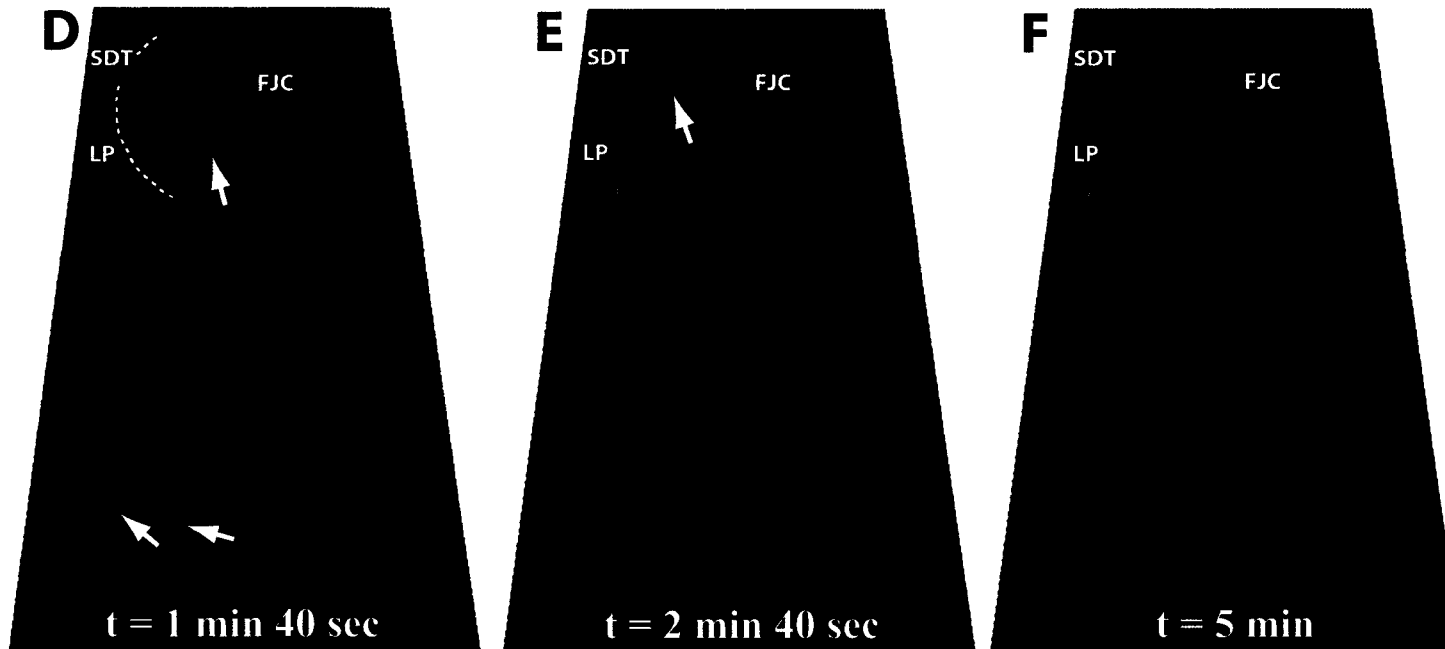


Figure 2.8: Snapshots from numerical simulation of surface waves in Resurrection Bay generated by the moving slide mass. Slide locations: SDT - Seward downtown, LP - Lowell Point, FJC - Fourth of July Creek. Dashed lines and arrows indicate positions of different wave fronts (see text for reference).

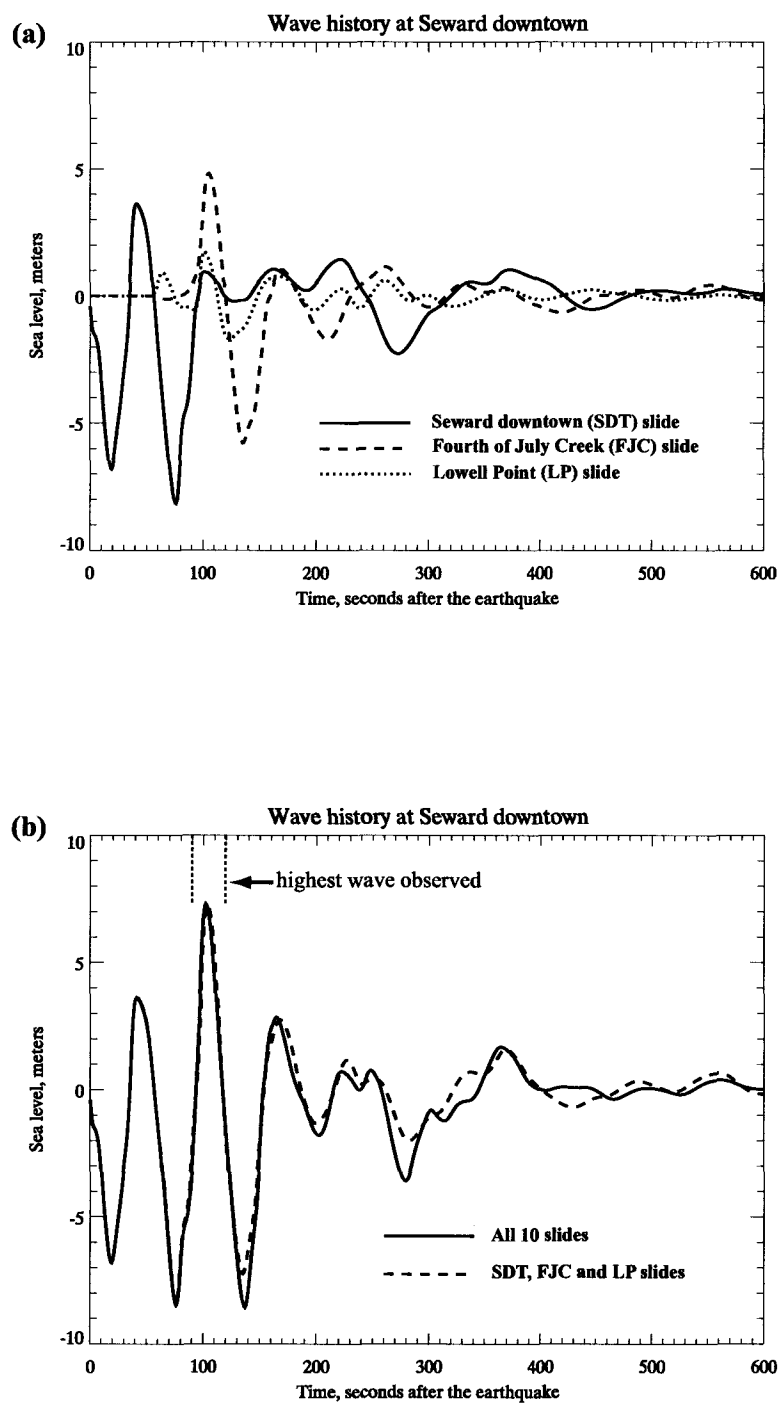


Figure 2.9: Simulated water level at Seward downtown.

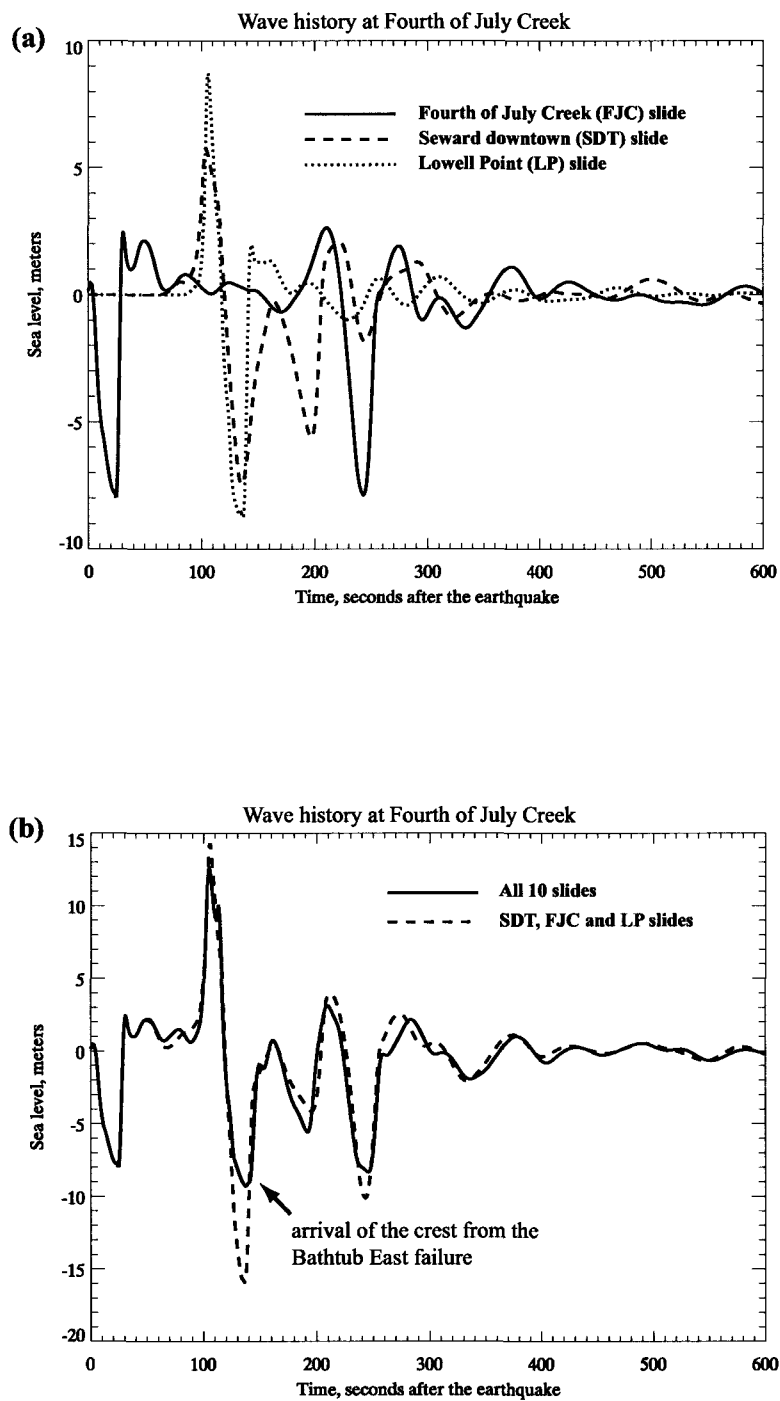


Figure 2.10: Simulated water level at Fourth of July Creek.

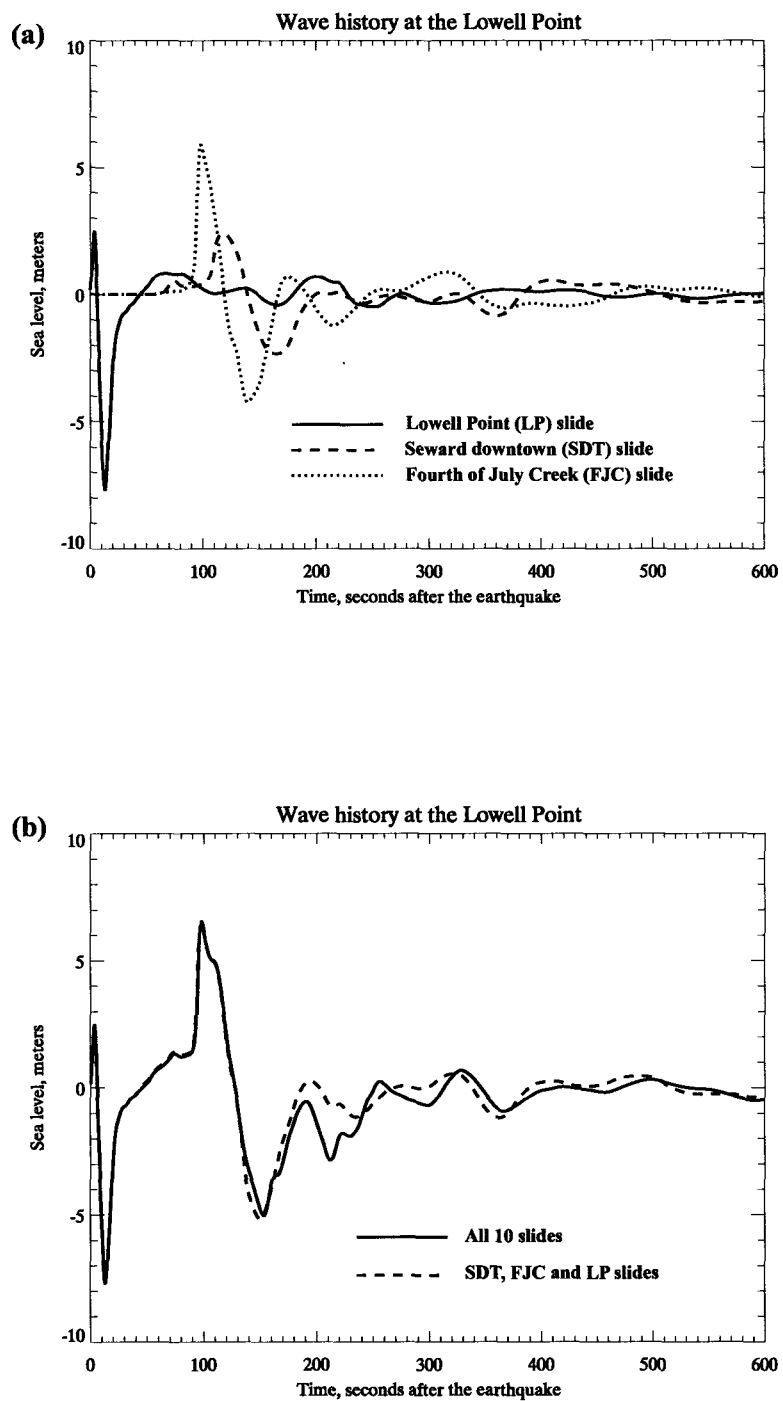


Figure 2.11: Simulated water level at Lowell Point.

Chapter 3

Combined effects of tectonic and landslide-generated tsunami runup at Seward, Alaska during the M_W 9.2 1964 earthquake¹

3.1 Abstract

We apply a recently developed and validated numerical model of tsunami propagation and runup to study the inundation of Resurrection Bay and the town of Seward by the 1964 Alaska tsunami. Seward was hit by both tectonic and landslide-generated tsunami waves during the M_W 9.2 1964 megathrust earthquake. The earthquake triggered a series of submarine mass failures around the fjord, which resulted in landsliding of part of the coastline into the water, along with the loss of the port facilities. These submarine mass failures generated local waves in the bay within 5 minutes of the beginning of strong ground motion. Recent studies estimate the total volume of underwater slide material that moved in Resurrection Bay to be about 211 million m^3 (*Haeussler et al.*, 2007). The first tectonic tsunami wave arrived in Resurrection Bay about 30 minutes after the main shock and was about the same height as the local landslide-generated waves.

Our previous numerical study, which focused only on the local landslide-generated waves in Resurrection Bay, demonstrated that they were produced by a number of different slope failures, and estimated relative contributions of different submarine slide complexes into tsunami amplitudes (*Suleimani et al.*, 2009). This work extends the previous study by calculating tsunami inundation in Resurrection Bay caused by the combined impact of landslide-generated waves and the tectonic tsunami, and comparing the composite inundation area with observations. To simulate landslide tsunami runup in Seward, we use a viscous slide model of *Jiang and LeBlond* (1994) coupled with nonlinear shallow water equations. The input data set includes a high resolution multibeam bathymetry and LIDAR topography grid of Resurrection Bay, and an initial thickness of slide material based on pre- and post-earthquake bathymetry difference maps. For simulation of tectonic tsunami runup, we derive the 1964 coseismic deformations from detailed slip distribution in the rupture area, and use them as an initial condition for propagation of the tectonic tsunami.

¹E. Suleimani, D.J. Nicolsky, P. Haeussler and R. Hansen, 2010, "Combined effects of tectonic and landslide-generated tsunami runup at Seward, Alaska, during the M_W 9.2 1964 earthquake", published in *Pure and Applied Geophysics*, DOI 10.1007/s00024-010-0228-4.

The numerical model employs nonlinear shallow water equations formulated for depth-averaged water fluxes, and calculates a temporal position of the shoreline using a free-surface moving boundary algorithm. We find that the calculated tsunami runup in Seward caused first by local submarine landslide-generated waves, and later by a tectonic tsunami, is in good agreement with observations of the inundation zone. The analysis of inundation caused by two different tsunami sources improves our understanding of their relative contributions, and supports tsunami risk mitigation in south-central Alaska. The record of the 1964 earthquake, tsunami, and submarine landslides, combined with the high-resolution topography and bathymetry of Resurrection Bay make it an ideal location for studying tectonic tsunamis in coastal regions susceptible to underwater landslides.

3.2 Introduction

The Prince William Sound tsunami of March 27, 1964 was generated by the M_w 9.2 Alaskan earthquake, the largest instrumentally recorded earthquake in North America. It ruptured an 800-km long section of the Aleutian megathrust, producing vertical displacements over an area of about 285,000 km² in south-central Alaska (*Plafker, 1969*). The area of coseismic subsidence included Kodiak Island, Kenai Peninsula, Cook Inlet and part of the northern Prince William Sound (Figure 3.1). The major zone of uplift was seaward of the subsidence zone, in Prince William Sound and in the Gulf of Alaska (*Plafker, 1969*). Although the ground shaking was long and violent, 92% of fatalities directly associated with this earthquake were caused by tsunami waves (*Lander, 1996*). The impact of coseismic crustal deformations on the ocean surface and on numerous water bodies in south-central Alaska was very complex. The vertical sea floor displacement generated a major tectonic tsunami that caused fatalities and great damage in Alaska, Hawaii, West Coast of the United States and Canada, and was recorded on tide gauges as far as Australia and New Zealand (*Spaeth and Berkman, 1972*). In addition to the major tectonic wave, about 20 local tsunamis were generated by submarine mass failures from the steep fjord walls in a number of bays in south-central Alaska (*Lander, 1996*).

The village of Seward in Resurrection Bay (Figure 3.1) was the only community that suffered from the combined effects of local landslide-generated waves and the tectonic tsunami during the 1964 earthquake (*Haeussler et al., 2007*). Strong ground shaking trig-

gered several underwater slides in Resurrection Bay within seconds of the beginning of the earthquake, and locally generated waves flooded the town one minute later. The first tectonic wave, which was as destructive as the earlier local waves, arrived from the Gulf of Alaska about 30 minutes after the main shock. Seward has the northeasternmost near-field observations of the tectonic tsunami. The effects of the 1964 earthquake and tsunami waves in Resurrection Bay, including wave amplitudes and extent of inundation, were documented by several investigators (*Wilson and Tørum, 1968; Lemke, 1967; Plafker, 1969*), and will be used in this work to verify results of numerical modeling.

The work described in this paper is part of an effort by the Alaska Earthquake Information Center to conduct tsunami inundation modeling and mapping for coastal communities in Alaska. The goal is to improve tsunami hazard assessment and mitigation in communities that are at risk for future tsunamis. To ensure that coastal communities are provided with tsunami inundation maps produced with scientifically solid and tested methodology (*Synolakis et al., 2008*), we validate and verify our numerical models of tsunami propagation and runup. The model that we use in this study (*Nicolisky et al., 2010*) was tested in a comprehensive set of analytical and field benchmarks suggested by NOAA with the purpose of establishing quality standards for tsunami inundation products (*Synolakis et al., 2007*). The work by *Nicolisky et al. (2010)* describes the numerical algorithm and summarizes results of analytical, laboratory, and field benchmarking. The purpose of this study is to improve our understanding of the different nature of submarine landslide tsunami compared to that of a tectonic tsunami, and to demonstrate that the near-field tectonic and landslide tsunami hazard can be assessed as it relates to south-central Alaska.

This paper presents the first complete numerical modeling study of tectonic and landslide-generated tsunami waves in Resurrection Bay, Alaska, during the 1964 Great Alaska earthquake. Because the 1964 tsunami waves at Seward are relatively well documented, this case provides a unique opportunity to study the integrated effects of tectonic and landslide-generated tsunami runup. The previous numerical study by *Suleimani et al. (2009)* focused only on local landslide-generated tsunami in Resurrection Bay. It tested the hypothesis that the waves were produced by a number of different slope failures, and showed that three slides in the upper bay were the major contributors of tsunami amplitudes at Seward and other fan deltas in the upper bay. We extend our previous work by first calculating tsunami

inundation at Seward and around Resurrection Bay by local landslide-generated waves. Then we model propagation and runup of tectonic tsunami waves that were generated by coseismic deformation of a large segment of the continental shelf in the Gulf of Alaska (Figure 3.1). The tectonic tsunami timing, which is relatively well known, can be an additional constraint on the source of the near-field tectonic tsunami. *Lemke* (1967) reported that, except for some minor secondary slumping, the trigger for local landslide-generated waves in Resurrection Bay ceased at the end of ground shaking, which was about 25 minutes before the arrival of the tectonic tsunami. Although it is possible that individual slides were triggered at different times after the initial ground shaking, there is no independent evidence to support this hypothesis. Therefore we assume that we can separate the tectonic and landslide tsunami sources, and that they are independent and can be modeled separately. After we characterize the tectonic and landslide tsunami hazard of south-central Alaska, we describe numerical models that we use to simulate tsunami waves in Resurrection Bay caused by the tectonic and landslide sources (Section 5.3). Section 3.5 outlines different source mechanisms, and we describe the numerical modeling results in Section 3.6. We complete the analysis by comparing the union of inundation areas computed independently for tectonic and landslide-generated waves with the observed composite inundation pattern, and analyze calculated and observed tsunami time series (Section 5.6). We demonstrate that our modeling approach can be used in tsunami inundation mapping of coastal communities located in seismically active regions, where tectonic tsunami hazard is combined with susceptibility of the fjord environment to underwater slope failures and locally generated waves.

3.3 Tsunami hazard in south-central Alaska

Coastal Alaska has a long record of tsunami waves generated by a variety of geologic sources, which include subduction zone earthquakes, active volcanoes, and submarine and subaerial landslides (*Lander*, 1996). Tectonic tsunamis originating off Alaska can travel across the Pacific and impact coastal areas hours after they were generated. However, the same waves are a near-field hazard for Alaska, and can reach coastal communities within minutes of the earthquake. Tsunami hazard varies substantially along the Alaska coastline, and includes the full spectrum of events from far-field tectonic tsunamis with relatively

low impact on the Alaska coast, to the dangerous combination of near-field tectonic and landslide-generated tsunami waves. The focus of this paper is on south-central Alaska (Figure 3.1), whose coastline is exposed to both local tectonic and landslide tsunami potential.

3.3.1 Tectonic tsunami hazard

The seismic and tsunami hazards in Alaska are controlled by processes along the Aleutian subduction zone, a seismically active plate boundary. Almost the entire length of the subduction zone ruptured in the past century in a series of large and great earthquakes (*Carver and Plafker, 2008*). The megathrust earthquakes of 1938, 1946, 1957, 1964, and 1965 generated Pacific-wide tsunamis that resulted in widespread damage and loss of life along the Pacific coast of Alaska and other exposed locations around the Pacific Ocean (*Lander, 1996*). The area of this study in south-central Alaska is characterized by very high rates of seismicity. Tectonic activity in the region is dominated by the convergence of the Pacific and North American Plates, which interact along the Aleutian megathrust (*Page et al., 1991*). Resurrection Bay is close to the northeast end of the Aleutian megathrust, where it is strongly coupled and has a shallow dip of 3-4 degrees. This zone has the potential to produce some of the largest earthquakes and tsunamis in the world, as demonstrated by the M_W 9.2 Great Alaska earthquake of 1964. The 1964 rupture area extended from Prince William Sound (PWS) to the southern end of Kodiak Island (KI) (Figure 3.1). The major long period trans-Pacific tsunami was generated by the uplift of the continental shelf in the Gulf of Alaska that resulted from slip on the megathrust, although the highest and the most destructive waves in the near field were probably generated by vertical displacements on megathrust splay faults (*Plafker, 2006*). There were two areas of high moment release, representing the two major asperities of the 1964 rupture zone: the PWS asperity and the KI asperity (*Christensen and Beck, 1994*). This result was very similar to those derived from several studies that involved joint inversion of different combination of seismic, tsunami and geodetic data sets (*Holdahl and Sauber, 1994; Johnson et al., 1996; Ichinose et al., 2007*). Analysis of historical earthquake data in PWS and KI regions (*Nishenko and Jacob, 1990*) showed that the KI asperity produced both large and great earthquakes more frequently and also independently of the PWS asperity.

The eastern part of the Aleutian megathrust is the only section of the subduction zone for which information on great historic earthquakes is available: nine paleosubduction earthquakes in the past ~5000 years are recognized from paleoseismic evidence of sudden land changes and tsunami deposits (*Carver and Plafker, 2008*). Although the 1964 tsunami was the most destructive event experienced in Alaska in recorded history, a recent paleoseismic study (*Shennan et al., 2009*) showed that earthquakes about 1500 and 900 years BP ruptured a larger area than that of the 1964 earthquake. The rupture area was calculated to be 23,000 km² greater than that of the 1964 earthquake, with a 15% increase in seismic moment. The authors concluded that the larger extent and the amount of deformation of the penultimate earthquake also contributed to greater tsunamigenic potential. Therefore, it is possible that the worst-case tsunami scenario for coastal communities in the Gulf of Alaska could exceed in magnitude the 1964 event.

3.3.2 Landslide tsunami hazard

Tsunamis caused by slope failures are a significant hazard in the fjords of coastal Alaska and other high-latitude fjord coastlines. *Kulikov et al. (1998)* analyzed tsunami catalog data for the North Pacific coast and showed that this region has a long record of tsunami waves generated by submarine and subaerial landslides, avalanches and rockfalls. Those authors also found that, in the majority of cases, tectonic tsunamis that arrive in bays and fjords from the open ocean have relatively small amplitudes, but a great number of local landslide-generated tsunamis have much larger wave amplitudes. For example, as a result of the 1964 earthquake, about 20 local submarine and subaerial landslide tsunamis were generated in Alaska (*Lander, 1996*), which accounted for 76% of the tsunami fatalities. *Kulikov et al. (1998)* noted that, due to the sparse population of the area, the actual number of historical landslide tsunami events is unknown, and probably much greater than the number of events observed or recorded.

The coast of south-central Alaska has numerous fjords (Figure 3.1). In a fjord setting, rivers and streams emanate from the glacier that initially eroded the valley, forming a fjord-head delta and depositing sediment that easily loses strength during an earthquake. *Lee et al. (2002)* studied different regions of the US Exclusive Economic Zone and found that Alaskan fjords are likely the most susceptible environment to slope failures. *Masson*

et al. (2006) divide all factors that contribute to initiation of submarine landslides into two groups: the factors related to geological properties of landslide material (e.g. overpressure due to rapid deposition), and those associated with external events (e.g. earthquakes or sea level change), noting that usually more than one factor may contribute to a single landslide event. *Hampton et al.* (1996) note that in a fjord environment, where the deltaic sediment is deposited rapidly, the sediment builds up pore-water pressures and could liquefy under extreme low tide conditions or ground shaking during an earthquake, due to low static shear strength. While ground shaking is one of the most common triggering mechanisms for submarine slope failures, the close relationship has been demonstrated between coastal landslides and extreme low tides (*Thomson et al.*, 2001; *Kulikov et al.*, 1998). Human activities can also trigger submarine landslides (*Masson et al.*, 2006; *Thomson et al.*, 2001; *Bornhold et al.*, 2001). Because of these diverse mechanisms, assessment of landslide-generated tsunami hazard is a challenging task. For the Alaska tsunami inundation mapping project, we use the approach for estimating long-term landslide tsunami hazard developed by *Bornhold et al.* (2001). The approach consists of two steps: analysis of historical events and verification of model results with runup observations at the site; and numerical simulation of hypothetical tsunami scenarios. In this study we contribute to the first step by modeling inundation of Seward caused by locally generated tsunami waves on March 27, 1964.

3.3.3 1964 tsunami in Resurrection Bay: history and observations

The town of Seward is near the northwest corner of Resurrection Bay, about 200 km south of Anchorage (Figure 3.1). The entire head of Resurrection Bay is a fjord-head delta that was built by the Resurrection River. Lowell Point, Tonsina Point, and Fourth of July Creek are locations of other alluvial fans that extend into the bay as fan deltas (Figure 3.2). The flat floor of the bay extends north to south, with its deepest part being approximately 300 meters below sea level. The bay is separated from the Gulf of Alaska by a sill, which inhibits sediment transport by tidal currents to the southern part of the bay (*Haussler et al.*, 2007).

The town of Seward is built mostly on the Lowell Creek alluvial fan (the Lowell Creek fan is different than the Lowell Point fan, which lies to the south). In years before the

earthquake, additional land for waterfront facilities was created by artificial fill of loose sand and gravel along the shoreline. The 1964 earthquake at Seward was characterized by strong ground motion that lasted about 3-4 minutes (*Lemke, 1967*). Ground shaking triggered a series of slope failures within the fjord that resulted in landsliding of part of the Seward waterfront into the bay, along with the loss of the port facilities (*Wilson and Tørum, 1968; Haeussler et al., 2007*). The slope failures generated an initial drawdown of water at the Seward waterfront about 30 seconds after the ground started to shake, when the water level suddenly dropped about 6 meters (*Lemke, 1967*). The highest locally generated wave at Seward was about 6-8 meters high and hit the waterfront about 1.5-2.0 minutes after the shaking began, causing much damage. The Seward tide gauge was located on a dock that collapsed into the bay as a result of the submarine failures. Although the tidal record was lost, the sequence of waves generated by the slope failures was reconstructed from observations provided by eyewitnesses (*Wilson and Tørum, 1968; Lemke, 1967*).

The first tectonic tsunami wave came into the bay about 30 minutes after the earthquake, impacting the entire width of the bay (*Wilson and Tørum, 1968*). This wave was as high as the initial landslide-generated waves. The wave extended further inland in the river delta at the head of the bay, than any of the local waves. According to observations, the waves continued to arrive for about 10 hours after the earthquake.

3.3.4 Previous studies

A number of engineering, geologic and geophysical papers related to landslides and tsunami waves in Resurrection Bay were published in the years following the 1964 earthquake. The investigations conducted in the Resurrection Bay area right after the earthquake by *Lemke (1967)*, *Wilson and Tørum (1968)*, and *Shannon and Hilts (1973)* confirmed that strong ground motion during the earthquake caused several submarine slope failures along the Seward waterfront and in other areas within the upper bay. There is a consensus among all the investigators that the large waves observed during ground shaking were generated by the underwater slope failures.

Wilson and Tørum (1968) compiled the chronological sequence of waves in Seward and other locations in Resurrection Bay during and after the earthquake, and interpreted the eyewitness accounts in the form of inferred marigram. The authors acknowledged though

that "at best this marigram can convey only a crude picture of the true state of affairs", due to uncertainty of the eyewitnesses' accounts. The authors investigated oscillating properties of Resurrection Bay and gave a comprehensive overview of tsunami damage at Seward.

Lemke (1967) summarized results of geologic investigations that were conducted in the Resurrection Bay area right after the earthquake, and compiled the maximum observed tsunami runup in downtown Seward and at the head of Resurrection Bay, which is shown by the yellow dashed line in Figures 3.3 and 3.4, respectively. The observed maximum inundation line at Seward represents the combined effects from both local landslide-generated tsunami and the major tectonic tsunami, whereas the observations of maximum run-up at the head of the bay delineate the area that was flooded mostly by seismically generated waves. *Lemke (1967)* also described the geologic setting of Seward and other nearby fan deltas, analyzed triggering mechanism of the submarine landslides, and provided the sequence and interpretation of waves in the bay. He concluded that the major factors that contributed to the total volume and aerial extent of the slide material were the long duration of ground motion, the configuration of underwater slopes, and the type of sediment forming these slopes - unconsolidated and fine-grained materials. He noted that the stability of the sediment was also decreased by the low tidal level at the time of the earthquake, and by the rapid drawdown of water due to the initial slope failure, which prevented the pore water from draining from the sediment quickly enough to maintain hydrostatic conditions.

Shannon and Hiltz (1973) conducted a subsurface geotechnical investigation of materials that failed in Resurrection Bay during the 1964 earthquake. They found that failures consisted of loose alluvial sand and gravel, marine silts and fine sands. It was shown that high artesian pressures within aquifers of the Resurrection River delta combined with the extra load caused by waterfront artificial fill and the shoreline development also contributed to the slope failures. The authors inferred that large masses of sediment might have been transported over great distances into the deep part of Resurrection Bay. Both *Lemke (1967)* and *Shannon and Hiltz (1973)* concluded that underwater slope failures have not improved slope stability of the Seward waterfront, and thus the same slopes could be expected to fail again during the next large earthquake in the same manner as they did during the 1964 earthquake.

The most recent geologic studies by *Lee et al. (2006)* and *Haeussler et al. (2007)* uti-

lized a 2001 NOAA high-resolution multibeam bathymetry survey of Resurrection Bay (*Labay and Haeussler, 2008*) to study the morphology and depth changes of the fjord bottom. This high quality data set helped to visualize a variety of seafloor features related to these submarine slides for the first time. *Lee et al. (2006)* identified remains of the Seward waterfront that failed in 1964 as a result of strong ground shaking, and debris flows that correspond to failures of the Resurrection River delta. Their analysis showed that the 1964 earthquake could potentially have triggered different failure types simultaneously. *Haeussler et al. (2007)* provided analysis of bathymetric data and high resolution subbottom profiles of Resurrection Bay and showed convincing evidence of massive submarine slope failure. The location and extent of submarine mass failures were estimated based on analysis of pre- and post-earthquake bathymetry. *Haeussler et al. (2007)* created a bathymetric difference grid that shows depth changes in the bay after the 1964 earthquake. They concluded that several failures initiated along the fjord walls at relatively shallow depths, and the mass flows produced by these failures transported most of the material as far as 6 to 13 km into the deepest part of the fjord, covering the entire basin with a flow deposit. The total volume of slide material was estimated at 211 million m³. The authors derived a map of the slide material thickness from the bathymetric difference grid, identified 10 different landslide areas and calculated their volumes.

In the first numerical modeling study of local tsunamis in Resurrection Bay, *Suleimani et al. (2009)* utilized the findings of *Haeussler et al. (2007)* to investigate the contribution of individual slide complexes to the observed tsunami amplitudes at Seward and other locations around the bay. *Suleimani et al. (2009)* used the viscous slide model of *Jiang and LeBlond (1994)* coupled with nonlinear shallow water equations to test the hypothesis that the local tsunami waves in Resurrection Bay were produced by a number of different slope failures. The distribution of the slide material from *Haeussler et al. (2007)* served as an initial condition for simulation of the slide motion and the surface water waves that it generated. The numerical models confirm that the waves observed at the Seward waterfront and in several other locations in Resurrection Bay were caused by multiple submarine slope failures. The models indicate that three slides in the northern part of the bay were the major contributors to the tsunami amplitudes at Seward, and that the contribution from other slide complexes was negligible.

While these most recent studies described above do provide analysis of causes and effects of the submarine landslides and locally generated tsunami waves in Resurrection Bay, they give much less attention to the tectonically generated wave. According to observations (*Lemke, 1967; Wilson and Tørum, 1968*), this wave was as high and destructive as local waves, but penetrated much further inland at the head of the bay. This study is an attempt to make the analysis complete by modeling the integrated effects of tsunami runup at Seward caused by both tectonic and landslide-generated waves.

3.4 Methodology

In this section we describe numerical tools and data used to simulate tsunami waves from the 1964 earthquake and landslides in Resurrection Bay. There are three major components in the numerical algorithm: the nonlinear shallow water model for tsunami propagation, a moving boundary scheme that tracks the temporal position of the shoreline for calculation of inundation, and a viscous slide model coupled with shallow water equations for simulation of landslide tsunamis.

3.4.1 Model description

We simulate tsunami propagation and inundation with a nonlinear shallow water model that is formulated for depth-averaged water fluxes in both spherical and rectangular coordinates. Here we give a brief overview of the model and describe its major features, while the work by *Nicolisky et al. (2010)* provides the full description of the model, including its mathematical formulation and numerical implementation. In a problem of tsunami runup, the shallow water equations are solved in a water domain that changes its geometry in time due to variable position of the shoreline. Our model employs the fictitious domain method, in which the water domain is embedded into a larger domain that is fixed in time (*Marchuk et al., 1986*). The advantage of this method is in using the same governing equations for both dry and wet domains that allows for all variables to be continuously extended through the boundary between the domains. Other methods commonly used in solving the numerical problem of tsunami runup are discussed in *Nicolisky et al. (2010)*. In order to calculate the extent of water domain at every time step, we use a free-surface moving boundary algorithm, which determines the position of the shoreline based on the

direction of the water flux between the adjacent grid cells. The shallow water equations, which are approximated by finite differences on a staggered grid, solved semi-implicitly in time using a first order scheme. We efficiently parallelized the algorithm using the domain decomposition technique. The finite difference scheme is coded in FORTRAN using the Portable Extensible Toolkit for Scientific computation (PETSc). The model uses ocean surface displacement due to an underwater earthquake as an initial condition. NOAA recently published a technical memorandum that outlines major requirements for numerical models used in inundation mapping and tsunami forecasting, and describes a procedure for model evaluation (*Synolakis et al.*, 2007). Using the NOAA's procedure as a guideline, *Nicolisky et al.* (2010) validated the tsunami model that is used in this study through a comprehensive set of analytical benchmarks, and tested it against laboratory and field data.

To simulate tsunami runup produced by landslide-generated waves, we use a numerical model of a viscous underwater slide with an arbitrary shape, which deforms in three dimensions. The model assumes full interactions between the deforming slide and the water waves that it generates. This type of viscous or Newtonian model was initially proposed by *Jiang and LeBlond* (1994), and it is adequate for describing landslides made of fine-grained water-saturated deformable sediments. Submarine sediments in different coastal areas may have different rheological behavior due to grain size distribution and chemical composition (*Jiang and LeBlond*, 1993). Another model used for characterization of underwater slides is a Bingham visco-plastic model, in which a finite yield stress has to be applied to the fluid for deformation to occur (*Mei and Liu*, 1987; *Liu and Mei*, 1989; *Jiang and LeBlond*, 1993). The Bingham model is most applicable to dynamics of concentrated cohesive mud, a mixture of water and very fine particles of clay minerals (*Mei and Liu*, 1987). The results of a subsurface geotechnical investigation described in Section 5.4 indicate that the viscous slide model by *Jiang and LeBlond* (1994) is adequate for description of underwater slides in Resurrection Bay. *Fine et al.* (1998) further improved the model by including realistic bathymetry, and also by correcting errors in the governing equations. We apply here the corrected version of the model presented in *Thomson et al.* (2001). The model assumptions as well as its applicability to simulate underwater landslides are discussed by *Jiang and LeBlond* in their formulation of the viscous slide model (*Jiang and LeBlond*, 1992, 1994), and also by *Rabinovich et al.* (2003) and *Thomson et al.* (2001). Other depth-integrated

numerical models of landslide-generated waves are summarized in *Suleimani et al. (2009)*.

The physical system consists of two layers - the upper one is water, and the lower layer is slide material. The slide is assumed to be an incompressible viscous fluid. We assume a sharp interface between the layers, with no mixing allowed between water and sediments. The disturbance of the water surface is produced by the motion of the deforming slide, which is driven only by the force of gravity. The equations for the slide were initially derived under the assumption that it rapidly reaches a steady state regime, and horizontal velocities have a parabolic vertical profile (*Jiang and LeBlond, 1994*). In this model, the slide and the surface waves are fully coupled, meaning that not only does the motion of the slide affect the water surface, but a change in water surface pressure influences the slide thickness. The variable that couples the two systems is the total water depth above the slide. *Titov and Gonzalez (2001)* applied the model for source determination study of the 1998 Papua-New Guinea tsunami. The model was successfully applied to simulate tsunami waves in Skagway Harbor, Alaska, generated by collapse of a dock on November 3, 1994 (*Fine et al., 1998; Thomson et al., 2001*). The results of numerical simulations were in good agreement with the tide gauge record in Skagway Harbor, which is one of numerous fjords in south-eastern Alaska. *Rabinovich et al. (2003)* simulated potential underwater landslides in British Columbia fjords, in geologic settings similar to Resurrection Bay, and they used the model for tsunami hazard assessment. Most recently, this model was applied by *Suleimani et al. (2009)* to simulate multiple submarine slope failures in Resurrection Bay, Alaska, during the Great Alaska earthquake of 1964, and to study the contribution of individual slide complexes to the observed tsunami amplitudes at Seward and other locations around the bay. In this work, we made the model more robust by implementing the moving boundary algorithm, which allows for calculation of runup on the shore, as well as for the "wetting" and "drying" of the slide surface.

3.4.2 Data and numerical grids

To simulate the 1964 tectonic tsunami waves, which were generated by coseismic bottom deformation of the continental shelf of south-central Alaska, we used five nested telescoping grids, or digital elevation models, as input data for the tsunami modeling. These nested grids allow us to propagate waves from the deep waters of the tsunami

source region in the Gulf of Alaska to shallow coastal areas of Resurrection Bay. The external grid spans the entire North Pacific with the grid step of 2 arc-minutes, which corresponds to 1.85×3.7 km at latitude 60°N . The intermediate grids have resolution of 24, 8 and 3 arc-seconds (370×741 m, 123×247 m, and 48×97 m, respectively). Bathymetry data for low and intermediate resolution grids come from the ETOPO2 data set (<http://www.ngdc.noaa.gov/mgg/global/etopo2.html>) and NOAA's National Ocean Service surveys (<http://www.ngdc.noaa.gov/mgg/bathymetry/hydro.html>). The computational time step is different for each grid and is calculated according to the Courant-Friedrichs-Levy (CFL) stability criterion. The numerical simulation used a constant Manning's roughness of $0.03 \text{ s} \cdot \text{m}^{-1/3}$.

The highest resolution grid covers northern Resurrection Bay, including Seward, Lowell Point and Fourth of July Point (Figure 3.2), with the grid step of $\Delta x = \Delta y = 15$ m. *Labay and Haeussler* (2008) developed this grid using the best available high-resolution topography and multibeam bathymetry from the following data sets: (1) low-altitude LIDAR topography collected for the Kenai Watershed Forum in 2006, (2) U.S. Army Corps of Engineers harbor soundings for the Seward City Marina and surroundings collected in 2006, and (3) multibeam bathymetric surveys of Resurrection Bay, conducted by NOAA's National Ocean Service in 2001 (*Labay and Haeussler*, 2008). In this grid, the combined bathymetric and topographic data allow for application of the moving boundary condition for calculation of runup heights and the extent of tsunami inundation.

One of the challenges in near-field earthquake-triggered tsunami modeling is to account for coseismic and post-seismic tectonic land changes, and also to account for a difference between the datum of the numerical grid and the tide stage at the time of the earthquake. The high-resolution numerical grid of combined bathymetry and topography data for Resurrection Bay by *Labay and Haeussler* (2008) was referenced to the tidal datum of Mean High Water (MHW) (*Labay and Haeussler*, 2008). Tide was low at the time of the main shock, which was one of the major factors contributed to the large scale of landsliding (*Lemke*, 1967). However, the low tide also helped to lessen the amount of damage from the first tectonic wave. According to the NOAA tide calculator (<http://tidesandcurrents.noaa.gov>), the first tectonic wave arrived at the local tide minimum, which corresponds to 0.175 m below Mean Lower Low Water (MLLW).

Vertical tectonic land changes at Seward are demonstrated in Figure 3.5. The land-mass in the Seward area experienced coseismic subsidence (CS) of about 1.15 m (*Lemke, 1967*); as a result, many areas that were above sea level before the earthquake, became submerged after the earthquake. *Larsen et al. (2003)* analyzed relative sea level changes from tide gauge records at 15 sites along the coast of south-central Alaska to determine vertical crustal motions in the period from 1937 to 2001. From their analysis, the total postseismic uplift (PU) at Seward was estimated to be about 20 cm. The following equation therefore provides the relationship between the water depth in Resurrection Bay at the time of the earthquake, H_1 , and the present water depth, H_2 , which was measured in 2001 by the NOAA multibeam bathymetry survey:

$$H_1 = H_2 - CS + PU - \Delta H, \quad (3.1)$$

where $\Delta H (> 0)$ is a difference between the present MHW datum and sea level at the time of the earthquake. By using the adjusted vertical datum in the bathymetry grid, the numerical model reproduces the effects of tsunami inundation occurring at Seward under conditions close to those that were present in the 1964 earthquake. The value of ΔH is different for the cases of tectonic and landslide tsunami calculations, due to a slight difference in the stage of tide between the times when underwater slope failures were triggered, and when the tectonic wave arrived.

3.5 Tsunami sources

3.5.1 Justification of separation of source mechanisms

In his interpretation of types and origin of waves observed in Resurrection Bay on March 27, 1964, *Lemke (1967)* noted that sliding terminated at the end of ground shaking, which means that all local waves were generated within the first 2-3 minutes of the beginning of the earthquake. From results of numerical simulations, *Suleimani et al. (2009)* estimated that it took the slide masses about half an hour to get transported from the steep fjord slopes to the deepest part of the fjord. The slide motion was sub-critical with Froude number $Fr < 1$ (*Pelinovsky and Poplavsky, 1996; Fine et al., 2003*), and was characterized by leading crests that rapidly propagated offshore ahead of the moving slides (*Suleimani et al., 2009*). Since the initial stages of slide motion are most important for wave generation

(*Harbitz et al.*, 2006), it is reasonable to assume that the motion of the slides after the termination of ground shaking did not produce any significant wave activity. The first tectonic wave arrived about 25 minutes after shaking stopped, when the locally generated waves had subsided (*Lemke*, 1967); therefore we assume that these events are independent and can be modeled separately. Our focus is on simulating tectonic and landslide tsunami waves at Seward to demonstrate that the inundation zone was a product of two tsunami events. We will compare the integrated effects of landslide and tectonic tsunami inundation with the observed inundation pattern.

3.5.2 Landslide tsunami sources

The numerical study of landslide-generated waves in Resurrection Bay by *Suleimani et al.* (2009) derived the conclusion that slides initiated in the upper bay were the major contributors of tsunami wave energy there during the period of ground shaking. The study demonstrated that waves in the bay were generated by 10 different slides that moved during the earthquake, but the highest locally generated wave observed at the Seward waterfront can be reproduced by the superposition of waves generated by slides offshore of downtown Seward, Lowell Point, and Fourth of July Creek. The locations of these three slides and their thickness distribution, which was derived by *Haeussler et al.* (2007) from the bathymetric difference grid, are shown in Figure 3.6. We use these slide complexes as a source of locally generated waves in our numerical study. The given distribution of the slide material serves as an initial condition for tsunami simulation. The total volume for these slides was estimated at approximately 80 million m³ (*Haeussler et al.*, 2007).

3.5.3 Tectonic tsunami sources

There are several existing models of coseismic deformation of the 1964 Great Alaska earthquake that yield the asperity and slip distribution patterns of the rupture area. *Holdahl and Sauber* (1994) inverted geodetic and geologic measurements of the surface deformation for the slip distribution of the 1964 rupture, using a priori slip estimates from tsunami modeling on the oceanic part of the fault plane. The models by *Johnson et al.* (1996) and *Ichinose et al.* (2007) are based on joint inversion methods, each of them using different combinations of seismic, geodetic and tsunami data sets. The model by *Santini et al.* (2003) employs

the Monte Carlo method to generate different slip distribution patterns, and the most recent study by *Suito and Freymueller (2009)* presents the coseismic deformation model developed jointly with the afterslip model in order to describe the postseismic deformations caused by the 1964 earthquake. In this paper we consider three coseismic deformation models of the 1964 earthquake to determine the initial condition for simulation of tectonic tsunami waves in Resurrection Bay. We refer to the deformation models by abbreviations of the primary authors last names: JDM, the model by *Johnson et al. (1996)*; IDM, the model by *Ichinose et al. (2007)*; and SDM, the model by *Suito and Freymueller (2009)*.

A detailed analysis of the 1964 rupture zone was presented by *Johnson et al. (1996)* through joint inversion of tsunami and geodetic data. To derive a slip distribution, they inverted far-field tsunami wave forms from 23 tidal stations in the Pacific Ocean, and geodetic data in the form of vertical displacements and horizontal vectors. The fault model consisted of eight subfaults representing the Kodiak asperity, nine subfaults in the Prince William Sound asperity, and one subfault representing the Patton Bay fault (Figure 3.1), one of the two megathrust splay faults that ruptured during the earthquake (*Plafker, 1967*). The inversion results indicated two regions of high slip corresponding to areas of high moment release derived by *Christensen and Beck (1994)* from long period P-wave seismograms: the Prince William Sound asperity with an average slip of 18 m, and the Kodiak asperity with an average slip of 10 m.

Ichinose et al. (2007) estimated the spatial and temporal distribution of slip for the 1964 earthquake from joint inversion of teleseismic P waves, far-field tsunami records from 9 tidal stations, and geodetic leveling survey observations. The fault model consisted of 85 subfaults on the megathrust and 10 subfaults along the Patton Bay fault. The inversion results indicated 3 areas of major seismic moment release, where slip was more than twice the average. The contribution of tsunami Green's functions was improved in this model compared to that in JDM by introducing higher resolution grids surrounding the tide gauge stations and by using nonlinear hydrodynamic wave equations with a moving boundary condition.

Suito and Freymueller (2009) introduced a new coseismic deformation model of the 1964 earthquake, which was developed jointly with the afterslip model. SDM uses a realistic geometry with an elastic slab of very low dip angle. Coseismic displacements and

postseismic deformations are calculated using a finite element method on a high resolution 3-D mesh. The main difference between SDM and other models is in prediction of slightly higher slip near the down-dip end of the rupture. Also, SDM assumes that the Patton Bay splay fault extended much farther to the south-west than it did in JDM and IDM, in order to explain subsidence along the southern coast of the Kenai Peninsula (Figure 3.1).

We used the equations of *Okada (1985)* to calculate vertical coseismic displacements for each of the three deformation models described above (Figure 3.7). We simulated tsunami waves generated by these three source functions and compared the results in the far- and near-field regions. The tsunami wave forms, arrival times and amplitudes were almost identical for all three deformation models in the far field, but the same sources produced very different results in the near field (*Suleimani et al., 2008*). These findings agree with the conclusions of *Geist (2002)* who investigated effects of rupture complexity on local tsunami amplitudes. He demonstrated that for shallow subduction zone earthquakes, such as the 1964 earthquake, changes in slip distribution result in significant variations in the local tsunami wave field, suggesting that the near-field tsunami runup is highly sensitive to variability of slip along the rupture area. All coseismic deformation models of the 1964 tsunami have one limitation in common: they are not constrained by observations of tsunami in the near field (*Plafker et al., 1969; Plafker, 1969*). The preliminary numerical study by (*Suleimani et al., 2008*) confirmed the conclusion derived by *Plafker (2006)* that local splay faults played crucial role in generating large tsunami amplitudes observed along the coastlines of the Kenai Peninsula, Kodiak Island, and Montague Island (Figure 3.1).

3.6 Numerical simulations

We performed runup calculations using a high-resolution grid of combined bathymetric and topographic data for the upper Resurrection Bay (Figure 3.6). This data set reflects the most recent configuration of the Seward waterfront and the position of the shoreline. The boat harbor in the north-eastern corner of the bay, the breakwaters, and the cruise ship terminal (Figure 3.3) did not exist in 1964. In order to recreate the conditions at the time of the earthquake, we digitally removed the breakwaters and all other constructions in the harbor area by replacing the corresponding data points with the pre-1964 bathymetric soundings. Then, we adjusted the bathymetry of the landslide source and deposition areas in order

to define the pre-earthquake depths in Resurrection Bay. In the numerical simulation of landslide-generated waves, the slide material moved down from the offshore slopes into the deepest part of the fjord, filling the north-south depression with sediment (Figure 3.2). Because we assume that the tectonic wave arrived to the bay after the slide motion had terminated, we used the new modified bathymetry of Resurrection Bay with the slide material redistributed on the fjord bottom for simulation of the tectonic tsunami. We did not modify the land topography around the bay to match it to the pre-earthquake topography, because the pre-1964 elevation data in Alaska are of very poor quality, especially in the coastal zone. Instead, we used the high-quality topographic LIDAR data (*Labay and Haeussler, 2008*).

3.6.1 Inundation of Resurrection Bay by landslide-generated waves

We extend the previous work of *Suleimani et al. (2009)* by calculating runup of local waves caused by submarine slope failures in Resurrection Bay during the 1964 earthquake. The computational domain is shown in Figure 3.6. This area is covered by a continuous bathymetry-topography grid with horizontal resolution of 15 meters (*Labay and Haeussler, 2008*). The distribution of the slide material serves as an initial condition for tsunami simulation. At the southern open boundary of the grid, we specify the radiation boundary condition for the water waves. The boundary condition for the slide mass allows the slide to leave the computational domain without reflection. The moving boundary condition at the shore line and at the slide-water interface allows for wetting and drying of land as described in *Nicolisky et al. (2010)*. We assume that the slides were initially at rest, then triggered by ground shaking at $t = 0$, and moved afterwards only under the force of gravity. In our model all slides started moving at the same time, because there is no independent evidence of slides being triggered at different times. Following *Thomson et al. (2001)*, we ran the numerical simulation with a time step $\Delta t = 0.01$ seconds, which is at least an order of magnitude smaller than the value required by the CFL stability criterion for water waves.

The maximum observed extent of inundation at Seward and at the head of the bay is shown in Figures 3.3 and 3.4, respectively, by the yellow dashed line. The inundation line at Seward was digitized from the U.S. Army Corps of Engineers aerial photo of Seward that was taken one day after the earthquake, and the maximum observed extent of inundation

at the head of the bay was digitized from the geologic map (*Lemke, 1967*). The observed inundation line represents the maximum runup reached by one or more waves, of both local and tectonic origin, and therefore delineates the composite inundation zone. The blue line in Figures 3.3 and 3.4 outlines the area inundated by simulated landslide-generated waves at Seward and at the head of the bay, respectively. At the Seward waterfront (Figure 3.3), the calculated inundation area is not significantly different from the observed one, while in the area adjacent to the modern harbor and Seward highway the observed and calculated extents of inundation are far apart. The calculated inundation caused by landslide-generated waves in this area follows the 1964 shoreline, and the observed inundation extends beyond the lagoon, which is to the west from the Seward highway. This result agrees with observations (*Lemke, 1967*) that locally generated waves did not reach the highway, and people were able to drive out of the town on this road across the lagoon after the ground shaking ceased. This road was completely blocked by houses, boats, and other debris brought later by the tectonically generated waves. In 1964, the lagoon extended to both sides of the highway, while the eastern part of it is now covered with artificial fill and is home to a new business district, harbor and port facilities. We did not modify elevations in this area to match them to the 1964 topography, and that probably explains why the inundation line did not extend further inland.

The results of runup simulation at the Resurrection River delta (Figure 3.4) show that the inundation area caused by landslide-generated waves is much smaller than the observed composite inundation area. This result also agrees with observations that the tectonic wave extended much further inland at the head of the bay than any of the locally generated waves (*Lemke, 1967*). This is explained by the fact that tectonically generated waves had much larger wavelengths and therefore carried more energy than the landslide-generated waves. Also, the locally generated wave that did the greatest damage in downtown Seward arrived from the Fourth of July Creek slide (Figure 3.6). This wave approached Seward from the south-east, and therefore did not inundate far inland in the north-western part of the town, in the lagoon area. Numerical results show that the same wave dissipated quickly when it reached the intertidal zone at the head of the bay.

There is no documented inundation line at Lowell Point and Fourth of July Creek. The blue contour in Figures 3.8 and 3.9 outlines the calculated inundation areas. According

to several eyewitness accounts (*Lemke, 1967; Wilson and Tørum, 1968*), the first wave hit Lowell Point at the north-east corner of the fan when ground was still shaking. It penetrated inland several hundred feet, which corresponds to the position of the calculated inundation line in the northern part of the fan delta. The timing of the wave and its direction indicate that this wave was generated by the slide offshore the Seward waterfront. From observations of debris position and scars on trees (*Lemke, 1967*), it was concluded that another wave came to Lowell Point from the east and overran the shore moving to the west. The largest wave, which hit Lowell Point about 30 min after the first one, came from the south and did most of the damage at Lowell Point. Because of its arrival time and amplitude, it was most probably the tectonically generated wave.

According to *Lemke (1967)*, it was difficult to reconstruct the number of waves and their directivity patterns at Fourth of July Creek (Figure 3.9). The extent of the inundation in some areas was marked by a debris line several hundred feet or more inland. *Wilson and Tørum (1968)* cited an account of one witness who reported the wave "running inland about a quarter of a mile" (1320 ft, 402 m). The distance from the westernmost tip of the fan delta to the calculated inundation line for landslide-generated waves is about 260 m (850 ft).

3.6.2 Inundation of Resurrection Bay by a tectonic tsunami

We performed numerical simulations of tectonic tsunami runup in northern Resurrection Bay using the three source functions discussed in Section 3.5.3. Coseismic deformations calculated from JDM, IDM, and SDM (Figure 3.7) served as initial conditions for water surface. Because relatively large waves kept arriving at Seward until about 11:30 pm on March 27, 1964, we ran computer simulations for 8 hours of physical time. We evaluate coseismic deformations for each of the source models by analyzing the tsunami arrival time, phase of the first wave, and extent of the inundation zone.

The arrival time of the first tectonic wave at Seward is a critical constraint on tectonic source models. The wave was observed to be large with a positive first motion (arriving as a crest) that came to Seward about 25 minutes after the shaking stopped, or about 30 minutes after the beginning of the earthquake. Also, arrival times of the same tectonic wave to Whidbey Bay and Puget Bay (Figure 3.1) were about 19 and 20 minutes after

the shaking started (*Plafker, 1969*), and the reported first motion was also positive. We calculated time series of the tectonic tsunami at the Seward waterfront for each of the source functions (Figure 3.10). We show the series for the first 3 hours after the earthquake to clearly illustrate the arrival of the first wave. The wave modeled with the SDM initial condition best matches observations. It has the right polarity, and the arrival time of 35 min after the beginning of the earthquake is very close to observations. The wave modeled with the JDM has a negative phase, and the wave corresponding to IDM has small amplitude and late arrival.

The modeled inundation at the head of the bay shows critical differences between the three models (Figure 3.4). The tectonic wave corresponding to JDM penetrated deeper inland and completely inundated the airport. These results vastly overestimate inundation of the airport area (the wave was reported to flood the airstrip only partially) and the rest of the river delta. The wave simulated with the IDM deformations produced little inundation in the delta and did not flood the airstrip. The wave associated with SDM produced an inundation zone that matches observations better than inundation zones corresponding to the IDM and JDM waves. The observed inundation line (yellow dashed line) has two pronounced lobes in the Resurrection River delta. The SDM line matches the right lobe very well. The discrepancy between the lines in the area of the left lobe could be explained by natural and anthropogenic changes in the topography of the river delta due to redirection of the multiple river channels.

Numerical simulations of the three source models produce similar results in downtown Seward, but differ significantly in the region north of town near the boat harbor (Figure 3.3). The inundation line associated with SDM is the closest to the observed line. Modeling results agree with observations of the tectonic wave in the area of modern harbor, that the wave crashed into the lagoon, and debris completely blocked the Seward highway (*Lemke, 1967*). The inundation line produced with the IDM deformations greatly underestimates the flooded area, whereas the JDM line extends further inland than the observed inundation line. The landslide-generated waves inundated further inland in the downtown area than the SDM tectonic waves did. We note that at the southern end of the Seward fan the inundation lines corresponding to SDM and to the landslides, circle around the Alaska SeaLife Center. During the recent construction of this facility, the waterfront area was raised up

substantially with respect to its elevation at the time of the earthquake, which explains the discrepancy with the observed inundation line. Overall, the union of inundation areas computed for landslide-generated waves and for the SDM-produced tectonic waves, is in good agreement with the observed composite inundation zone.

The results of numerical simulation of tectonic scenarios at Lowell Point and Fourth of July Creek (Figures 3.8 and 3.9) show that tectonic waves corresponding to the SDM and JDM scenarios produced greater inundation than that of the landslide-generated waves. These results can not be tested against observations of debris lines, because of the lack of eyewitness accounts of the wave sequence. The debris line was about 30 and 25 feet above mean lower low water at Lowell Point and Fourth of July Creek, respectively, which roughly corresponds to tsunami runup of the JDM-produced tsunami waves.

3.7 Conclusions

The numerical simulations of tectonic and landslide-generated tsunami runup in Resurrection Bay generated by the 1964 earthquake are consistent with observations of the tsunami wave sequence. The town of Seward was flooded within 5 minutes of the beginning of the strong ground shaking by local waves generated by multiple submarine mass failures. The tectonic tsunami wave arrived at Seward about 25-30 minutes after shaking stopped, when the locally generated waves had subsided, which allowed for separation of the tsunami source mechanisms in the numerical model. Our numerical results agree with the interpretation given by *Lemke (1967)* of the observed maximum tsunami runup at Seward and at the head of the bay as a composite inundation area. We demonstrated that the runup zone is a product of two events: the maximum runup at the Seward waterfront was produced by both local landslide-generated waves and the tectonic waves, and the areas next to the modern harbor, lagoon, and in the Resurrection River delta were flooded primarily by the tectonic tsunami.

We determined the source of the landslide-generated tsunami waves, which inundated Seward immediately after the earthquake, from the analysis of tsunami time series in the upper Resurrection Bay (*Suleimani et al., 2009*). We found that three slide complexes in the upper bay generated the local waves that were the major contributors to tsunami runup at Seward. To define a source for tectonic tsunami waves, we used outputs of three

co-seismic deformation models of the 1964 earthquake as initial conditions for modeling tectonic tsunami runup in Resurrection Bay. All three source functions produced different tsunami amplitudes, arrival times, and inundation areas at Seward and other locations in the upper bay, and the model of *Suito and Freymueller (2009)* fits the observations well. The model of *Johnson et al. (1996)* overestimates tsunami runup, and the model of *Ichinose et al. (2007)* tends to underestimate tsunami runup. The presented results suggest that initial tsunami wave amplitudes in the source area of the 1964 earthquake, which are product of coseismic displacements, are crucial for the near-field tsunami modeling, and that the inundation results are sensitive to the fine structure of slip distribution. The combination of inundation areas produced by local waves from the three major slides in the upper bay, and the tectonic waves simulated with the source function of *Suito and Freymueller (2009)*, produced a good match with observations.

When analyzing results of numerical modeling and comparing them with observations, we take into account several limitations of the model. One of them, and probably the most important, is the de-coupling of tides and tsunamis. The last seismic wave at Seward was reported about 11 hours after the earthquake. During this time, tidal level made a full cycle changing from its minimum at the time of the earthquake, then to the maximum at midnight, and then back to minimum at the time when the last wave was observed. The waves that came on the rising tide could have been amplified due to interactions of tsunami waves with tides. *Myers and Baptista (2001)* studied the importance of dynamic superposition of tides and tsunami waves and concluded that nonlinear tsunami-tide interactions could be important and need to be included in local tsunami inundation studies. Also, the model simulates only free seiches induced by tilting of a water basin as a result of coseismic deformations in the rupture area, and those initiated by landslides. It does not take into account forced seiches caused by passing of seismic waves (*Barberopoulou et al., 2006*). Future work will include the development of a tsunami model that dynamically simulates tides and accounts for nonlinear tsunami-tide interactions, and simulates seiches in bays and harbors due to horizontal motion of the side walls. Our future study of the 1964 tsunami source function will determine the important source parameters and the essential components of the numerical model that affect the near-field inundation modeling of tsunami waves generated by earthquakes on the Aleutian megathrust.

3.8 Acknowledgments

This study was supported by NOAA grants 27-014d and 06-028a through Cooperative Institute for Arctic Research. We thank Prof. Efim Pelinovsky and one anonymous reviewer for helpful suggestions that improved this manuscript. Dr. Alexander Rabinovich gave us a number of critical comments and valuable recommendations that we greatly appreciate. The authors also thank Eric Geist and Jason Chaytor for their thorough and constructive reviews. We are grateful to Prof. Jeff Freymueller for valuable discussions, and to Dr. Hisashi Suito for providing us with parameters of his model. Numerical calculations for this work are supported by a grant of High Performance Computing resources from the Arctic Region Supercomputing Center at the University of Alaska Fairbanks as part of the US Department of Defense HPC Modernization Program.

Bibliography

- Barberopoulou, A., A. Qamar, T. Pratt, and W. Steele (2006), Longperiod effects of the Denali earthquake on water bodies in the Puget Lowland: observations and modeling, *Bull. Seism. Soc. Am.*, 96(2), 519–535, doi:10.1785/0120050090.
- Bornhold, B., R. Thomson, A. Rabinovich, E. Kulikov, and I. Fine (2001), Risk of landslide-generated tsunamis for the coast of British Columbia and Alaska, in *2001 An Earth Odyssey. Proceedings of the Canadian Geotechnical Conference*, pp. 1450–1454.
- Carver, G., and G. Plafker (2008), Paloseismicity and neotectonics of the Aleutian subduction zone - an overview, in *Active tectonics and seismic potential of Alaska*, edited by J. Freymueller, P. Haeussler, R. Wesson, and G. Ekström, Geophysical Monograph Series 179, pp. 43–63, AGU, Washington, DC.
- Christensen, D., and S. Beck (1994), The rupture process and tectonic implications of the Great 1964 Prince William Sound earthquake, *Pure Appl. Geophys.*, 142(1), 29–53.
- Fine, I., A. Rabinovich, E. Kulikov, R. Thomson, and B. Bornhold (1998), Numerical modelling of landslide-generated tsunamis with application to the Skagway Harbor tsunami of November 3, 1994, in *Proc. Int. Conf. on Tsunamis*, pp. 211–223, Paris.
- Fine, I., A. Rabinovich, R. Thomson, and E. Kulikov (2003), Numerical modeling of tsunami generation by submarine and subaerial landslides, in *Submarine Landslides and Tsunamis, NATO Science Series, Series IV: Earth and Environmental Sciences, vol. 21*, edited by A. Yalciner, E. Pelinovsky, E. Okal, and C. Synolakis, pp. 69–88, Kluwer Academic Publishers.
- Geist, E. (2002), Complex earthquake rupture and local tsunamis, *J. Geophys. Res.*, 107(B5), 1–16.
- Haeussler, P., H. Lee, H. Ryan, K. Labay, R. Kayen, M. Hampton, and E. Suleimani (2007), Submarine slope failures near Seward, Alaska, during the M9.2 1964 earthquake, in *Submarine Mass Movements and their consequences*, edited by V. Lykousis, D. Sakellariou, and J. Locat, pp. 269–278.
- Hampton, M., H. Lee, and J. Locat (1996), Submarine landslides., *Rev Geophys*, 34, 33–59.

- Harbitz, C., F. Løvholt, G. Pedersen, and D. Masson (2006), Mechanisms of tsunami generation by submarine landslides: a short review, *Norwegian Journal of Geology*, 86, 255–264.
- Holdahl, S., and J. Sauber (1994), Coseismic slip in the 1964 prince william sound earthquake: A new geodetic inversion, *Pure Appl. Geophys.*, 142, 55–82.
- Ichinose, G., P. Somerville, H. Thio, R. Graves, and D. O’Connell (2007), Rupture process of the 1964 prince william sound, alaska, earthquake from the combined inversion of seismic, tsunami, and geodetic data, *J. Geophys. Res.*, 112(B07306).
- Jiang, L., and P. LeBlond (1992), The coupling of a submarine slide and the surface waves which it generates, *J. Geophys. Res.*, 97(C8), 12,731–12,744.
- Jiang, L., and P. LeBlond (1993), Numerical modeling of an underwater Bingham plastic mudslide and the waves which it generates, *J. Geophys. Res.*, 98(C6), 10,303–10,317.
- Jiang, L., and P. LeBlond (1994), Three-dimensional modeling of tsunami generation due to a submarine mudslide, *J. Phys. Oceanogr.*, 24(3), 559–572.
- Johnson, J., K. Satake, S. R. Holdahl, and J. Sauber (1996), The 1964 prince william sound earthquake: Joint inversion of tsunami and geodetic data, *J. Geophys. Res.*, 101, 523–532.
- Kulikov, E., A. Rabinovich, I. Fine, B. Bornhold, and R. Thomson (1998), Tsunami generation by landslides at the Pacific coast of North America and the role of tides, *Oceanology*, 38(3), 361–367.
- Labay, K., and P. Haeussler (2008), Combined high-resolution LIDAR topography and multibeam bathymetry for upper Resurrection Bay, Seward, Alaska, U.S. Geological Survey Digital Data Series 374, <http://pubs/usgs.gov/ds/374/>.
- Lander, J. (1996), *Tsunamis affecting Alaska. 1737–1996*, no. 31 in NGDC Key to Geophysical Research, National Geophysical Data Center, Boulder, Colo.

- Larsen, C., K. Echelmeyer, J. Freymueller, and R. Motyka (2003), Tide gauge records of uplift along the northern Pacific-North American plate boundary, 1937 to 2001, *J. Geophys. Res.*, 108(B4), 2216, doi:10.1029/2001JB001685.
- Lee, H., W. Schwab, and J. Booth (2002), Submarine landslides: an introduction., in *Submarine Landslides: Selected Studies in the US Exclusive Economic Zone*, US Geological Survey Bulletin, edited by W. Schwab, H. Lee, and D. Twichell, pp. 1–13.
- Lee, H., H. Ryan, R. Kayen, P. Haeussler, P. Dartnell, and M. Hampton (2006), Varieties of submarine failure morphologies of seismically-induced landslides in Alaska fjords, *Norwegian Journal of Geology*, 86, 221–230.
- Lemke, R. (1967), Effects of the Earthquake of March 27, 1964, at Seward, Alaska, U.S. Geological Survey Professional Paper 542-E, 48 pp.
- Liu, K., and C. Mei (1989), Slow spreading of a sheet of Bingham fluid on an inclined plane, *J. Fluid Mech.*, 207, 505–529.
- Marchuk, G. I., Y. A. Kuznetsov, and A. M. Matsokin (1986), Fictitious domain and domain decomposition methods, *Sov. J. Numer. Anal. Math. Modelling*, 1, 3–35.
- Masson, D., C. Harbitz, R. Wynn, G. Pedersen, and F. Løvholt (2006), Submarine landslides: processes, triggers and hazard prediction, *Phil. Trans. R. Soc. A*, 364, 2009–2039, doi:10.1098/rsta.2006.1810.
- Mei, C., and K. Liu (1987), A Bingham-plastic model for a muddy seabed under long waves, *J. Geophys. Res.*, 92(C13), 14,581–14,594.
- Myers, E., and A. Baptista (2001), Analysis of factors influencing simulations of the 1993 Hokkaido Nansei-Oki and 1964 Alaska tsunamis, *Nat. Hazards*, 23, 1–28.
- Nicolisky, D., E. Suleimani, and R. Hansen (2010), Validation and verification of a numerical model for tsunami propagation and runup, *Pure Appl. Geophys.*, doi:10.1007/s00024-010-0231-9.
- Nishenko, S., and K. Jacob (1990), Seismic potential of the Queen Charlotte-Alaska-Aleutian seismic zone, *J. Geophys. Res.*, 95(B3), 2511–2532.

- Okada, Y. (1985), Surface deformation due to shear and tensile faults in a half-space, *Bull. Seism. Soc. Am.*, 75, 1135–1154.
- Page, R., N. Biswas, J. Lahr, and H. Pulpan (1991), Seismicity of continental Alaska, in *Neotectonics of North America*, edited by D. Slemmons, E. Engdahl, M. Zoback, and D. Blackwell, Geol. Soc. Am., Decade Map V. 1, pp. 47–68, Boulder, Colorado.
- Pelinovsky, E., and A. Poplavsky (1996), Simplified model of tsunami generation by submarine landslides, *Phys. Chem. Earth*, 21(12), 13–17.
- Plafker, G. (1967), Surface faults on Montague Island associated with the 1964 Alaska Earthquake, U.S. Geological Survey Professional Paper 543-G, 42 pp.
- Plafker, G. (1969), Tectonics of the March 27, 1964 Alaska Earthquake, U.S. Geological Survey Professional Paper 543-I, 74 pp.
- Plafker, G. (2006), The great 1964 Alaska Earthquake as a model for tsunami generation during megathrust earthquakes with examples from Chile and Sumatra, Abstracts of the AGU Chapman Conference on the Active Tectonics and Seismic Potential of Alaska.
- Plafker, G., R. Kachadoorian, E. Eckel, and L. Mayo (1969), Effects of the Earthquake of March 27, 1964 on various communities, U.S. Geological Survey Professional Paper 542-G, 50 pp.
- Rabinovich, A. B., R. E. Thomson, B. D. Bornhold, I. V. Fine, and E. A. Kulikov (2003), Numerical modelling of tsunamis generated by hypothetical landslides in the Strait of Georgia, British Columbia, *Pure Appl. Geophys.*, 160(7), 1273–1313.
- Santini, S., M. Dragoni, and G. Spada (2003), Asperity distribution of the 1964 Great Alaska earthquake and its relation to subsequent seismicity in the region, *Tectonophysics*, 367, 219–233, doi:10.1016/S0040-1951(03)00130-6.
- Shannon, W., and D. Hilts (1973), Submarine landslide at Seward, in *The Great Alaska Earthquake of 1964. Engineering*, pp. 144–156, National Academy of Sciences, Washington, D.C.

- Shennan, I., R. Bruhn, and G. Plafker (2009), Multi-segment earthquakes and tsunami potential of the Aleutian megathrust, *Quaternary Science Reviews*, 28, 7–13.
- Spaeth, M., and S. Berkman (1972), Tsunami of March 28, 1964, as recorded at tide stations and the Seismic Sea Waves Warning System, in *The Great Alaska Earthquake of 1964. Oceanography and Coastal Engineering*, pp. 38–100, National Academy of Sciences, Washington, D.C.
- Suito, H., and J. Freymueller (2009), A viscoelastic and afterslip postseismic deformation model for the 1964 Alaska earthquake, *J. Geophys. Res.*, 114(B11404), doi: 10.1029/2008JB005954.
- Suleimani, E., N. Ruppert, M. Fisher, D. West, and R. Hansen (2008), The contribution of coseismic displacements due to spaly faults into the local wavefield of the 1964 Alaska tsunami, in *Eos Trans. AGU, Fall Meet. Suppl.*, vol. 89(53), abstract OS43D-1334.
- Suleimani, E., R. Hansen, and P. Haeussler (2009), Numerical study of tsunami generated by multiple submarine slope failures in Resurrection Bay, Alaska, during the M_w 9.2 1964 earthquake, *Pure Appl. Geophys.*, 166, 131–152, doi:10.1007/s00024-004-0430-3.
- Synolakis, C., E. Bernard, V. Titov, U. Kânoğlu, and F. González (2007), Standards, criteria, and procedures for NOAA evaluation of tsunami numerical models, *NOAA Tech. Memo. OAR PMEL-135, NTIS: PB2007-109601*, NOAA/Pacific Marine Environmental Laboratory, Seattle, WA, 55 pp.
- Synolakis, C., E. Bernard, V. Titov, U. Kânoğlu, and F. González (2008), Validation and verification of tsunami numerical models, *Pure Appl. Geophys.*, 165, 2197–2228.
- Thomson, R. E., A. B. Rabinovich, E. A. Kulikov, I. V. Fine, and B. D. Bornhold (2001), On numerical simulation of the landslide-generated tsunami of November 3, 1994 in Skagway Harbor, Alaska, in *Tsunami Research at the End of a Critical Decade*, edited by G. T. Hebenstreit, pp. 243–282, Kluwer.
- Titov, V., and F. Gonzalez (2001), Numerical study of the source of the July 17, 1998 PNG tsunami, in *Tsunami Research at the End of a Critical Decade*, edited by G. T. Hebenstreit, pp. 197–207, Kluwer.

Wilson, B., and A. Tørum (1968), The tsunami of the Alaskan Earthquake, 1964: Engineering evaluation, U.S. Army Corps of Engineers, Technical memorandum No. 25, 401 p.

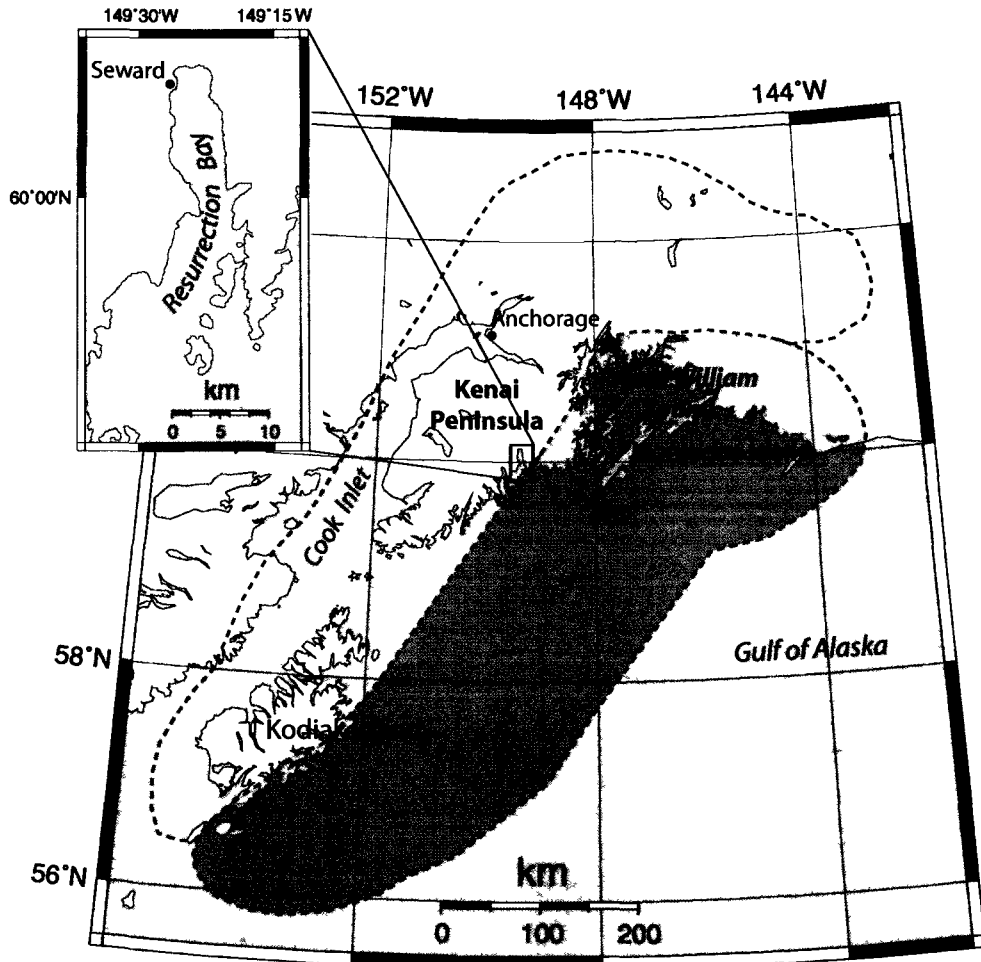


Figure 3.1: Map of south-central Alaska with the rupture zone of the $M_w 9.2$ 1964 Great Alaska earthquake. The star indicates the earthquake epicenter. The dashed contour delineates regions of coseismic uplift (shaded) and subsidence of the 1964 rupture area (Plafker, 1969). The inset map includes Resurrection Bay, which is shown in detail in Figure 3.2. Notations: 1 - Whidbey Bay, 2 - Puget Bay, PBF - Patton Bay fault.

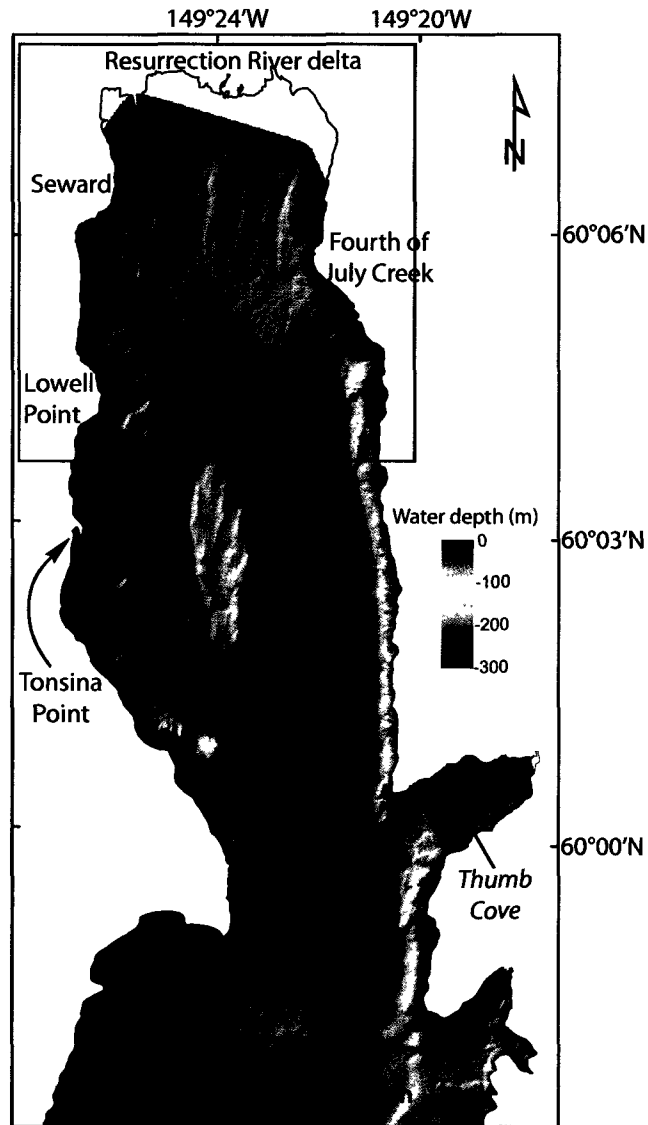


Figure 3.2: Multibeam bathymetric image of Resurrection Bay. The dashed black lines indicate bounds of the major fan deltas. The area of the upper Resurrection Bay outlined by the black rectangle is shown in Figure 3.6.

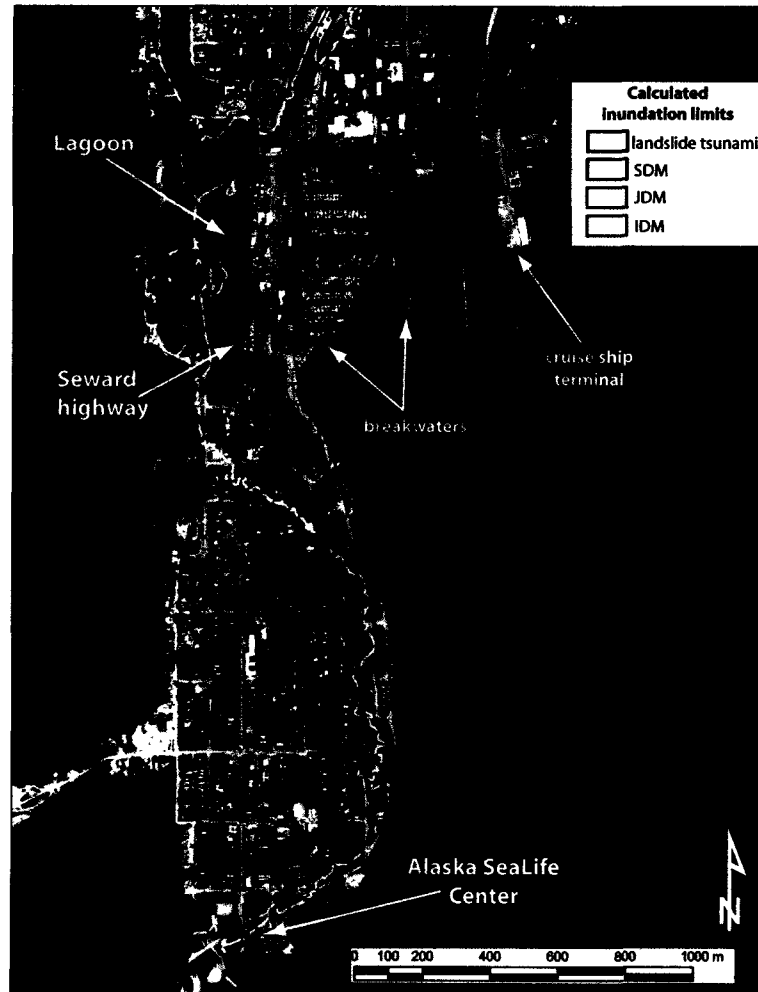


Figure 3.3: Observed 1964 inundation line at Seward, shown by the dashed yellow contour (from *Lemke (1967)*), and inundation limits calculated for different tectonic tsunami sources and the landslide source. Orthophoto image courtesy of National Resources Conservation Service, USDA, 1996.

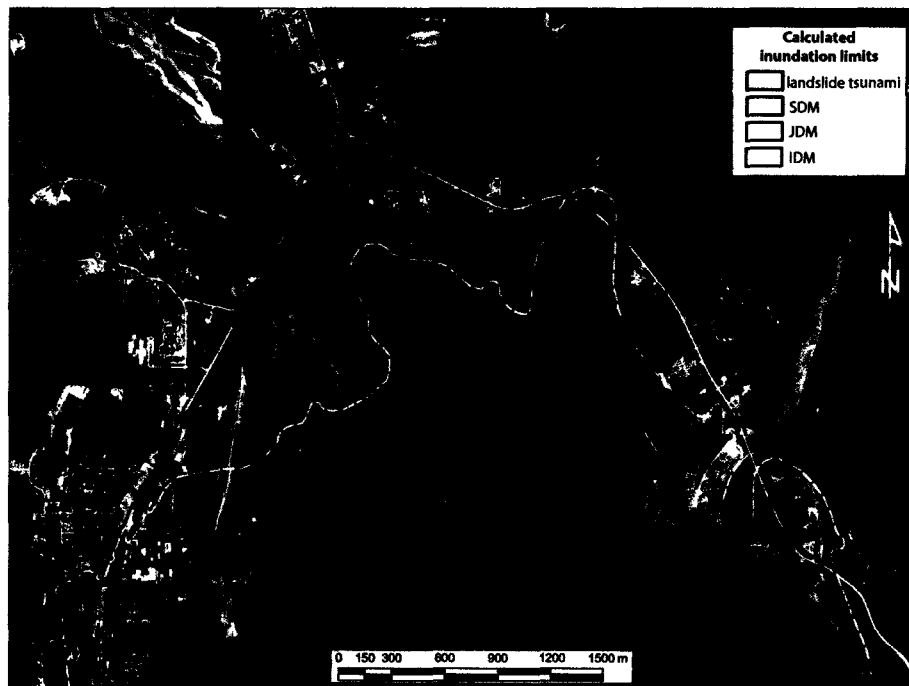


Figure 3.4: Observed 1964 inundation line at the head of Resurrection Bay, shown by the dashed yellow contour (from *Lemke (1967)*), and inundation limits calculated for different tectonic tsunami sources and the landslide source. Orthophoto image courtesy of National Resources Conservation Service, USDA, 1996.

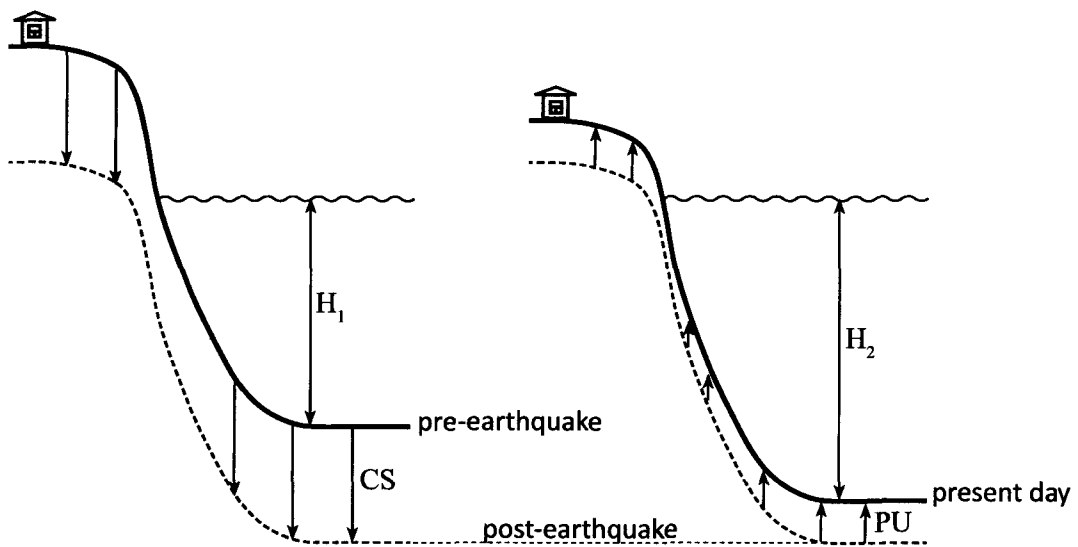


Figure 3.5: A diagram that shows vertical tectonic land changes during and after the 1964 earthquake. H_1 is the bathymetry before the earthquake, H_2 is the present day bathymetry, CS is coseismic subsidence, PU is postseismic uplift. Note that the diagram is not to scale.

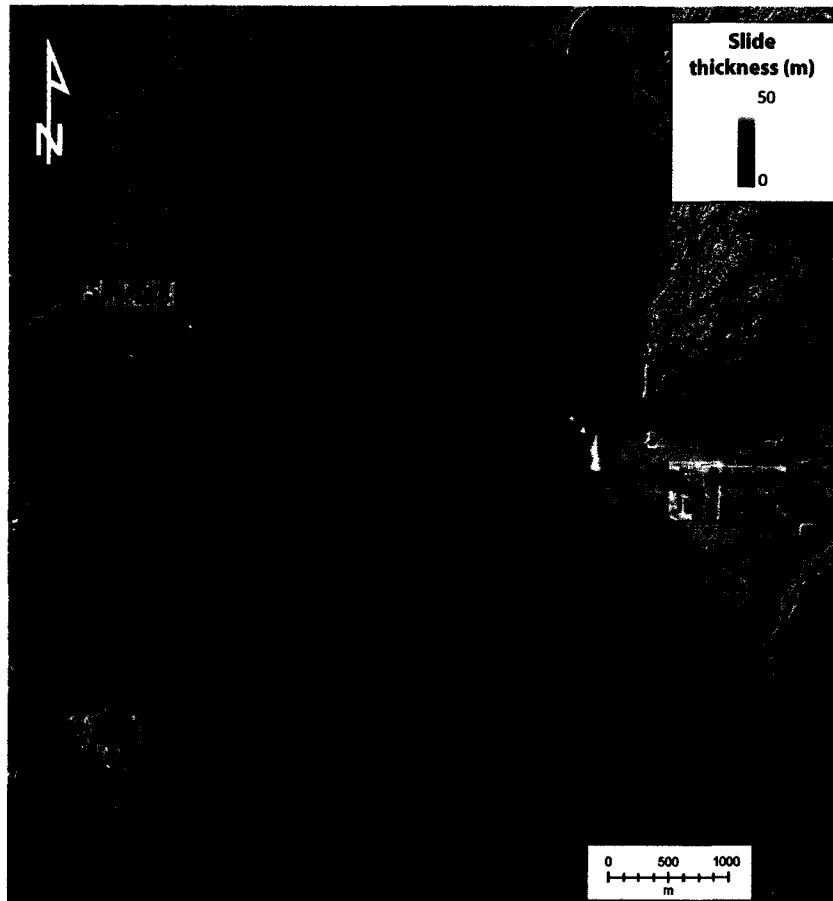


Figure 3.6: Reconstructed thicknesses and initial extent of the three major slide complexes in the upper Resurrection Bay. Orthophoto image courtesy of National Resources Conservation Service, USDA, 1996.

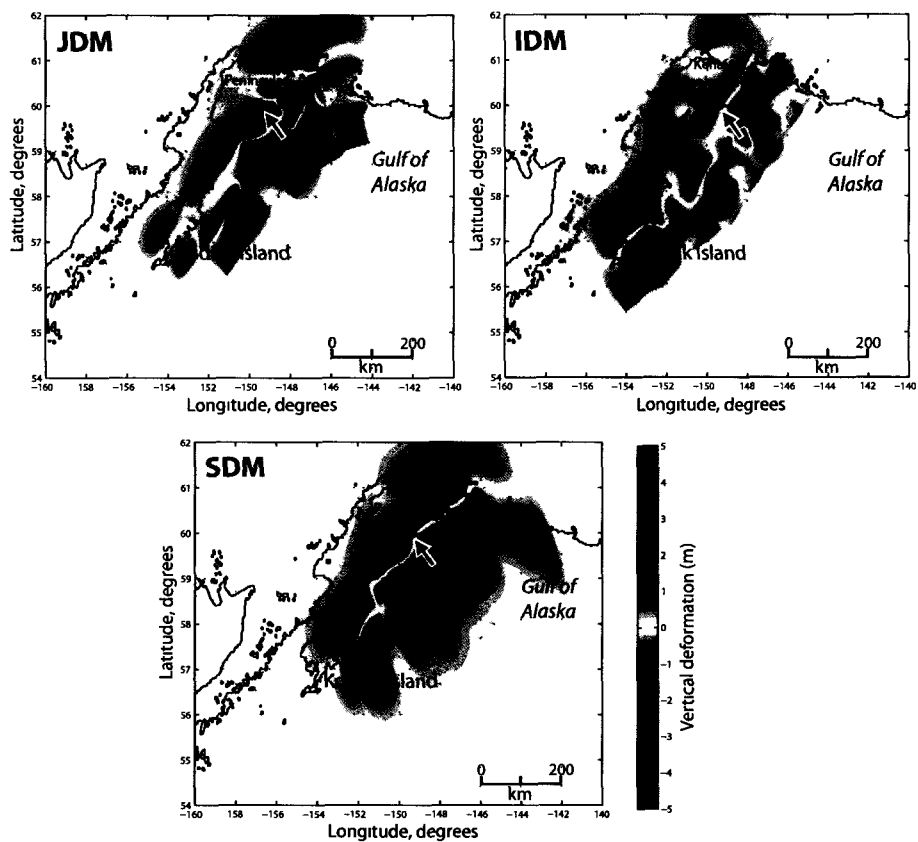


Figure 3.7: Vertical coseismic displacements calculated from the deformation models of *Johnson et al. (1996)* (JDM), *Ichinose et al. (2007)* (IDM), and *Suito and Freymueller (2009)* (SDM). The arrow points at the entrance to Resurrection Bay.



Figure 3.8: Inundation limits calculated for different tectonic tsunami sources and the landslide source at Lowell Point. Orthophoto image courtesy of National Resources Conservation Service, USDA, 1996.



Figure 3.9: Inundation limits calculated for different tectonic tsunami sources and the landslide source at Fourth of July Creek. Orthophoto image courtesy of National Resources Conservation Service, USDA, 1996.

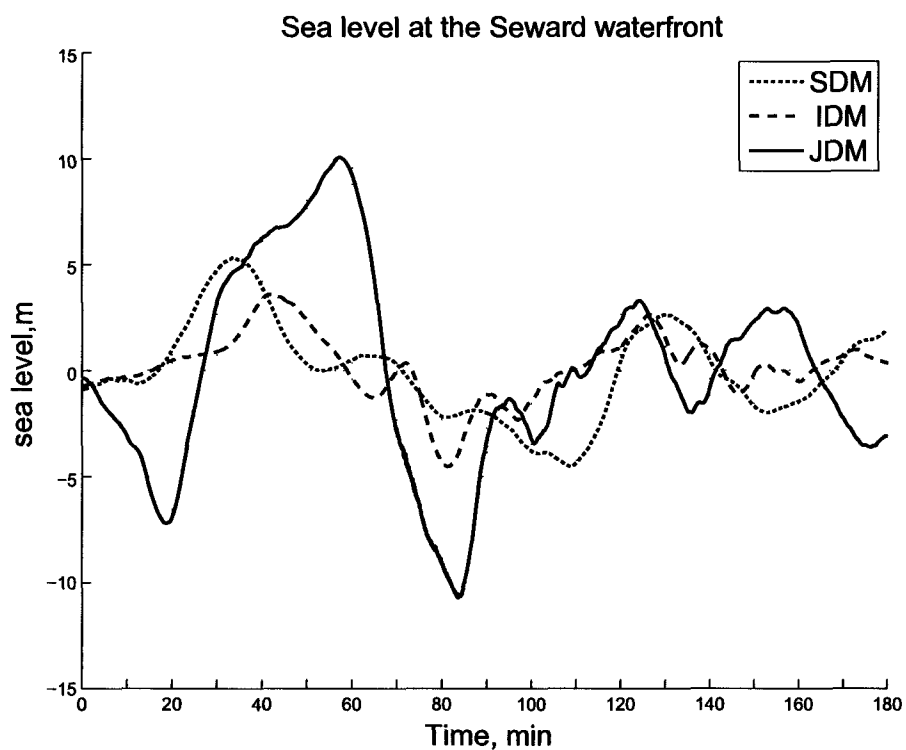


Figure 3.10: Simulated tectonic tsunami waveforms at Seward waterfront for three different source functions. Time $t = 0$ corresponds to the 1964 earthquake's origin time.

Chapter 4

Inundation Modeling of the 1964 tsunami in Kodiak Island, Alaska¹

4.1 Abstract

In this work a numerical modeling method is used to study tsunami waves generated by the Great Alaska Earthquake of 1964 and their impact on Kodiak Island communities. The numerical model is based on the nonlinear shallow water equations of motion and continuity which are solved by a finite-difference method. We compare two different source models of the 1964 tsunami. It is shown that the results of the near-field inundation modeling strongly depend on the slip distribution within the rupture area. These results are used for evaluation of tsunami hazard in the Kodiak Island communities.

4.2 Introduction

Seismic events that occur within the Alaska-Aleutian subduction zone have a high potential for generating both local and Pacific-wide tsunamis. Tectonic tsunami waves originating in Alaska can travel across the ocean and destroy coastal towns hours after they are generated. However, they are considered to be a near-field hazard for Alaska, and can reach Alaskan coastal communities within minutes after the earthquake. Therefore, community preparedness plays a key role in saving lives and property. Evacuation areas and routes have to be planned in advance, which makes it essential to have an estimate for the potential flooding area of coastal zones in the case of a local tsunami. To help mitigate the large risk that earthquakes and tsunamis pose to Alaskan coastal towns, we participate in the National Tsunami Hazard Mitigation Program by evaluating and mapping potential inundation of Alaska coastlines using numerical modeling of tsunami wave dynamics.

The communities for inundation modeling are selected in coordination with the Alaska Division of Emergency Services with consideration to location, infrastructure, availability of bathymetric and topographic data, and willingness for a community to incorporate the results in a comprehensive mitigation plan. Kodiak Island was identified as a high-priority region for Alaska inundation mapping. There are a number of communities with relatively large populations and significant commercial resources. They are in need of tsunami

¹E. Suleimani, R. Hansen and Z. Kowalik, 2003, "Inundation modeling of the 1964 tsunami in Kodiak Island, Alaska", published in *Submarine Landslides and Tsunamis*, edited by A.C. Yalciner, E.N. Pelinovsky, E. Okal and C.E. Synolakis, NATO Science Series, Kluwer Acad. Publ., Dordrecht, p. 191-201.

evacuation maps which show the extent of inundation with respect to human and cultural features, and evacuation routes. The purpose of this case study is to model tsunami waves generated by the 1964 earthquake and to compare the extent of the computed inundation zone with observations. This experiment is set to test the model that will be applied to produce tsunami inundation maps for Alaskan coasts. The maps will summarize information on historical tsunamis in the region and the results of model runs for different source scenarios.

4.3 Numerical Model

The numerical model used in this study is based on the vertically integrated nonlinear shallow water equations of motion and continuity, which also include effects of friction and Coriolis force. Written in a spherical coordinate system, these equations are (*Murty, 1984; Pelinovsky, 1996*):

$$\frac{\partial U}{\partial t} + \frac{U}{R \cos \varphi} \frac{\partial U}{\partial \lambda} + \frac{V}{R} \frac{\partial U}{\partial \varphi} - fV = -\frac{g}{R \cos \varphi} \frac{\partial \xi}{\partial \lambda} - \frac{rUW}{D}, \quad (4.1)$$

$$\frac{\partial V}{\partial t} + \frac{U}{R \cos \varphi} \frac{\partial V}{\partial \lambda} + \frac{V}{R} \frac{\partial V}{\partial \varphi} + fU = -\frac{g}{R} \frac{\partial \xi}{\partial \varphi} - \frac{rVW}{D}, \quad (4.2)$$

$$\frac{\partial \xi}{\partial t} = \frac{\partial \eta}{\partial t} - \frac{1}{R \cos \varphi} \left[\frac{\partial(DU)}{\partial \lambda} + \cos \varphi \frac{\partial(DV)}{\partial \varphi} \right], \quad (4.3)$$

where λ is longitude, φ is latitude, t is time, U and V are horizontal velocity components along longitude and latitude, $W = \sqrt{U^2 + V^2}$, ξ is variation of sea level from equilibrium, η is the bottom displacement, g is the acceleration of gravity, R is radius of the Earth, f is the Coriolis parameter, $D = H + \xi - \eta$ is the total water depth, and r is the bottom friction coefficient.

Various approaches to deriving a numerical solution of the above system of equations were outlined in *Imamura (1996)* and *Titov and Synolakis (1998)*. In this study, we apply a space-staggered grid which requires either sea level or velocity as a boundary condition. The first order scheme is applied in time and the second order scheme is applied in space. Integration is performed along the north-south and west-east directions separately in a way that is described in *Kowalik and Murty (1993)*. To apply this procedure, the system of

equations (4.1)-(4.3) is split in time into two subsets. First, these equations are solved along the longitudinal direction,

$$\begin{aligned} \frac{U^{m+1} - U^m}{T} + \left(\frac{U}{R \cos \varphi} \frac{\partial U}{\partial \lambda} \right)^m + \left(\frac{V}{R} \frac{\partial U}{\partial \varphi} \right)^m - (fV)^m = \\ = -\frac{g}{R \cos \varphi} \left(\frac{\partial \xi}{\partial \lambda} \right)^m - \left(\frac{rUW}{D} \right)^m, \end{aligned} \quad (4.4)$$

$$\frac{1}{2} \frac{D^* - D^m}{0.5T} = -\frac{1}{R \cos \varphi} \frac{\partial (D^m U^{m+1})}{\partial \lambda}, \quad (4.5)$$

and next along the latitudinal direction,

$$\begin{aligned} \frac{V^{m+1} - V^m}{T} + \left(\frac{U}{R \cos \varphi} \frac{\partial V}{\partial \lambda} \right)^m + \left(\frac{V}{R} \frac{\partial V}{\partial \varphi} \right)^m + (fU)^{m+1} = \\ = -\frac{g}{R} \left(\frac{\partial \xi}{\partial \varphi} \right)^m - \left(\frac{rVW}{D} \right)^m, \end{aligned} \quad (4.6)$$

$$\frac{1}{2} \frac{D^{m+1} - D^*}{0.5T} = -\frac{1}{R} \frac{\partial (D^m V^{m+1})}{\partial \varphi}. \quad (4.7)$$

The calculation of sea level starts from time step m , and the intermediate value of the total water depth D^* is obtained after integration along the first direction. Afterwards, this value is carried over to the other direction to derive the total water depth and the sea level at the $(m+1)$ time step.

In order to propagate the wave from a source to various coastal locations, we use embedded grids, placing a coarse grid in a deep water region and coupling it with finer grids in shallow water areas. We use an interactive grid splicing, therefore the equations are solved on all grids at each time step, and the values along the grid boundaries are interpolated at the end of every time step. The radiation condition is applied at the open ocean boundaries (*Reid and Bodine, 1968*). At the water-land boundary, the moving boundary condition is used in those grids that cover areas selected for runup calculations (*Kowalik and Murty, 1993*). At all other land boundaries, the velocity component normal to the coastline is assumed to be zero.

4.4 The Source Model for the 1964 Tsunami

We have started this project with the modeling of the 1964 Alaska tsunami, because this event is probably the worst case tsunami scenario of a tsunami for the Kodiak Island communities. The 1964 Prince William Sound earthquake generated one of the most destructive

tsunamis observed in Alaska and the west coast of the US and Canada. The major tectonic tsunami was generated in the trench area and affected all the communities in Kodiak and the nearby islands. There were also about 20 local submarine and subaerial landslide-generated tsunamis in Alaska that account for 75% of all tsunami fatalities in the region. In Kodiak, the tsunami caused 6 fatalities and about \$30 million in damage. This tsunami was studied in depth by a number of authors (*Kachadoorian and Plafker, 1967; Wilson and Tørum, 1968; Plafker, 1969; Plafker et al., 1969*). The observed inundation patterns for several locations on Kodiak Island are available for calibration of the model.

Tsunami propagation models use output of the submarine seismic source models as an initial condition for the ocean surface displacement, which then propagates away from the source. The amplitude of this initial disturbance is one of the major factors that affect the resulting runup amplitudes along a coastline. One of the source models used in the tsunami generation problem is a double-couple model of an earthquake source. *Okada (1985)* developed an algorithm to calculate the distribution of coseismic uplift and subsidence resulting from the motion of the buried fault. The fault parameters that are required to compute the deformation of the ocean bottom are location of the epicenter, area of the fault, dip, rake, strike and amount of slip on the fault. It was demonstrated by *Christensen and Beck (1994)* that there were two areas of high moment release, representing the two major asperities of the 1964 rupture zone: the Prince William Sound asperity and the Kodiak Island asperity. The segmentation of the source area suggests that the single-fault model with uniform slip is not adequate to describe the slip distribution of this earthquake. A detailed analysis of the 1964 rupture zone was presented by *Johnson et al. (1996)* through joint inversion of the tsunami waveforms and geodetic data. Authors derived a detailed slip distribution for the 1964 earthquake, which is shown in Figure 4.1.

To construct a source function for the 1964 event, we used their fault model that has 8 subfaults representing the Kodiak asperity of the 1964 rupture zone, 9 subfaults in the Prince William Sound asperity, and one subfault representing the Patton Bay fault on Montague Island. Since the contribution of this fault to the far-field tsunami waveforms was negligible, *Johnson et al. (1996)* removed the effect of this fault by subtracting the deformation due to it from all geodetic observations. We used the equations of *Okada (1985)* to calculate the distribution of coseismic uplift and subsidence resulting from the given slip

distribution (Figure 4.2). Then, the derived surface deformation pattern was used as the initial condition for tsunami propagation.

4.5 Modeling of the 1964 Tsunami in Kodiak

First, we modeled the 1964 tsunami waves using the described above rupture model consisting of 18 subfaults, each having its own parameters. To verify the accuracy of the far-field calculations, we compared numerical results with the observations at the Sitka and Yakutat tide gauges. Tsunami amplitudes were computed at the grid points closest to the tide gauges. Figure 4.3 shows the observed and calculated tsunami wave histories at the two locations. The plots indicate that the time of arrival of the first wave and its amplitude are in good agreement with the observations. Our goal was also to estimate the importance of the detailed slip distribution of the rupture zone for the near-field inundation modeling. To accomplish that, we compared two source models of the 1964 event: a single-fault model with uniform slip distribution, and the model consisting of 18 subfaults. The amount of slip on the single fault was calculated in a way that preserves the seismic moment. The resulting surface deformation was computed using the Okada algorithm (*Okada, 1985*) and used in the tsunami model as the initial condition.

Figure 4.1 shows the area of this study, which is covered by the largest grid of 2 arc-minute resolution. We use four embedded grids in order to increase resolution from 2 arc-minutes (2 km x 3.7 km at 59°N) in the Gulf of Alaska to 21.8 m x 27.5 m in the two grids that cover the communities of Kodiak City and the Kodiak Naval Station, where runup modeling is performed. The embedded grids are shown in Figure 4.4. The largest one of 24 arc-second resolution covers the lower part of Cook Inlet and waters around Kodiak Island. The north-eastern part of the island is covered by the 8 arc-second grid, and the Chiniak Bay is covered by the 3 arc-second grid. There are two more high-resolution grids covering the areas inside the Chiniak Bay where runup calculations are performed. They are shown as two rectangles in the inset map. In these grids, the combined bathymetric and topographic data allow for application of the moving boundary condition and calculation of the runup heights and extent of the inundation. We assume that the displacement of the ocean surface from the equilibrium position is equal to the vertical component of the ocean floor deformation due to the earthquake rupture process. This ocean surface displacement

is the initial condition for the computation of tsunami wave field in the region.

For the communities of Kodiak City and the Kodiak Naval Station (Figure 4.4), the observed inundation was documented in July of 1964 by *Kachadoorian and Plafker* (1967). Kodiak City, the largest community on the island, suffered the greatest damage from the tsunami waves. Figures 4.5 and 4.6 show computed and observed inundation lines for the Kodiak City and the U.S. Coast Guard Base (formerly the Kodiak Naval Station), respectively. The blue line delineates the area inundated in 1964 according to the data collected after the event by the U. S. Army Corps of Engineers and the personnel of the Kodiak Naval Station. The solid red line shows the inundated area computed using the complex source function of 18 subfaults, and the dashed red line corresponds to the inundation zone calculated from the simple one-fault source model. The observed area of maximum inundation at the Kodiak Naval Station is taken from *Kachadoorian and Plafker* (1967). The results show that the complex source model with detailed slip distribution describes the inundation zone much better than the simple one-fault model. The one-fault model greatly underestimates the extent of flooding caused by the 1964 tsunami waves.

The simulated tsunami wave history at the Kodiak Naval Station is shown in Figure 4.7. The zero time corresponds to the earthquake origin time. The arrows indicate observed arrivals of the first three waves at the Naval Station (*Wilson and Tørum*, 1968). There is an agreement with the observations only for the first wave, but its amplitude is underestimated. The calculated arrival times for the second and the third waves do not match the observations. Using animation of the tsunami wave field, we found that the first wave arrives from the fault in the Kodiak asperity with the amount of slip of 14.5 meters. The second and the third arrivals result from the interaction of the waves coming from the faults in the Prince William Sound asperity (22.1 meters and 18.5 meters of slip), and the waves already refracted from the Kodiak shores. We have assumed that the discrepancy in computed arrival times is related to the uncertainty in the source function. Numerical experiments have shown that modifying the amount of slip on individual subfaults can cause significant changes in both arrival times and maximum wave amplitudes at particular locations. These experiments demonstrate that the near-field inundation modeling results are very sensitive to the fine structure of the tsunami source, and that the slip distribution is one of the important components of the input data required for tsunami runup calculations.

4.6 Discussion

Locally-generated tsunami waves pose a significant hazard for coastal Alaska, and better understanding of the tsunami source mechanism is crucial for hazard mitigation. Numerical analysis has shown that the detailed knowledge of the coseismic ocean bottom uplift and subsidence is very important for the near-field inundation modeling. When the tsunami is generated in the vicinity of the coast, the direction of the incoming waves, their amplitudes and times of arrival are determined largely by the initial displacements of the ocean surface in the source area, because the distance to the shore is too small for the waves to disperse. Comparison between the two source models for the 1964 tsunami indicates that using the source model of 18 subfaults with detailed slip distribution within the rupture area produces the inundation line closest to that observed in 1964. The results show the need for detailed studies of the source mechanism of tsunamigenic earthquakes in application to the near-field inundation modeling. Computed time series at the distant stations in Sitka and Yakutat show good agreement with observations. Computations in the region located close to the tsunami source (Kodiak Island) show that the calculated runup agrees well with the documented inundation area, but the timing of observed and calculated arrivals of the maximum tsunami wave is out of phase. This discrepancy could be related to the method of the tsunami waveforms inversion used in the construction of the source model (*Johnson et al.*, 1996). The tsunami waveforms that were used in the joint inversion had an average duration of 100 min, and almost all of them were recorded at distant locations. In this study we try to match the computed and observed arrival times for the second and the third waves (120 min and 180 min) at the Kodiak Naval Station. This area is much closer to the source than any of the tide gauges that provided the records for the joint inversion algorithm. Also, observations were taken in small bays on Kodiak Island that introduce local effects into the tsunami wave field. We would like to approach this problem through investigation of the natural mode of oscillations in semi-enclosed water bodies and by modifying parameters of the source function. Our preliminary experiments show that a water body whose own periods of oscillations are close to an incident tsunami wave period responds by generating higher runup and larger reflected waves, and also that the resonance response of a small bay depends on the time span of the incident tsunami wave train. Longer tsunami wave trains cause a stronger resonance response to occur. This can be used to demonstrate that

large runup heights in bays can be caused not only by the first wave, but by later waves as well due to local resonant effects.

4.7 Acknowledgments

The authors wish to thank Dr. Fumihiko Imamura for the Fortran code of the Okada algorithm he kindly provided. This study was supported in part by the National Tsunami Hazard Mitigation Program through NOAA grant NA67RJ0147, by the Alaska Department of Military and Veteran Affairs (grant RSA-0991007) and by the Alaska Science and Technology Foundation (grant ASTF-971002).

Bibliography

- Christensen, D., and S. Beck (1994), The rupture process and tectonic implications of the Great 1964 Prince William Sound earthquake, *Pure Appl. Geophys.*, 142(1), 29–53.
- Imamura, F. (1996), Review of tsunami simulation with a finite difference method, in *Long-Wave Runup Models*, edited by H. Yeh, P. Liu, and C. Synolakis, pp. 25–42, World Scientific.
- Johnson, J., K. Satake, S. R. Holdahl, and J. Sauber (1996), The 1964 prince william sound earthquake: Joint inversion of tsunami and geodetic data, *J. Geophys. Res.*, 101, 523–532.
- Kachadoorian, R., and G. Plafker (1967), Effects of the earthquake of March 27, 1964 on the communities of Kodiak and nearby islands, U.S. Geological Survey Professional Paper 542-F, 41 pp.
- Kowalik, Z., and T. Murty (1993), *Numerical Modeling of Ocean Dynamics*, Advanced Series on Ocean Engineering, Volume 5, World Scientific.
- Murty, T. (1984), Storm Surges - Meteorological Ocean Tides, Bull. 212, Fisheries Res. Board, Ottawa, Canada, 897 pp.
- Okada, Y. (1985), Surface deformation due to shear and tensile faults in a half-space, *Bull. Seism. Soc. Am.*, 75, 1135–1154.
- Pelinovsky, E. (1996), *Tsunami Waves Hydrodynamics*, Institute of Applied Physics, RAS, Nizhny Novgorod, Russia.
- Plafker, G. (1969), Tectonics of the March 27, 1964 Alaska Earthquake, U.S. Geological Survey Professional Paper 543-I, 74 pp.
- Plafker, G., R. Kachadoorian, E. Eckel, and L. Mayo (1969), Effects of the Earthquake of March 27, 1964 on various communities, U.S. Geological Survey Professional Paper 542-G, 50 pp.
- Reid, R., and B. Bodine (1968), Numerical model for storm surges in Galveston Bay, *J. Waterway Harbor Div.*, 94(WWI), 33–57.

Titov, V., and C. Synolakis (1998), Numerical modeling of tidal wave runup, *J. Waterw. Port Coast. Ocean Eng.*, 124, 157–171.

Wilson, B., and A. Tørum (1968), The tsunami of the Alaskan Earthquake, 1964: Engineering evaluation, U.S. Army Corps of Engineers, Technical memorandum No. 25, 401 p.

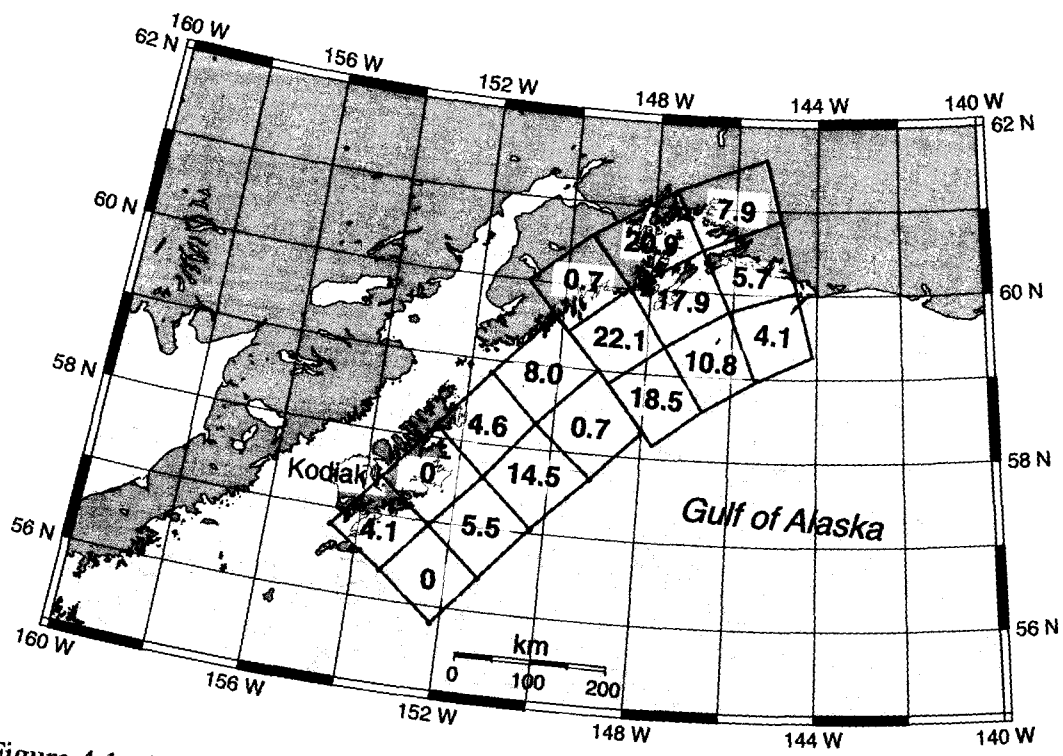


Figure 4.1: Area map and slip distribution of the 1964 rupture from *Johnson et al.* (1996). Numbers represent slip in meters on every subfault.

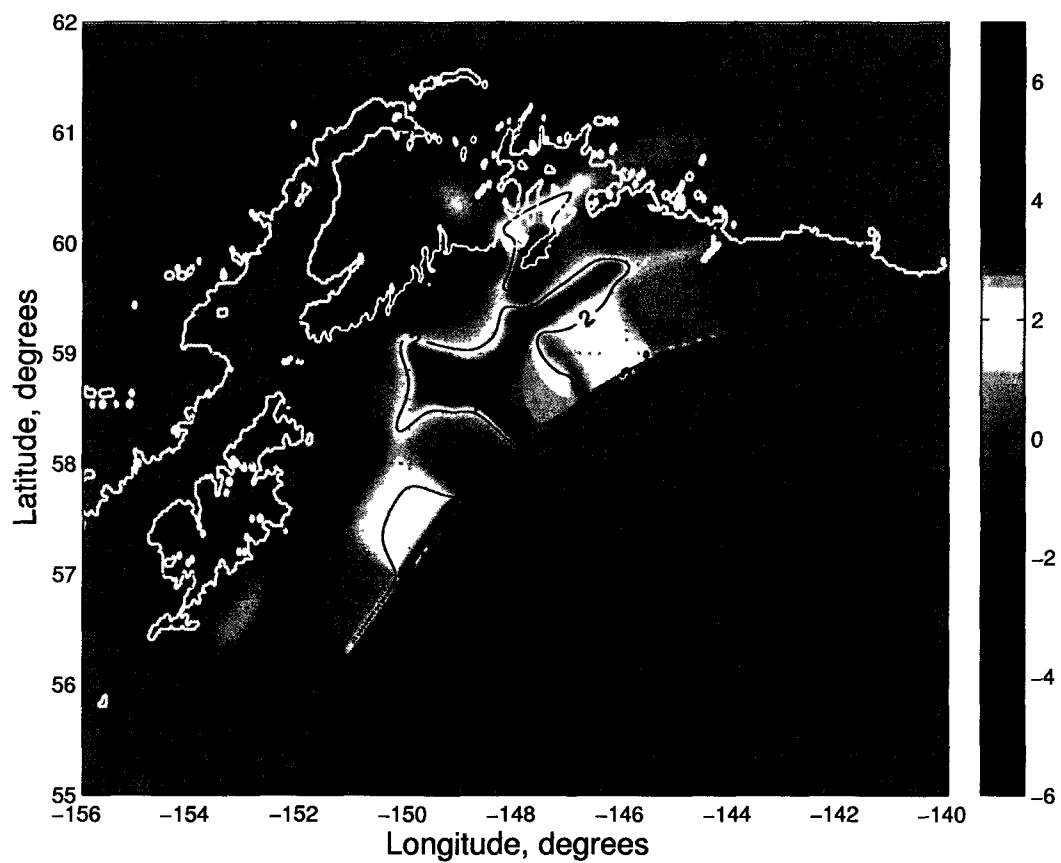


Figure 4.2: Coseismic vertical deformation of the 1964 earthquake (in meters), calculated from the slip distribution presented in Figure 4.1.

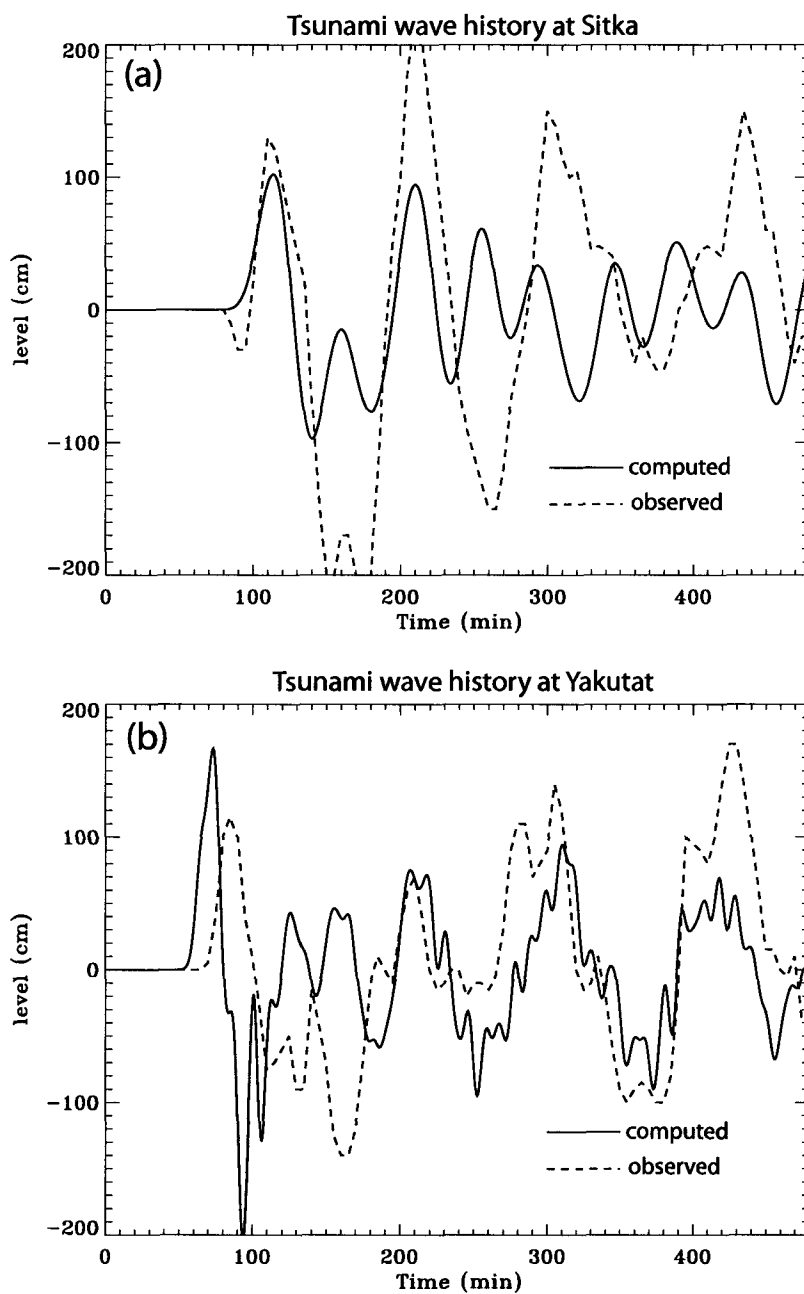


Figure 4.3: Computed and observed tsunami amplitudes at Sitka (a) and Yakutat (b) tide gauges.

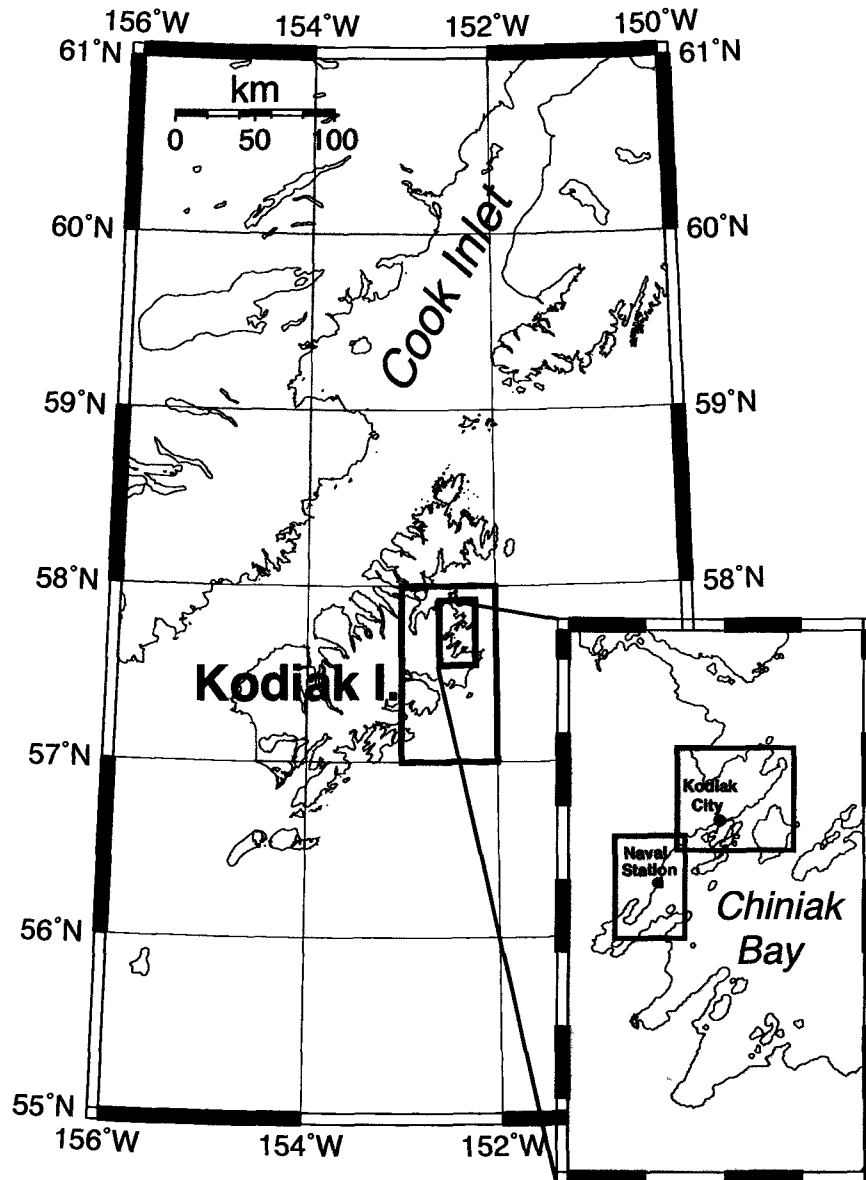


Figure 4.4: The Kodiak Island grid of 24 arc-second resolution. The two rectangles delineate the 8 arc-second and the 3 arc-second grids. The inset map shows the 3 arc-second grid that includes higher resolution grids for the communities of Kodiak City and the Kodiak Naval Station.

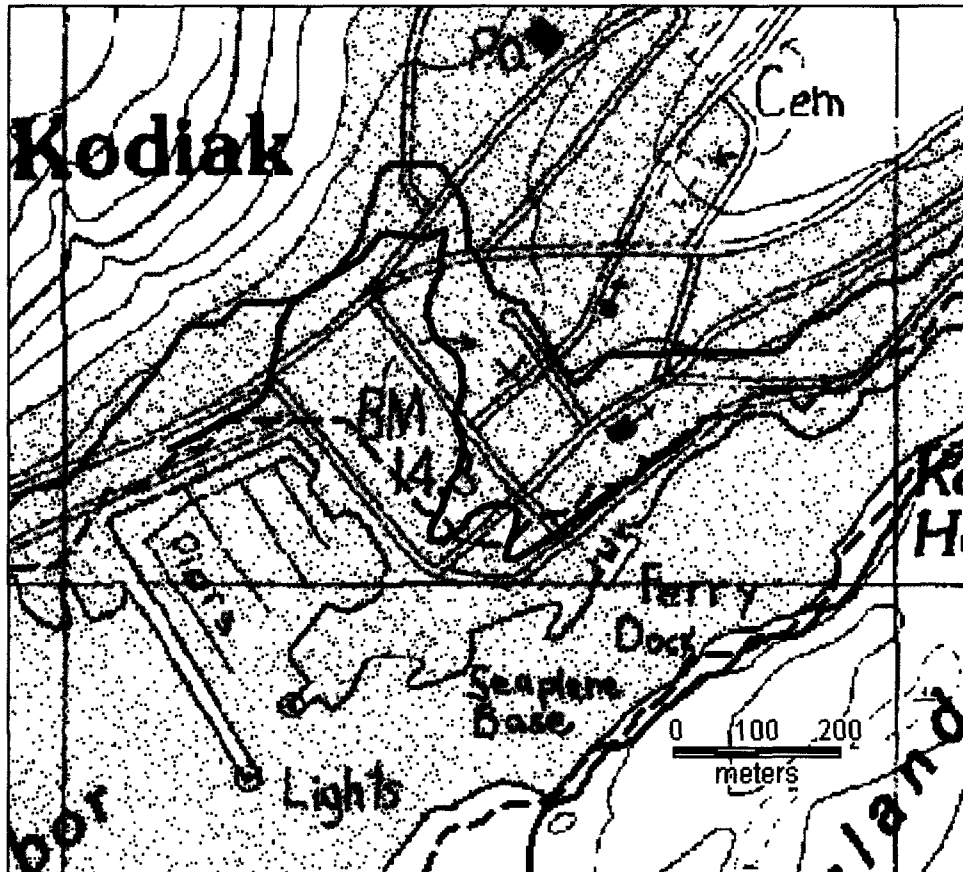


Figure 4.5: Observed (blue) and computed (red) inundation lines for the Kodiak downtown area. Solid red line delineates inundation calculated using the 18-fault model; the dashed red contour outlines the inundation area that was calculated using the single fault model.

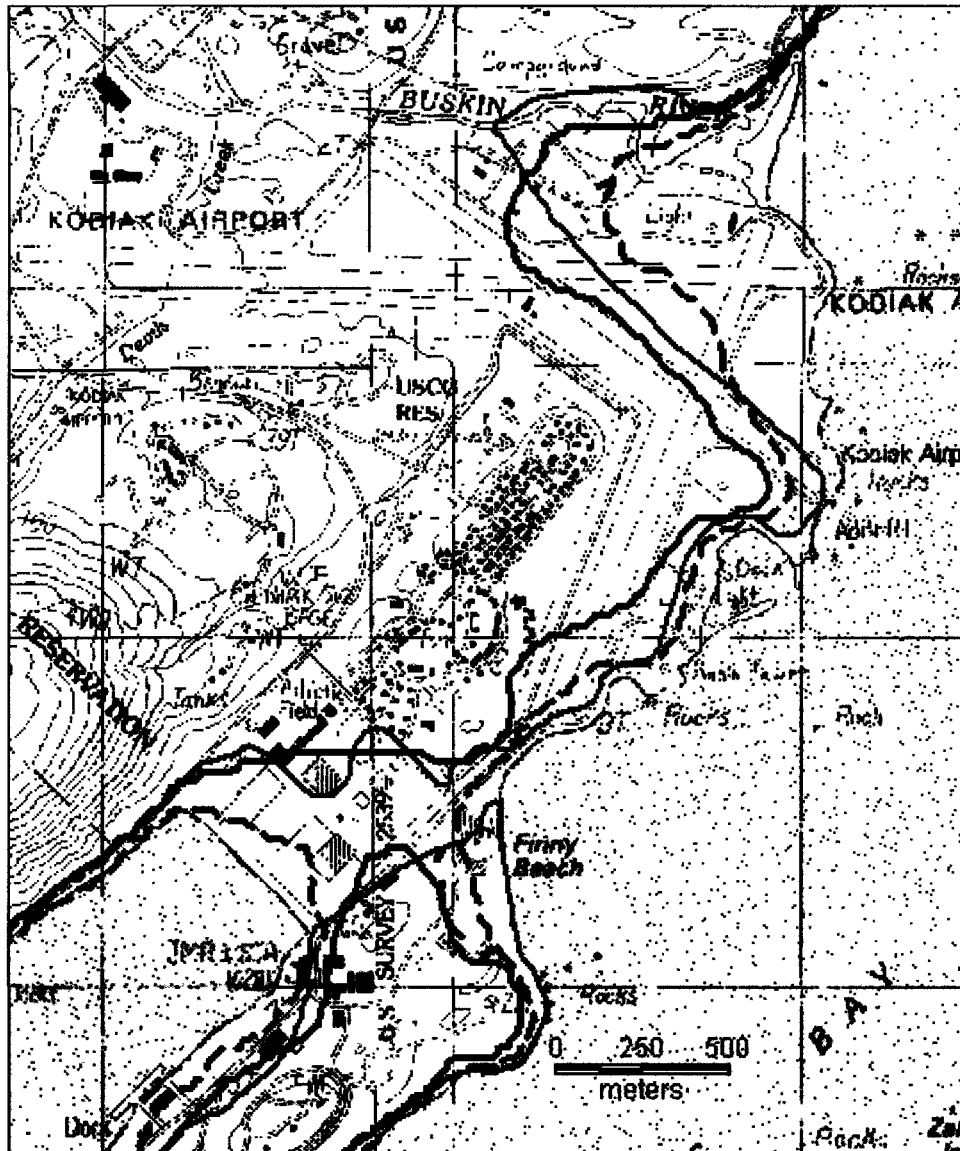


Figure 4.6: Observed (blue) and computed (red) inundation lines for the US Coast Guard Base, formerly the Kodiak Naval Station. Solid red line delineates inundation calculated using the 18-fault model; the dashed red contour outlines the inundation area that was calculated using the single fault model.

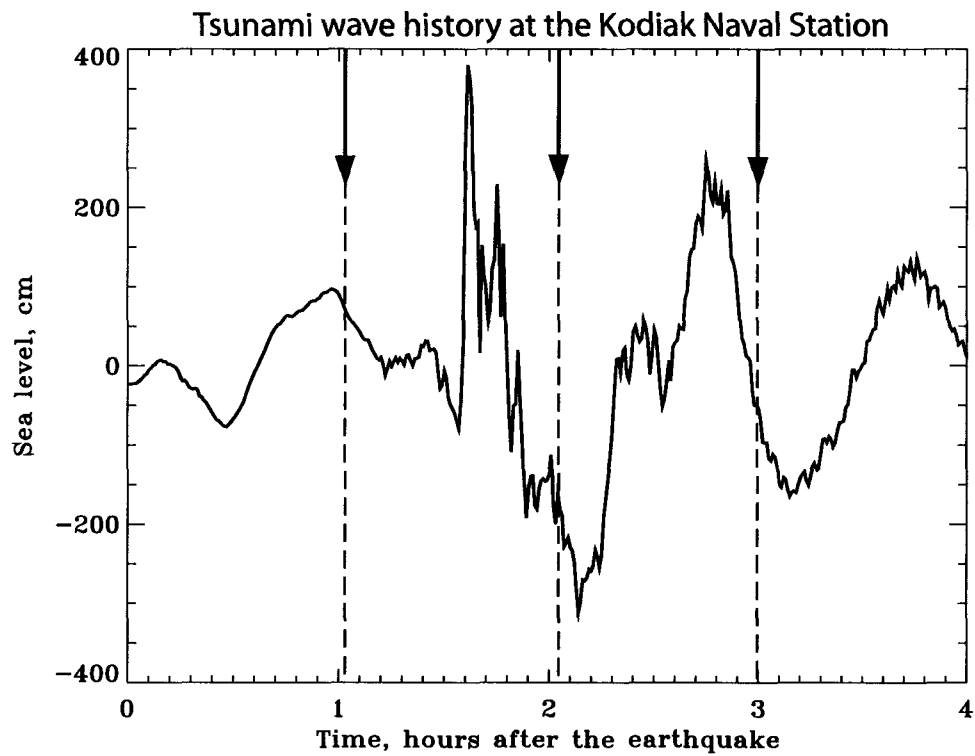


Figure 4.7: Computed wave history at the Kodiak Naval Station. The arrows indicate the observed arrivals of the first three waves.

Chapter 5

Near-field modeling of the 1964 Alaska tsunami: a source function study¹

5.1 Abstract

Near-field observations of tsunami waves generated by the M_w 9.2 1964 Alaska earthquake reveal a complex relationship between the tsunami wave field in the source area and regional coseismic slip in south-central Alaska. The documented times and amplitudes of first arrivals, measured runup heights and inundation areas along the coasts of the Kenai Peninsula and Kodiak Island suggest that secondary splay faults played an important role in generating destructive tsunami waves. We conduct a tsunami numerical modeling study to test a hypothesis that a significant amount of slip needs to be placed on intraplate splay faults, and to evaluate the extent of these faults in order to explain the coseismic displacements and near-field tsunami observations. The newly revised coseismic deformation model of the 1964 earthquake extends the Patton Bay fault offshore beyond its mapped dimensions on land to about 150°W , which approximately corresponds to the boundary of plate coupling along the Kenai Peninsula coast derived from previous GPS and postseismic deformation studies. The results of tsunami numerical modeling in the Kodiak Island region demonstrate that the new coseismic deformation model provides a good estimate of slip on the megathrust in the Kodiak asperity, and confirm that it was an important feature of the 1964 tsunami generation mechanism. We investigate the possible contribution of coseismic horizontal displacements into the initial tsunami wave field by calculating the component of the ocean surface uplift due to horizontal motion of the steep ocean bottom slopes. The tsunami simulations reveal that including deformation due to horizontal displacements in the source function results in an increase of far-field tsunami amplitudes at all distant locations, while this modification of the tsunami source produces only a very localized effects in the near field. Our approach for discretization of the fault geometry and redistribution of slip can augment future research of the 1964 tsunami source as well as inversion studies that use tsunami observations and measurements in the near field, where the modeling results are highly susceptible to the complexity of the tsunami source.

¹E. Suleimani and J. Freymueller, "Near-field modeling of the 1964 Alaska tsunami: a source function study", prepared for submission to Journal of Geophysical Research.

5.2 Introduction

The Great Alaska Earthquake of March 27, 1964 generated the most destructive tsunami ever observed in North America. Of the 131 fatalities associated with this earthquake, 122 were caused by tsunami waves (*Lander, 1996*). Although tragic, the number of deaths was fortunately far smaller than that in the 2004 Indian Ocean tsunami due to low population density on the Alaska coast and an operational tsunami warning system. The major tectonic tsunami, which was generated by displacement of the ocean floor between the trench and the coastline, caused fatalities and great damage in Alaska, Hawaii, and the west coast of the United States and Canada. The earthquake ruptured an 800-km long section of the Aleutian megathrust, producing vertical displacements over an area of about 285,000 km² in south-central Alaska (*Plafker, 1969*). The area of coseismic subsidence included Kodiak Island, Kenai Peninsula, Cook Inlet and part of the northern Prince William Sound (Figure 5.1). The major zone of uplift was seaward of the subsidence zone, in Prince William Sound and in the Gulf of Alaska (*Plafker, 1969*). In addition to the tectonic tsunami waves, more than twenty local tsunamis were generated by submarine and subaerial landslides in coastal Alaska.

The rupture area of the 1964 earthquake is at the eastern end of the Aleutian Megathrust (Figure 5.1). This subduction zone has a history of producing large and great earthquakes and generating both local and Pacific-wide tsunamis. The coseismic crustal movements that characterize this area have a high potential for producing tsunamigenic seafloor displacements. All of the most recent great earthquakes of 1938, 1946, 1957, 1964 and 1965 ruptured different segments of the megathrust and generated tsunami waves that resulted in widespread damage and loss of life along the Alaska Pacific coast and other exposed locations around the Pacific Ocean (*Lander, 1996*).

Nishenko and Jacob (1990) compiled a record of past large and great earthquakes along the Pacific/North American plate boundary, using historical and instrumental observations and paleoseismic investigations. They summarized the earthquake history by plotting the most recent rupture zones and the current seismic gap locations in the space-time diagram. In order to describe the recurrence behavior of different parts of the plate boundary that are characterized by distinctive tectonic regimes, *Nishenko and Jacob (1990)* defined segments of the Aleutian megathrust as subduction zone sections that are repeatedly ruptured

by large and great earthquakes, or as gaps between rupture segments. The adjacent segments are allowed to break together in a single event, much larger than an event that each of the segments can produce separately. According to their model, south-central Alaska includes three segments of the megathrust: the Yakataga-Yakutat (YY), Prince William Sound (PWS), and Kodiak Island (KI) segments (Figure 5.1). Although both PWS and KI segments ruptured during the 1964 earthquake, they have different earthquake histories. As summarized by *Nishenko and Jacob* (1990), the KI segment has produced large and great earthquakes independently of the PWS segment, with the recurrence interval for the Kodiak asperity estimated as low as 60 years, while that for the PWS asperity appears to be several centuries. The YY segment at the eastern end of the megathrust represents a complex collision zone where the Yakutat microplate moves northwest toward central Alaska at 48 mm/yr (*Carver and Plafker*, 2008). This segment translates the predominantly strike-slip motion to the east from it to shallow-dipping subduction to the west (*Nishenko and Jacob*, 1990). The interaction between the Yakutat block and the Pacific and North America plates is complex and not well characterized. Part of the YY segment probably ruptured in the 1964 earthquake, and other parts ruptured during the two great (M_w 8.1 and 8.2) Yakutat Bay earthquakes of September 1899 (Figure 5.1). *Plafker and Thatcher* (2008) recently reevaluated the mechanisms of these earthquakes and concluded that the 1899 earthquake sequence most likely did not fill the offshore part of the Yakataga seismic gap that lies between the 1964 rupture area and the epicentral area of the 1899 earthquakes. *Plafker and Thatcher* (2008) suggested that the YY segment has a high potential for a future tsunami-genic earthquake.

The recent work by *Shennan et al.* (2009) tests the hypothesis that in some seismic cycles megathrust segments can combine, as proposed in the segmentation model by *Nishenko and Jacob* (1990), and produce earthquakes larger than historical earthquakes. The authors present paleoseismic evidence that earthquakes 900 and 1500 years BP ruptured two adjacent segments of the Aleutian megathrust (the PWS and KI segments) in addition to an eastward extension of the PWS segment that involved the margin of the Yakutat microplate. The authors suggested that an increase in seismic moment is less significant than an increase in tsunami potential of this multi-segment rupture, due to coseismic uplift over large area of shallow continental shelf off Yakataga coast. *Carver and Plafker* (2008) recognized

nine paleosubduction earthquakes in the past ~ 5000 years from paleoseismic evidence of sudden land changes and tsunami deposits in the eastern part of the Aleutian megathrust, which is the only section of the subduction zone where information on great historic earthquakes is available. The 1964 earthquake is the most recent of these events, and probably not the largest one. Since it is well documented, the study of its source parameters provides insights into the tsunami potential of south-central Alaska.

Field surveys that are usually conducted after major tsunamis have become systematic in the past two decades, and provided scientists with detailed data sets of runup heights along affected coasts (*Okal and Synolakis, 2004*). In his study of the relationship between local tsunamis and earthquake source parameters, *Geist (1999)* noted that many tsunami events produced unexpectedly large inundation, given the magnitude of the earthquake, and suggested that a complex relationship exist between local runup heights and the source mechanism of tsunami waves. The most dramatic example of the complexity of the source function was the 2004 Sumatra tsunami. Flow depths and runup heights in the near-field were significantly larger than those documented for any of the tectonically generated tsunamis of the same or greater magnitude. *Plafker et al. (2006)* suggested that alternate sources, such as secondary intraplate faults, may have contributed to the tsunami generation, in addition to the slip on the Sumatra megathrust. Similarly, data from the Alaska Earthquake of 1964 show that a substantial amount of the total fault slip can be divided between the megathrust and intraplate splay faults (*Plafker, 2006, 1969*). This implies that the initial tsunami wave can be higher and closer to the shore than the wave simulated based on the assumption that all the slip occurred on the megathrust. All populated coasts around the Gulf of Alaska were in the near-field zone of the 1964 tsunami, and the secondary intraplate faults may have had very significant effects on local tsunami runup heights and arrival times. Other tsunami generation mechanisms can also be responsible for discrepancies between observed tsunami amplitudes and modeling results. Based on the analysis of the seismically-inverted sea floor deformation of the 2004 Sumatra-Andaman earthquake, *Song et al. (2008)* concluded that a significant portion of the total tsunami energy was due to the horizontal displacements of the seafloor. Since the geometry of the 1964 rupture was similar to that of the Sumatra earthquake, and the large coseismic horizontal displacements were observed, it is reasonable to assume that they had sizable contribution to tsunami

generation during the Great Alaska earthquake.

One of the motivations for this study is the value of the 1964 tsunami observations and measurements for the Alaska Tsunami Mapping project. The Alaska Earthquake Information Center conducts tsunami inundation mapping for coastal communities in Alaska, providing guidance to local emergency officials in tsunami hazard assessment (*Suleimani et al.*, 2002, 2005, 2010). For many locations in the Gulf of Alaska, the 1964 tsunami generated by the $M_W 9.2$ Great Alaska earthquake could be the credible worst-case tsunami scenario, since it was well documented and extensively studied. While we use the fully tested and validated numerical model of tsunami propagation and runup (Section 5.3.2), the main challenge in modeling the 1964 tsunami, as any real-world tsunami event, remains in overcoming uncertainties of the initial conditions (*Synolakis et al.*, 2008), which is the definition of the source function of the tectonic tsunami. The earlier modeling study of the 1964 tsunami in Kodiak Island has demonstrated that the near-field runup modeling requires a good knowledge of the slip distribution in the rupture area (*Suleimani et al.*, 2003). It is a challenging task to build a tsunami source function that would fit all observations of the 1964 earthquake and tsunami, which include seismic and geodetic data, far- and near-field tsunami amplitudes, arrival times and values of runup along the coast. The reasons for that are different levels of uncertainties in each data set, and the lack of constraints on some important model parameters, such as slip at shallow depths on the megathrust. Our goal is to improve the definition of the 1964 tsunami source and to create an algorithm through which the slip distribution and other model parameters can be easily modified for future studies. This will contribute to better understanding of the tsunami threat to Alaska coast and to more efficient tsunami hazard mitigation.

This paper presents the first near-field numerical modeling study of the 1964 tsunami source mechanism. We determine the important features of the coseismic slip model and the essential components of the numerical model that affect the near-field inundation modeling of tsunami waves. The next section describes the numerical tools and data that we use to simulate and analyze the effects of tsunami waves along the coasts of the Kenai Peninsula and Kodiak Island. Section 5.4 outlines existing studies of the spatial and temporal coseismic slip distribution of the 1964 rupture area, and describes our results of the 1964 tsunami simulation using two previously published coseismic slip models. Section 5.5 de-

scribes the process of building a new source function of the 1964 tsunami that is based on the fault geometry and the initial coseismic slip distribution derived by *Suito and Freymueller (2009)*. We present the Okada-type discretization of the fault surface, and discuss how different features of the slip model affect the tsunami modeling results in the near field. We complete the analysis by presenting the new source function of the 1964 tsunami that includes the effects of the splay fault displacements and the component of the vertical deformation of the sea surface due to horizontal displacements on the megathrust (Section 5.6). We demonstrate that our approach for discretization of the fault geometry and redistribution of slip can augment future research of the 1964 tsunami source as well as inversion studies that use tsunami observations and measurements in the near field, where the modeling results are highly susceptible to the complexity of the tsunami source.

5.3 Methodology

In this section we describe numerical tools and data that we use to study the 1964 tsunami in the near field. The unique numerical setup of this problem is defined by the location of the tsunami source with respect to the coastal areas where we investigate effects of tsunami waves. Numerical modeling and analysis of tsunami observation data are applied to regions that are located inside the rupture area of the 1964 earthquake, such as Kodiak Island and the Kenai Peninsula (Figure 5.1). This makes the tsunami modeling results extremely sensitive to the fine structure of the tsunami source, as well as the quality and resolution of the bathymetry and topography data in the near-field region. This study is not aimed at the inversion of tsunami and geodetic data for the reasons given in *Suito and Freymueller (2009)*: the coseismic displacement data suffer from systematic errors, inconsistencies and uneven geographical distribution, and inversions of these data are usually controlled by assumed data weights and other model parameters. Also, hydrodynamic inversion of tsunami runup data has not been defined yet as a well-posed problem due to complexity of coastal effects and nonlinearity of the mathematical problem (*Synolakis et al., 2007*). We perform forward modeling of tsunami propagation and runup to study the relationship between the coseismic slip distribution in the 1964 earthquake rupture area and the tsunami observations in the near field. There are two major components in the numerical algorithm: the code that calculates initial ocean surface deformation due to coseismic displacements using

the equations of Okada (Okada, 1985), and the nonlinear shallow water model of tsunami propagation and runup that employs the derived ocean surface deformation as an initial condition.

5.3.1 Tsunami data

The M_w 9.2 Great Alaska earthquake and tsunami of 1964 were extensively studied in the years following the earthquake. The results of investigations and analysis of collected data were published in a series of six professional papers by the US Geological Survey, and later in eight volumes by the National Committee on the Alaska Earthquake of the National Academy of Sciences. The collected data included seismic, geologic and geodetic measurements, observations of tsunami waves, and measurements of runup heights and inundation areas. A number of studies of coseismic slip distribution in the 1964 rupture provided summary of seismic, geologic and geodetic data sets, including their limitations and biases (Christensen and Beck, 1994; Holdahl and Sauber, 1994; Johnson *et al.*, 1996; Santini *et al.*, 2003; Ichinose *et al.*, 2007; Suito and Freymueller, 2009).

We focus here on the 1964 tsunami data, which consist of two parts - the far-field tidal station data and the near-field observations and measurements. The vertical sea floor displacement generated a major tectonic tsunami that was recorded on more than 100 analog tide gauges all around the Pacific Ocean and as far as Australia and New Zealand (Spaeth and Berkman, 1972). Johnson *et al.* (1996) and Ichinose *et al.* (2007) used different subsets of this data set in their joint inversion studies of tsunami, geodetic and seismic data. In spite of the large number of tide-gauge records, their use is limited in the inversion studies of slip distribution because many of the tidal stations are located in bays, inlets and harbors, where high-resolution grids need to be placed around each station in order to provide enough grid points to resolve those water bodies (Ichinose *et al.*, 2007). Also, the effects of the splay fault displacements could be negligible on the far-field tsunami amplitudes, and therefore slip on the splay faults can not be inverted from the tide gauge data (Johnson *et al.*, 1996).

A number of engineering, geologic and geophysical papers published in the years following the 1964 earthquake contain near-field tsunami observation data at many locations along the Alaska coast (Wilson and Tørum, 1968; Plafker, 1969; Kachadoorian and Plafker, 1967; Plafker *et al.*, 1969; Van Dorn, 1972). The data consists of tsunami polar-

ity and arrival times, tsunami wave amplitudes, runup heights and inundation zones. The two major types of waves observed in the rupture area of the 1964 earthquake were local landslide-generated waves and a tectonic tsunami wave train, all resulting in a complicated wave pattern. In Prince William Sound and Cook Inlet, the tilting of the sea bed produced seiches that lasted for hours, and in several locations these were amplified by a rising tide long after the wave action due to the tectonic tsunami had subsided (*Wilson and Tørum, 1968*). G. Plafker compiled tsunami runup data along the coasts of Kodiak Island and the Kenai Peninsula in the form of a tsunamigram (Figure 5.2). The use of the runup data in the numerical study of a source mechanism requires high-resolution grids of combined bathymetry and topography for the area where runup measurements were performed. The availability of such data sets is limited in Alaska, and there are just a few studies that made use of them (*Suleimani et al., 2003, 2010*).

In spite of the large base of the 1964 near-field tsunami observations and measurements, not all of them can be used in this work. In order to study the tectonic source function, we need to use only the data that are clearly related to the tectonic tsunami, and were not altered by effects of local landslide-generated waves and seiches. We selected those observations of the tectonic tsunami and compiled them in Table 5.1. The locations listed in the table are shown in Figures 5.3, 5.4, and 5.5.

5.3.2 Numerical model and grids

Over the past twenty years, a number of numerical methods have been developed for simulation of tsunami waves. Many of them use the shallow water approximation to the full set of the 3-D Navier-Stokes equations (*Titov and Synolakis, 1995; Imamura, 1996; Goto et al., 1997; Titov and Synolakis, 1998; Lynett et al., 2002; George and LeVeque, 2006; Liu et al., 2007; Zhang and Baptista, 2008; Nicolsky et al., 2010*). This approximation has proven to be robust not only for simulation of tsunami propagation in deep ocean but also for prediction of runup of both non-breaking and mildly breaking waves (*Synolakis, 1986*). This property of the shallow water equations make them applicable for modeling tsunami waves in most geophysical scenarios.

We simulate tsunami propagation and inundation with a nonlinear shallow water model, which is formulated for depth-averaged water fluxes in both spherical and rectangular co-

ordinates. The parallel numerical code solves shallow water equations of motion and continuity using a staggered leapfrog finite-difference scheme. The work by *Nicolisky et al.* (2010) provides the full description of the model, including its mathematical formulation and numerical implementation. This model was validated through a comprehensive set of analytical benchmarks and tested against laboratory and field data, according to the NOAA's requirements for evaluation of tsunami numerical models (*Synolakis et al.*, 2007, 2008). The algorithm is efficiently parallelized using the domain decomposition technique. The finite difference scheme is coded in FORTRAN using the Portable Extensible Toolkit for Scientific computation (PETSc). We use the equations of *Okada* (1985) to calculate the distribution of coseismic uplift and subsidence resulting from a given slip model. Then, the derived surface deformation is used as the initial condition for tsunami propagation.

To simulate the 1964 tectonic tsunami waves, which were generated by coseismic bottom deformation of the continental shelf in south-central Alaska (Figure 5.1), we used a set of nested telescoping grids, or digital elevation models, as input data for the tsunami modeling. These nested grids allow us to propagate waves from the deep waters of the tsunami source region in the Gulf of Alaska to shallow coastal areas of Kodiak Island and Kenai Peninsula (Figure 5.6). The external grid of the lowest resolution spans the entire North Pacific with the grid step of 2 arc-minutes, which corresponds to 1.85×3.7 km at latitude 60°N . The intermediate grids have resolution of 24, 8 and 3 arc-seconds (370×741 m, 123×247 m, and 48×97 m, respectively). Bathymetry data for low and intermediate resolution grids come from the ETOPO2 data set and NOAA's National Ocean Service surveys (<http://www.ngdc.noaa.gov/>). The computational time step is different for each grid and is calculated according to the Courant-Friedrichs-Levy (CFL) stability criterion. The numerical simulation used a constant Manning's roughness of $0.03 \text{ s} \cdot \text{m}^{-1/3}$.

5.4 Existing coseismic deformation models of the 1964 earthquake

In this section, we review previous studies of the asperity structure and coseismic slip distribution of the 1964 rupture area. We use two published coseismic slip models to generate the static vertical displacement of the seafloor, which is translated into the initial condition for tsunami propagation. Then we analyze results of numerical simulations for both models in the far and near field.

5.4.1 Review of the previous studies

The rupture history of the 1964 earthquake was determined by *Christensen and Beck* (1994) from inversion of teleseismic P waves. They demonstrated that there were two areas of high moment release, representing the two major asperities of the 1964 rupture zone: the first and the largest moment pulse corresponded to the PWS asperity, and the second and smaller pulse of moment release was located in the KI asperity.

Holdahl and Sauber (1994) constructed the first detailed fault model of the 1964 earthquake. They used the geodetic data to invert for a distribution of slip on 39 rectangular subfaults in the PWS region with dip changing from 8° to 12° , and on 28 subfaults in the KI region with dip values between 8° and 9° . One fault plane representing the Patton Bay fault was assigned to model the large uplift on Montague Island due to slip on this splay fault. The slip distribution on the landward part of the fault was constrained using the vertical coseismic displacements from leveling measurements, tide gauge data, and geologic data, and using horizontal displacement vectors derived from triangulation surveys. In order to constrain slip on the oceanic part of the fault plane, *Holdahl and Sauber* (1994) used slip estimates derived from the tsunami waveform inversion as a priori information. The resulting distribution of slip shows three zones of higher slip that correspond to the region south of Prince William Sound with the largest slip being near Montague Island, the region east of Kodiak Island, and a small region at the northeast end of the rupture. The total seismic moment calculated from this geodetically inverted slip model is 5.9×10^{22} Nm with the assumed rigidity of 30 GPa.

A more detailed analysis of the 1964 rupture was performed by *Johnson et al.* (1996) through joint inversion of the tsunami waveforms and geodetic data. They simplified the fault model of *Holdahl and Sauber* (1994) by merging four subfaults into one in order to reduce the effort to generate the tsunami Green's functions. They inverted 23 tsunami waveforms noting that the amplitudes of the synthetic waveforms were generally less than amplitudes of the observed ones. The resulting model consists of 9 subfaults in the PWS asperity, 8 subfaults in the KI asperity, and one subfault is assigned to the Patton Bay fault. *Johnson et al.* (1996) also modified depths of the subfaults in the PWS asperity making the fault geometry there consistent with the rupture on the Yakutat terrane - North American plate interface. As a result, the dip values in their model change from 8° to 3° in the down-

dip direction on the PWS subfaults. The derived slip distribution supports the division of the rupture zone into two different segments as it was indicated by *Christensen and Beck* (1994), although the Kodiak asperity was derived by *Johnson et al.* (1996) entirely from the tsunami data. This rupture model has total seismic moment of 6.3×10^{22} Nm with a rigidity of 40 GPa.

Santini et al. (2003) used the fault geometry, the geodetic data and the seismic moment of 5.8×10^{22} Nm with a rigidity of 55 GPa to calculate the 1964 slip distribution by the Monte Carlo method. The fault area was divided into 120 subfaults, and a large number of possible slip distributions with fixed seismic moment were generated minimizing the misfit between the predicted and observed displacement data. The results confirmed the previous findings of two areas of higher slip, one below Prince William Sound, and one in the Kodiak Island area. The authors also showed correlation between the distribution of locked asperities in their model and the locations of the $M_W \geq 6$ earthquakes that were recorded after the 1964 event.

One of the most recent studies of the rupture process of the 1964 earthquake by *Ichinose et al.* (2007) applied the combined inversion of seismic, tsunami and geodetic data to estimate the spatial and temporal distribution of slip and rake. The input data sets for the least squares inversion included 35 teleseismic P wave records, 9 tide gauge records from the stations closest to the source region, and vertical ground displacements. The contribution of tsunami Green's functions was improved in this model compared to that in the joint inversion algorithm of *Johnson et al.* (1996) by introducing higher resolution grids surrounding the tide gauge stations and by using nonlinear hydrodynamic wave equations with a moving boundary condition. The resulting rupture model resembles the previously developed models but differs in a way that it consists of three major areas of moment release, or higher slip, defined as regions where slip was more than twice the average. The third asperity that is not present in the rupture models described above is located beneath the continental shelf and slope, along the line that separates the PWS and KI segments in Figure 5.1. This rupture model has the total seismic moment of 5.52×10^{22} Nm with the assumed rigidity of 60 GPa.

5.4.2 Modeling and analysis

In this section we examine two published coseismic slip models of the 1964 earthquake, for which detailed fault geometry and slip distribution were available for calculation of the initial condition for tsunami simulation. These are the deformation models (DM) by *Johnson et al. (1996)* and *Ichinose et al. (2007)*, to which we will refer by abbreviations of the primary authors last names: JDM and IDM, respectively. Figure 5.7 shows vertical coseismic deformation calculated for the two models using their fault geometries and spatial variations of slip. The resulting distributions of coseismic uplift and subsidence serve as the initial conditions for the tsunami propagation model. It is obvious that deformation patterns of JDM and IDM differ in many key locations, and that the distribution of tsunami energy in the near field can be expected to be different as well. The area of larger uplift offshore Kodiak Island is located more to the northeast in JDM compared to that in IDM. Another region of large uplift in JDM, which is located southeast of the Kenai Peninsula, corresponds to low deformation values in IDM. The region of significant subsidence at the northern end of the rupture area, which is very prominent in JDM, does not exist in IDM. *Suito and Freymueller (2009)* also noted that IDM does not predict the observed uniform subsidence along the southern coast of the Kenai Peninsula, which is reproduced better in JDM.

We performed numerical calculations using the JDM and IDM source functions. In every case, the initial water disturbance propagated through the North Pacific grid of 2 arc-minute resolution, and through the set of embedded grids of increasing resolution in the tsunami near-field region (Figure 5.6). Figure 5.8 presents the distribution of tsunami energy calculated from the tsunami propagation model for the JDM and IDM source functions. These are the plots of maximum computed tsunami amplitudes during the first 12 hours of wave propagation simulation. Over the entire model run, only the maximum value of the tsunami amplitude was stored for each grid point. Both tsunami sources show strong directivity of energy radiation toward the west coast of the US and Canada, which confirms the findings of *Ben-Menahem and Rosenman (1972)* that the 1964 tsunami had a pronounced beaming effect. The maximum amplitudes resulting from the JDM source function show slightly stronger energy concentration in the far field, while the IDM source produces an energy field that splits into three separate beams corresponding to the three as-

perities in the model. Both model runs show amplitude enhancements in the coastal areas of southern Alaska, British Columbia, and the western US states.

We calculated the energy distribution for the same two sources in the near field of the 1964 tsunami. Figure 5.9 presents the maximum amplitude plots in the Kodiak Island area (plots a,c) and in the area of Prince William Sound (plots b,d). These plots show dramatic difference between the energy field generated by the JDM and IDM source functions. In the Kodiak area, all energy gets concentrated along the northeastern shore of the island in the JDM scenario, and offshore the southeastern part of the island in the IDM scenario. In the Prince William Sound grid, the maximum wave amplitudes produced in the IDM scenario (plot d) are due to motion on the splay fault at the southwestern tip of Montague Island. In the JDM scenario (plot b), the highest waves in this region are produced by displacements on megathrust.

We analyze time series for the JDM and IDM source scenarios at the locations listed in Table 5.1 and shown in Figure 5.3, along the southern shore of the Kenai Peninsula (Figure 5.10) and on the Kodiak Island (Figure 5.11). The position of zero on each plot was adjusted to reflect the post-earthquake sea level. The calculated time series show that the two source functions produce very different waveforms at these critical locations, which were exposed to the initial impact of the tectonic tsunami waves. The JDM source produces amplitudes that are higher in general at all locations, and there is no systematic preference for one of the source functions in terms of matching the arrival times and wave amplitudes. There is only one place where simulated time series are in good agreement with observations both in terms of arrival time and the amplitude of the first wave. At Puget Bay, which is the closest point to the splay fault (Figure 5.3), the first calculated crest for both sources arrives at about 20 minutes, although the wave generated by the JDM source has a preceding withdrawal, which was not reported by eyewitnesses. Both sources failed to match the wave arrivals and amplitudes at Seward and Naval Station, the critical locations where tsunami waves were well documented. These discrepancies between observations and modeling results suggest that the JDM and IDM source functions do not adequately describe the near-field tsunami waves, and the further studies of the slip distribution are required.

5.5 The new source function of the 1964 tsunami

It was shown in the the previous section that the initial displacements of the ocean surface in the rupture area, derived from the coseismic deformation models by *Johnson et al.* (1996) and *Ichinose et al.* (2007), do not generate a good match to tsunami arrivals along the Kenai Peninsula and Kodiak Island coasts. Here we attempt to build a source function that better fits tsunami observations in the near-source region. We start with the new model recently introduced by *Suito and Freymueller* (2009). This model was developed as a 3-D viscoelastic model in combination with an afterslip model, using realistic geometry with a shallow-dipping elastic slab. The purpose of the study was to describe the postseismic deformation that followed the 1964 earthquake. Important modifications in the fault geometry resulted in a revision of the 1964 coseismic model. The authors used the inversion-based model by *Johnson et al.* (1996) as a basis for their coseismic slip model, adjusting it to the new geometry and critically reinterpreting the coseismic data. One critical change was the extension of the Montague Island high-angle splay fault from its subaerial outcrop to a longer length along the southern Kenai Peninsula coast to explain the pattern of subsidence in this area. The authors preferred forward finite-element modeling for calculation of coseismic slip due to inconsistency and systematic errors in coseismic displacement data. At the same time, their resulting slip distribution resembles that derived from inversion models of *Holdahl and Sauber* (1994), *Johnson et al.* (1996), and *Ichinose et al.* (2007).

5.5.1 Discretization of the fault geometry

Our goal is to construct a source function of the 1964 tsunami that will explain the near-field tsunami observations. Also, we want to test a hypothesis proposed by *Suito and Freymueller* (2009) that the Patton Bay fault extends as far as the western end of Kenai Peninsula. Although submarine mapping may be needed to prove that, we will use the analysis of the near-field tsunami arrival times and polarity of first arrivals to constrain the submarine extent of the fault. We started with the fault geometry and slip distribution of *Suito and Freymueller* (2009) that are shown in Figure 5.12. The slip model consists of 36 polygons, or elements, with a single value of slip assigned to each element. It is obvious that the geometry of the fault can not be represented with such coarse discretization, which applies only to variations of slip, therefore each of the elements was divided into a number

of subelements that have different values of strike, dip, and rake. First, we corrected the position of the splay fault line with respect to the Montague Island coast, since in the original model it was shifted to the south by a distance approximately equal to the width of the southern part of the island. It is not a substantial shift, but tsunami arrival times in the area close to the fault could be sensitive to this difference in the source location. To correct that, we used the Patton Bay fault line digitized from a geologic map by *Tysdal and Case* (1979), and moved the appropriate splay fault elements in such a way that the new line of strikes coincides with the mapped section of the fault on Montague Island. Figure 5.12 shows the elements of the corrected splay fault model and the slip distribution along the fault. The highest values of slip are assigned to the mapped section of the Patton Bay fault, with smaller values given to the elements of the northeast and southwest fault extensions.

The tsunami model uses the equations of *Okada* (1985) for a finite rectangular fault to generate the initial condition for tsunami propagation. The Okada's fault geometry requires certain relationship between strike, dip and rake angles. Since the finite element model of *Suito and Freymueller* (2009) deals with elements that are parallelograms of different sizes, they can not be used directly in our tsunami model for calculation of initial ocean surface displacement. In order to adapt their slip model for our purposes, we first discretize each subelement into a number of small parallelograms. This number, which we call the discretization factor, can vary in the model. Then, we approximate each of the parallelograms with a best-fit rectangle of the same area and strike, preserving the seismic moment. As a last step, we recalculate the values of dip and rake angles based on Okada's conventions, which require the dip direction to be perpendicular to the strike, and rake being counted counterclockwise from the strike. The resulting Okada-type discretization of the fault geometry is presented in Figure 5.13. This rupture model has total seismic moment of 7.7×10^{22} Nm with a rigidity of 50 GPa, as given in *Suito and Freymueller* (2009). The bottom plot uses the 3-d view of both megathrust and splay fault parts of the model geometry to illustrate the relative steepness of the splay fault (dip values between 10° and 60°) with respect to the megathrust (dip values between 4.5° and 7.9°). The resulting coseismic deformation of the 1964 rupture calculated using the Okada algorithm as a superposition of unit deformations, is shown in Figure 5.14.

5.5.2 Splay fault contribution to the local tsunami wave field

A number of studies published in the years following the 1964 earthquake analyzed data on coseismic displacements and land features associated with the system of splay faults, as well as tsunami arrival times and tsunami amplitudes along the coast of Kenai Peninsula and Kodiak Island (*Plafker, 1965, 1967; Kachadoorian and Plafker, 1969; Plafker et al., 1969; Plafker, 1969, 1972*). *Plafker (1967)* presented the most detailed description and tectonic analysis of the Patton Bay and Hanning Bay reverse faults during the 1964 Alaska earthquake. He gave a full report of surface rupture and fault motion, as well as several pieces of evidence suggesting that the Patton Bay fault marks the northern end of a system of discontinuous faults that continues in the ocean floor well past where the Patton Bay fault is currently mapped, for additional 480 km. The fault was traced on land for about 35 km, and also on the seafloor southwest of the Montague Island for about 27 km (*Malloy and Merrill (1972)*; see also Figure 5.3). *Plafker (1967)* used observations of tsunami amplitudes and arrival times of 19 minutes to the Kenai Peninsula shore and 38 minutes to the southeast coast of Kodiak Island to suggest that this wave crest was probably generated within a narrow belt that extended southwest from Montague Island all the way to Kodiak Island (shown by the red dashed line in Figure 5.2). He also discussed other indications of possible continuation of the fault, such as well defined submarine fault scarps in the inferred zone of the fault, and the concentration of the aftershock activity in the area.

More recently, *Plafker (2006)* re-examined the 1964 tectonic displacement data and tsunami observations, post-seismic tide gauge records, and the paleoseismic history of the eastern section of the Alaska-Aleutian subduction zone. He demonstrated a direct relationship between local tectonic deformation and tsunami generation by analyzing tsunami arrival times, measured runup heights and distribution of wave damage in Kodiak Island and Kenai Peninsula. He derived a conclusion that a major fraction of total slip needs to be partitioned between the megathrust and intraplate splay faults in order to explain the coseismic displacements and near-field tsunami observations. Figure 5.2 supports this statement in a form of a tsunamigram that plots distribution of measured runup along the coast of Kodiak Island and Kenai Peninsula, showing that the largest waves were generated much closer to the shore than they would have been in the case of the slip being entirely on megathrust. We can use numerical modeling to test the hypothesis that the subsidiary faults

within the upper plate were a major contributor to vertical displacements that generated large tsunami waves.

Holdahl and Sauber (1994) used the description given by *Plafker (1967)* as a basis for their model of the Patton Bay fault used in an inversion of geodetic data. *Johnson et al. (1996)* modified the initial megathrust slip model of *Holdahl and Sauber (1994)* for their joint inversion of geodetic and tsunami data, but kept the splay fault model the same. These two studies used only the mapped extent of the fault, approximately 70 km. *Johnson et al. (1996)* assumed that contribution of the Patton Bay fault to the far-field tsunami amplitudes was small enough to be neglected, and performed joint inversion only for the major subfaults on the megathrust. They removed the effect of this fault by subtracting the deformation due to the fault from all geodetic observations. *Ichinose et al. (2007)* assigned the length of 140 km to the Patton Bay fault in their coseismic model, extending it further to the southwest. *Suito and Freymueller (2009)* thought that the very high slip on the fault suggested that the fault may be much longer, and extended it to the western end of the Kenai Peninsula. The extension was also required to simulate the pattern on subsidence along the southern coast of the Kenai Peninsula, and to be able to explain relationship between values of horizontal and vertical displacements in the area. *Suito and Freymueller (2009)* did not extend the splay fault as far as *Plafker (1967)* has suggested, that is to the area offshore the Sitkalidak Island (Figure 5.4; see also point 3 in Figure 5.2), but rather extended it at a different angle along the southern coast of the Kenai Peninsula (Figure 5.12).

In this section we investigate the contribution of the subsidiary faulting to local tsunami wave amplitudes and tsunami arrival times. We set up a numerical experiment to test the hypothesis that the Patton Bay extends farther than its mapped dimensions (*Plafker, 1967, 2006*). We will analyze tsunami arrival times and polarity of the first arrivals to four locations on Kenai Peninsula, for which observations are available: Rocky Bay, Seward, Whidbey Bay and Puget Bay (Figure 5.3). Since Seward is the only populated location at the southern shore of Kenai Peninsula, there is a limited amount of good quality tsunami data that can be used to constrain the source function of the Patton Bay fault. First, we calculate the coseismic surface deformation that results from motion on the splay fault in order to understand the pattern of uplift and subsidence that would have been generated by the splay fault alone. The result presented in Figure 5.15 definitely shows the narrow band

of subsidence along the Kenai Peninsula coast. *Suito and Freymueller (2009)* proposed this extent of the splay fault in order to explain the relatively uniform subsidence along the coast. They argued that subsidence from slip on the megathrust was centered farther inland. We divide the southwestern extension of the fault into 11 segments that correspond to the elements in the fault model (Figures 5.12 and 5.15), and constructed 11 source functions by removing segments one by one from the southwestern extension of the fault. For each of the resulting splay fault sources, we calculated the superposition of the coseismic deformation resulted from motion on the megathrust and on the splay fault.

In order to determine what length of the splay fault produces the tsunami field that fits the observations best, we first modeled tsunami propagation using these source functions as the initial conditions in the tsunami model. Results of tsunami time series calculations for all 11 sources at 4 locations allowed us to distinguish 4 major cases for comparison and analysis - the fault of the full model length; the fault with 4 segments removed from its southwestern end; the fault with 7 segments removed; the fault of the length that approximately corresponds to its mapped extent, where the values of slip change in the model from 7.5 m to 3 m on the up-dip element, and to 5 m on the down-dip element of the fault (Figure 5.12). The resulting surface deformations corresponding to these 4 sources are shown in Figures 5.14 and 5.16. The plots show that different lengths of the splay fault affect the deformation pattern only in the vicinity of the Kenai Peninsula, changing the amount of subsidence along the shore and the position of the hinge line that separates areas of tectonic uplift and subsidence. In order to determine which extent of the splay fault provides the best match to the observations, we analyze time series at several locations on Kenai Peninsula along its southern shore, which was exposed to the initial impact of tsunami waves (Figure 5.3). The position of zero on each plot was adjusted to reflect the post-earthquake sea level, since Rocky Bay and Seward subsided during the earthquake, and Whidbey Bay and Puget Bay experienced tectonic uplift.

Rocky Bay. Rocky Bay is a critical location for our study, because it is at the end of the proposed extension of the splay fault. It was the site of a small logging camp, which subsided about 1.5 meters during the earthquake. The first crest was about 2.7 meters high and arrived about 30 min after the earthquake, but an eyewitness did not pay much attention to the time of wave arrivals (*Plafker et al., 1969*). It was noted however that the first crest

was preceded by a withdrawal. The calculated time series at Rocky Bay are shown in Figure 5.17. It is obvious that the full-length splay fault generates an amplitude that is too high, and the crests, which correspond to sources with the mapped extent of the fault and with the 7 segments removed, arrive too late. The source with 4 segments removed fits observations better than others sources do. Also, the calculated arrival time of about 40 minutes after the earthquake seems logical, since at about 30 minutes the waves were reported at Seward with a high degree of accuracy. If we assume that the splay fault does not extend as far as the end of the Kenai Peninsula, then it takes the waves additional time to reach Rocky Bay.

Seward. The town of Seward in Resurrection Bay is the only location along the Kenai Peninsula coast that has a detailed and reliable record of tsunami waves (*Lemke, 1967*). Seward suffered from the combined effects of local landslide-generated waves and the major tectonic tsunami. The locally generated wave at Seward was about 6-8 m high observed about 1.5-2 minutes after the shaking began. The tectonic tsunami wave came into the bay about 30 to 35 minutes after the beginning of the earthquake, and it was as high as the landslide-generated wave (*Plafker, 1969; Wilson and Tørum, 1968; Lemke, 1967*). The Seward time series in Figure 5.17 demonstrate that all sources except for the fault with the mapped extent provide a very good match to both the arrival time and the observed amplitude. The simulated waves arrive just 2 to 3 minutes later than the observed wave, and it could be due to the splay fault being too far from the shoreline in the model. The Seward results clearly demonstrate that the tectonic wave, which came to Resurrection Bay about 30 minutes after the earthquake, was generated by displacements on the splay fault that definitely extends beyond its mapped length. Also, it was shown by *Suleimani et al. (2010)* that the coseismic deformations based on the source model of *Suito and Freymueller (2009)* produce the inundation zone at Seward that matches best the documented runup.

Whidbey Bay. An eyewitness at the small logging camp located at the head of Whidbey Bay recorded the arrival of the first wave at 19.5 minutes after he felt the first shock (*Plafker et al., 1969*). This wave ran up to an estimated elevation of 10 meters above mean lower low water. The time series in Figure 5.18 shows that the simulated wave arrives about 6 minutes later. Since the observed arrival is a reliable observation, it means that the source of the wave crest in the model is too far away from the shore in the vicinity of Whidbey Bay.

It is hard to estimate the runup height from the tsunami wave amplitude without detailed inundation modeling. We need to mention though that tectonic uplift elevated the area of the camp between 45 and 60 cm, while the calculated uplift in the model is about 2 meters (Figure 5.14). The time series show that the only scenario that greatly underestimates the amplitude of the wave is the one with the mapped extent of the fault. Also, this scenario generated a significant initial water withdrawal, which was not observed at Whidbey Bay.

Puget Bay. A small logging camp in Puget Bay was badly damaged by tsunami waves (Plafker *et al.*, 1969). The area experienced tectonic uplift of about 1.5 m. According to observations, the first wave arrived 20 minutes after the earthquake began (Plafker *et al.*, 1969), which agrees with calculated time series in Figure 5.18. Again, the plot shows that the only scenario that stands alone is the mapped extent of the fault. The amplitude of the first wave seems too low in order to make an observed runup of 5.5 m. This discrepancy could result from overestimation in the model of coseismic uplift at Puget Bay - the deformation plots in Figure 5.14 show that the calculated uplift there is between 3 and 4 meters.

The analysis of the tsunami time series along the southern coast of the Kenai Peninsula, and results of tsunami inundation modeling at Seward (Suleimani *et al.*, 2010), allow us to conclude that the splay fault extends as far as the boundary between 4th and 5th segments in Figure 5.15, but not as far as the western tip of the peninsula. To find possible explanations for this result, we investigated the connection of the splay fault and the megathrust by plotting subfault elements of both models within the depth band of 18 to 25 km, within which the deepest part of the splay fault is located (Figure 5.19). If we assume that the splay fault is not an independent source that ruptured separately from the megathrust in the previous events, but rather a feature that gets triggered only by megathrust earthquakes, then it has to be connected to the megathrust. Figure 5.19 shows that at about 150°W the splay fault disconnects from the megathrust, since it has to reach deeper in order to originate from it. The end of the splay fault at 150°W also approximately corresponds to the boundary of plate coupling according to Zweck *et al.* (2002), and the boundary between positive and negative interseismic slip deficits (Suito and Freymueller, 2009). The justification of the splay fault extension into Prince William Sound will require some additional modeling and analysis, since the wave pattern in the sound was very complex. The arrivals

of tectonic waves were masked by large locally landslide-generated waves in Valdez and Whittier (*Coulter and Migliaccio, 1966; Kachadoorian, 1965*). There were a number of observations of unexplained waves in Prince William Sound that could be associated with undocumented slides and seiches generated by large horizontal displacements of the steep fjord walls (*Plafker, 1969*). Also, the slip values are large on the megathrust subfault elements in the model (Figure 5.12), and as a result, coseismic displacements are also large, and it is difficult to differentiate the effect of the splay fault displacements on the resulting coseismic deformations.

The coseismic model of *Johnson et al. (1996)* was built under the assumption that contribution of the Patton Bay fault to the far-field tsunami waveforms was small enough to be neglected. We test this assumption by propagating tsunami waves to the locations along the Pacific coast of the United States and Canada (Figure 5.20). The waveforms presented in Figures 5.21 and 5.22 demonstrate that inclusion of the splay fault into the source function does not change either the arrival times or the wave amplitudes of the first arrival for any of the time series locations. At some locations the splay fault has a minimal effect on later arrivals, which confirms the assumption given in *Johnson et al. (1996)*.

5.5.3 Contribution of horizontal displacements to tsunami generation

In many tsunami studies in the past, the effect of horizontal displacements was neglected when the ocean surface deformation was calculated as an initial condition for tsunami propagation. However, it has been shown already by a number of authors that there is a possibility of tsunami generation by horizontal motions of the sea floor, either during strike-slip earthquakes, or during subduction zone earthquakes, in which horizontal displacements generate a significant portion of the ocean surface uplift. *Tanioka and Satake (1996)* investigated two events in which horizontal displacements due to faulting contributed to tsunami generation. They found that in the first case the strike-slip fault was normal to the coastline and therefore to the bottom slope, and the slope moved in the direction perpendicular to its gradient. Since the horizontal displacements were large relative to the vertical displacements, the horizontal effects became significant. In the second event, the combination of shallow dipping thrust and a very steep trench slope generated the similar horizontal motion of the bottom slope that resulted in ocean surface uplift. This generation mecha-

nism is illustrated by a diagram in Figure 5.23. *Johnson and Satake* (1997) investigated the 1946 Aleutian tsunamigenic earthquake, which was an example of the faulting geometry described in *Tanioka and Satake* (1996). The source had a shallow dip of 6° , and was under the steep slope of the Aleutian trench. The authors found that including the horizontal component of the bottom motion into calculation of the initial ocean surface uplift did not alter the shape of the waveforms, but dramatically increased the tsunami amplitude by almost a factor of 2 at all tide gauges. *Song et al.* (2008) analyzed seismically-inverted sea floor deformation of the 2004 Sumatra-Andaman earthquake and found that the vertical displacements alone were not sufficient to generate the powerful tsunami, and that the two thirds of the satellite-recorded tsunami wave height was due to the horizontal displacements. It was demonstrated that the horizontal motions of faulting in this tsunami generated kinetic energy 5 times larger than the potential energy due to the vertical motion. The directivity pattern of tsunami energy propagation was also best explained by including horizontal forcing into the source mechanism.

The faulting geometry of the 1964 earthquake suggests that its coseismic horizontal displacements could have sizable contribution into tsunami amplitudes. First, the earthquake mechanism was a shallow-dipping thrust, with dip values changing from 4.5° in the PWS asperity to 7.9° in the Kodiak asperity, according to the model parameters from *Suito and Freymueller* (2009). Second, the significant amount of coseismic deformation occurred in the area of the steep slopes of the Aleutian trench in the Gulf of Alaska. To estimate horizontal land movement, triangulation surveys were carried out after the earthquake in the land portion of the deformation area. *Plafker* (1969) summarized their results, which indicated that the magnitude of horizontal displacements was much greater than that of vertical ones, although vertical displacements were also unusually large. The movement over Prince William Sound and Kenai Peninsula was directed mostly to the southeast, that is nearly perpendicular to the trench. *Plafker et al.* (1969) give the range of horizontal displacements from about 5 to 20 meters, the maximum displacement being measured at the southwest end of Montague Island. *Plafker* (1969) investigated the relationship between the horizontal and vertical regional displacements and found that areas of maximum horizontal displacements generally coincided with that of vertical displacements, and that the horizontal displacement vectors were approximately normal to the isobases. There were

no observations of direct damage caused by horizontal displacements. *Plafker et al.* (1969) hypothesized that many unexplained waves in Prince William Sound, which were observed almost immediately after the earthquake and were definitely not associated with landslides, could have been induced by a sudden horizontal movement of steep fjord walls.

We set up a numerical modeling experiment to study the possible contribution of horizontal displacements into the initial tsunami wave field. The limitation of our model is in its ability to account only for the static vertical deformation of the ocean surface that results from horizontal motion of the bottom. The other component, which is transfer of kinetic energy from a moving slope into the water column, is not simulated in the current model. We construct two tsunami sources - one that includes the vertical deformation due to horizontal displacements, and one that was derived using the vertical displacements only. Then, we compare tsunami wave heights and arrival times generated by the two sources in the near and far field.

According to *Tanioka and Satake* (1996), the vertical displacement of the ocean surface ξ_h , which is resulted from the horizontal motion of the ocean bottom slope, can be calculated as a dot product of the horizontal displacement vector \vec{d} and the gradient of the bottom slope:

$$\xi_h = d_x \frac{\partial H}{\partial x} + d_y \frac{\partial H}{\partial y}, \quad (5.1)$$

where H is bathymetry, and d_x and d_y are the east-west and north-south components of the horizontal displacement vector. We calculated the bottom slope gradients over the 1964 deformation area in the 24-arcsecond grid that covers Gulf of Alaska (Figure 5.6), and used the equations of *Okada* (*Okada*, 1985) to derive the horizontal displacements vectors on the same grid. The resulting vertical deformation is presented in Figure 5.24. The plot shows a number of important features of the deformation field. First, the areas of maximum deformation due to horizontal displacements appear to coincide with the regions where vertical displacements were also large. Second, the maximum deformations are distributed within the band of large bathymetry gradients, which is the expected result that follows from Equation 5.1. There are two pronounced maxima in the deformation field - one in the Kodiak asperity south-east of Kodiak Island, and the second one in the PWS asperity, south of Montague Island. The maximum value of the vertical deformation due to horizontal displacements is 1.55 m. Another interesting feature of the deformation field is the initial

depression of the sea surface by about 0.5 m in the eastern parts of Cook Inlet and Shelikof Strait. (Waller, 1966) reported waves observed in Cook Inlet and Kachemak Bay within 5 minutes after the main shock, traveling perpendicular to the shores. These waves remained unexplained, because the evidence of slumping or sliding was not found. The waves could be seiches generated by the tilting of the sea surface due to horizontal motion of the water basin.

As the next step, we calculate the maximum tsunami amplitudes for the source function shown in Figure 5.24. Since vertical and horizontal deformation occur together during the rupture process, the tsunami source in this experiment is hypothetical, but it helps to estimate where the effects of the added deformation due to horizontal displacements could be significant in the near field. Figure 5.25 shows maximum tsunami amplitudes in the Gulf of Alaska generated only by horizontal displacements. It demonstrates that the tsunami energy from the deformation maximum in the Kodiak asperity is directed toward the section of the Kodiak coast between Cape Chiniak and Dangerous Cape (Figure 5.4). This stretch of the coast is the area of the maximum measured runup (Plafker and Kachadoorian (1966); see also Section 5.5.4). The second deformation maximum in the PWS asperity generates tsunami waves whose energy is directed toward the coast of Kenai Peninsula, west of Resurrection Bay. There are no measurements or observations of tsunami in this area.

Figure 5.26 presents simulated time series at 4 locations on the eastern coast of Kodiak Island, for which observations of the tsunami arrival time or wave amplitude exist. The time series were calculated first for the initial ocean surface uplift ξ_z that was derived from vertical displacements only, and then for the total vertical deformation ($\xi_z + \xi_h$), derived for both vertical and horizontal displacements. The results show that the waveforms were almost identical for the two sources, and the amplitude was only 5 to 7% larger for the second source, which included vertical deformation due to horizontal bottom motion. We perform a similar experiment for the far field and calculate tsunami amplitudes at the locations along the Pacific coast of the United States and Canada (Figure 5.20). The waveforms are presented in Figures 5.21 and 5.22 for three initial conditions - the ocean surface uplift due to a) only vertical displacements on megathrust, b) due to combination of vertical and horizontal displacements on megathrust, and c) due to vertical displacements on megathrust and the splay fault. The time series show that horizontal displacements have an effect on

the first arrival, while the splay fault affects the waveforms later during the tsunami propagation span. Similar to the near-field results, the waveforms are identical for cases "a" and "b", but difference in tsunami amplitudes is more significant - the amplitudes are 10 to 18% larger for the source that includes horizontal displacements.

The study of horizontal impulses of the continental slope during the 2004 Sumatra-Andaman earthquake concluded that the momentum force they generated was the major contributor to the tsunami wave height and to the tsunami directivity pattern (*Song et al.*, 2008). Similarly, in the case of the 1964 earthquake the horizontal motion of the bottom slope was directed seaward, mostly to the southeast. It means that the kinetic energy transferred to the water from the moving bottom was directed toward the west coast of the United States and Canada. The potential energy of the 1964 tsunami computed for the coseismic model that includes effects of the splay fault and horizontal displacements is 4.1×10^{15} J. As a comparison, the potential energy estimated by *Lay et al.* (2005) for the 2004 Sumatra-Andaman earthquake was 4.2×10^{15} J. In order to estimate the relative importance of the kinetic energy transfer during the 1964 earthquake, we used an algorithm similar to that described in *Song et al.* (2008). The authors used seismic waveform inversions to calculate the seafloor displacement as a function of time over the rupture area and within the total rupture period. Then, the displacement velocity of the seafloor was derived as a function of time. In the absence of the time-dependent seafloor displacements, we estimated the velocities using displacement times from the 1-Hz GPS records of the 2003 Tokachi-Oki earthquake, which gave the average time of 20 seconds (*Emore et al.*, 2007). The kinetic energy of the 1964 tsunami corresponding to displacement times of 10, 20 and 30 seconds was calculated as 7.6×10^{15} J, 1.9×10^{15} J, and 8.4×10^{14} J, respectively. The range of values demonstrates that this simple model for estimation of kinetic energy is very sensitive to the duration of the bottom motion, and even the slow case produces the kinetic energy that is still a significant 20% portion of the potential energy. We can therefore assume that underestimation of the 1964 tsunami wave heights at tide gauges located along the US west coast by many existing models could possibly result from not accounting for the momentum force in tsunami genesis. To test this hypothesis, we would need to develop a fully coupled earthquake-tsunami generation model that allows for the time-dependent kinetic energy transfer from the bottom motion into the water column.

To summarize our findings discussed in Sections 5.5.2 and 5.5.3, we present the coseismic source function that results from the analysis of the splay fault extent along the southern shore of the Kenai Peninsula, and from investigation of the horizontal displacements contribution to tsunami amplitudes. Figure 5.27 shows the superposition of three deformation fields: the uplift of the ocean surface due to vertical displacements on megathrust, that due to coseismic horizontal motion of the ocean bottom, and uplift due to displacements on the splay fault, which extends to about 150°W.

5.5.4 Coseismic slip in the Kodiak asperity

It was first demonstrated by *Christensen and Beck* (1994) that the Kodiak Island region of high moment release is an important feature of the coseismic rupture of the 1964 earthquake. *Nishenko and Jacob* (1990) analyzed historical earthquake data in the PWS and the KI segments (Figure 5.1) and concluded that the Kodiak Island segment produced both large and great earthquakes more frequently and also independently of the PWS segment. It was also shown that the recurrence interval for the Kodiak asperity may be as low as 60 years. *Johnson et al.* (1996) used joint inversion of tsunami wave forms and geodetic data and the initial fault model by *Holdahl and Sauber* (1994) to derive a detailed slip distribution of the 1964 rupture area. They confirmed that the Kodiak asperity was a prominent characteristic of the 1964 coseismic rupture. The deformations of the ocean bottom in this area generated destructive tsunami waves that reached the exposed eastern shore of Kodiak Island between 20 minutes and 1 hour after the earthquake. The tsunami waves had the most catastrophic effect on the Kodiak Island communities during and after the earthquake, causing 18 deaths and extensive property damage (*Plafker and Kachadoorian*, 1966).

The first study of the 1964 tsunami runup on Kodiak Island (*Suleimani et al.*, 2003) employed numerical modeling to simulate tsunami impact on the communities of Kodiak City and Kodiak Naval Station. The authors used the coseismic deformation model by *Johnson et al.* (1996) to generate the initial ocean surface displacement in the tsunami source region. It was shown that the results of the near-field inundation modeling strongly depend on the slip distribution within the rupture area, because the complexity of the source function is combined with the proximity of the coastal zone. While the the calculated

runup agreed relatively well with the observed inundation, the calculated and observed arrival times at the Kodiak Naval Station were out of phase. Since the arrival times are more sensitive to the fine structure of the tsunami source than the inundation area, it was concluded that more research on the coseismic slip distribution around Kodiak is required for tsunami modeling studies.

To study the 1964 tsunami wave field around Kodiak Island, we apply the newly developed source function (Figure 5.27), modified from *Suito and Freymueller (2009)* as described above in Sections 5.5.2 and 5.5.3. We generate the initial ocean surface displacements using the Okada algorithm (*Okada, 1985*), simulate propagation of tsunami waves through the set of nested grids (Figure 5.6), and calculate maximum tsunami amplitudes in the 8-arcsecond grid of Kodiak Island the way it is described in Section 5.4.2. The maximum-amplitude plot presented in Figure 5.28 shows a number of interesting results. First, it supports the observation that the waves were high and destructive only along the eastern exposed ocean coast of Kodiak Island, and that waves along the southwest coast and on the Shelikof Strait side of the island were small and did not inundate above the normal high tide levels (*Plafker and Kachadoorian, 1966*). Second, the numerical results show a concentration of the highest waves at the coastal locations exactly where the highest runup was measured: at the uninhabited shore between Cape Chiniak and Narrow Cape, and on the southeast beach at Sitkalidak Island. These locations are marked by black crosses in Figure 5.28. Also, the vertical deformation component resulting from large horizontal displacements in the Kodiak asperity contributed to higher tsunami amplitudes along the shoreline between Cape Chiniak and Dangerous Cape (see also Figure 5.25, which shows maximum tsunami amplitudes generated by horizontal displacements only). These results demonstrate that the calculated directions of tsunami energy concentration in the vicinity of Kodiak Island agree well with the observations of tsunami impact in 1964. However, a maximum-amplitude plot displays the highest amplitudes that occur at any single location over the entire duration of a tsunami event, which was about 12 hours in the case of the 1964 tsunami. At some locations the maximum runup was caused by the first wave, which was the largest one even though it arrived on low tide, but in many places the highest runup coincided with high tide, which came about 6 hours after the earthquake (*Plafker and Kachadoorian, 1966; Plafker et al., 1969; Wilson and Tørum, 1968*). Therefore, to

determine whether the vertical deformations calculated from the assumed coseismic slip distribution in the Kodiak asperity produce the initial tsunami wave that matches the observations, we need to examine arrival times as reliable indicators of the spatial origins of the leading tsunami wave crest. To do that, we analyze time series at several locations on Kodiak Island along its south-eastern shore, which was exposed to the initial impact of tsunami waves (Figure 5.4).

Kaguyak. *Wilson and Tørum* (1968) reported that the first wave arrived at the small fishing village of Kaguyak about 20 minutes after the earthquake, which agrees well with the modeling results (Figure 5.29). This first wave originated in the area of higher slip just offshore the southern tip of the island, marked by letter "A" in Figure 5.14. The initial ocean surface displacements generated by the updip vertical motions are marked by letter "B". Estimating the speed of the wave front as $c = \sqrt{gH}$, where g is the coefficient of gravity and H is depth, we calculate that it took the waves originated in this area about 55 minutes to reach the coast, which agrees well with the arrival time of the second crest at Kaguyak.

Old Harbor. The village is located in the Sitkalidak Strait that separates Kodiak and Sitkalidak Island. It was almost entirely destroyed by tsunami waves. According to observations (*Kachadoorian and Plafker*, 1969), the initial wave struck the community 48 minutes after the earthquake. The modeled arrival is in good agreement with observations (Figure 5.29), but the wave amplitude is probably underestimated. The time series point is located in the 8-arcsecond grid of Kodiak Island with resolution of about 125m x 250m (Figure 5.6), and the Sitkalidak Strait is not resolved by this grid. It means that we were not able to reproduce the effect of confluence of waves that arrived into the village from both sides of the strait causing an exceptionally high runup (*Wilson and Tørum*, 1968). The detailed modeling of runup in this area requires a high resolution DEM of combined bathymetry and topography.

Cape Chiniak. 38 minutes after the start of the earthquake, the Fleet Weather Central at the Kodiak Naval Station received a report from the US Coast Guard station about the arrival of a big tsunami wave at Cape Chiniak (*Plafker and Kachadoorian*, 1966). This warning resulted in evacuation of residents in the Kodiak area, which saved many lives. The calculated arrival time agrees well with the observations. The wave height was estimated

by eyewitnesses to be about 30 feet (9 meters). The simulated amplitude is about half of that value. The first wave at Chiniak originated at the area of high slip marked by letter "B" in Figure 5.14. In addition to consistent overestimation of tsunami amplitudes by eyewitnesses, the discrepancy could be due to low values of slip in this section of the Kodiak asperity.

Kalsin Bay. This point is in the 8-arc-second grid, resolution of the grid is about 125m x 250m. The time series point is located in deep water near the head of the bay. The calculated arrival is 55 minutes after the earthquake. This is one of the only 3 locations on the island where arrival times and runup heights were recorded instrumentally by USGS streamflow gauges (*Plafker and Kachadoorian, 1966*). In Kalsin Bay, the gauge was situated at a site near the mouth of Myrtle Creek, where the creek intersects with the Chiniak Highway. The elevation of this point is about 15 meters, and it subsided during the earthquake by about 1.5 meters. Obviously, it subsided enough to bring it within reach of the highest tsunami waves, but at the same time it was still too high to record astronomical tides after the earthquake, unlike the two other streamflow gauges on the other side of the island (*Plafker and Kachadoorian, 1966*). Those gauges, situated at the Shelikof Strait side of the Kodiak Island, were low enough to record tides after the earthquake. The Myrtle Creek gauge data show that the first wave arrived at the gauge about 70 minutes after the earthquake, or about 15 minutes after the calculated arrival of this wave into the bay. There are several possible explanations for this discrepancy. First we need to mention that the calculated arrival time of 55 minutes seems logical, given that the first wave in Kalsin Bay was the same wave that hit Cape Chiniak at 38 minutes after the earthquake and then, refracting around the Cape, first arrived to Kalsin Bay, and then was recorded with a high degree of accuracy at Naval Station at 63 minutes after the earthquake. The arrival time of 55 minutes fits very well between the arrivals to Cape Chiniak and Naval Station. Second, the deeper than actual depths used in the model could make the wave arrive sooner, since travel time strongly depends on water depth, and the bathymetry data in the 8-arc-second grid are not of high accuracy. Third, it takes some time for a wave to inundate dry land at elevation of about 15 meters, since friction effects start playing a more significant role. In order to calculate inundation of dry land and runup heights in Kalsin Bay, a good quality high-resolution grid of combined bathymetry and topography is required.

Kodiak Naval Station. This is the only location along the Gulf of Alaska coast that has a reliable record of tsunami waves (*Kachadoorian and Plafker, 1969*). Personnel of the Fleet Weather Central at the Kodiak Naval Station kept a log of arriving waves. The calculated time series at the Kodiak Naval Station is shown in Figure 5.30. The arrows and times next to them indicate observed arrivals of the first 5 waves. The modeling results are in good agreement with observations. The model was even able to reproduce the third bifurcated wave, which means that the distribution of slip in the fault model of Kodiak asperity produced the reasonable initial displacements of the ocean bottom. Since the slip distribution pattern and therefore the coseismic displacements are very complex, the visualization of the animated tsunami wave field is a good tool to analyze arrivals of waves and their sources in the rupture area. The animated tsunami propagation shows that the first crest at the Naval Station originated in the area of high slip in the Kodiak asperity indicated by letter "B" in Figure 5.14. This wave first hits the coastline between Cape Chiniak and Narrow Cape, and then refracts around Cape Chiniak and enters Chiniak Bay (Figures 5.4 and 5.5). Then the secondary crest forms in the same area of high slip offshore south-eastern part of Kodiak Island and arrives to the Naval Station an hour later. The previous numerical study of the 1964 tsunami waves in Kodiak presents the calculated time history at the Kodiak Naval Station, which does not compare well with the documented arrival times for the first three waves. (*Suleimani et al., 2003*). Our results show that the new source function provides a good match to the observations.

Kodiak City. Although both Kodiak City and the Kodiak Naval Station are in the St. Paul Harbor, separated only by 8 km along the coast (Figure 5.5), the wave histories were different at these two locations. The waves were arriving mostly from south-east to the Naval Station, which is an open location on the coast, and is sheltered from the north-east waves by Woody Island and Near Island. At Kodiak City the wave pattern was more complicated due to interference of waves arriving from 2 major directions - from southeast and from northeast, through the channel that separates the downtown Kodiak and the Near Island (Figure 5.5). Only very few eyewitness accounts exist for the reconstruction of wave history in Kodiak City (*Kachadoorian and Plafker, 1969*), because of the timely tsunami warning that prompted local residents to evacuate to higher ground. Observations of waves at Kodiak City were not as reliable as those at the Naval Station, and the times

are only estimates (*Kachadoorian and Plafker, 1969*). The calculated time series at Kodiak City (Figure 5.30, bottom plot) resembles the time series at the Naval Station, with waves arriving at about the same intervals. This result seems logical, since these two locations are very close to each other, and the arriving tsunami waves are long-period waves. However, the eyewitnesses reported two more waves at Kodiak City (marked by A and B) before the arrival of the third wave that was the first recorded at the Naval Station 63 minutes after the earthquake. These two waves arrived from northeast through the channel that separates Kodiak City from Near Island (Figure 5.5). The resolution of the numerical grid is not high enough to adequately represent the narrow channel and interference of northeastern waves with the waves that arrived from southeast.

The analysis of calculated tsunami time series at several locations along the southeastern shore of Kodiak Island shows that the new source function produces tsunami arrivals that agree well with the observations. This result suggests that the new coseismic deformation model provides a good estimate of slip in the Kodiak asperity.

5.6 Discussion and conclusions

We performed a near-field numerical study of the source of tsunami waves generated by the M_W 9.2 1964 Alaska earthquake. First, it was demonstrated that the previously published deformation models by *Johnson et al. (1996)* and *Ichinose et al. (2007)* generated very different tsunami wave fields in the rupture area of the 1964 earthquake and produced tsunami arrival times and amplitudes that did not agree with the near-field observations. These results indicated that some features of the slip distribution responsible for the near-field tsunami generation were critically different in the considered models. We used then the most recent coseismic slip model of *Suito and Freymueller (2009)* as a base for the new source function of the 1964 tsunami, and performed discretization of the fault elements and their conversion into the Okada-type elements. The new fault geometry allowed for modification and redistribution of slip, and for calculation of the resulting coseismic deformation of the 1964 rupture as a superposition of unit deformations using the equations of *Okada (1985)*.

We investigated the effect of the secondary intraplate faults on local tsunami waves by conducting a numerical experiment, which tested a hypothesis that the Patton Bay fault

extends farther than its mapped dimensions (*Plafker, 1967*). We corrected the original position of the splay fault line with respect to the Montague Island coast in the fault geometry, and used the near-field tsunami modeling results and observations of the tsunami arrival times and polarity of first arrivals to constrain the fault length along the southern coast of the Kenai Peninsula. Our proposed extent of the fault to about 150°W approximately corresponds to the boundary between positive and negative interseismic slip deficits (*Suito and Freymueller, 2009*). In the coseismic model, this boundary also corresponds to the disconnect between the splay fault and the megathrust. The splay fault in our model is longer than that in the coseismic models of *Holdahl and Sauber (1994)*, *Johnson et al. (1996)* and *Ichinose et al. (2007)*, but does not reach the western tip of the Kenai Peninsula, as it was proposed in the original model by *Suito and Freymueller (2009)*. The analysis of the far-field tsunami time series demonstrated that inclusion of the splay fault into the source function changes neither the arrival times nor the wave amplitude of the first arrivals, confirming the assumption that the splay fault has little effect on the tsunami far field and can be excluded from the waveform inversion (*Johnson et al., 1996*).

We conducted a numerical modeling experiment to study the possible contribution of horizontal displacements into the initial tsunami wave field by calculating the component of the ocean surface uplift due to horizontal motion of the steep ocean bottom slopes. Unlike the splay fault, the horizontal displacements had a pronounced effect on the far-field tsunami with 10 to 18% increase in wave amplitudes of the first arrival at several locations on the Pacific west coast. At the same time, it was shown that horizontal displacements had very localized effect in the near field. The area of maximum vertical deformation due to horizontal displacements was in the Kodiak asperity and directed tsunami energy toward the eastern coast of Kodiak Island, where maximum runup was observed. Another local deformation maximum increased tsunami amplitudes along the short section of the southern coast of the Kenai Peninsula.

The analysis of tsunami impact on the southeastern shore of Kodiak Island confirmed that the Kodiak asperity was an important and robust feature of the 1964 rupture (*Christensen and Beck, 1994*; *Holdahl and Sauber, 1994*; *Johnson et al., 1996*; *Ichinose et al., 2007*). We have demonstrated that the new coseismic deformation model provides a good estimate of slip in the Kodiak asperity. The important finding that came out from our study

is that in this area, the coseismic slip on the megathrust alone is capable of producing the tsunami arrivals and amplitudes that agree well with the observations, and the splay fault is not needed to be extended along the Kodiak shore in order to match the tsunami data. We were not able to utilize the runup measurements along this coastline due to absence of combined bathymetry and topography data sets for calculation of runup, and this will be an essential next step in the source function study. The outcome of runup simulations can modify the current match between observations and modeling results, but since we begin with the generally good agreement with data, only minor redistribution of slip in the Kodiak asperity should be required.

To summarize the results of our numerical study of the 1964 tsunami source, we point out that the features of the model, such as horizontal displacements on the megathrust and the secondary intraplate faulting, were shown to have different impacts on tsunami amplitudes in the Prince William Sound asperity versus that in the Kodiak asperity, and also different effects on the far-field tsunami modeling results. Accounting for the initial ocean surface uplift due horizontal motion of the bottom increases the amplitudes of the first arrivals in the far field, while the splay fault affects the waveforms later during the tsunami propagation span. Both source features have effect in the near field, but in different locations. While the displacements on the mapped section of the Patton Bay fault and its offshore continuation have very strong effects on the tsunami arrivals, amplitude and inundation at the Kenai Peninsula sites, the horizontal bottom motion influences tsunami wave field mostly in the Kodiak region.

When analyzing results of numerical modeling and comparing them with observations, we need to mention several limitations of the model. One of them is that the model accounts only for the static vertical deformation of the ocean surface that results from vertical and horizontal displacements on the fault. The other component, which is transfer of kinetic energy from a horizontally moving bottom slope into the water column, is not simulated in the current model. Accounting for this transfer of energy directed toward the west coast of the United States will most probably result in increase of tsunami amplitudes, which so far have been underestimated in previous modeling studies. Also, the model does not take into account the effects of propagating rupture, using only the static coseismic deformation of the seafloor. For earthquakes with extremely long rupture zones, such as the 1964 Alaska

and 2004 Sumatra earthquakes, modeling the dynamic rupture could introduce corrections into the near-field tsunami arrival times and amplitudes. *Song et al. (2008)* suggested that the effects of propagating rupture and kinetic energy transfer can be combined by applying 3-D earthquake forcing to the ocean model during the rupture period or the initialization period. The use of the near-field runup data was limited in this source function study due to lack of high-resolution combined bathymetry and topography DEMs in coastal locations where runup measurements were carried out. Also, at many places the highest runup was not caused by the first wave, but resulted from one of the later arrivals, which coincided with high tide and could have been amplified by interactions of tsunami waves and tides. In order to make use of those runup observations, the nonlinear tsunami-tide interactions need to be included into the model.

5.7 Acknowledgments

This study was supported by NOAA grants 27-014d and 06-028a through Cooperative Institute for Arctic Research. Numerical calculations for this work are supported by a grant of High Performance Computing resources from the Arctic Region Supercomputing Center at the University of Alaska Fairbanks as part of the US Department of Defense HPC Modernization Program. We are grateful to Dr. Dmitry Nicolsky for development of the Alaska Tsunami Online Mapping interface that we used for multiple model runs and analysis of the results. We also thank Rod Combellick and Keith Labay for providing us with digitized coordinates of nodes along the Patton Bay fault.

Bibliography

- Ben-Menahem, A., and M. Rosenman (1972), Amplitude patterns of tsunami waves from submarine earthquakes, *J. Geophys. Res.*, 77(17), 3097–3128, doi: 10.1029/JB077i017p03097.
- Carver, G., and G. Plafker (2008), Paloseismicity and neotectonics of the Aleutian subduction zone - an overview, in *Active tectonics and seismic potential of Alaska*, edited by J. Freymueller, P. Haeussler, R. Wesson, and G. Ekström, Geophysical Monograph Series 179, pp. 43–63, AGU, Washington, DC.
- Christensen, D., and S. Beck (1994), The rupture process and tectonic implications of the Great 1964 Prince William Sound earthquake, *Pure Appl. Geophys.*, 142(1), 29–53.
- Coulter, H., and R. Migliaccio (1966), Effects of the Earthquake of March 27, 1964, at Valdez, Alaska, U.S. Geological Survey Professional Paper 542-C, 36 pp.
- Emore, G. L., J. S. Haase, K. Choi, K. M. Larson, and A. Yamagiwa (2007), Recovering seismic displacements through combined use of 1-hz gps and strong-motion accelerometers, *Bull. Seism. Soc. Am.*, 97(2), 357–378, doi:10.1785/0120060153.
- Geist, E. L. (1999), Local tsunamis and earthquake source parameters, in *Tsunamigenic Earthquakes and Their Consequences*, *Adv. Geophys.*, vol. 39, edited by R. Dmowska and B. Saltsman, pp. 117–209, Academic Press.
- George, D. L., and R. J. LeVeque (2006), Finite volume methods and adaptive refinement for global tsunami propagation and inundation, *Science of Tsunami Hazards*, 24(5), 319–328.
- Goto, C., Y. Ogawa, N. Shuto, and F. Imamura (1997), Numerical method of tsunami simulation with the leap-frog scheme, *Manuals and guides 35*, Intergovernmental Oceanographic Commission of UNESCO: IUGG/IOC TIME Project.
- Holdahl, S., and J. Sauber (1994), Coseismic slip in the 1964 prince william sound earthquake: A new geodetic inversion, *Pure Appl. Geophys.*, 142, 55–82.

- Ichinose, G., P. Somerville, H. Thio, R. Graves, and D. O'Connell (2007), Rupture process of the 1964 prince william sound, alaska, earthquake from the combined inversion of seismic, tsunami, and geodetic data, *J. Geophys. Res.*, *112*(B07306).
- Imamura, F. (1996), Review of tsunami simulation with a finite difference method, in *Long-Wave Runup Models*, edited by H. Yeh, P. Liu, and C. Synolakis, pp. 25–42, World Scientific.
- Johnson, J., and K. Satake (1997), Estimation of seismic moment and slip distribution of the 1 April 1946 Aleutian tsunami earthquake, *J. Geophys. Res.*, *102*, 11,765–11,774.
- Johnson, J., K. Satake, S. R. Holdahl, and J. Sauber (1996), The 1964 prince william sound earthquake: Joint inversion of tsunami and geodetic data, *J. Geophys. Res.*, *101*, 523–532.
- Kachadoorian, R. (1965), Effects of the earthquake of March 27, 1964 at Whittier, Alaska, U.S. Geological Survey Professional Paper 542-B, 21 pp.
- Kachadoorian, R., and G. Plafker (1967), Effects of the earthquake of March 27, 1964 on the communities of Kodiak and nearby islands, U.S. Geological Survey Professional Paper 542-F, 41 pp.
- Kachadoorian, R., and G. Plafker (1969), Effects of the Earthquake of March 27, 1964 on the communities of Kodiak and nearby islands, U.S. Geological Survey Professional Paper 542-F, 41 pp.
- Lander, J. (1996), *Tsunamis affecting Alaska. 1737–1996*, no. 31 in NGDC Key to Geophysical Research, National Geophysical Data Center, Boulder, Colo.
- Lay, T., H. Kanamori, C. J. Ammon, M. Nettles, S. N. Ward, R. C. Aster, S. L. Beck, S. L. Bilek, M. R. Brudzinski, R. Butler, H. R. DeShon, G. Ekström, K. Satake, and S. Sipkin (2005), The Great Sumatra-Andaman Earthquake of 26 December 2004, *Science*, *308*(5725), 1127–1133, doi:10.1126/science.1112250.

- Lemke, R. (1967), Effects of the Earthquake of March 27, 1964, at Seward, Alaska, U.S. Geological Survey Professional Paper 542-E, 48 pp.
- Liu, P. L.-F., H. Yeh, and C. Synolakis (Eds.) (2007), *Advanced Numerical Models for Simulationg Tsunami Waves and Runup*, Advances in Coastal and Ocean Engineering, Vol 10, World Scientific, Proceedings of the Third International Workshop on Long-Wave Runup Models, Catalina, 2004.
- Lynett, P., T.-R. Wu, and P.-F. Liu (2002), Modeling wave runup with depth-integrated equations, *Coastal Engineering*, 46(2), 89–107.
- Malloy, R., and G. Merrill (1972), Vertical crustal movement on the sea floor, in *The Great Alaska Earthquake of 1964. Oceanography and Coastal Engineering*, pp. 252–265, National Academy of Sciences, Washington, D.C.
- Nicolisky, D., E. Suleimani, and R. Hansen (2010), Validation and verification of a numerical model for tsunami propagation and runup, *Pure Appl. Geophys.*, doi:10.1007/s00024-010-0231-9.
- Nishenko, S., and K. Jacob (1990), Seismic potential of the Queen Charlotte-Alaska-Aleutian seismic zone, *J. Geophys. Res.*, 95(B3), 2511–2532.
- Okada, Y. (1985), Surface deformation due to shear and tensile faults in a half-space, *Bull. Seism. Soc. Am.*, 75, 1135–1154.
- Okal, E., and C. E. Synolakis (2004), Source discriminants for near-field tsunamis, *Geophys. J. Intl.*, 158, 899–912.
- Plafker, G. (1965), Tectonic deformation associated with the 1964 Alaska Earthquake, *Science*, 148(3678), 1675–1687.
- Plafker, G. (1967), Surface faults on Montague Island associated with the 1964 Alaska Earthquake, U.S. Geological Survey Professional Paper 543-G, 42 pp.
- Plafker, G. (1969), Tectonics of the March 27, 1964 Alaska Earthquake, U.S. Geological Survey Professional Paper 543-I, 74 pp.

- Plafker, G. (1972), Alaska Earthquake of 1964 and Chilean Earthquake of 1960: implications for arc tectonics, *J. Geophys. Res.*, 77(5), 901–925.
- Plafker, G. (2006), The great 1964 Alaska Earthquake as a model for tsunami generation during megathrust earthquakes with examples from Chile and Sumatra, Abstracts of the AGU Chapman Conference on the Active Tectonics and Seismic Potential of Alaska.
- Plafker, G., and R. Kachadorian (1966), Kodiak and Nearby Islands, U.S. Geological Survey Professional Paper 543-D, 46 pp.
- Plafker, G., and W. Thatcher (2008), Geological and geophysical evaluation of the mechanisms of the Great 1899 Yakutat Bay earthquakes, in *Active tectonics and seismic potential of Alaska*, edited by J. Freymueller, P. Haeussler, R. Wesson, and G. Ekström, Geophysical Monograph Series 179, pp. 215–236, AGU, Washington, DC.
- Plafker, G., R. Kachadorian, E. Eckel, and L. Mayo (1969), Effects of the Earthquake of March 27, 1964 on various communities, U.S. Geological Survey Professional Paper 542-G, 50 pp.
- Plafker, G., S. Nishenko, L. Cluff, and M. Syahril (2006), The cataclysmic 2004 tsunami on NW Sumatra - preliminary evidence for a near-field secondary source along the western Aceh Basin, *Seism. Res. Lett.*, 77, 231.
- Santini, S., M. Dragoni, and G. Spada (2003), Asperity distribution of the 1964 Great Alaska earthquake and its relation to subsequent seismicity in the region, *Tectonophysics*, 367, 219–233, doi:10.1016/S0040-1951(03)00130-6.
- Shennan, I., R. Bruhn, and G. Plafker (2009), Multi-segment earthquakes and tsunami potential of the Aleutian megathrust, *Quaternary Science Reviews*, 28, 7–13.
- Song, Y., L. Fu, V. Zlotnicki, C. Ji, V. Hjorleifsdottir, C. Shum, and Y. Yi (2008), The role of horizontal impulses of the faulting continental slope in generating the 26 December 2004 tsunami, *Ocean Modelling*, 20, 362–379, doi:10.1016/j.ocemod.2007.10.007.

- Spaeth, M., and S. Berkman (1972), Tsunami of March 28, 1964, as recorded at tide stations and the Seismic Sea Waves Warning System, in *The Great Alaska Earthquake of 1964. Oceanography and Coastal Engineering*, pp. 38–100, National Academy of Sciences, Washington, D.C.
- Suito, H., and J. Freymueller (2009), A viscoelastic and afterslip postseismic deformation model for the 1964 Alaska earthquake, *J. Geophys. Res.*, 114(B11404), doi:10.1029/2008JB005954.
- Suleimani, E., R. Hansen, R. Combellick, G. Carver, R. Kamphaus, J. Newman, and A. Venturato (2002), Tsunami hazard maps of the Kodiak area, Alaska, Report of Investigations 2002-1, State of Alaska Department of Natural Resources, Division of Geological and Geophysical Surveys, 16 p., 4 sheets, scale 1:12,500.
- Suleimani, E., R. Hansen, and Z. Kowalik (2003), Inundation modeling of the 1964 tsunami in Kodiak Island, Alaska, in *Submarine Landslides and Tsunamis, NATO Science Series, Series IV: Earth and Environmental Sciences, vol. 21*, edited by A. Yalciner, E. Pelinovsky, E. Okal, and C. Synolakis, pp. 191–201, Kluwer Academic Publishers.
- Suleimani, E., R. Combellick, D. Marriott, R. Hansen, A. Venturato, and J. Newman (2005), Tsunami hazard maps of the Homer and Seldovia areas, Alaska, Report of Investigations 2005-2, State of Alaska Department of Natural Resources, Division of Geological and Geophysical Surveys, 28 p., 2 sheets, scale 1:12,500.
- Suleimani, E., D. Nicolsky, P. Haeussler, and R. Hansen (2010), Combined effects of tectonic and landslide-generated tsunami runup at Seward, Alaska, during the M_w 9.2 1964 earthquake, *Pure Appl. Geophys.*, doi:10.1007/s00024-010-0228-4.
- Synolakis, C. (1986), The Runup of Long Waves, Ph.D. thesis, California Institute of Technology, Pasadena, California, 228 pp.
- Synolakis, C., E. Bernard, V. Titov, U. Kânoğlu, and F. González (2007), Standards, criteria, and procedures for NOAA evaluation of tsunami numerical models, *NOAA Tech. Memo. OAR PMEL-135, NTIS: PB2007-109601*, NOAA/Pacific Marine Environmental Laboratory, Seattle, WA, 55 pp.

- Synolakis, C., E. Bernard, V. Titov, U. Kânoğlu, and F. González (2008), Validation and verification of tsunami numerical models, *Pure Appl. Geophys.*, 165, 2197–2228.
- Tanioka, Y., and K. Satake (1996), Tsunami generation by horizontal displacement of ocean bottom, *Geophys. Res. Lett.*, 23(8), 861–864.
- Titov, V., and C. Synolakis (1995), Modeling of breaking and nonbreaking long-wave evolution and runup using VTCS-2, *Journal of Waterway, Port, Coastal and Ocean Engineering*, 121(6), 308–316.
- Titov, V., and C. Synolakis (1998), Numerical modeling of tidal wave runup, *J. Waterw. Port Coast. Ocean Eng.*, 124, 157–171.
- Tysdal, R., and J. Case (1979), Geologic map of the Seward and Blying Sound quadrangles, Alaska, U.S. Geologic Survey Miscellaneous Investigation 1150, 12 p., 1 sheet, scale 1:250,000.
- Van Dorn, W. (1972), Source mechanism of the major tsunami, in *The Great Alaska Earthquake of 1964. Oceanography and Coastal Engineering*, pp. 111–139, National Academy of Sciences, Washington, D.C.
- Waller, R. (1966), Effects of the Earthquake of March 27, 1964, in the Homer area, Alaska, U.S. Geological Survey Professional Paper 542-D, 28 pp.
- Wilson, B., and A. Tørum (1968), The tsunami of the Alaskan Earthquake, 1964: Engineering evaluation, U.S. Army Corps of Engineers, Technical memorandum No. 25, 401 p.
- Zhang, Y., and A. Baptista (2008), An efficient and robust tsunami model on unstructured grids. Part I: Inundation benchmarks, *Pure Appl. Geophys.*, 165, 2229–2248.
- Zweck, C., J. Freymueller, and S. Cohen (2002), Three-dimensional elastic dislocation modeling of the postseismic response to the 1964 Alaska earthquake, *J. Geophys. Res.*, 107(B4), 1–12.

Table 5.1: Compilation of tsunami observations collected after the 1964 earthquake in the Gulf of Alaska. The locations listed in the table are shown in Figures 5.3 and 5.4.

No.	Location	Arrival (min)	First motion	Crest height (m)	Runup (m)	Source of data
Kenai Peninsula						
1	Rocky Bay	30 (?)	down	about 2.7 m	6	<i>Plafker et al. (1969)</i>
2	Seward	35	up	6-8 m	9.5	<i>Wilson and Tørum (1968); Lemke (1967)</i>
3	Whidbey Bay	19.5 ± 0.5	up		10.5	<i>Plafker et al. (1969)</i>
4	Puget Bay	20 ± 2	up		8.5	<i>Plafker et al. (1969)</i>
Kodiak Island						
5	Kaguyak	20	up	4.6	5	<i>Wilson and Tørum (1968); Plafker and Kachadoorian (1966)</i>
6	Old Harbor	48	up		3.7	<i>Plafker and Kachadoorian (1966)</i>
7	Cape Chiniak	38	up	9		<i>Plafker and Kachadoorian (1966)</i>
8	Kalsin Bay	70			4.6	<i>Plafker and Kachadoorian (1966)</i>
9	Kodiak Naval Station	63	up	3.5		<i>Kachadoorian and Plafker (1969)</i>
10	Kodiak City	45(?)	up	6	8	<i>Wilson and Tørum (1968); Kachadoorian and Plafker (1969)</i>

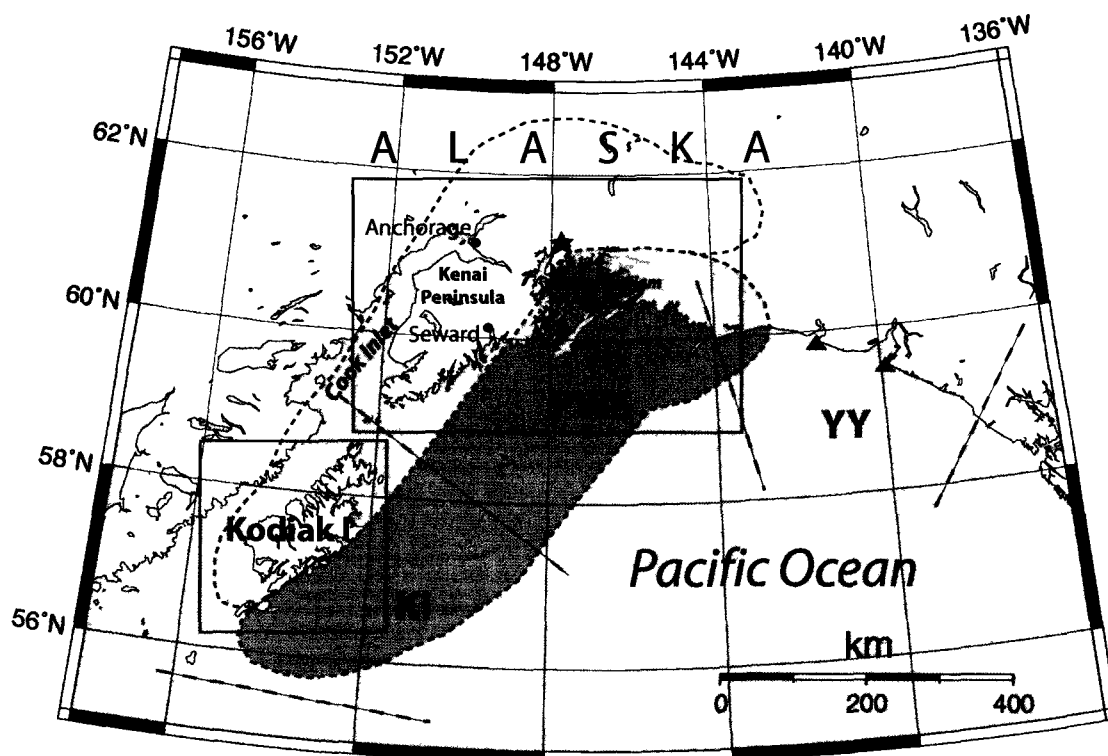


Figure 5.1: Map of south-central Alaska with the rupture zone of the $M_w 9.2$ 1964 Great Alaska earthquake. The star indicates the earthquake epicenter. The dashed contour delineates regions of coseismic uplift (shaded) and subsidence of the 1964 rupture area (Plafker, 1969). The rectangles outline the Prince William Sound and Kenai Peninsula areas, shown in detail in Figure 5.3, and the Kodiak Island area shown in Figure 5.4. Triangles indicate epicenters of two earthquakes of September 1899. Notations: KI - Kodiak Island, PWS - Prince William Sound, and YY - Yakutat-Yakutat segments.

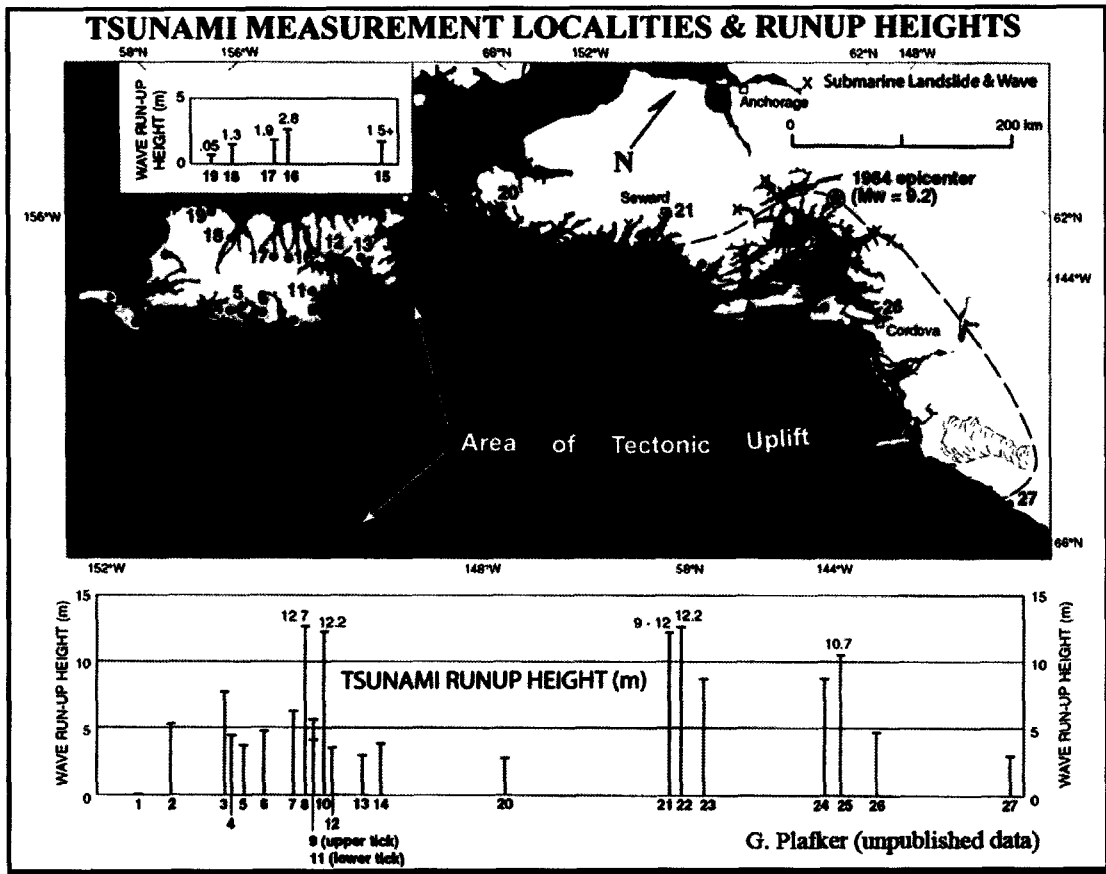


Figure 5.2: Tsunamigram that shows observed runup heights of the 1964 tsunami along the Kenai Peninsula coast and the Kodiak Island coast (from G. Plafker, personal communication).

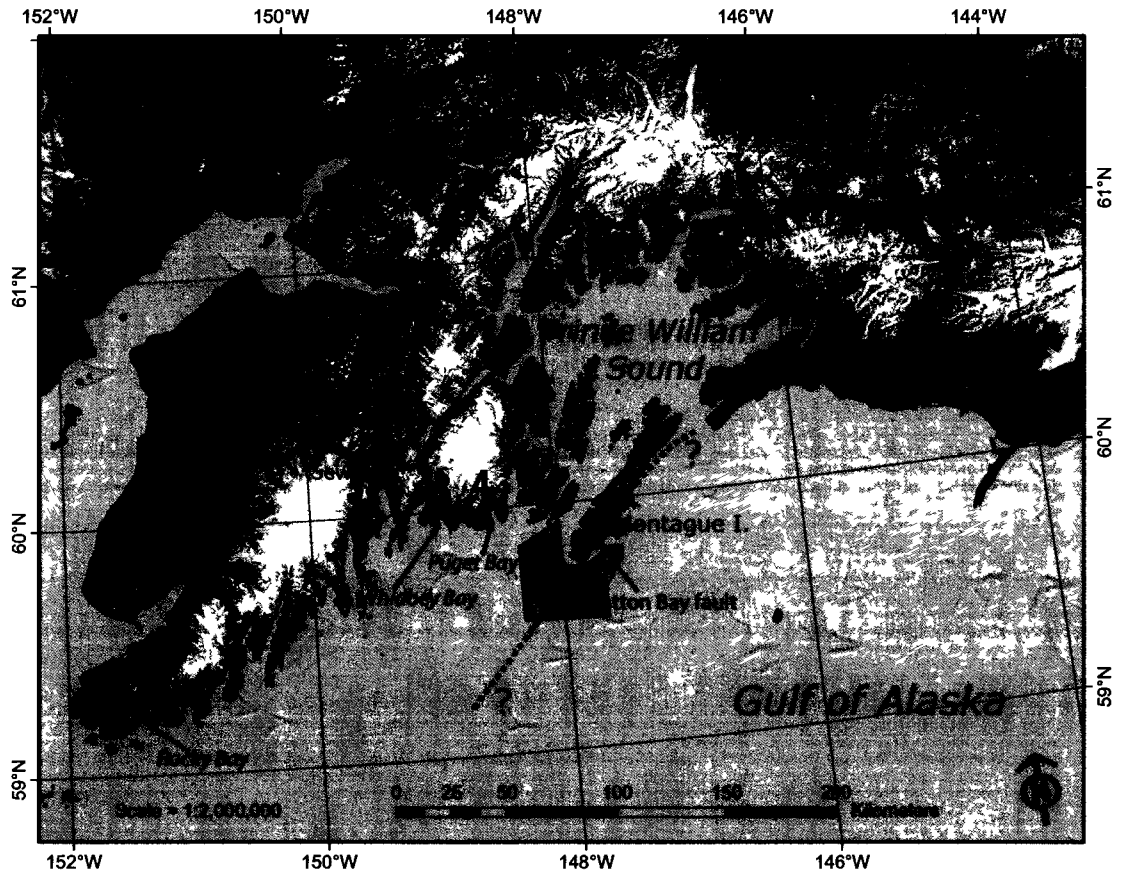


Figure 5.3: The Kenai Peninsula and Prince William Sound areas. The Patton Bay fault is shown by solid, dashed and dotted lines where it is mapped, approximated and inferred, respectively. The gray shaded polygon southwest of Montague Island outlines the area of the 1965 marine geophysical survey performed by ship "Surveyor" (*Malloy and Merrill, 1972*). Numbers indicate locations of time series points listed in Table 5.1.

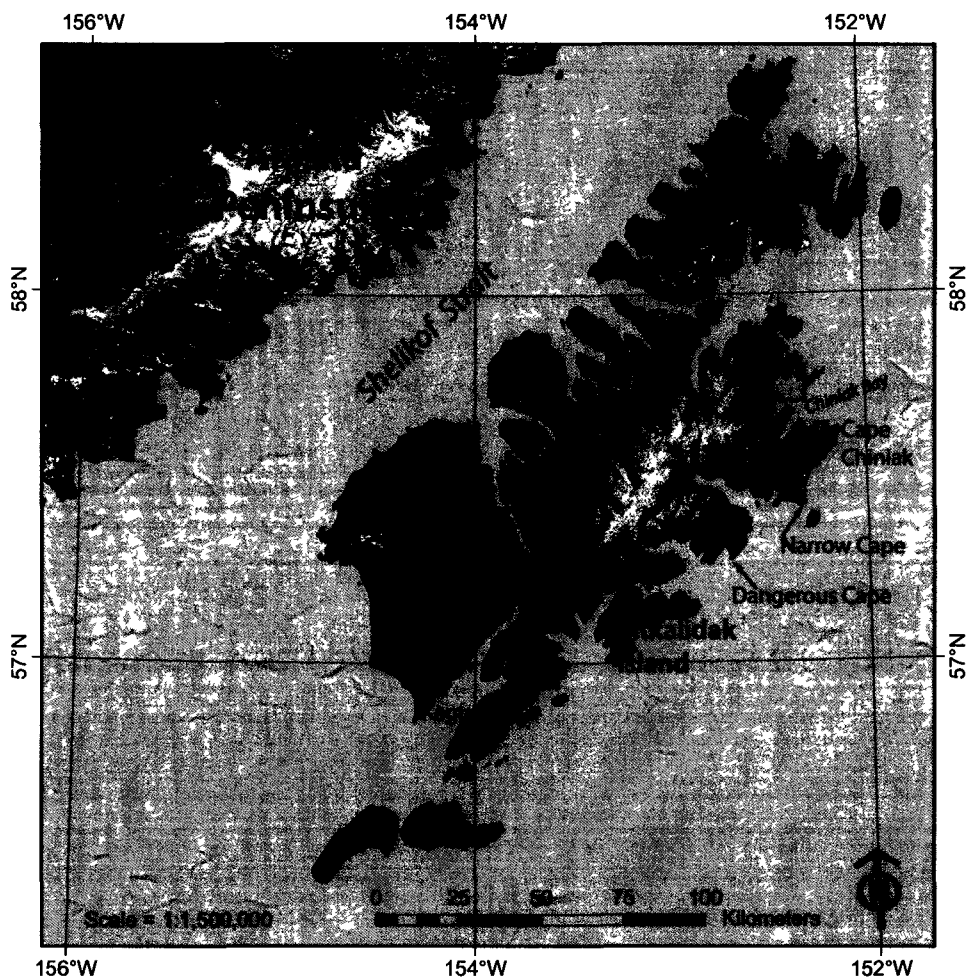


Figure 5.4: The Kodiak Island area. Numbers indicate locations of time series points listed in Table 5.1. The red triangle next to Kalsin Bay shows the location of the USGS streamflow gauge that recorded tsunami waves. The area outlined by the black rectangle that contains points 9 and 10 is shown in Figure 5.5.

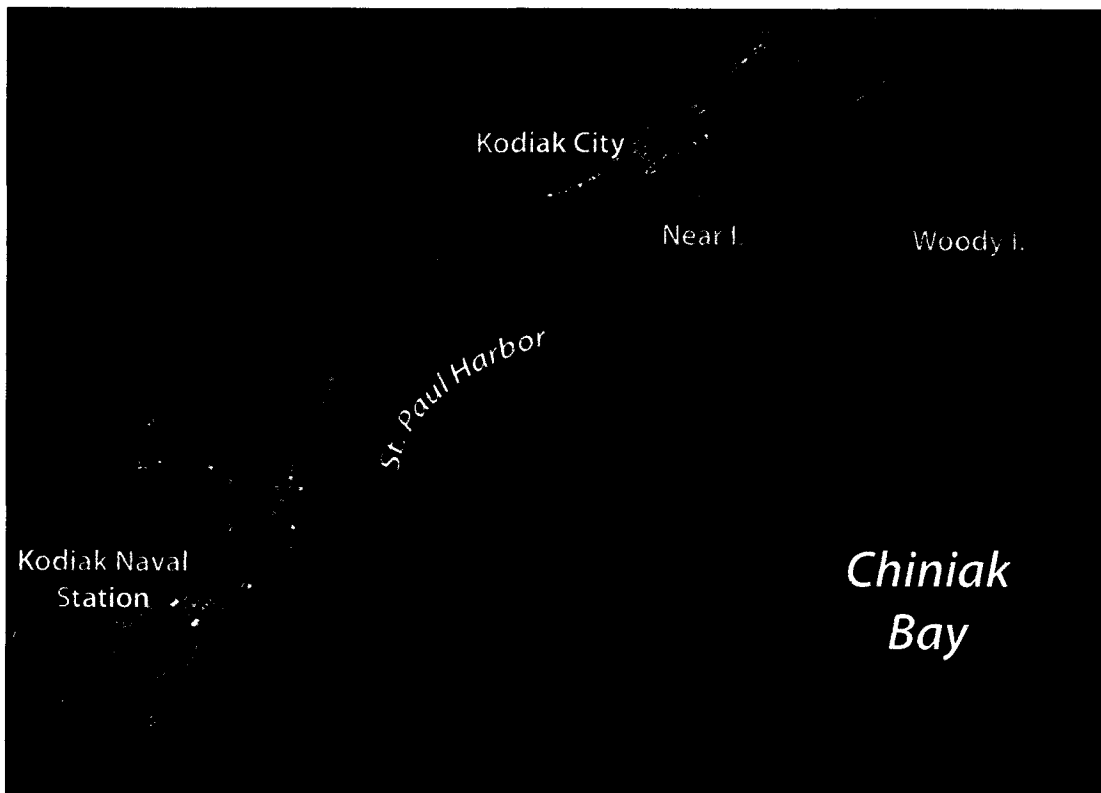


Figure 5.5: Kodiak City and Kodiak Naval Station in the St. Paul Harbor. Arrows indicate major directions from which the 1964 tsunami waves entered the harbor.

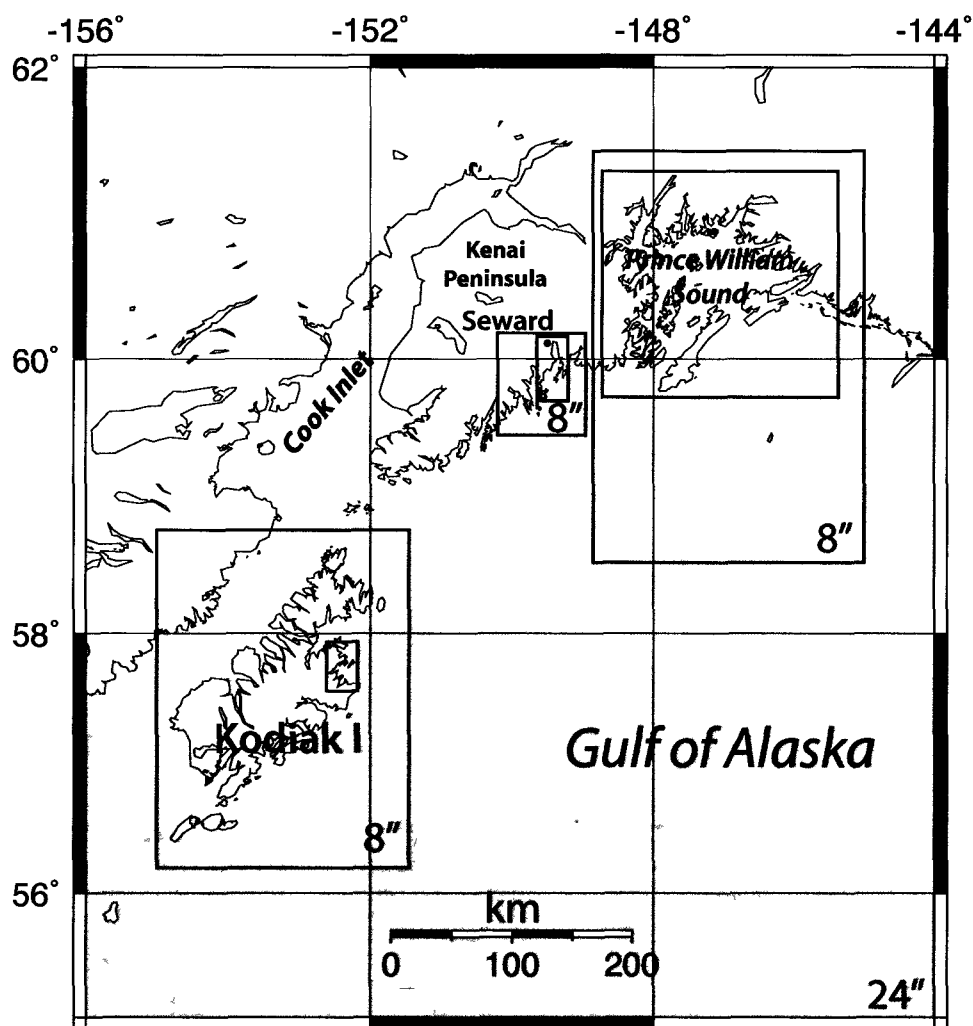


Figure 5.6: Embedded numerical grids of increasing resolution. The map area is covered by a grid with the resolution of 24 arc-seconds, which includes 3 grids of resolution of 8 arc-seconds around Kodiak Island, Prince William Sound, and Resurrection Bay, where Seward is located. Each of the 8-arc-second grids includes a 3-arc-second grid.

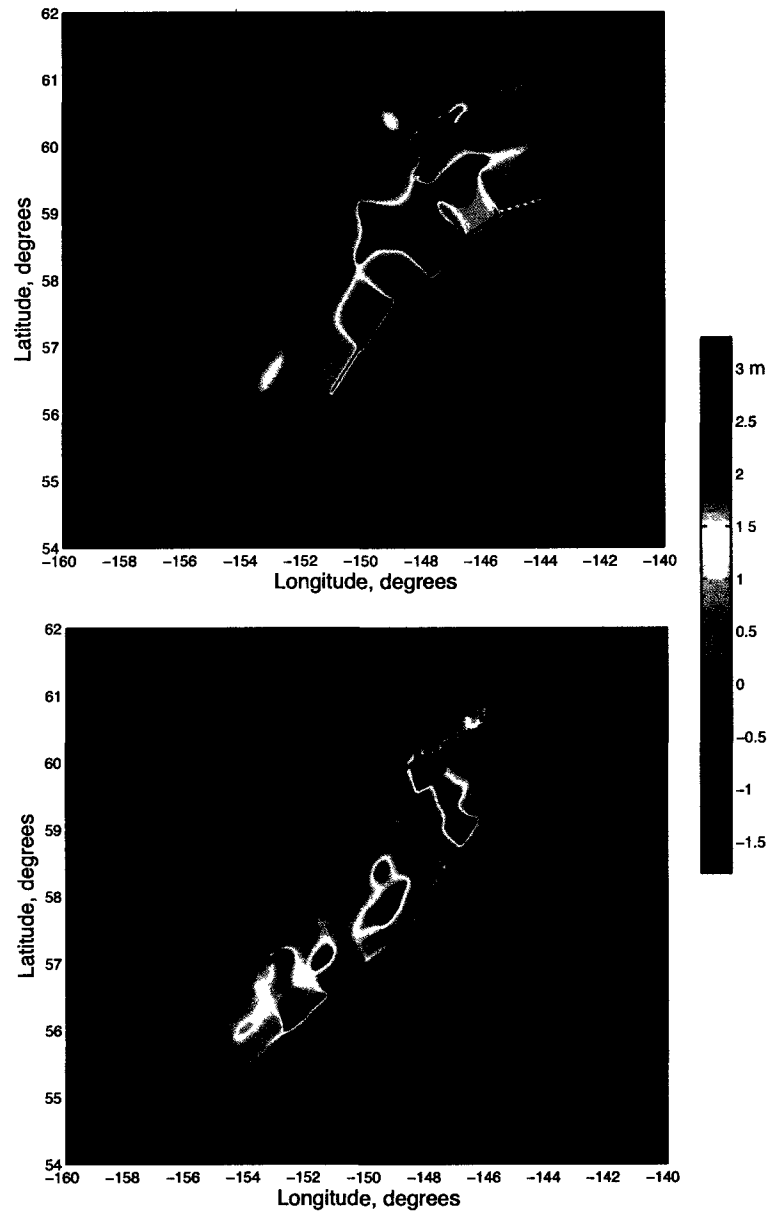


Figure 5.7: Vertical coseismic displacements in the 1964 rupture area based on the slip model by *Johnson et al. (1996)* (top) and *Ichinose et al. (2007)* (bottom).

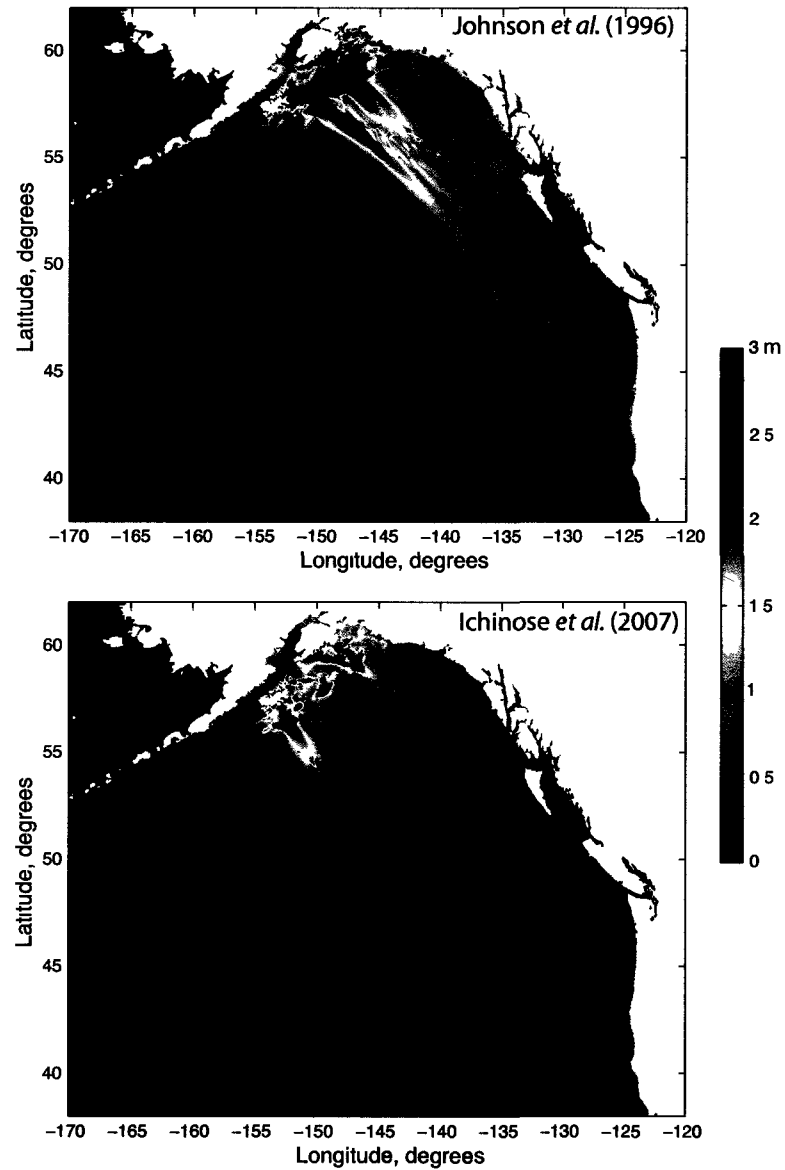


Figure 5.8: Maximum tsunami amplitudes along the West Coast of the United States and Canada calculated using deformation models by *Johnson et al. (1996)* (top) and *Ichinose et al. (2007)* (bottom).

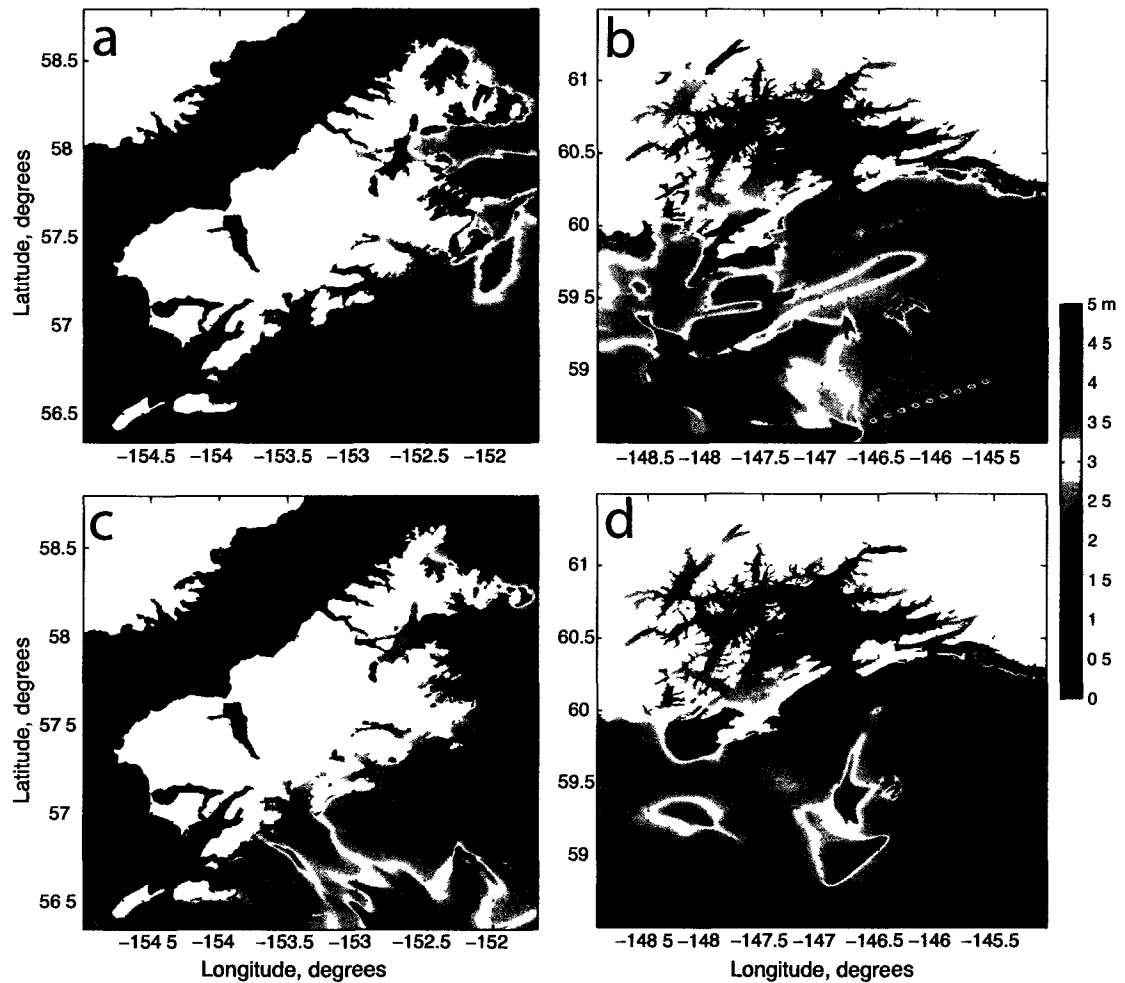


Figure 5.9: Maximum tsunami amplitudes in the Kodiak area (plots in the left column) and in the Prince William Sound area (plots in the right column), calculated using deformation models by *Johnson et al.* (1996) (a,b) and *Ichinose et al.* (2007) (c,d).

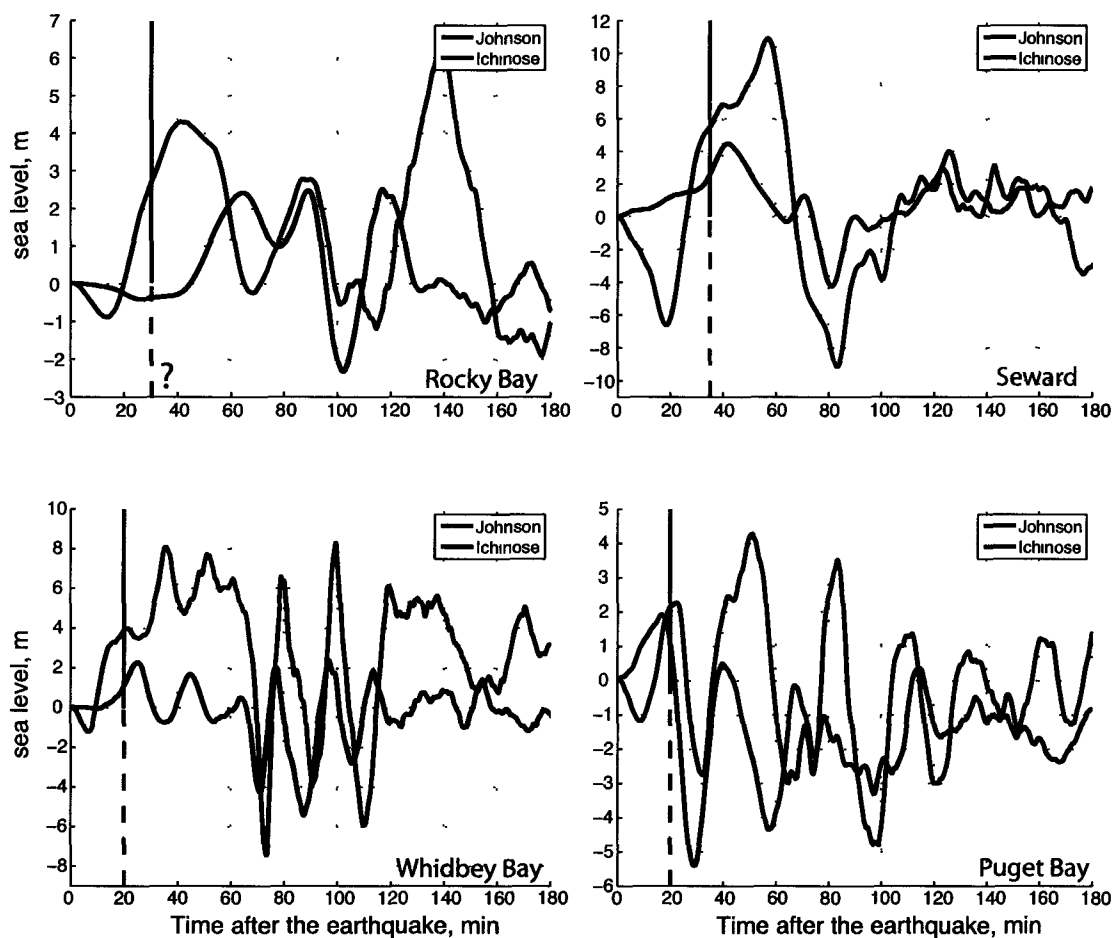


Figure 5.10: Time series at points 1-4 on Kenai Peninsula calculated using the source functions by *Johnson et al.* (1996) and *Ichinose et al.* (2007). The black line on each plot indicates the observed arrival time at this location (see Table 5.1). Where the polarity of the first arrival is known, the solid line above zero corresponds to the positive first arrival, and the solid line below zero corresponds to the negative first arrival.

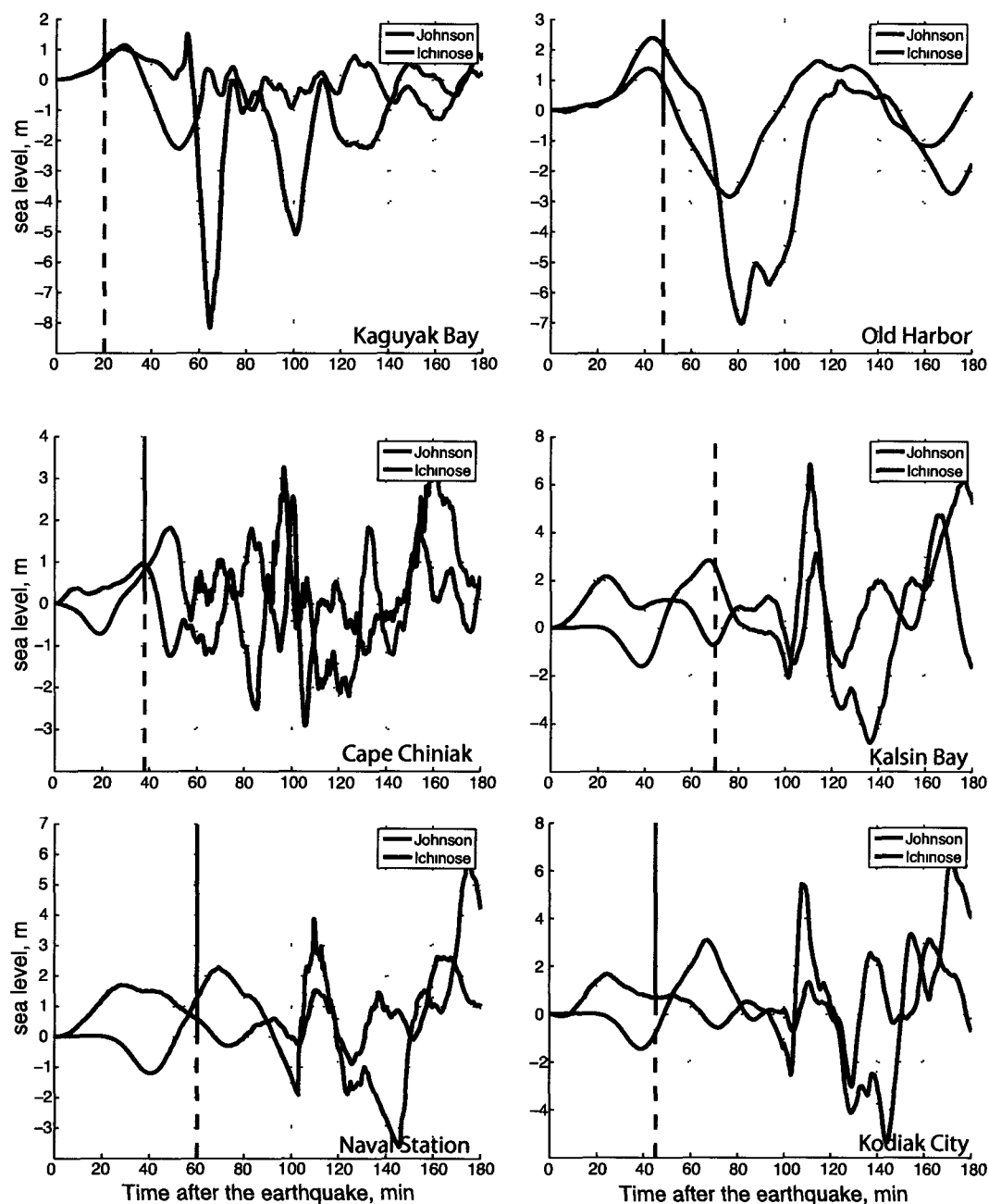


Figure 5.11: Time series at points 6-10 on Kodiak Island calculated using the source functions by *Johnson et al.* (1996) and *Ichinose et al.* (2007). The black line on each plot indicates the observed arrival time at this location (see Table 5.1). Where the polarity of the first arrival is known, the solid line above zero corresponds to the positive first arrival, and the solid line below zero corresponds to the negative first arrival.

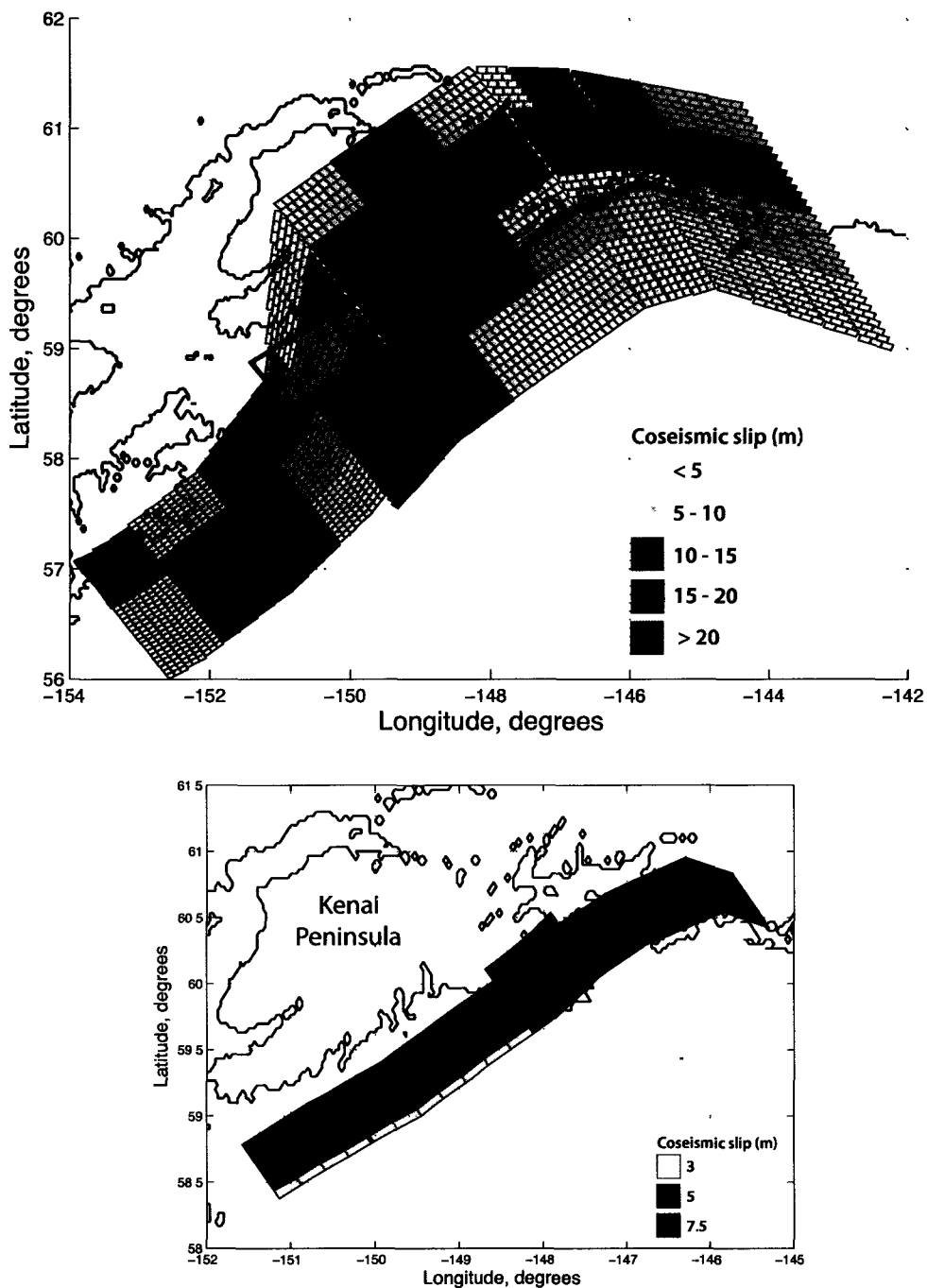


Figure 5.12: Estimated coseismic slip distribution (modified from *Suito and Freymueller (2009)*). The shaded polygon in the upper plot delineates the splay fault area, shown in detail in the bottom plot, and the black solid line indicates the length of the fault in our preferred model.

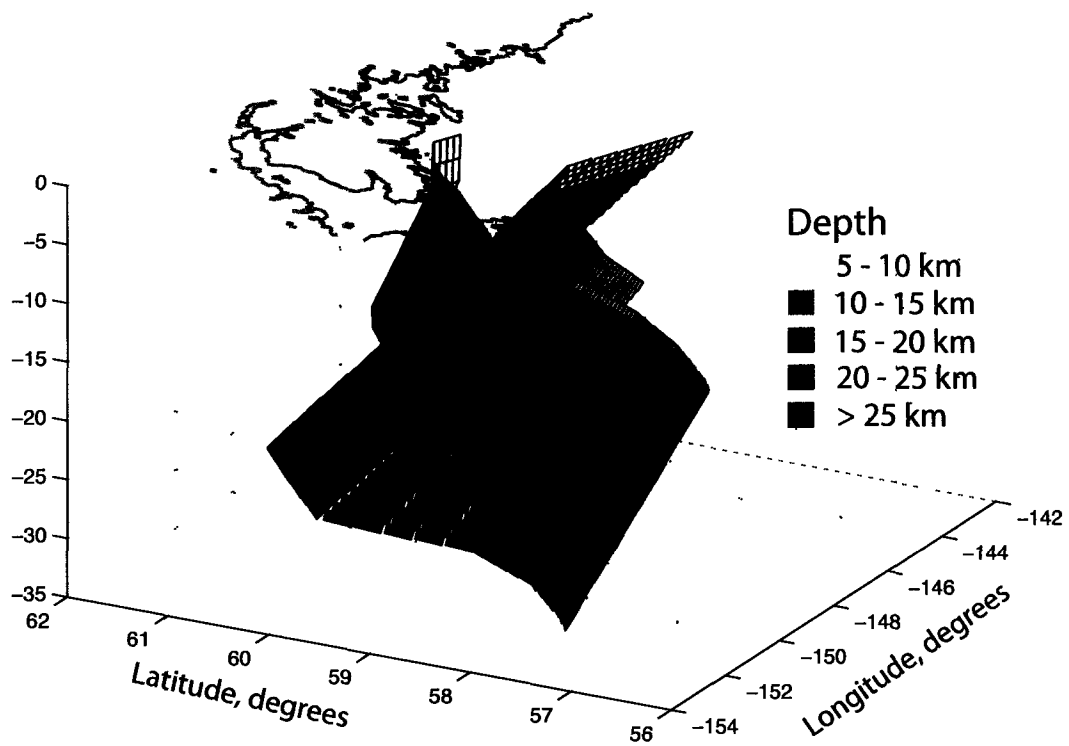


Figure 5.13: Discretization of finite elements of the slip model by *Suito and Freymueller (2009)* using the rectangular Okada-type subfault elements. Combined discretized models are shown for the geometry of megathrust and the splay fault.

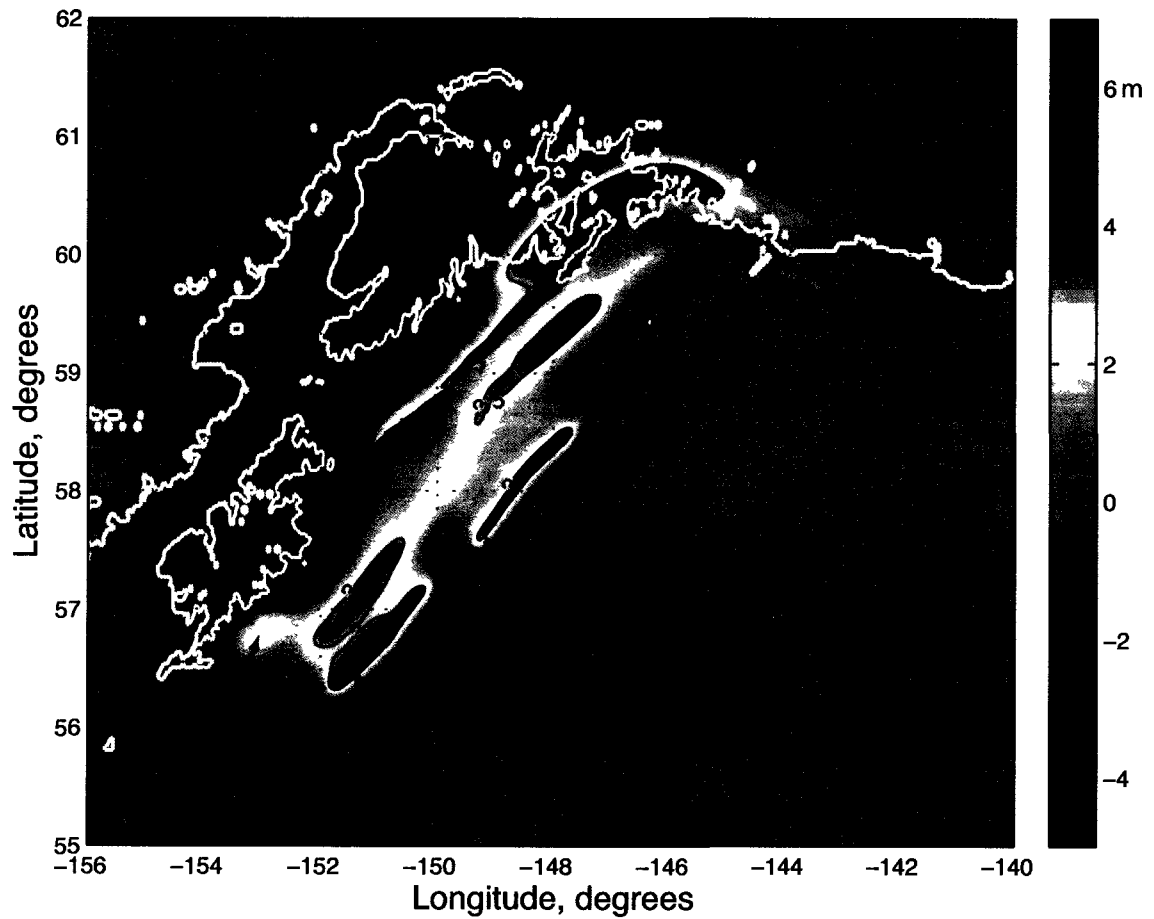


Figure 5.14: Calculated vertical deformations in the 1964 rupture area corresponding to the coseismic slip model of *Suito and Freymueller (2009)* presented in Figures 5.12 and 5.13. Letters "A" and "B" indicate areas of higher slip offshore the southern tip of Kodiak Island (see text for reference).

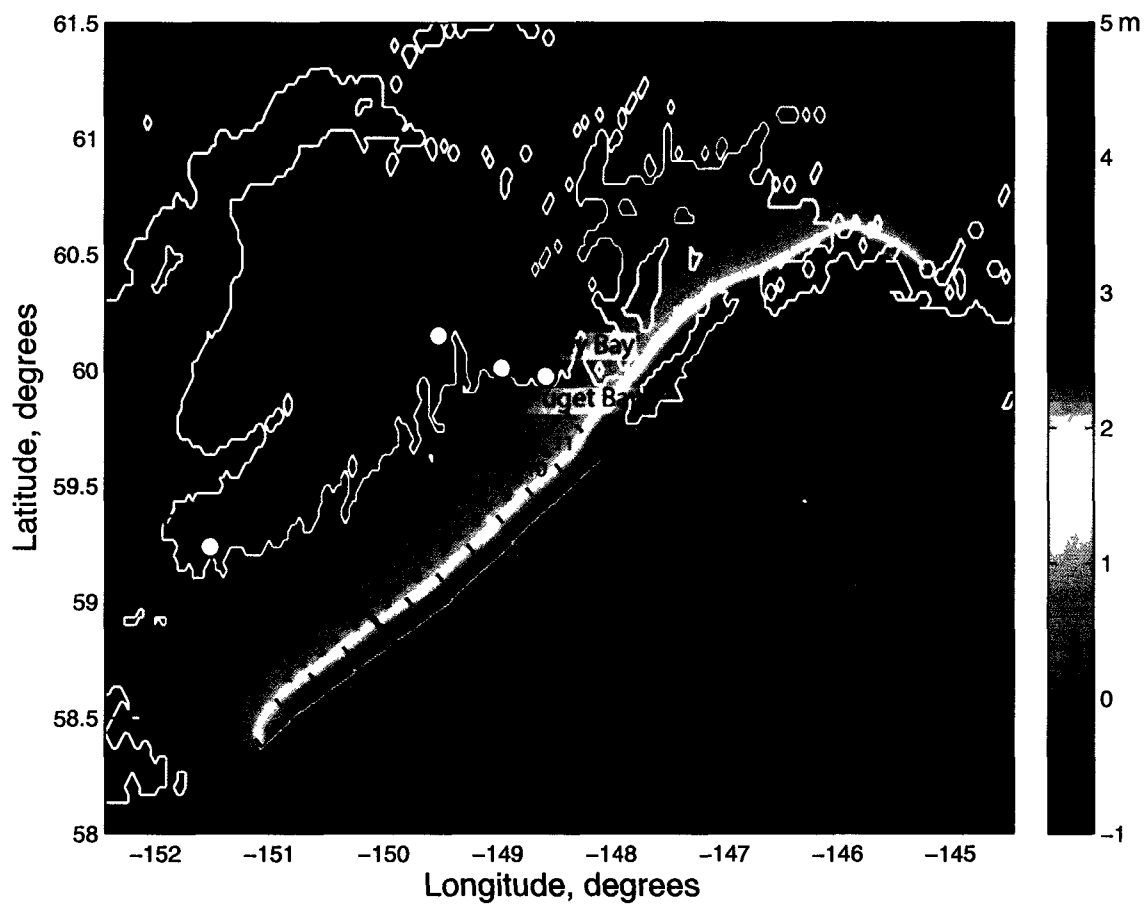


Figure 5.15: Calculated vertical coseismic deformations due to displacements on the splay fault. The proposed extension of the splay fault is divided into 11 segments for the numerical experiment in order to determine the credible extent of the fault based on observation of tsunami arrivals at several locations along the Kenai Peninsula coast. The solid line indicates the length of the fault in our preferred model.

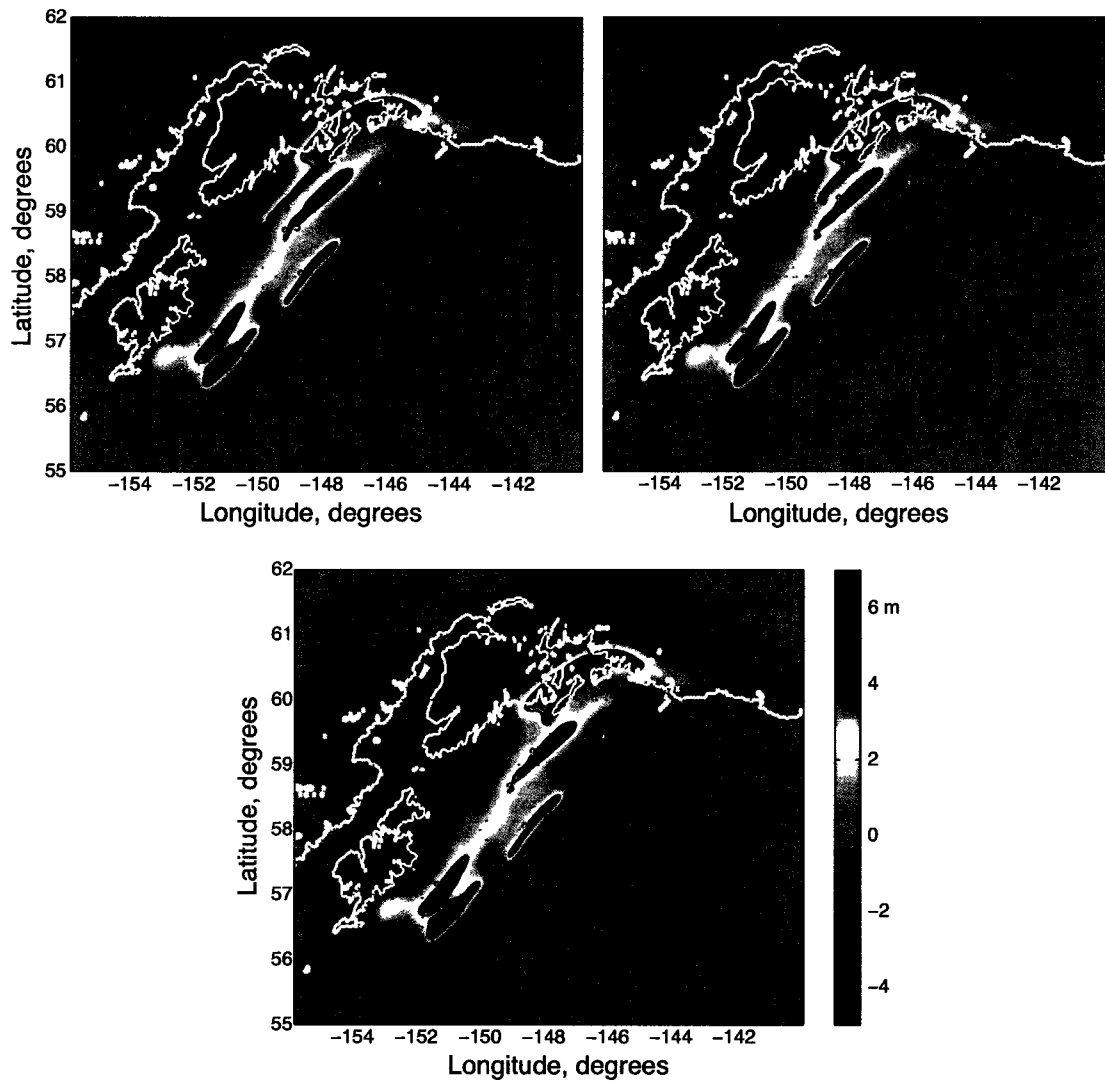


Figure 5.16: Calculated vertical coseismic deformations in the 1964 rupture area corresponding to different extents of the splay fault illustrated in Figure 5.15: a - first 4 segments removed, b - first 7 segments removed, c - all 11 segments removed (the mapped extent of the fault).

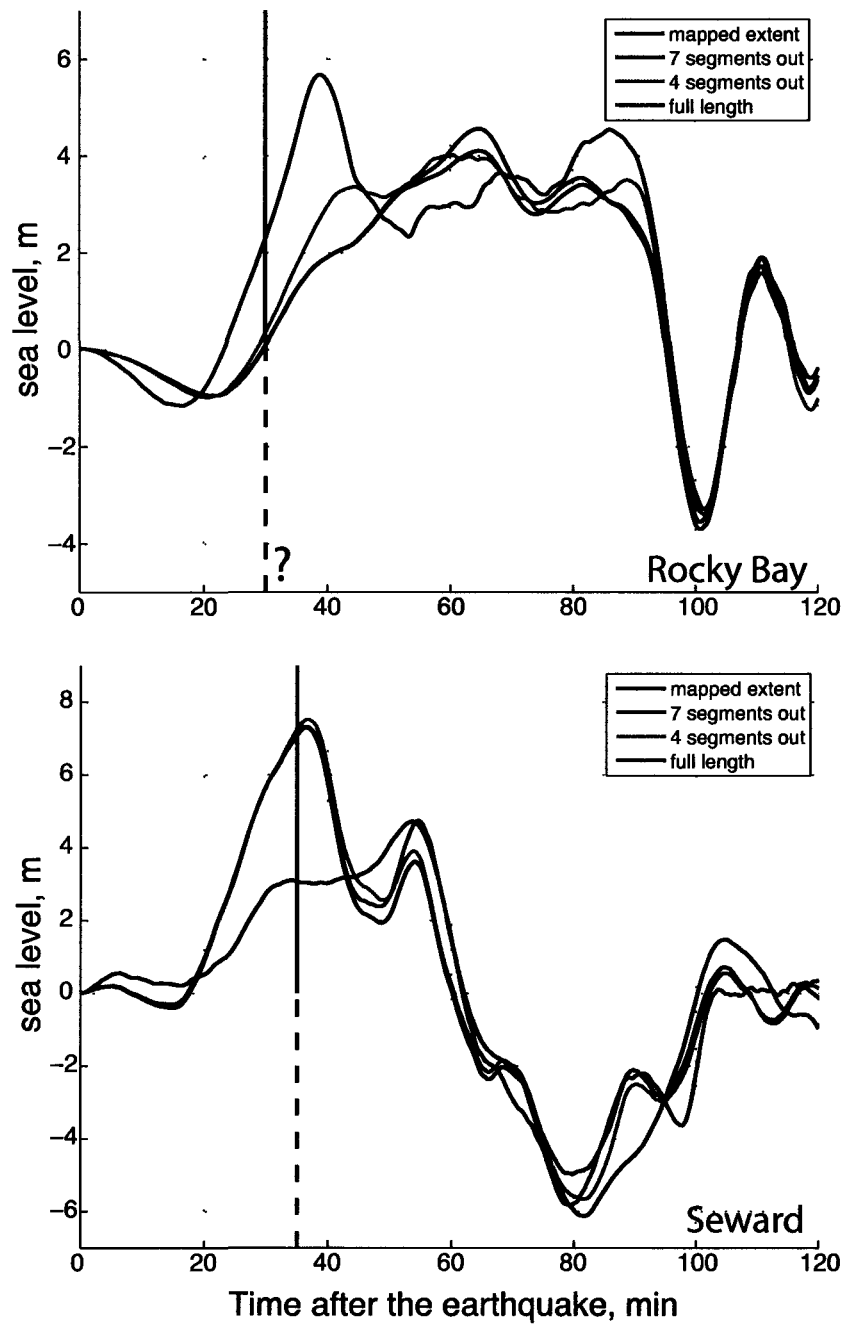


Figure 5.17: Simulated time series of tsunami waves at Rocky Bay and Seward for 4 different source functions of the splay fault. The black line on each plot indicates the observed arrival time at this location (see Table 5.1). The question mark in the upper plot indicates that the observation of arrival time is uncertain.

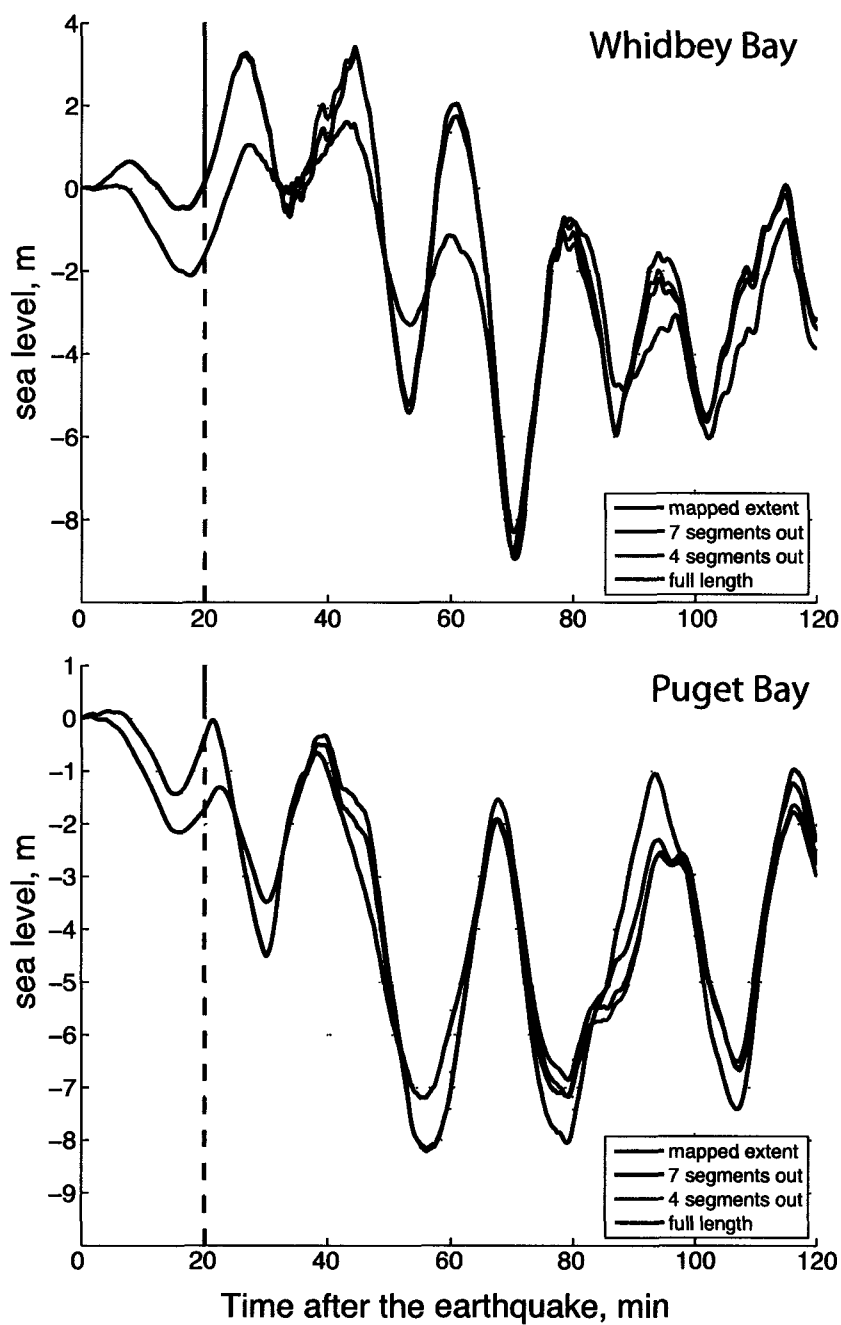


Figure 5.18: Simulated time series of tsunami waves at Whidbey Bay and Puget Bay for 4 different source functions of the splay fault. The black line on each plot indicates the observed arrival time at this location (see Table 5.1).

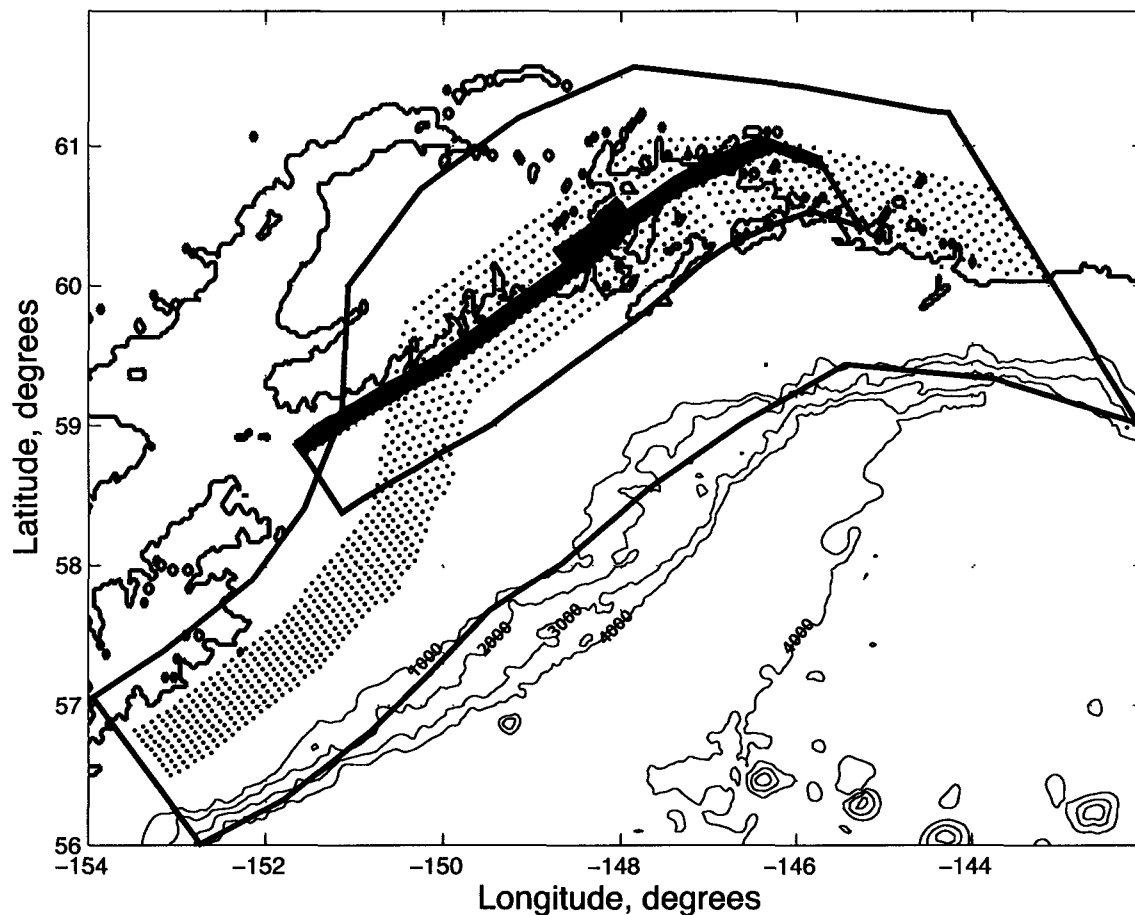


Figure 5.19: The location of the splay fault (blue polygon) with respect to the rupture on the megathrust (red polygon) in the coseismic model. The red dots indicate locations of the megathrust subfault elements that are between 18 and 25 km deep in the model. The blue shaded area inside the splay fault polygon are the elements located within the same depth band. The bathymetry contours show the steepest part of the ocean slope between 1000 and 4000 meters deep.

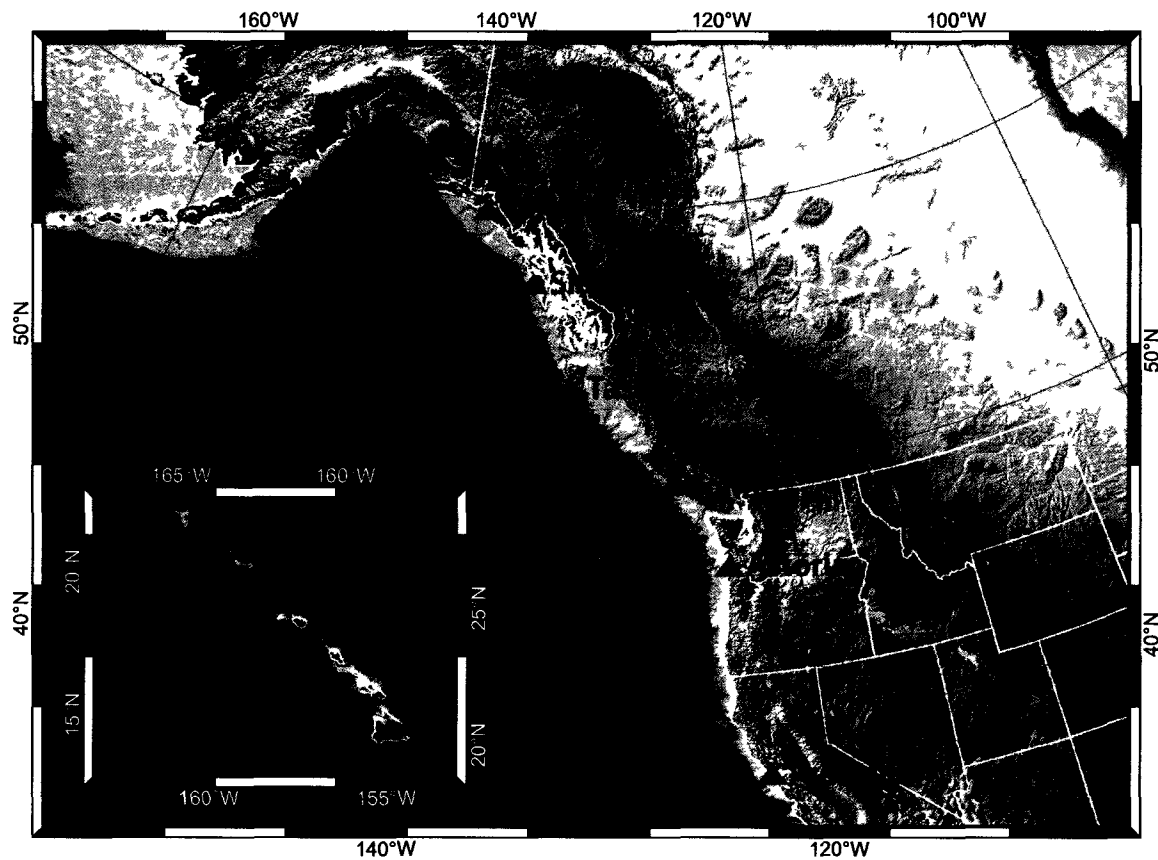


Figure 5.20: Time series points in the far field, along the West Coast of the United States and Canada. The dashed contours approximately delineate regions of coseismic uplift (pink) and subsidence (grey) of the 1964 rupture area.

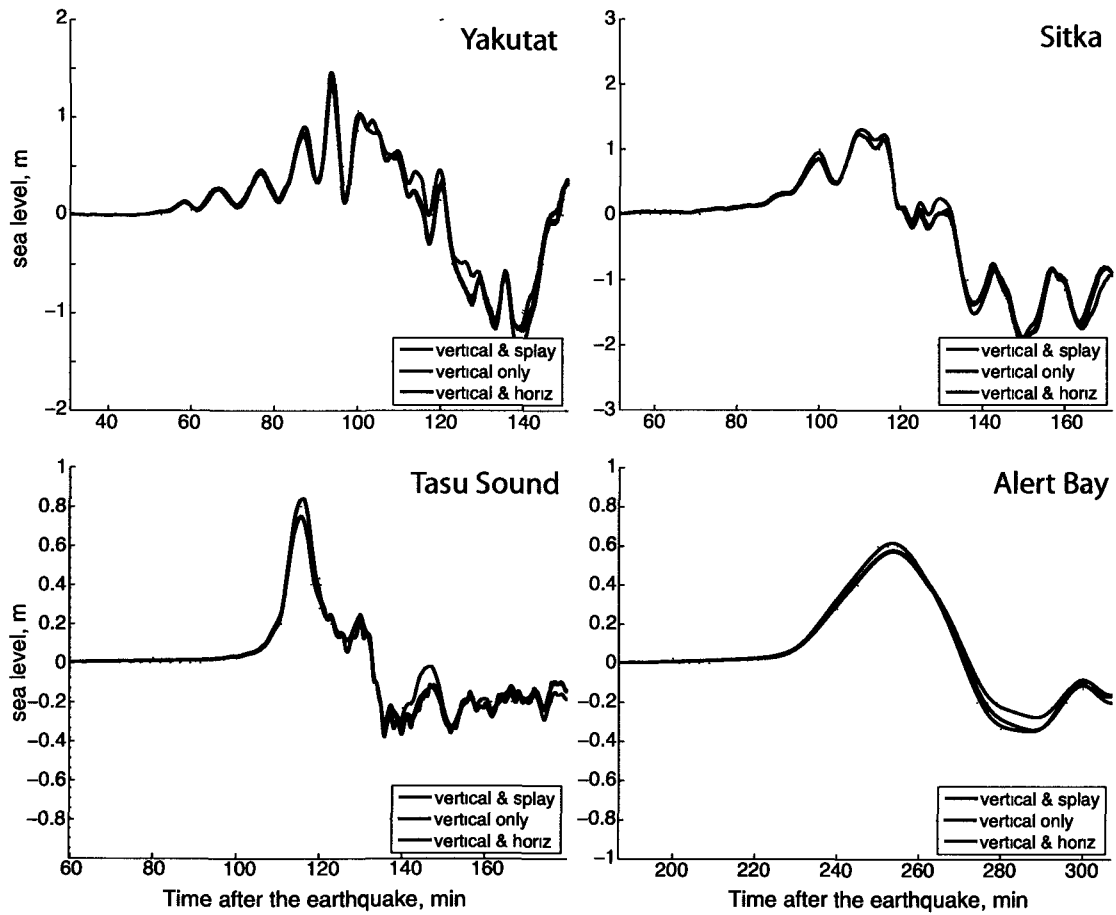


Figure 5.21: Simulated time series of tsunami waves in the far field at Yakutat, Sitka, Tasu Sound and Alert Bay for 3 different source functions.

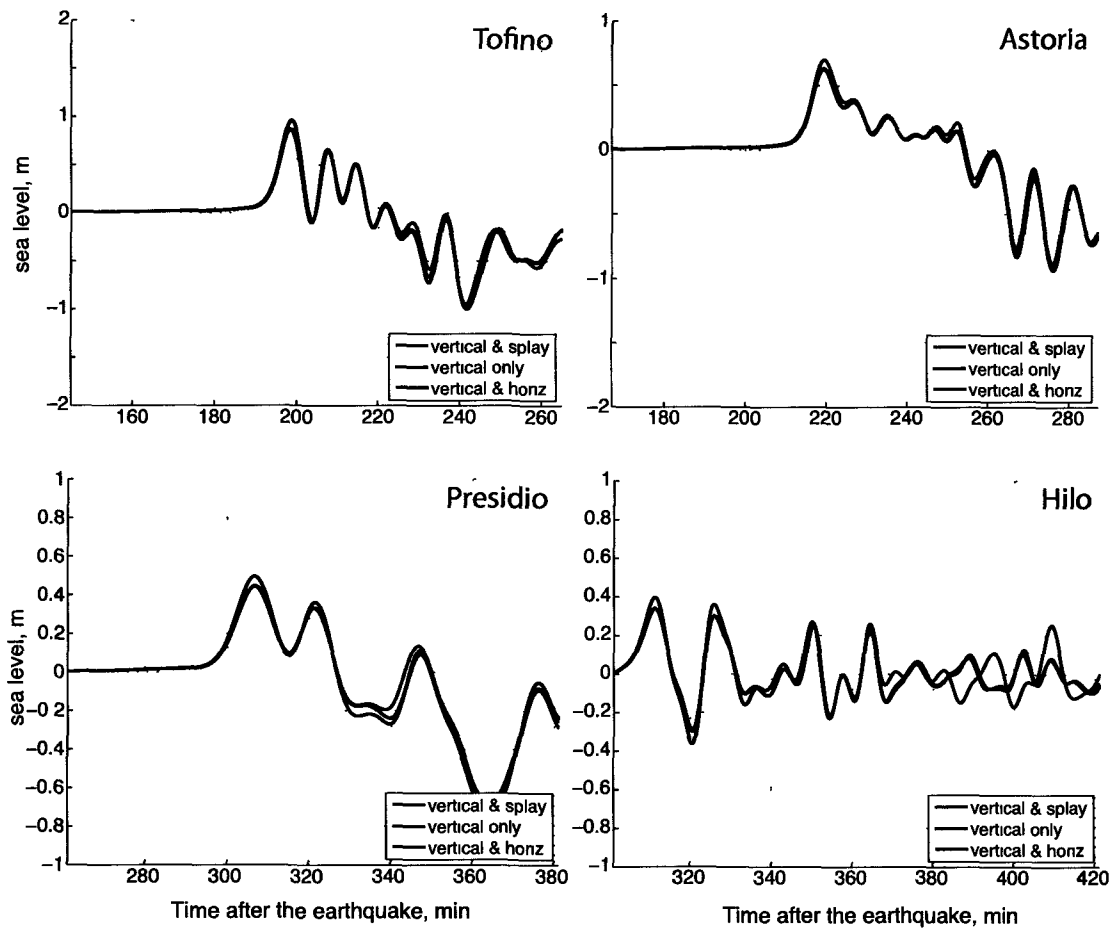


Figure 5.22: Simulated time series of tsunami waves in the far field at Tofino, Astoria, Presidio and Hilo for 3 different source functions.

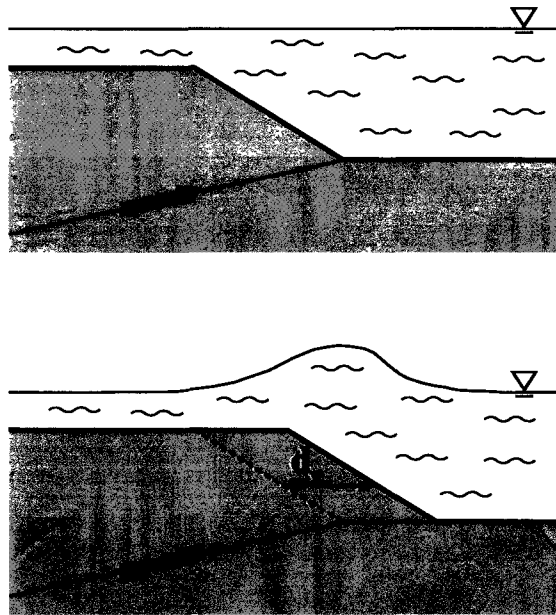


Figure 5.23: The diagram shows mechanism of tsunami generation by horizontal motion of the ocean bottom, where d_x is the horizontal displacement due to faulting (modified from *Tanioka and Satake (1996)*).

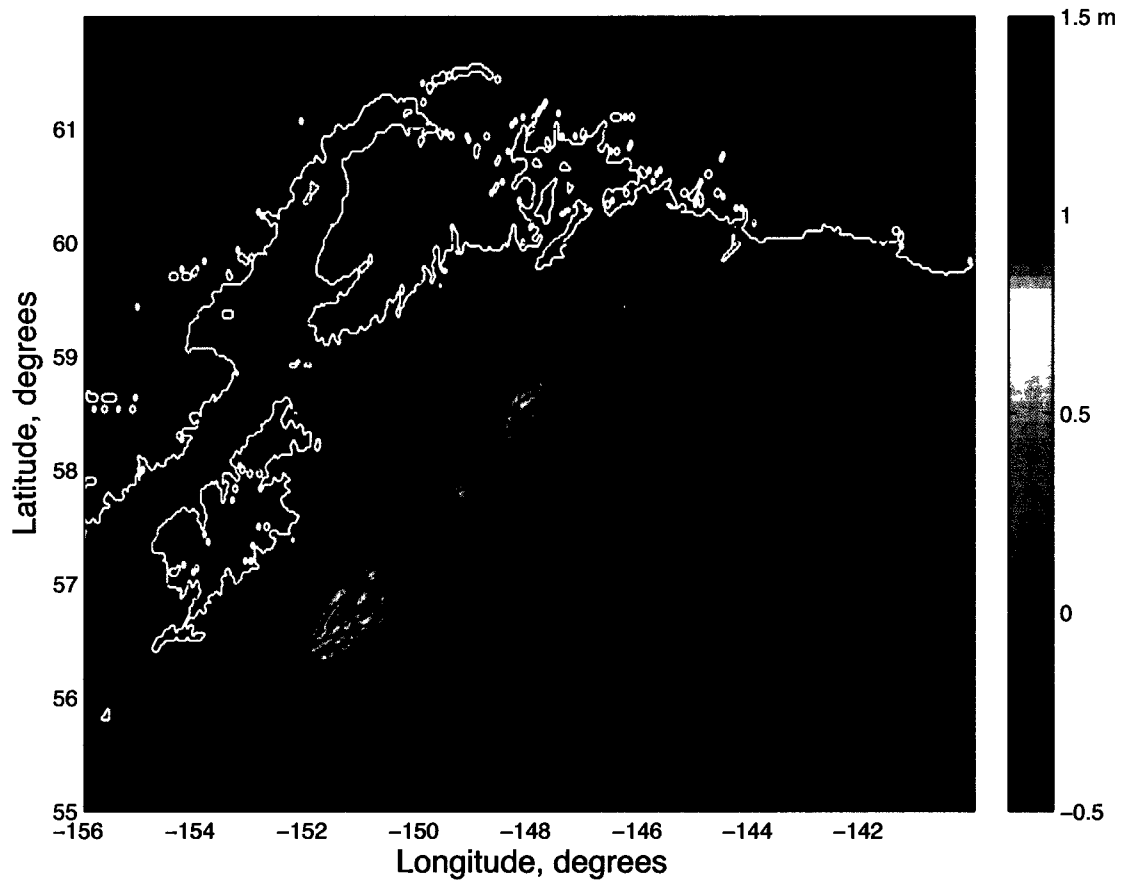


Figure 5.24: Calculated sea surface displacement due to horizontal motion of the sea floor during the 1964 earthquake. The white contour corresponds to the coastline, and the black lines are bathymetry contours that indicate the steepest part of the trench between 1000 and 4000 meters deep.

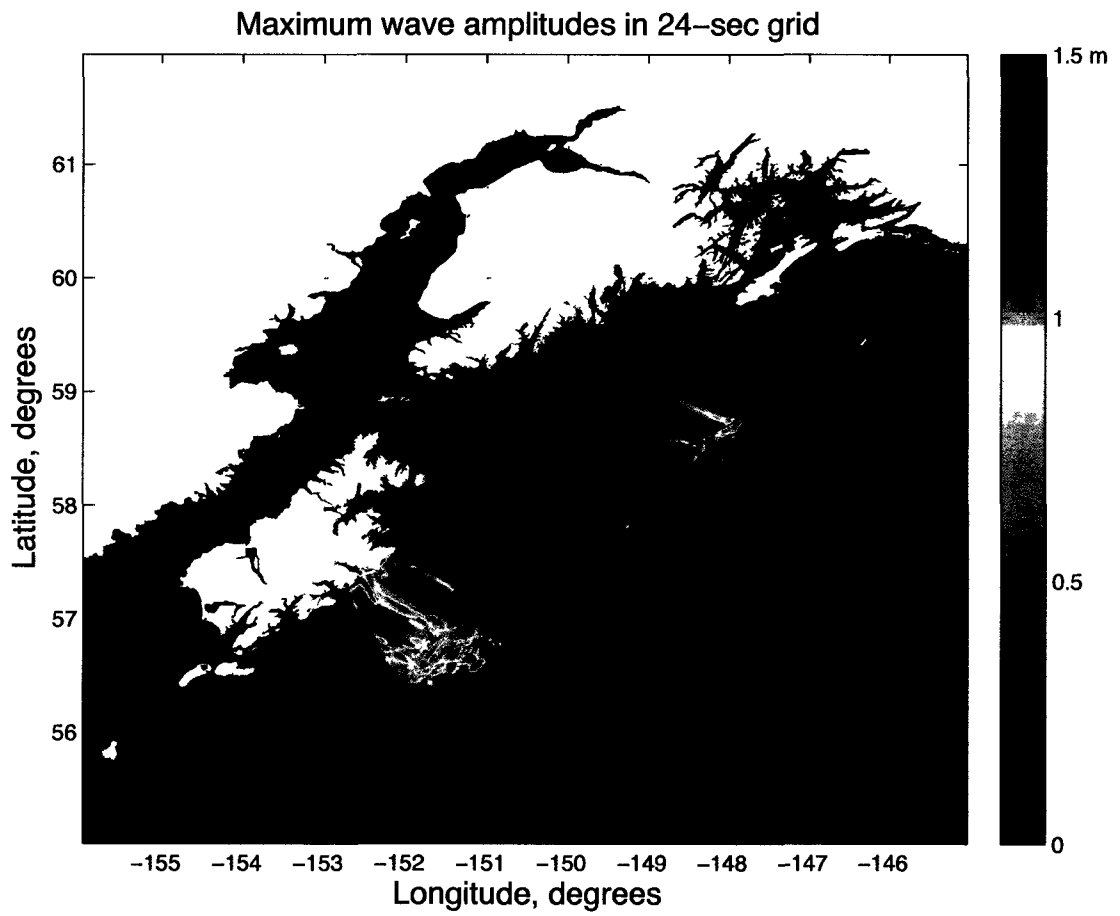


Figure 5.25: Maximum tsunami amplitudes due to horizontal deformations of the ocean bottom.

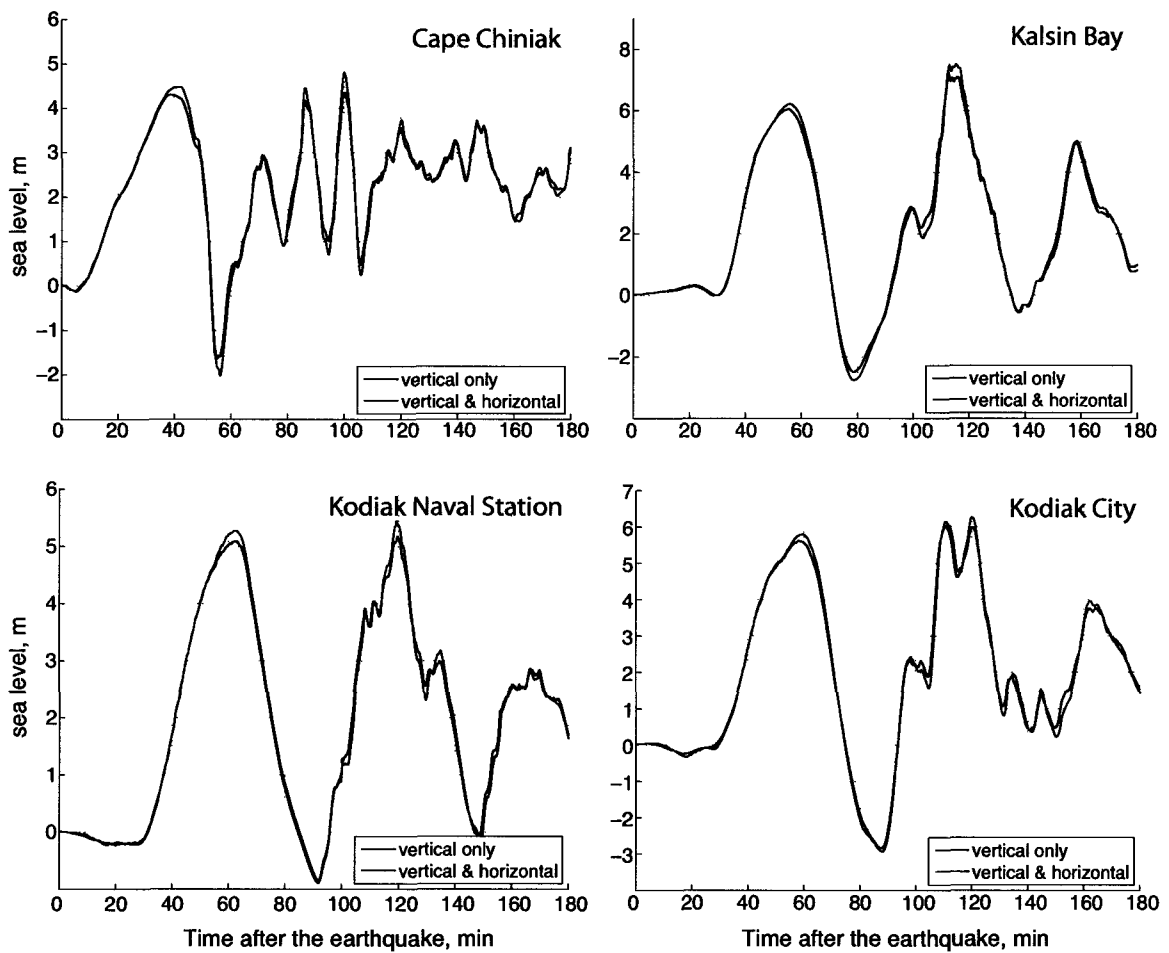


Figure 5.26: Simulated time series of tsunami waves generated by vertical motion of the bottom (black line) and by the combined vertical and horizontal motion (red line).

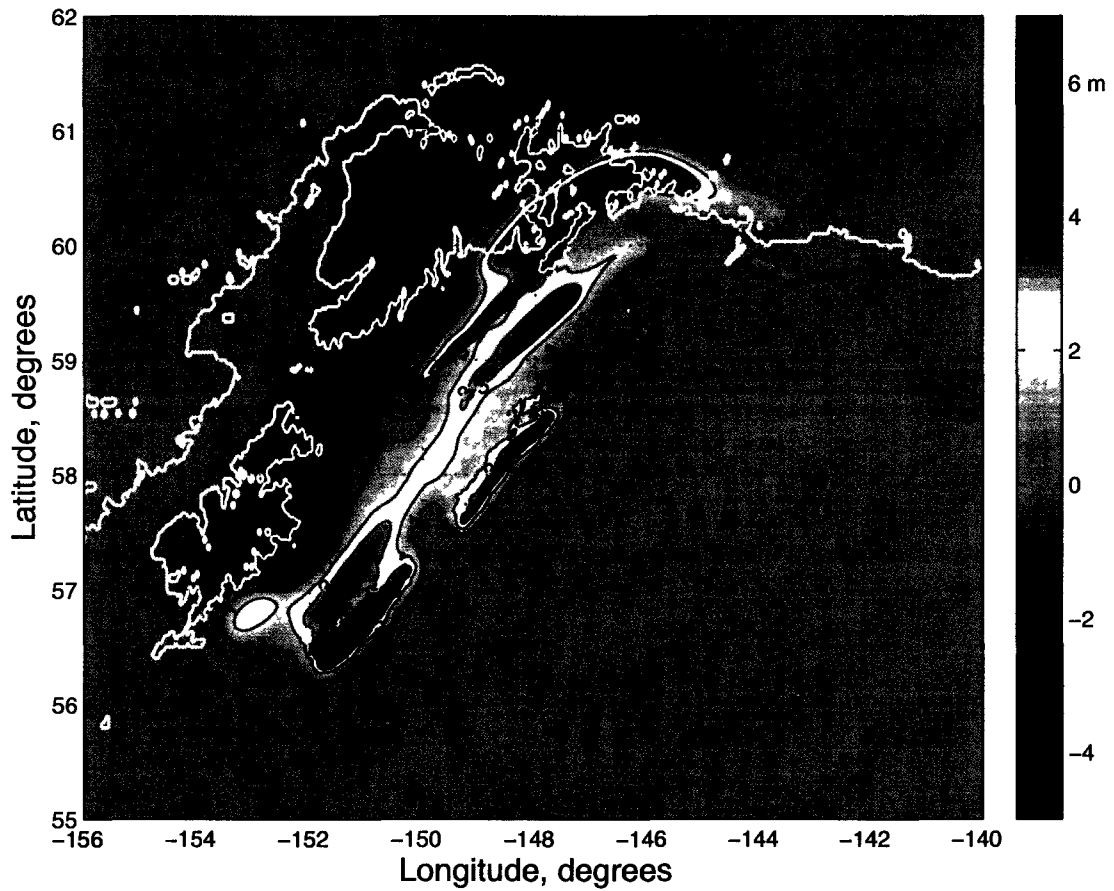


Figure 5.27: The resulting vertical coseismic deformations in the 1964 rupture area, derived from the superposition of vertical and horizontal displacements of the mega-thrust and the vertical displacements on the splay fault of the optimal extent.

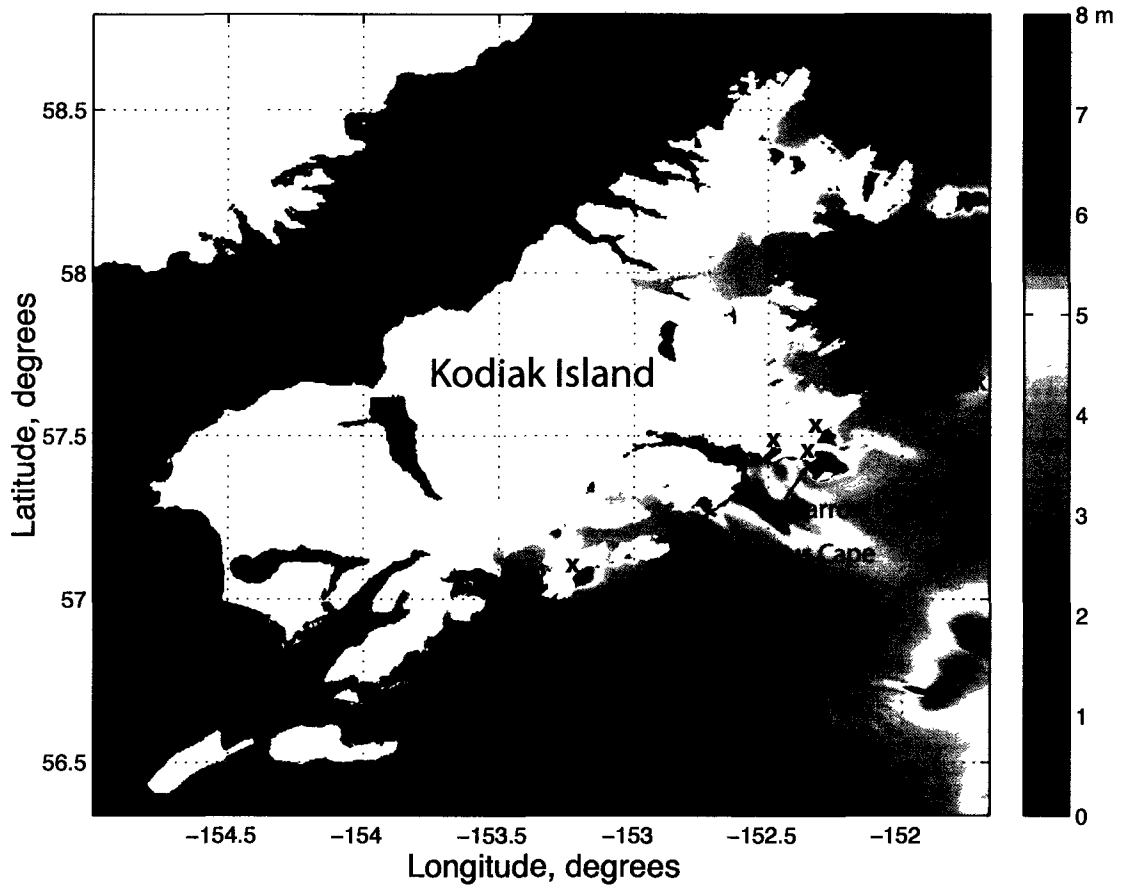


Figure 5.28: Simulated maximum tsunami amplitudes in the 8-arcsecond grid of Kodiak Island. The initial conditions correspond to the deformation model shown in Figure 5.27. Black crosses indicate localities of the highest measured runup (*Plafker and Kachadoorian, 1966*).

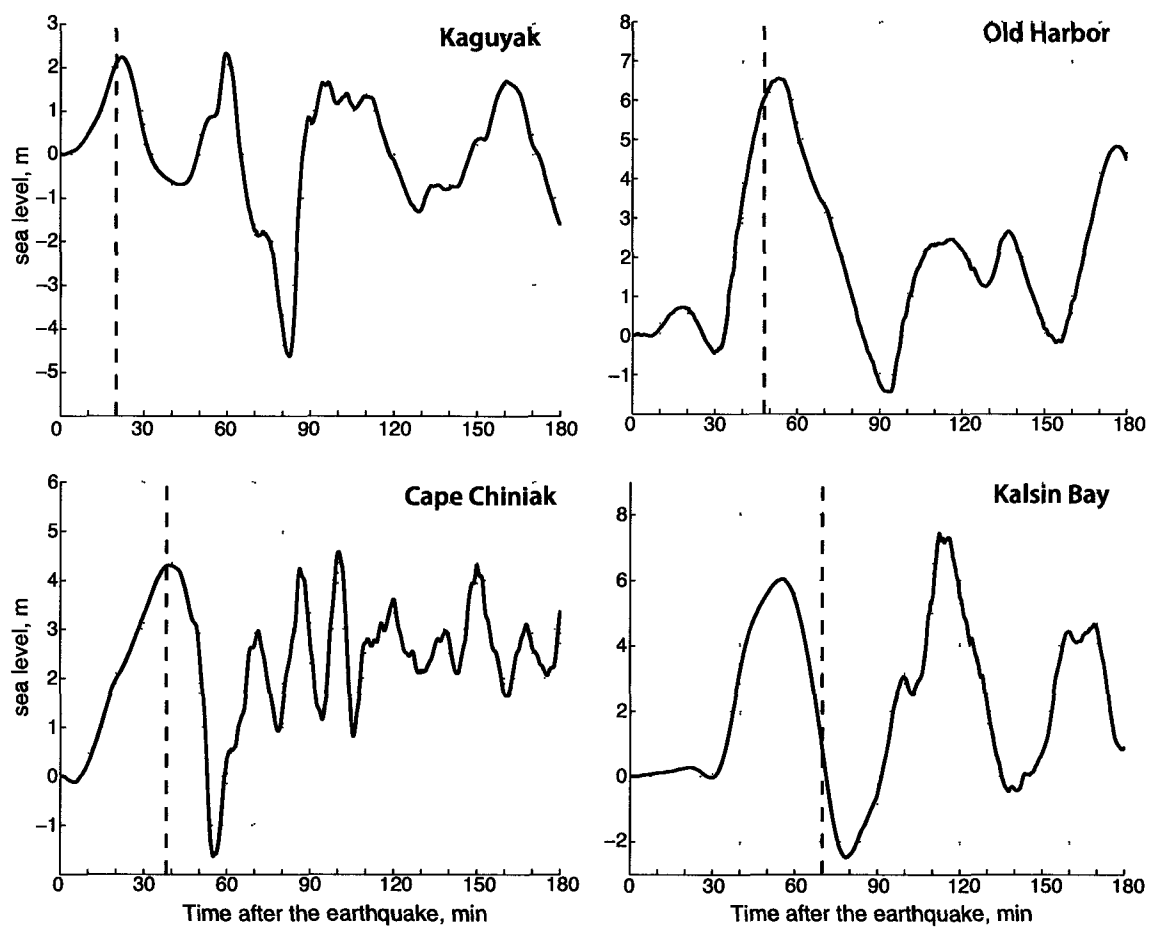


Figure 5.29: Simulated time series of tsunami waves at 4 locations on Kodiak Island. The initial conditions correspond to the deformation model shown in Figure 5.27. Dashed line on each graph indicates arrival of the first wave crest.

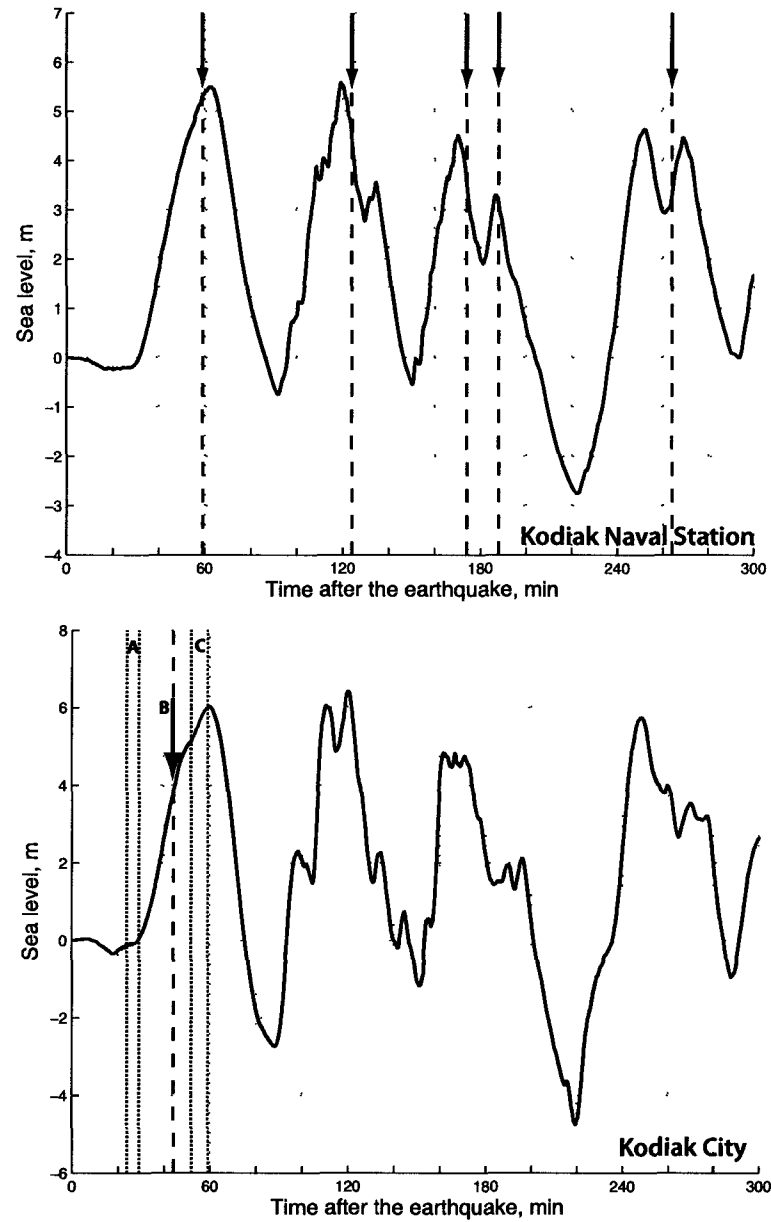


Figure 5.30: Simulated time series of tsunami waves at the Kodiak Naval Station and at the City of Kodiak. The initial conditions correspond to the deformation model shown in Figure 5.27. The arrows in the upper plot indicate the documented arrivals of the first five waves at the Naval Station. Letters A, B and C in the lower plot show observed arrivals of the first 3 waves in the City of Kodiak. The shaded areas indicate that the arrival time was within that interval.

Chapter 6

General Conclusions

The 1960 Chile, the 1964 Alaska, and the 2004 Indian Ocean tsunamis were generated by the three largest instrumentally recorded earthquakes. In all three events, the great majority of fatalities and most of the damage occurred in the near field. While existing numerical models were successful at predicting propagation of these tsunamis away from the source, they did not perform well in estimating effects of tsunami waves in the near field. The 1964 Alaska tsunami fits into this category of tsunami disasters for which near-field tsunami forecasting is challenging due to proximity of the large earthquake rupture zone to the coastal area, the complexity of slip distribution, and susceptibility of the glacial fjord environment to underwater slope failures. This thesis presents results of several near-field numerical modeling studies of tsunami waves produced by different sources during the M_w 9.2 1964 Alaska earthquake. The major tectonic tsunami was generated by the displacement of the ocean floor in the earthquake rupture area. This tectonic tsunami wave train propagated across the Pacific Ocean and was recorded as far as Australia and New Zealand. In addition, about 20 local landslide-generated tsunamis were caused by submarine mass failures from the steep fjord walls in a number of bays on Kenai Peninsula and in Prince William Sound.

I applied a viscous slide model coupled with nonlinear shallow water equations to study tsunami waves in Resurrection Bay, in south-central Alaska. The town of Seward, located at the head of Resurrection Bay, was hit hard by both tectonic and local landslide-generated tsunami waves during the 1964 earthquake. Resurrection Bay is a glacial fjord with large tidal ranges and sediments accumulating at a high rate on steep underwater slopes. These factors make the town vulnerable to locally generated waves produced by underwater slope failures. I utilized the recent geological findings of large-scale submarine slope failures in the bay during the 1964 earthquake, which estimated the total volume of underwater slide material that moved in Resurrection Bay during the earthquake to be about 211 million m^3 . The input data set included a high resolution multibeam bathymetry and LIDAR topography grid of Resurrection Bay, and an initial thickness of slide material based on pre- and post-earthquake bathymetry difference maps. The numerical modeling results confirmed the hypothesis proposed in recent geological studies that the earliest tsunami waves ob-

served in Seward resulted from multiple underwater landslides. I investigated the relative contributions of different submarine slide complexes and demonstrated that three slides in the upper bay were the major contributors of tsunami wave energy during and immediately after the earthquake. The numerical results showed good agreement with the observational data.

I used a numerical model of tsunami propagation and runup to study the inundation of Resurrection Bay and the town of Seward caused by the combined impact of landslide-generated waves and the tectonic tsunami. The numerical model employs nonlinear shallow water equations formulated for depth-averaged water fluxes, and calculates a temporal position of the shoreline using a free-surface moving boundary algorithm. The submarine mass failures generated local waves in the bay within 5 minutes of the beginning of strong ground motion, and the first tectonic tsunami wave arrived in Resurrection Bay about 30 minutes after the main shock and was about the same height as the local landslide-generated waves.

For simulation of tectonic tsunami runup, I derived the 1964 coseismic deformations from detailed slip distribution in the rupture area, and used that as an initial condition for propagation of the tectonic tsunami. To define a source for tectonic tsunami waves, I compared outputs of three coseismic deformation models of the 1964 earthquake and selected the model that fits the observations best. The numerical simulations of tectonic and landslide-generated tsunami runup in Resurrection Bay generated by the 1964 earthquake were consistent with observations of the tsunami wave sequence. Our numerical results agreed with the interpretation of the observed maximum tsunami runup at Seward and at the head of the bay as a composite inundation area. I demonstrated that the runup zone was a product of two events: the maximum runup at the Seward waterfront was produced by both local landslide-generated waves and the tectonic waves, and the areas next to the modern harbor, lagoon, and in the Resurrection River delta were flooded primarily by the tectonic tsunami. The calculated tsunami runup in Seward is in good agreement with observations of the inundation zone. The presented results also suggest that initial tsunami wave amplitudes in the source area of the 1964 earthquake, which are product of coseismic displacements, are crucial for the near-field tsunami modeling, and that the inundation results are sensitive to the fine structure of slip distribution.

I presented numerical modeling results for tsunami impact on the communities of Kodiak City and Kodiak Naval Station, Alaska, and analysis of observed and calculated tsunami time series and inundation zones. In this work two different coseismic deformation models of the 1964 rupture were used to generate the initial ocean surface displacement in the tsunami source region. The results of the near-field inundation modeling strongly depend on the slip distribution within the rupture area, because the complexity of the source function is combined with the proximity of the coastal zone. While the simulated runup agreed relatively well with the observed inundation, the calculated and observed arrival times at the Kodiak Naval Station were out of phase. Since the arrival times are more sensitive to the fine structure of the tsunami source than the inundation area, it was concluded that more research on the coseismic slip distribution around Kodiak is required for tsunami modeling studies.

I conducted the first near-field numerical modeling study of the 1964 tectonic tsunami source mechanism to examine the complex relationship between the tsunami wave field in the source area and regional coseismic slip in south-central Alaska. I analyzed the documented times and amplitudes of first arrivals, measured runup heights and inundation areas along the coasts of the Kenai Peninsula and Kodiak Island, which suggested that secondary splay faults played an important role in generating destructive tsunami waves. A numerical experiment was performed to test the hypothesis that a significant amount of slip needs to be placed on intraplate splay faults, and to evaluate the extent of these faults in order to explain the coseismic displacements and near-field tsunami observations. The newly revised coseismic deformation model of the 1964 earthquake extends the Patton Bay fault offshore beyond its mapped dimensions on land to about 150°W , which approximately corresponds to the boundary of plate coupling along the Kenai Peninsula coast derived from previous GPS and postseismic deformation studies. The results of tsunami numerical modeling in the Kodiak Island region demonstrated that the improved coseismic deformation model provided a good estimate of slip on the megathrust in the Kodiak asperity, and confirmed that it was an important feature of the 1964 tsunami generation mechanism. I showed that including deformation due to horizontal displacements in the source function resulted in an increase of far-field tsunami amplitudes at all distant locations, while this modification of the tsunami source produced only very localized effects in the near field.

The generation phase of tsunami evolution remains the biggest unknown in tsunami research. This is partially due to the fact that instrumental recordings of tsunami waves in the open ocean were unavailable until recently. The observations of tsunami waves propagating in the Pacific Ocean are currently provided by the NOAA's network of deep-ocean bottom pressure recorders coupled with the real-time reporting system, also known as DART. These deep-ocean tsunami records are used to solve the problem of reconstruction the slip distribution from far-field data, but the results of tsunami modeling using this source function won't be accurate for near-field forecasting in the tsunami source area. The solution could be a similar network located near the coast and on the continental shelf and slope, where tsunamis are generated. One example of such a network is the NEPTUNE Canada undersea observatory. This is the world's first regional cabled seafloor network that extends across the Cascadia subduction zone off the west coast of Vancouver Island and collects data in real time from an array of different ocean bottom instruments. The 6 stations are located at different depths, beginning from the continental shelf, then across the continental slope and abyssal plain to the mid-ocean ridge. The locations of bottom pressure sensors makes this network ideal for studies of tsunami generation by future Cascadia subduction zone earthquakes, accumulation and motion of sediments that could result in slope failures, and tsunami propagation across the continental slope and the shelf.

Looking into the future, one can hypothesize that instrumental recordings of tsunamis and other geophysical data from both deep ocean locations and near-shore cable networks will become more affordable, and more subduction zones will be covered with such undersea observatories. Then the amount of recorded data will be sufficient to perform accurate slip inversions for tsunami sources. Therefore, the results of the forward tsunami modeling in the far and near field can help to identify the important aspects of the tsunami generation mechanism that need to be taken into account by inversion studies. Based on the analysis of tsunami waves generated by the 1964 Great Alaska earthquake and the most recent 2004 Indian Ocean tsunami, these features of the tsunami source include the earthquake rupture propagating at finite spatially heterogeneous speed, the large displacements on the relatively steep splay faults, and the contribution of horizontal movements of the ocean floor into the initial tsunami amplitudes and kinetic energy.

The ultimate goal of tsunami research is to save lives. The success of any tsunami

mitigation program during future tsunami events will be determined by the survival rate of people living in the threatened communities, which largely depends on tsunami preparedness and public education about tsunami warning signs. For many locations in the Gulf of Alaska, the 1964 tsunami generated by the M_w 9.2 Great Alaska earthquake could be the credible worst-case tsunami scenario, since it was well documented and extensively studied. The numerical modeling studies included in this thesis benefit the Alaska Tsunami Inundation Mapping Project, which provides emergency managers in Alaska coastal communities with tsunami hazard assessment.

